The very early stage of the crystallization of thin PET films studied by ellipsometry, AFM, and grazing incidence X-ray scattering

Masaharu Ibaragi

(PhD Physics, Registration No: 100209185)

Submitted for the degree of Doctor of Philosophy

Department of Physics and Astronomy,
The University of Sheffield

September 2015

The University Of Sheffield.

Declaration

The work described in this thesis was undertaken at The University of Sheffield between October 2010 and September 2015 under the supervision of Professor Richard A. L. Jones. Unless stated, it is the work of the author and has not been submitted in whole or in part for any other degree at this or any other institution.

Masaharu Ibaragi
September 2015

The very early stage of the crystallization of thin PET films studied by ellipsometry, AFM, and grazing incidence X-ray scattering

Masaharu Ibaragi

Summary of Thesis

Chapter 1 introduces the background and importance of this thesis. Poly (ethylene terephthalate) (PET) is one of the most important polymer materials for industrial fields because of the good properties caused by its crystallinity, especially, control the kinetics of crystallization is a key technology for the productivity. Therefore, it is very useful to investigate the kinetics and mechanism of PET crystallization in detail. Usually, studies of crystallisation have focused only on the bulk state, but the surface is important in many practical materials, and there is reason to suppose that the mechanisms and kinetics of crystallisation in bulk and surface may be very different. Chapter 2 described the methodologies and theories of the experiments used in this study, that is, the protocol behind making thin PET samples, and the measurements used to study them; ellipsometry, atomic force microscopy, and grazing incidence X-ray scattering. In Chapter 3, how to make good samples, that is, the improvement in the surface roughness of thin PET films, was described in detail. The difficulty of making thin PET film samples was shown by reference to the literature and my original data, and the procedure introduced dealt successfully with these problems by choosing good combinations of solvents and making samples under suitable condition. In Chapter 4, I turn to sample aging, that is, the period after the sample is made, which strongly influences the kinetics or effectiveness of the crystallization, especially in the early stage (the induction time). I hypothesised that this aging effect was caused by a relaxation related to molecule conformations, that is, the relaxation by annealing before crystallization, which should increase the trans conformation. This is similar to the order of the PET molecules in the crystal, so pre-ordering or nucleation should take place more easily after this conformational change. In Chapter 5, the major data of this study, obtained by GI-WAXS, ellipsometry, and AFM, are introduced. Before crystallization starts, there was an

intermediate state, which was clearly different from both the amorphous and crystal states in the morphology. The size of this structure was around from 10 to 30 nm. This should be the pre-ordering present in thin PET film. The validity of results of measurements related to the pre-ordering and whether it detects the pre-ordering or not were discussed with the literature in Chapter 6. The length scale of the pre-ordering measured in this study was similar to the literature in which pre-ordering has previously been detected in bulk samples. And the influences of film thickness and annealing temperature were also discussed. Differences of crystallization and pre-ordering between bulk and thin films of PET with detailed data of kinetics were shown in Chapter 7. Basically, induction time and the crystal growth rate of thin films were longer and slower than those in the bulk as measured by ellipsometry. The explanation for this should be from the “thickness effect”. But effects due to the proximity to the free surface would emerge in thinner films, below 50 nm or so, and this could cause some interesting phenomenon because the surface effect is counter to the “thickness effect”.

Publicly presented work

1. IOP Polymer Physics Group Biennial Conference, The University of Sheffield, UK, 2013. Poster entitled “The very early stage of the crystallization of thin PET flilms studied by ellipsometry, AFM, and grazing incidence X-ray scattering”.

2. IOP Polymer Physics Group Biennial Conference, The University of Manchester, UK, 2015. Poster entitled “The very early stage of the crystallization of thin PET flilms studied by ellipsometry, AFM, and grazing incidence X-ray scattering”.

Acknowledgements

First and foremost I would like to thank Richard Jones for his supervision and support throughout this project. He has provided constant encouragement and guidance whilst allowing me a high level of freedom that has enabled me to learn how to work independently. He has spent considerable time and effort with me in the 5 years of my doctoral course. I sincerely appreciate this and the wonderful opportunity to study under such a brilliant and great professor.

Andrew Parnell is acknowledged for his exceptional contribution to the project on a day-to-day basis, partly through his splendid experience with the experimental system and his unfading energy and enthusiasm for performing research. He is especially acknowledged for his contribution to experiments in synchrotron facilities, where he has consistently gone above and beyond the call of duty in his efforts to enable the team to take home the best possible data. He has always supported me both officially and privately during my time in Sheffield and after come back to Japan. There are not enough words to express my gratitude.

Mark Latham is acknowledged for his excellent contribution to the project especially experiments at synchrotron facilities. He discussed the technical points in my experiments with me and it was actually great help for my study. He also gave me very sincere friendship and encouraged me very much during my PhD.

Yohei Kamata is acknowledged for his brilliant contribution to the project on experiments and data analysis. His GI-WAXD experiments and data for my samples were a good reference and helped the direction of my study. He also helped me privately very much.

Andrew Dennison and Daniel Toolan are acknowledged for their great help with synchrotron experiments, along with Simon Brown at ESRF and Andrew Smith at Diamond.

Nicholas Mullin is acknowledged for useful discussions and technical helps about AFM. Alan Dunbar, Mike Weir, and Tao Wang are also acknowledged for their sincere instructions and discussions about the project, especially how to use the Woollam M-2000V ellipsometer.

Sasha Mykhaylyk, Patrick Fairclough, Mark Geoghegan, and Jamie Hobbs are acknowledged for their higher academic advice and instructions for the project in discussions and interviews.

Rita Saddler is acknowledged for her sincere help about my administrative work in the University. Amy Hall, Ana Lorena, Youmna Mouhamad, Ateyyah AL-Baradi, Yu Pen, Warren Taylor, Maryam Raftari, and Christopher Clarkson are also acknowledged for their kind friendship. They all encouraged and advised me when I was in trouble or depressed, and spared brilliant time during my time in Sheffield.

Tetsuo Mohri, Takayuki Ikehara, Mikihito Takenaka, and Hajime Tanaka are acknowledged for introducing Professor Richard Jones to me and their kind instruction and advice for my stay in Sheffield. Without their great help, I could not be in Sheffield.

Misao Hashimoto, Masaaki Igarashi, Tsutomu Sugiura, Yuji Kubo, Kenichi Uemura, Koichi Nose, Hiroshi Kajiro, and Shinichi Terashima are acknowledged for kind understanding and cooperation to study in Sheffield from Nippon Steel & Sumitomo Metal Corporation. They always encouraged me to acquire the doctoral degree and covered many things during my absence. Toyoji Aoki and Saya Kuroda are also acknowledged for their sincere support to live abroad from our company. They always guided me and solved many problems and troubles during my time in UK.

My wife Yuko has always provided a huge amount of help, belief and understanding during the five years of my PhD to date with my daughter Hanae. She has shown great patience and has been a steady foundation during the emotional roller-coaster of research.

My sincerest thanks go to my family, in particular my parents Yasuyuki and Eiko, my sister and brother Miho and Masaaki, my parents in law Noriyasu Saito and Chizuko Saito, and my sister in law Hisako Saito.

Finally there are many people I wish to thank for making Sheffield a great place to work but they are far too numerous to list here.

Symbols and abbreviations

a	Molecule stem diameter
AFM	Atomic Force Microscope
B	Positive coefficient
DSC	Differential scanning calorimeter
FTIR	Fourier Transform Infrared Spectroscopy
Δg	The change amount of free energy
G(D)	The crystal growth rate in a film of thickness D
G(∞)	The crystal growth rate in the bulk
GI-SAXS	Grazing Incidence Small Angle X-ray Scattering
GI-WAXS	Grazing Incidence Wide Angle X-ray Scattering
HFIP	1,1,1,3,3,3-Hexafluoro-2-propanol
ΔH_m	The latent heat of melting per unit volume
l	crystal lamella thickness
l^*	crystal lamella thickness when the crystal growth rate is maximum
M_n	number-average molar mass
M_w	weight-average molar mass
PE	Polyethylene
PET	Poly (ethylene terephthalate)
PP	Polypropylene
PS	Polystyrene
PSD	Power Spectrum Density
Q	scattering vector
q	cantilever quality factor
R^p	Fresnel reflection coefficients of p-waves in elliptically polarized light
R^s	Fresnel reflection coefficients of s-waves in elliptically polarized light
RMS	root mean square
ΔS	The reduction in entropy
SAXS	Small angle X-ray scattering
SANS	Small angle neutron beam scattering
Si	Silicon
t	Time
T	Temperature

T_m	Melting point
$T_m(\infty)$	Ideal thermodynamic value
T_0	The Vogel-Fulcher temperature
T_c	the temperature of the maximum nucleation rate
T_{CM}	Transition temperature of mesophase and crystal phase
T_{cb}	critical temperature for binodal separation of fluid (or amorphous polymer) and crystal
T_g	Glass transition temperature
$T_{g,1}$	Glass transition temperatures of a surface layer
$T_{g,2}$	Glass transition temperatures of a bulk(intermediate) layer
$T_{g,3}$	Glass transition temperatures of a layer near substrate
$T_{g,bulk}$	Glass transition temperatures of a bulk sample
$T_{g.s}$	Glass transition temperature of the surface
TGA	Thermal Gravity Analysis
WAXD	Wide angle X-ray diffraction
z	Rate coefficient in the Avrami exponent
α	incident angle
$ß$	The Avrami exponent.
Δ	phase difference in elliptically polarized light
δ	solubility parameter
μ	Dimensionless constant
v	Crystal growth velocity
λ	wavelength in nitrogen
λ_1	texture length scale observed by AFM
λ_2	texture length scale observed by GI-SAXS
σ_f	Substantial inter facial energy
τ_0^{-1}	Microscopic frequency at the Vogel-Fulcher temperature
$ø_c$	Crystal degree
Ψ	amplitude ratio in elliptically polarized light

Contents

Chapter 1

Introduction and Literature review

1.1 Background of this study

Poly (ethylene terephthalate) (PET) is one of the most important engineering plastic materials currently used industrially. I say this because this material is used for many applications, for example, liquid crystal displays, plastic bottles, protective films, the fibres of clothes, laminated steel materials [1], and so on [2]. PET film is also used for many potential and emerging technology applications of the future, for example, as the backsheet (rear cover) of Silicon photovoltaic power devices (Solar panel) [3, 4]. The development of PET for advanced applications in electronics and energy devices, such as printed electronics, represented by flexible flat displays or flexible photovoltaic is certainly progressing. It is the case that PET is quite essential as a polymer material because of its promise for future technologies and also the current everyday use of PET in human life [5, 6, 7]. The reason why PET is useful and used for so many applications in the world is because PET has tolerance to high temperature and also possesses high tensile strength. This combination of desirable properties is in part caused by the crystalline microstructure of PET. Detailed studies of PET crystallization would enable more advanced technologies and other applications in the future. In addition, PET is often used as a bare material or laminated with other materials in practical use. Therefore the analysis of PET surface behaviour is very important as there are also many interesting deviations from bulk like behaviour of polymers at surfaces or interfaces. These differences may well cause differences in crystallization between bulk and surface. The study of thin films is an effective method to investigate the properties of polymer surfaces or interfaces, because thin films have much larger proportion of surface and interface area than bulk samples.

For these reasons, I have performed a detailed study of PET crystallinity, especially the very early stage of crystallization in thin PET films. This work examines and clarifies the crystallization kinetics of PET thin films, also to observe differences in pre-ordering between bulk and thin films, and to reveal and to consider the unique properties in the crystallization of the PET thin films, due to thin film geometry. Because the investigation of the early stage of the crystallization is very important for this purpose, I focused especially on the very early stage of crystallisation from an entirely amorphous film. Besides, the initial stages of crystallization are very important for industrial fields as the initial state influences crystal morphologies and growth kinetics, as the performance of PET based goods and being able to manufacture products effectively depends on them.

In this thesis I report the survey of the background physics and key research literature, the method and details of the experiments, how to make good PET thin film samples, the results, discussion, and future work. In this study of PET thin films, Ellipsometry, Atomic Force Microscope (AFM), Grazing Incidence X-ray scattering were used to investigate the early crystallization of thin PET films. Ellipsometry analysis of thin films is highly effective to estimate the thickness of polymer films [8, 9, 10] and it was used for measurements of the film thickness change with time and temperature, to follow the kinetics of crystallization. AFM was used for observations of the film surface and crystal morphologies. Grazing Incidence Wide Angle X-ray Scattering (GI-WAXS) was adopted to analyse the crystalline structure of thin PET films and Grazing Incidence Small Angle X-ray Scattering (GI-SAXS) was utilized to observe the pre-ordering of the PET crystals.

1.2 Polymers

A polymer is a giant molecule made up of many repeat units covalently joint together in the form of a long chain, and is also known as a macromolecule. Usually polymers represent organic compounds, containing carbon atoms together with hydrogen, oxygen, nitrogen, and halogens, etc. The schematic image of a typical polymer is shown as Figure 1.1 with the repeating structure of polyethylene and the monomer unit on its own. In this case, the repeat unit, or monomer, is ethylene and this unit building up of many monomers into a chain as a polymer, termed polyethylene. If the monomer unit is

changed, of course it is possible to make many other kinds of polymer materials. The structure of PET monomer is shown in Figure 1.2 [11]. The monomer of PET is synthesized by ethylene glycol and terephthalic acid with dehydration, and here the value of n indicates the number of monomers in a particular macromolecule. This is related to the degree of polymerization or the average molecule weight (M_w) and influences many important properties of polymer materials. We can see very easily that polymer materials have infinite potential because of the infinite number of combinations of monomers and molecular weight. That is, the physical properties have a lot of variability and are controlled by tuning monomer chemistry and molecular weight.

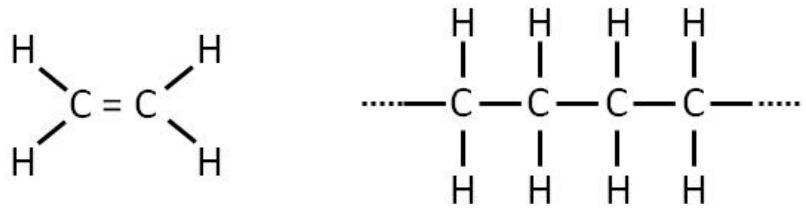

Figure 1.1: Structure images of ethylene and polyethylene.

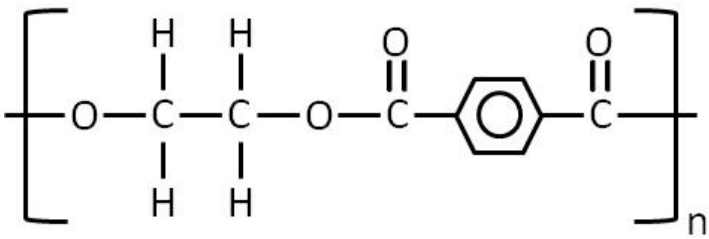

Figure 1.2: Structural image of Poly (ethylene terephthalate) (PET). PET is synthesized by ethylene glycol and terephthalic acid with hydration, and n indicates the number of monomers in a macromolecule [11].

Long chain molecules show very interesting properties different from small organic molecules, non-organic materials, or metallic materials, for example, they exhibit very strong viscoelasticity effects. The behaviour of the glass transition in polymers is also another vitally important effect in polymer and understanding it is very important in polymer physics and has effects on the crystallization kinetics. There are many other kinds of transitions in polymer materials, for instance, crystallization, melting, and relaxation phenomena.

A glass is a material which is identical in its state of order with a liquid, that is to say, it has some short-range order but no long-range order, but which behaves

mechanically like a solid. The temperature at which the system drops out of equilibrium is known as the glass transition temperature and is marked by changes in certain easily measurable thermodynamic properties of polymer; for example, at the glass transition the heat capacity and expansivity change discontinuously. In addition, around the glass transition temperature, mechanical properties change very rapidly, resulting in the familiar contrast between the rather stiff behaviour of a polymer glass and the rubbery properties of a polymer melt of high relative molecular mass. Polymer glasses can be considered as static and immobile, but, at above the glass transition temperature, individual chains and chain segments are able to move relative to one another. I would like to add to the description of glass transition state that as a polymer melt is cooled enough, the segmental mobility decreases until a temperature is reached at which the timescale of polymer motion is out of the experimental time scale [12].

The crystallization and melting point is the clearest thermal transition for crystalline polymers such as PET. Usually, crystalline polymers are semi-crystalline, consisting of a composite of very small crystals in a matrix of much less ordered material, with a fraction of between 20% and 60% of the material being present in the crystalline state [13]. Polymer crystals consist of chain-folded structures with partially aligned or packed molecules. The melt is reverse process of crystallization, that is, the molecular alignment become loose and disordered and the molecules move and diffuse randomly. However, as polymers are entangled (above the entanglement molecular weight), so it takes a long time for molecules to arrange themselves in crystals. Even quite modest cooling rates allow one to produce a glass. Basically, it is difficult to apply polymers to the equilibrium state of thermodynamics because of the slow kinetics caused by long chain molecules and entanglement. Therefore, most polymer materials are considered as semi-crystalline polymers although some of them are crystalline as equilibrium structures. The nature of crystallization is described in more detail in Chapter 1.3.

In glassy polymers, large-scale conformational changes are inhibited but the possibility of localized conformational transitions remains. These can be observed macroscopically, for example, as a detectable change in the shape of the loaded sample results, which can be related to a single characteristic time only. And we also need to consider the passage from a non-equilibrium situation, created by the sudden imposition of an external field, to the new equilibrium. The change is accompanied and driven by a decrease in the free energy. Using mechanistic terms one could say that a system that at first, when having an enhanced free energy, is ‘strained’, ‘relaxes’ while going to the

equilibrium. Correspondingly, all these retarded transitions into a new equilibrium are generally addressed as relaxation processes [14].

Representative relaxation is the configuration of the molecules. The relaxation time assumes a temperature dependence that strongly departs from the temperature dependence of the characteristic time of vibrations of molecules. The configurational relaxation time appears to diverge at a finite temperature, the Vogel-Fulcher temperature. Experimentally, it is found that the temperature dependence of the relaxation time, and thus the viscosity, follows an empirical law known as the Vogel-Fulcher law [15].

In my study, some transitions and relaxations are key factors because the kinetics of crystallization or pre-ordering are influenced by polymer chain mobility, configurations, or conformations of molecules. I describe how these factors are related to the early stage of crystallization in later chapters.

1.3 Crystallization of polymers

It is important to understand the general nature of crystallization of polymer materials to investigate the early stage of crystallization in thin films. Crystals of polymers are composed of stacked layers and can be partially crystalline or semi-crystalline [13, 16]. Crystalline polymers have a hierarchical structure, that is there are different structures on different length scales. The basic unit of most polymer crystals is the chain-folded lamellae. The lamellar thickness l is independent of molecular weight and a typical value for l would be about 10 nm. Lamellae are separated by amorphous non-crystalline regions.

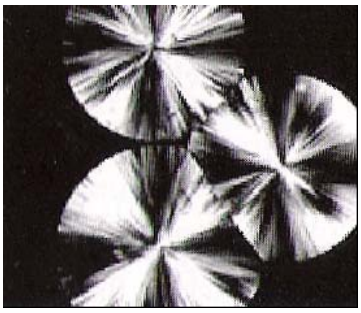

Figure 1.3: An optical microscope image of typical Spherulite of poly(L-lactic acid) under crossed polarizers [16].

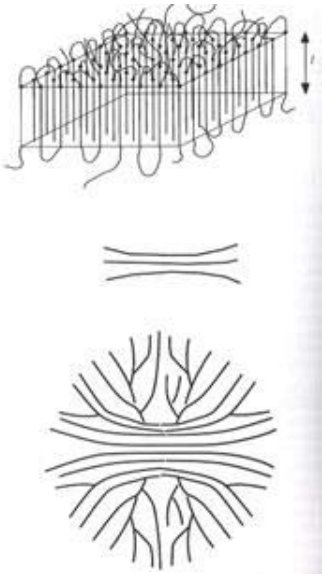

Figure 1.4: Scheme of polymer crystal structures; A chain-folded lamella (the basic unit in semi-crystalline polymer), three lamellae, and spherulite from lamellae radiating and branching from a central nucleus [13].

The chain-folded lamellae are themselves organised into larger scale structures called spherulites, as shown as Figure 1.3. These structures consist of sheaves of individual lamellae which grow out from a central nucleus, until finally the whole space is filled by these structures. Figure 1.4 illustrates a scheme of these hierarchical structures.

The initial stage of crystallization is to straighten the individual molecules. The free energy change of crystallization has to compensate for the loss of entropy associated with straightening. The nucleation steps of crystals are progressed via an embryo (Concentration fluctuations from the bulk) [17]. Thermal fluctuations form in these melt

embryos, i.e., particles with an enhanced inner order. If the size of an embryo surpasses a critical value it turns into the nucleus of a growing crystal; smaller embryos disappear again. Nucleation is a bulk property to be described by a rate, τ_{nuc}^{-1}, per unit volume. Experiments on ensembles of μm sized melt droplets allow a determination when the nucleation time τ_{nuc} is much longer than the time required by the expanding crystallite to cover the whole droplet. In general, the nucleation occurs heterogeneously; the nucleation is induced by some triggers, for example, nucleation agents or impurities, on the other hand, homogeneous nucleation; the nucleation occurs homogeneously without any triggers, is not the usual case. Under practical conditions, nucleation mostly starts on the surface of low molar mass particles, which come into the sample either uncontrolled, or deliberately as nucleating agents.

In one view of crystallisation, mesophases play an important role. Mesophases are states in which the degree of molecular order between the amorphous melt and full crystallisation. Mesophases are important for crystallization because the packing of molecules occurs through mesophases. The crystallization scheme is separated into three parts, (1)T >> T_g : lamellar crystal, (2)quench to $T \leq T_g$: small lamellar crystal, (3)$T > T_{CM}$: extended chain crystal. Here, T is temperature, T_g is the glass transition temperature, and T_{CM} is the transition temperature of mesophase and crystal phase [18]. Strobl has suggested a scheme for these kinds of mesophases which is shown in Figure 1.5[16, 19]. In his report, a multistage model is shown as follows. Rather than directly attached to the crystal surface, chain segments of the melt are first incorporated in a thin layer with mesomorphic structure in front of the crystallite. The mesomorphic layer thickens spontaneously. When a critical thickness is reached, a crystal block forms by a first-order transition. In the last step the excess energy of the fold surface is reduced. This mesophase model is different from models invoking nucleation or crystallization through spinodal decomposition, although both involve some kind of intermediate state between amorphous and crystal.

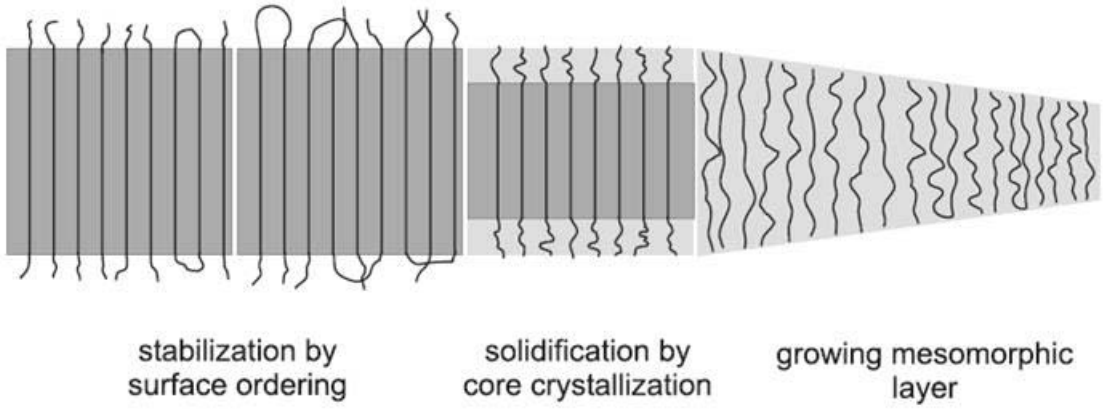

Figure 1.5: Scheme of polymer crystallization from mesophase, multistage model of polymer crystal growth, suggested by Strobl [16].

The studies of Kaji and Imai changed the situation of traditional theories of polymer crystallization. The molecule ordering before crystallization is different from the mesophase and was proved by clear experimental data, summarised by the formula "SAXS before WAXD". This phenomenon is described as follows by Kaji *et al*. [20]. In 1967 Yeh and Geil reported the novel structure of the so-called nodules, with ball-like particles with an average diameter of 7.5 nm and average interparticle spacing of about 12 nm, which was observed in the melt quenched amorphous glass of poly(ethylene terephthalate) (PET) by electron microscopy [20, 21]. On the basis of this observation, Yeh proposed a model with ordered domains of loosely folded chains for the amorphous structure of polymers, called the folded-chain fringed micellar grain model [20, 22]. This model caused great controversy at the time [20, 23, 24] because it contradicted Flory's well-known theoretical model[20, 25] predicting that the amorphous structure is orderless and consists of homogeneously interpenetrated Gaussian (or ideal) polymer chains. Imai *et al.* carried out SAXS studies on the structural changes that take place during the induction period of the crystallization of PET, which led to the surprising finding that some kind of spinodal decomposition really occurs during the induction period before primary crystal nucleation [20, 26, 27]. It was noted that the initial characteristic wavelength was about 15 nm, which agrees well with the above-mentioned inter-nodular spacing. This was a controversial finding but is now more widely accepted.

Olmsted et al suggested a new interesting theory of pre-ordering of molecules by spinodal decomposition before crystallization as follows [28]. The coupling between density and chain conformation induces a liquid-liquid binodal within the equilibrium liquid/crystal solid coexistence region. At low enough temperatures, the liquid branch

gives a spinodal buried entirely within the equilibrium liquid/crystal coexistence region. If a melt is quenched inside the spinodal described in a phase diagram, it will phase separate into two coexisting liquids, given by the common tangent construction, with a coarsening interconnected domain texture. The two liquids differ in their distributions of conformations, with the denser liquid adopting a distribution closer to that needed for crystalline packing. One of the coexisting liquids is closer in density and conformation to the crystal phase than the original melt, and has a lower energy barrier to crystallization, so inducing "spinodal-assisted nucleation." My simplified understanding of this theory is that the density fluctuation caused from spinodal decomposition induces nucleation or an embryo, and the mechanism of this is different from other kinds of early stage crystallization. In the crystallization induced by spinodal decomposition, the role of molecules located together side by side is all that is needed, in the dense area they are weakly ordered and the other domain the molecules exist randomly like a liquid state and nucleating agents are not needed. Polymer long chains often make this dense part by folding own chain and become a chain-folded lamella. But this recently suggested theory insisting that the combination of density fluctuation and chain order is one of triggers of crystallization is still regarded by some with scepticism compared with classical mechanisms of crystallization through mesophase or heterogeneous nucleation. The main point of mesophase is that the ordering molecules make a barrier of activation energy of nucleation low, on the other hand, the spinodal decomposition proceeds nucleation spontaneously by the density fluctuation and it basically does not need an activation energy of nucleation. Besides, there are a still a number of problems, for example, to begin with, why does the density fluctuation occur? We do not have a clear answer to whether spinodal decomposition is necessary for this kind of nucleation or crystallization or not.

Shear also enhances the kinetic role of the hidden binodal. Mykhaylyk *et al* also reported that in rotating parallel-plate flow, that is, under shear conditions, a clear boundary is observed between oriented and unoriented material which is dependent on both the shear rate and the total strain [29]. The necessary conditions for the formation of oriented nuclei are that the shear rate should be larger than the inverse Rouse time of the longest chain in the ensemble and that mechanical work above a critical threshold is required. Under this shear situation, the shish-kebab structure is often observed. This structure is an oriented spherulite formed by shear stress. The onset of long-range ordering prior to crystal growth was revealed by Terrill *et al*. [30]. Pre-nucleation density fluctuations play an integral role in the nucleation of polymer crystallization.

We can imagine that the kinetics of the early stage of crystallization is influenced very much by how the mechanisms for making nuclei or crystal embryos, as discussed in these reports. I will discuss the relationship between my data and theories, which are mainly related to the intermediate state of crystals in Chapters 6 and 7.

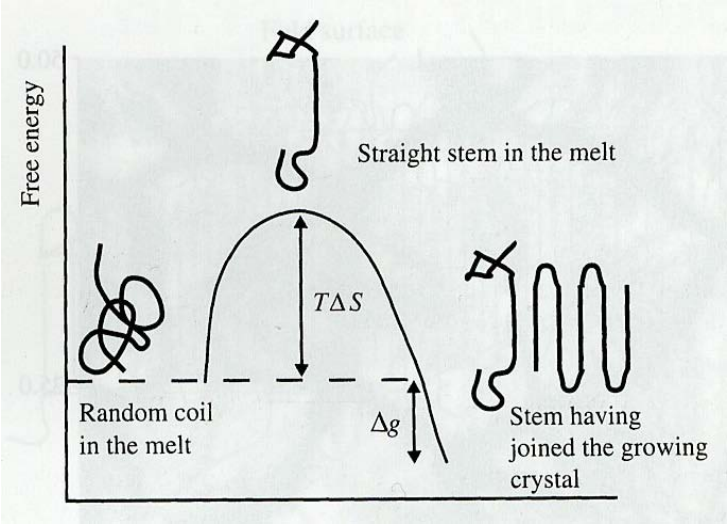

Figure 1.6: Free energy changes when a stem of polymer joins the growing crystal from the melt [13].

Building up of a spherulite becomes a sequential process where some rapidly growing dominant lamellae at first set up a scaffold frame that is subsequently filled by slower growing subsidiary lamellae. The crystal growth velocity then depends on the temperature and lamellae thickness. There is a balance between temperature and thickness related to a free energy of crystallization. This kind of fundamental crystal theory is written in text books discussed as follows, for example, [13]. Figure 1.6 shows that In order to join a polymer chain to the crystal, a polymer chain which has random configuration in the melt must straighten itself out at first [13]. This leads to a reduction in entropy ΔS. Only when a random fluctuation has changed to such a straight length of chain can join the growing crystal lamellae, finishing up with a free energy Δg lower than its energy in the melt. Δg is written as follows considering the change in free energy when one polymer stem, of length *l*, joins the crystal if the cross sectional area of the stem is a^2.

$$\Delta g = -\frac{\Delta H_m \Delta T}{T_m(\infty)} l a^2 + 2a^2 \sigma_f \qquad (1.1)$$

Here, l is crystal lamellar thickness, a is molecule stem diameter, ΔH_m is the latent heat of melting per unit volume, T is temperature, $\Delta T = T_m(\infty) - T$, $T_m(\infty)$ is ideal thermodynamic value of $T_m(l)$, the melting point of the crystal lamellar thickness l, σ_f is an inter facial energy.

Now, we can estimate both the rate at which segments leave the crystal to rejoin the melt as follows.

$$\text{melt} \rightarrow \text{crystal rate} = \tau^{-1} \exp\left(-\frac{\Delta S}{k_B}\right)$$
$$\text{crystal} \rightarrow \text{melt rate} = \tau^{-1} \exp\left(-\frac{(T\Delta S - \Delta g)}{k_B T}\right) \qquad (1.2)$$

where τ^{-1} is a microscopic frequency. The difference between these two rates gives us the net crystallisation rate u, defined as the number of stems attached to a given site per unit time as follows.

$$u = \tau^{-1} \exp\left(-\frac{\Delta S}{k_B}\right)\left[1 - \exp\left(\frac{\Delta g}{k_B T}\right)\right] \qquad (1.3)$$

In order to simplify this equation, we can assume that $\Delta g / k_B T$ is small enough to expand the exponential. Writing for the velocity of crystal growth v is as follows.

$$v = a\tau^{-1} \exp\left(-\frac{\Delta S}{k_B}\right)\frac{\Delta g}{k_B T} \qquad (1.4)$$

The velocity of crystal growth has the dependence on the thickness of the crystal l [13]. The entropy loss ΔS, in equation 1.1, on straightening out a length l of the chain is proportional to the number of segments in the length to be straightened. If we write $\Delta S = \mu\ l/a$ where μ is a dimensionless constant. This gives us

$$v(l) = (\text{constant})\left(2a^2\sigma_f - \frac{\Delta H_m \Delta T_m}{T_m(\infty)} la^2\right)\exp\left(-\frac{\mu l}{a}\right) \qquad (1.5)$$

This equation expresses that there is a certain thickness l^* for which the growth rate is a maximum [13]. We can find l^* by differentiating equation 1.5; this yields

$$l^* = \frac{a}{\mu} + \frac{2\sigma_f T_m(\infty)}{\Delta H_m (T_m(\infty) - T)} \qquad (1.6)$$

Here, μ is a dimensionless constant. We see that the deeper the quench the thinner the resulting crystals will be. We can also use this approach to predict the temperature dependence of the crystal growth rate. To do this we simply substitute the fastest growing crystal thickness *l** from equation 1.6 into the crystal growth velocity, equation 1.5. The important point here is what determines the microscopic frequency τ^{-1}. This gives a measure of the rate of conformational rearrangements of a polymer coil in melt. These conformational rearrangements involve the complicated internal dynamics of a polymer chain. From the principle of time-temperature superposition, we can write the microscopic frequency, τ^{-1}, in the Vogel Fulcher form as follows [13].

$$\tau^{-1} = \tau_0^{-1} \exp\left(\frac{-B}{T - T_0}\right) \qquad (1.7)$$

Here, τ_0^{-1} is a microscopic frequency at the Vogel-Fulcher temperature, *B* is a positive

coefficient, T_0 is the Vogel-Fulcher temperature,

Putting all this together, we can find the kinetics of crystal growth, that is growth velocity *v*, is described below (Equation 1.8) [13].

$$v = \frac{a\tau_0^{-1}}{ek_B T} \frac{a^3}{\mu} \frac{\Delta H_m \Delta T}{T_m(\infty)} \exp\left(\frac{-B}{T - T_0}\right) \exp\left(\frac{2\mu\sigma_f T_m(\infty)}{a\Delta H_m \Delta T}\right) \qquad (1.9)$$

The Avrami equation, equation 1.9, indicates the growth shapes of crystals.

$$\phi_c(t) \propto 1 - \exp -(zt)^{\beta} \qquad (1.10)$$

Here, *t* is the time, $\varnothing_c$ is the crystallinity, *z* is the rate coefficient, *ß* is the Avrami exponent. The coefficient *ß* = 3 indicates growth of a constant number density of spheres with a constant rate. Crystallization occurs from molecule bundles and this bundle model can be described statistically [18]. We have many choices for defining crystallinity and the selection depends on the method of determination. For example, we can define the crystallinity of a sample by a measurement of the density of a sample, because the density of the crystal and amorphous phases are different. Other methods

such as X-ray scattering, Raman spectra, Nuclear magnetic resonance spectroscopy (NMR), and Differential scanning calorimeter (DSC) are also generally used.

Secondary crystallizaion often occurs in polymer crystals [31]. The crystallization is not finished at the first chosen crystallization temperature and continues on cooling to room temperature, proceeding by two different modes of secondary crystallization. Especially broad crystallization and melting ranges are observed for polymers that include a small amount of a non-crystallizable co-unit, such as short-chain branches or chemically different monomers. Sometimes, secondary crystallization produces larger crystals than the initial primary crystallization process. Surface crystallization and melting are important for my project and related to this secondary crystallization mechanism. The structures of the amorphous intercrystalline layers in a semicrystalline polymer are different from a polymer melt because all the chain sequences are fixed with their ends in the crystallites and the concentration of entanglements is enhanced. A shift in the crystal/amorphous interface necessitates a rearrangement of the chains within the crystallites, which can only be accomplished if the chains possess sufficient mobility within the crystals. I have to consider the features of these rearrangements in my work on surface crystals.

1.4 Polymer physics in thin films and the surface

Polymer thin films often have particular physics different from that of the bulk. This is mainly caused by the strong surface effect and the constrained, narrow volume for macromolecules. I would like to discuss the basic nature of surfaces first.

A surface tension is observed at the surface contacting a liquid droplet. The surface of a fluid behaves as if it were a taut membrane; if one cuts such a membrane one has to apply a given force per unit length of cut to hold the surface together. Thus surface tension has the dimensions of a force per unit length. This must be numerically equal to the free energy of the surface [32]. This surface energy is mainly determined by the cohesive forces of molecules, that is, intermolecular forces such as hydrogen bonds. Interfacial tensions and surface tensions of solids can also be considered and measured by free energy, using the concepts of contact angle and wetting. These surface tensions are functions of temperature, because they are related to free energy, and generally, surface tension is reduced at higher temperatures. Surface tensions also a function of

molecular weight, and surface tension increases at higher molecular weight. As described above, surface tensions are determined by the intermolecular forces, and intermolecular forces reduce at elevated temperature because of higher molecule mobility and increase at higher molecular weight, for example, polymers, because a polymer has a higher melting point than its constituent monomers or oligomers. Density is also related to surface tension. A higher density indicates higher intermolecular forces, as a result, it is associated with higher surface tensions.

The dynamics of the polymer surface may be different from those of the bulk because the polymer segments near a surface are mobile enough to reach full thermodynamic equilibrium, but for the chains in the bulk this is not so. We can call this a surface effect. Representative surface effects of thin polymer films are the reduction in the glass transition temperature and also the increase of thermal expansion rate, as reported below.

Keddie, Cory and Jones, and Kawana *et al*, and many other researchers, have reported that the glass transition temperature of polymers films decreases as the thickness of the film is reduced [8, 9, 10].

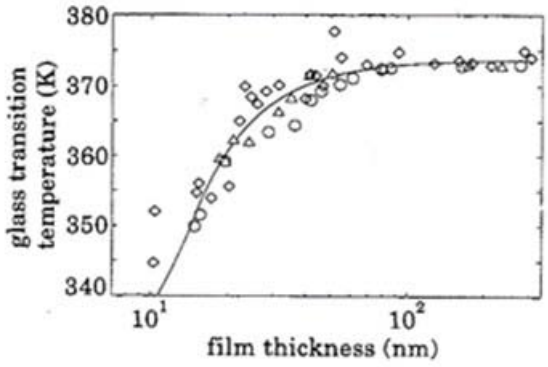

Figure 1.7: The glass transition temperature T_g as a function of film thickness for polystyrene (PS) [8].

Figure 1.7 shows T_g vs film thickness for polystyrene (PS) films measured using ellipsometry. The surface of the glassy film is thought to possess a liquid like layer whose size diverges as the glass transition temperature. When polymer films are thin that a reduction in thickness leads to a reduction in overall T_g, the surface-layer T_g actually increases with a reduction in overall thickness, whereas the substrate-layer T_g decreases (Figure 1.8) [33]. Torkelson *et al.* also determined that the enhancement of dynamics at a surface affects T_g several tens of nanometres into the film. The extent to

which dynamics smoothly transition from enhanced to bulk states depends strongly on nano-scale confinement effects. These results indicate that the gradient in T_g dynamics is not abrupt, and that the size of a cooperatively rearranging region (CRR) is much smaller than the distance over which interfacial effects propagate [33]. From the literature, local relaxation occurs in a CRR by collective motion of many small molecules or polymer segments. The accepted size of a CRR near Tg ranges from 1 to 4nm. However, the length scale at which confined glass formers deviate from bulk Tg is typically larger than the size of a CRR.

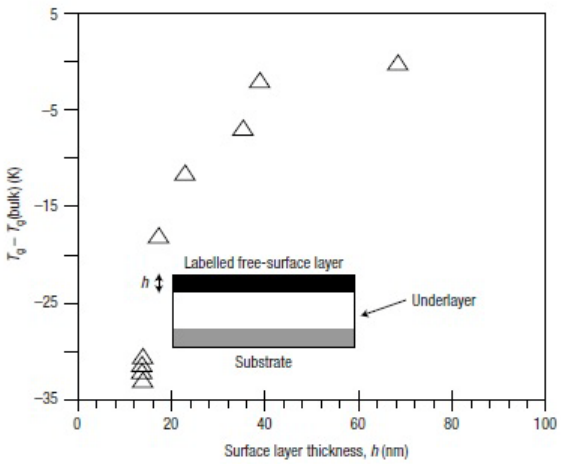

Figure 1.8: T_g-T_g(bulk) identified by fluorescence for pyrene-labelled PS free-Surface layers of variable thickness placed on top of constant bulk-like (~270 nm) unlabelled PS underlayers [33].

The cooperative segmental mobility of an ultrathin film may be expected to have an anomalously broad relaxation distribution [34]. For thinner films the transition width is broadened, while the strength of the transition, defined by the difference between the expansivities in the liquid and glassy state, is reduced [10]. The expansivity in the glassy state is higher than the amorphous part in the bulk. A layer of roughly constant thickness, of order 10 nm, near the surface of the film has liquidlike thermal properties

Because of the surface effect mentioned above, physics in thin polymer films are somewhat different from the bulk. Therefore it follows that the theories of crystallization in thin films are considered to differ from those of the bulk. There are many studies of the crystallization of thin polymer films and most of them show that basic crystal unit is the same in both thin films and bulk. But the crystallization kinetics, crystallinity, or macro structures in thin films are different from the bulks. The crystallization of some polymer thin films grow by propagating waves of dendritic arms [35]. The growth pulsation period increases sharply with decreasing film thickness. In thin films of polypropylene, the centres of spherulites are found to consist invariably of complex arrays of intercrossing lamellae [36]. Radiating from the central regions are frondlike growths fronts. Each of the fronds is composed of a cluster of ribbonlike leaders covered with dense arrays of lamellar branches. Branching is initiated on the thin (010) faces of the lamellae.

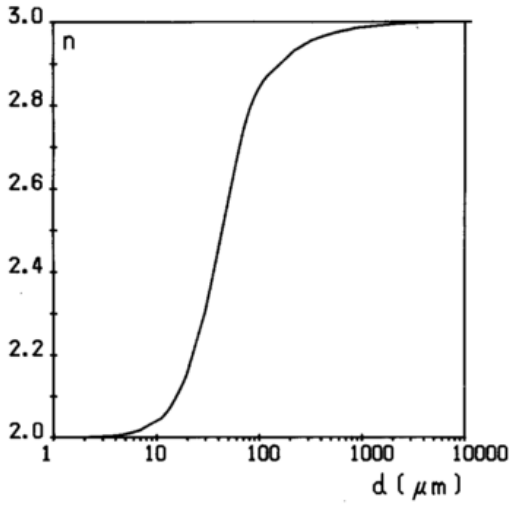

Figure 1.9: Plot of the Avrami exponent n vs film thickness d investigated in bulk [37].

There are many studies of the relation between crystallinity and film thickness. Billon *et al.* applied the Avrami equation to calculate this [37, 38]. The main effect of decreasing thickness are a slower than average crystallization of the film and a decrease in the Avrami exponent caused by a slower crystallization of the polymer close to the surface (Figure 1.9). However, Schultz *et al*. find that thin specimens exhibit anomalously low values of the Avrami coefficient and argue that values inferred from thin film specimens should be treated with circumspection [39]. Dalnoki *et al.* reported that a remarkable slowing down of the crystal growth is observed at all temperatures studied for films with a thickness of less than ~ 100 nm [40]. Zhan *et al*. also find that for films at thickness below about 100 nm, the crystallization process is strongly hindered, resulting in a low degree of crystallinity in these films [41]. In addition, Despotopoulou *et al.* [42], Taguchi *et al.*[43], and Massa *et al.* [44] also reported similar results. However, these studies refer only to the crystallinity of thin films with the mobilities of the molecules influenced by the surface without the effect of the substrate. On the other hand, Sawamura *et al.* investigated isotactic polystyrene thin films for this problem including the influence of substrate [45]. The lateral crystal growth rate of isotactic polystyrene lamellae developing in thin films (ranging from 20 nm to 500 nm) decreases with decreasing film thickness. From this study, they developed an equation that related growth rate and thickness : $G(D)= G(\infty)(1-d/D)$, where G(D) is the growth rate in a film of thickness D, $G(\infty)$ is the growth rate in the bulk. And they found that d is a constant with a value of approximately 6 nm. Therefore, they proposed that the constant value of d corresponds to the tube diameter in the reptation model that describes polymer dynamics, and that near the substrate this diameter is reduced,

thereby reducing the mobility of the molecules, and consequently the crystal growth rate. Ma *et al.* calculated dynamic Monte Carlo simulations of polymer crystallization confined in thin films of thicknesses comparable to the polymer-coil sizes [46]. They found that at high temperatures slippery walls slightly enhance the crystallization rate with the decrease of film thickness, and the surface-assisted crystal nucleation results in dominant edge-on lamellar crystals (chain axis parallel to the wall); on the contrary, sticky walls significantly depress the crystallization rate, and the random crystal nucleation yields preferentially flat-on lamellar crystals (chain axis normal to the wall). The growth of self-seeded crystals demonstrates that the flat-on dominance is a kinetic phenomenon due to a stronger restriction on the thickening growth of edge-on lamellar crystals. Here, slippery walls and sticky walls mean the surface and the substrate respectively. Schönherr *et al.* also find that the substrate would influence the crystallinity or the crystallization rate [47]. These ideas are highly relevant to my study. Hutchinson says that the aging of the amorphous phase is also important for crystallization [48]. He mentions that the amorphous phase may be regarded as consisting of two regions: the bulk amorphous regions, which are relatively distant from the crystalline lamellae, and constrained amorphous regions, which are close to the surfaces of the crystalline lamellae, and are constrained in their structural rearrangement by these lamellae.

1.5 Literature review of crystallization of thin PET films

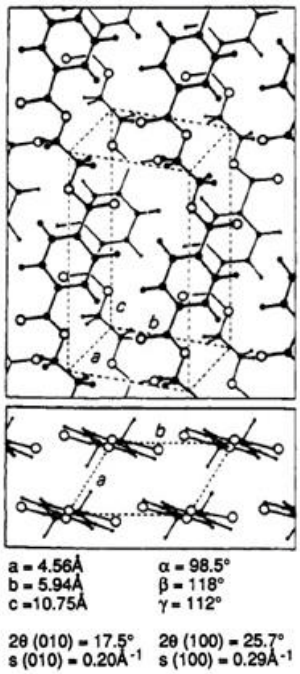

Figure 1.10: The structure of PET crystal. The crystal of PET has three crystal planes (a, b, and c), and the distances of these planes are 4.56 Å, 5.96 Å, and 10.75 Å respectively. This crystal structure is triclinic [11, 49].

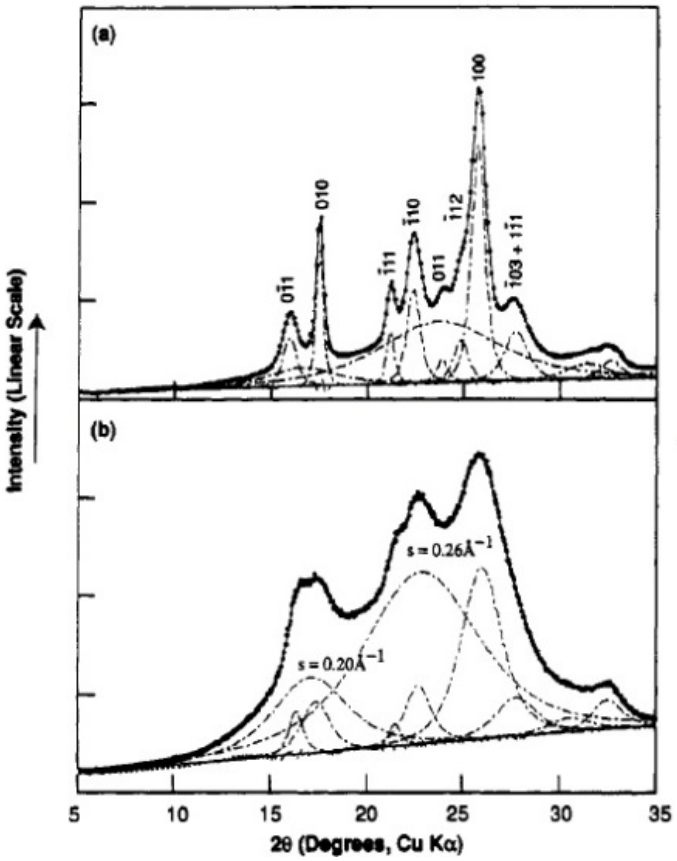

Figure 1.11: The WAXD profile of PET crystal [49]. PET crystal planes and distances of planes shown in Figure 1.10 are calculated from this.(a) is highly crystalline powder, and (b) is partially crystallized film by annealing.

The molecular formula of PET is shown in Figure 1.2 and its crystal structure is shown in Figure 1.10 [11, 49]. The crystal of PET has three crystal planes (a, b, and c), and distances of these planes are 4.56 Å, 5.96 Å, and 10.75 Å. This crystal structure is triclinic. Figure. 1.11 shows the WAXD (wide angle X-ray diffraction) profile of PET crystal and PET crystal planes and distances of planes above are calculated from this [49]. Because a sample of PET consists of crystals and amorphous parts as same as other crystalline polymers, the diffraction pattern is broadened as the amount of amorphous component included in the sample is increased. Sakai *et al.* reported that a terrace-like morphology has a single crystal structure [50]. The growth front of the terrace shows instabilities of periodic or groove patterns.

Jukes *et al*. showed that crystal structure in thin PET film is the same as bulk PET and also revealed that PET crystallization progresses rapidly in specific directions and especially rapidly on the surface [51]. Hobbs *et al.* also revealed similar phenomena using in situ analysis of PE by AFM [52]. They found that the crystal growth at the

surface is in some way different from that in the rest of the film, perhaps due to a difference in mobility of the chains in the surface layer or a difference in the surface energies, and hence barriers to crystal growth are different, when a free surface is present. We might expect to always see considerably enhanced growth at the surface, or some other similar effect, which has not been observed as yet. Following on from this study, I expect that AFM is also effective for the study of PET surface crystallization.

In x-ray studies, Imai *et al.* revealed that the former long-period peak of PET crystal is considerably lower than the latter and obeys the spinodal decomposition kinetics [53]. This was also measured by light scattering and SANS (small angle neutron beam scattering) from the viewpoint of the orientation fluctuations of rigid molecular segments occurs and this ordering process agrees with spinodal decomposition. Imai *et al.* also says that in the induction period, the crystallization involves a kind of phase separation of spinodal decomposition [54]. The size of the dense domains caused by the density fluctuations in the induction period are large compared with the lamellae thickness. These dense domains are not the embryos predicted by the classical nucleation theory. The crystal nuclei are not formed until the dense domains grow to a certain critical size, 85Å. The critical size of crystal nuclei appearing in the dense domains is 14Å [54]. The onset of long-range ordering prior to crystal growth was revealed in PP, PE, and PET by Ryan *et al*. [55]. In rapid crystallizations, large scale order of oriented SAXS was measured before the development of crystalline peaks measured by WAXD [20]. However, this "SAXS before WAXD" was not reported in thin PET films so far and there are a lot of unclear points in its crystallization process and kinetics although crystallinity is very important for PET. Therefore, this kind of past studies and theories are very important for the study of the early stage of crystallization in thin PET films. I will discuss the literature and my data in detail in Chapter 6.

In a study of film extension, Blundell *et al*. revealed that primary crystallization fits a first-order transformation with little change in the rate of crystallization observed over a 30ºC temperature range [56]. In this study, all oriented crystallization occurred after final extension. Kuem *et al.* says that there are two stages of crystallization in oriented PET chains [57]. Firstly, bundles of highly oriented chains including the mesophase are responsible for the first stage of crystallization (at 80ºC -100ºC). But those of less ordered or non-oriented chains are for the second crystallization stage beyond 140 °C. The structural transformation from the transient mesophase to the triclinic crystal structure was interpreted by the chain sliding mechanism, leading to the tilted (001) planes against the fiber axis. The point of the

study of film extension is that oriented chains might behave as dense parts described in the theory of Ryan *et al* above and it might induce crystallization.

There are some studies and published literature on crystallization in thin PET films. Durell *et al.* reported the detailed investigation of the molecular configuration and long-range order at the surface of spin-cast PET thin films spin-cast onto an etched Si (001) surfaces during crystallisation from the amorphous state for a range of annealing temperatures [58]. The structural ordering was observed at the surface at annealing temperatures of 80ºC -95ºC., lower than that in the bulk, involving local parallel alignment of chains in the plane of the surface with the benzene rings oriented preferentially with the ring plane parallel to the surface. The study of the comparison of crystallization between surface and bulk in thin PET films reported by Jukes *et al.* shows that ordering occurs significantly faster at the surface in the temperature range 90-100 °C (close to the bulk glass transition temperature of 75 °C). The (0 -1 1) and (0 1 0) peaks narrow more rapidly and achieve a lower width, indicating that the crystallization progresses more rapidly in these crystallographic directions. This enhanced ordering is attributed to a combination of surface energy effects, which promote localized packing, and to an enhanced segmental mobility near the free surface [51]. Bertold *et al.* present a the study of the cold crystallization process in PET spin-coated ultrathin films (35 nm) [59]. The conformational change associated to the formation of crystal phase during annealing at 107 °C was measured in real time, by monitoring both intensity and frequency shift of trans and gauche conformer bands of the PET glycol segment. The experimental findings in this study were interpreted in terms of weak interaction between PET films and silicon substrate, which does not provide slowing down of crystallization kinetics as observed on other substrates. This results in a dominant effect of the polymer/air interface, where faster kinetics are observed. The near-surface crystallization behaviour of PET films of various thickness, spin-cast from solution onto silicon substrates, has been studied by Shinotsuka *et al*. [60]. The surface crystallization process is associated with a top-surface region (measured to be of about 13 nm in depth) of lower glass transition temperature, where, at temperatures between the surface and bulk crystallization temperatures, only the material in the more-mobile surface region is able to reorganize to form crystals. But they also say that this phenomenon is observed for films of all the thicknesses studied and it is therefore concluded that this is not specifically a thin-film phenomenon, rather a surface-specific phenomenon possible in material of any thickness. However, this implies that the surface effect becomes dominant in thin films because thin films have a high proportion of surface and this should make some special circumstances in thin

polymer films. Of course, these studies of crystallization in thin PET films are useful and important, but so far there are no studies of the pre-ordering or some intermediate state between crystal and amorphous in thin PET films to date.

As described above, we can see that there are many studies of crystalline PET. However, it seems there are no studies or literature concerning the early stages of crystallization in thin PET films or discussions of the kinetics of pre-ordering, or dependence of the kinetics on thickness, or the morphologies of PET crystal, amorphous, and the intermediate state like pre-ordering or mesophase. Especially, I would like to emphasize one of the most important achievements of this study is that I have found the proper procedure to make high quality thin PET film samples, although PET is difficult to handle because of its tricky properties, that is, the semi-crystalline nature with its complex molecular structure including aromatic rings, it is vulnerable to humidity, and has poor solubility in most solvents. It is not entirely clear in the literature for thin PET studies that they are directly comparable with each other. This is due to the striking differences in the procedures used to make the samples, and I am not sure that all of them are suitable to study these early stage processes. The tricky properties of PET make the study of crystallization in thin PET film difficult, and there are still a lot of unclear problems in this field. My study would change this situation and the detailed sample preparation procedure is shown in Chapter 3.

As I mentioned at the beginning of this chapter, PET is one of the most important polymer materials and its good properties are caused by its crystalline structure. Therefore, it should be very important and useful to investigate the process of PET crystallization in detail for both academic and industrial field. In this study, I investigate the early stage of crystallization of thin PET films by ellipsometry, GI-X-ray scattering, and AFM in detail and discuss the pre-ordering, kinetics, and morphologies of them, and my data and discussions show the detailed kinetics, morphologies, and specific mechanisms of thin PET crystallization and a suggestion of the detection of the pre-ordering in thin PET films.

Chapter 2

Methodologies and theories for experiments

In this chapter, the methodologies and theories of the experiments used in this study will be described, that is, the protocol behind making thin PET samples, and the measurements used to study them; ellipsometry, atomic force microscope, and grazing incidence X-ray scattering. This chapter should be helpful for understanding how and why these methodologies were used in this study.

2.1 Method for making thin PET Samples

Figure 2.1 shows a brief scheme used to make thin PET film samples in this study. First of all, PET solution was made by dissolving a solid PET pellet, using solvent. Next, a thin film was made by spin-coating. Then any residual solvent was removed by placing the samples in a vacuum oven. Finally, the samples were heated at 285 °C in order to melt and cancel any crystals that might have been created during the spin coating process, and then thermally quenched quickly on a bulk metal whose temperature was controlled to room temperature.

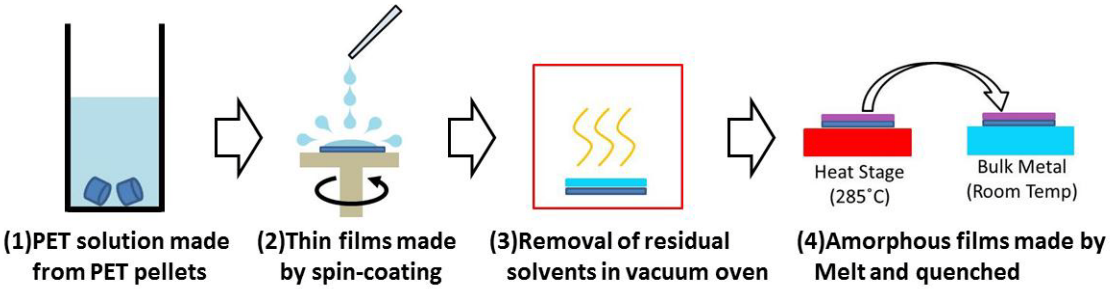

Figure 2.1**:** The scheme used to make thin PET film samples.

Homo poly(ethylene-terephthalate) (PET) pellets were used in this study. This PET has number-averaged molecular weight Mn=27,500 and polydispersity Mw/Mn = 2.4. The melting point (T_m) and glass transition temperature (T_g) are 250 °C and 75 °C respectively, as shown from the DSC data in Figure 2.2. There were also two crystallization temperatures at 160 °C and 190 °C, low and high crystallization temperature. The DSC measurement was operated in the temperature range 25 °C to 300 °C, and subsequently then down in temperature from 300 °C to 25 °C with cooling and heating rates of 10 °C / minutes. PET pellets are usually crystalline to some extent, therefore the pellet used for this measurement was melted at above 280 °C and then quenched by plunging into iced water in order to see the actual thermal behaviour of amorphous PET.

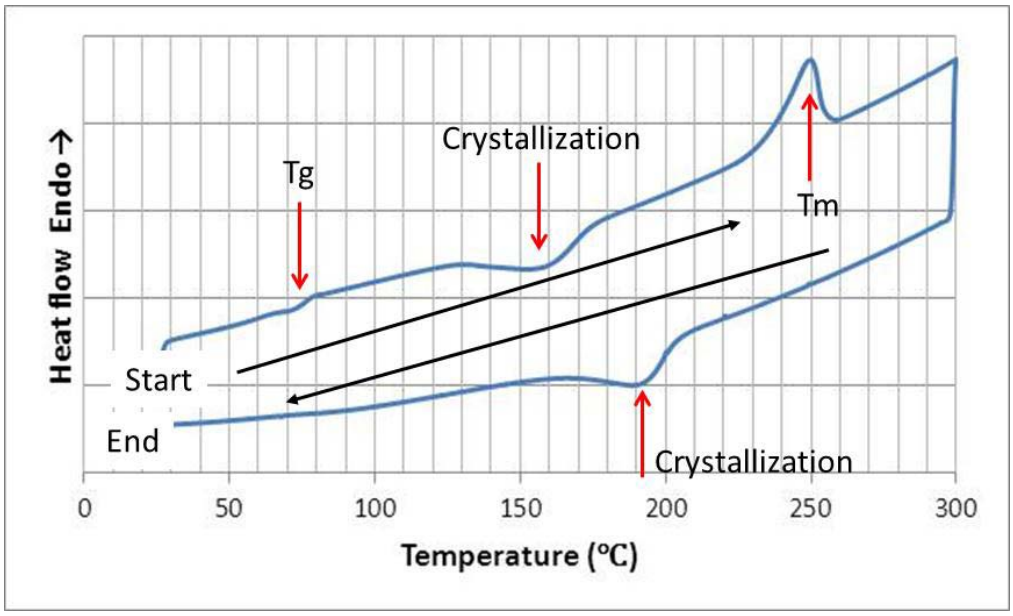

Figure 2.2: DSC data of a PET pellets. The temperature ramped from 25 °C to 300 °C and then back down from 300 °C to 25 °C with 10 °C/min. We can see that T_g and T_m are around 75 °C, and 250 °C respectively.

To prepare the PET solutions for spin coating, the PET was first dissolved at 3wt% in 1,1,1,3,3,3-Hexafluoro-2-propanol (HFIP) and heated at 100 °C in a sealed small glass bottle for 1 hour. This was used as the starting basic PET solution. Then various concentrations of PET solution were made with addition of further solvent, for example, HFIP for further dilution and 2-chrolophenol to improve flatness of the spin coated sample surface.

The PET solution was then spin coated onto polished single crystal silicon wafers, the thickness of the PET thin film samples was controlled by spin coating at various different sample rotation rates. To improve the solution's wetting properties, the oxide surface of the silicon wafers were cleaned by oxygen plasma. The thickness of the thin films ranged from 50 nm to 250 nm in this study. The surface roughness, measured as the root mean square (RMS), of these samples were all between 0.2 ~ 0.5 nm before annealing. This level of flatness is equal to the roughness of a liquid surface [61, 62].

Then samples were dried in a vacuum oven at 200 °C for 4 hours to remove any residual solvent. Finally, the samples were melted at 285 °C for 20 minutes and immediately quenched onto a flat bulk metal kept at room temperature to cancel any crystals.

Because the solvent recipe and the procedure developed and used for making thin PET films are highly important for this study, I will make detailed discussions of this in Chapter 3.

2.2 Ellipsometry

2.2.1 Introduction

Ellipsometry has been widely used for analysis of thin polymer films before. There are many studies of thin polymer films using ellipsometry because this technique can analyse very slight changes of thickness and volume of thin films, for example, [63, 64, 65, 66, 67].

The thickness and refractive index of very thin films on flat substrates are observed by ellipsometry and importantly it can be used for non-destructive precise measurements of these quantities. It works well as an in-situ measurement as long as there is a straight light line from light source to a sample and by reflection to a detector. The reason why ellipsometry is one of the best ways to see film thickness change due to crystallization with temperature and time under controlled atmosphere, is its extreme sensitivity and time resolution. Typical ellipsometry data for the thickness and refractive index of a thin PET film is shown in Figure 2.3.The initial film thickness was 150 nm and the refractive index was measured at a wavelength of 600 nm. The blue solid lines indicate thickness and refractive index in each plot, and the red broken lines indicate the sample temperature. The horizontal axis indicates time. The vertical axis “Normalized Thickness” indicates thin film sample thickness divided by the initial room temperature thickness.

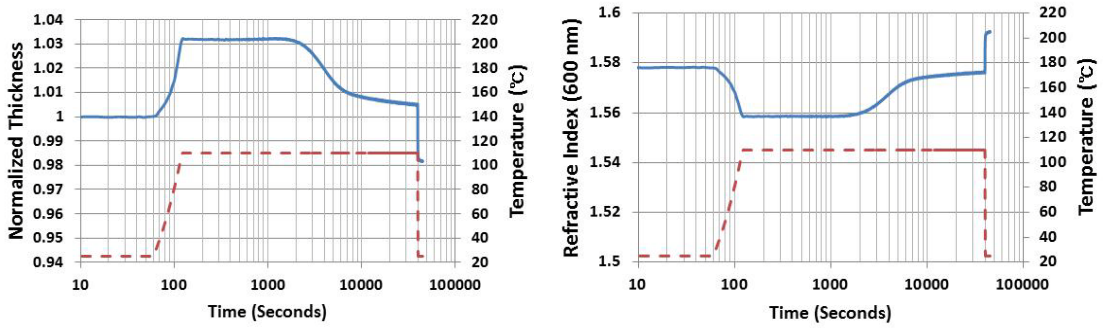

Figure 2.3: Typical ellipsometry data of PET film thickness (left) and refractive index (right) as a function of isothermal annealing at a fixed temperature (150nm, 110 °C, for 10 hours). The PET film becomes more crystalline with time.

In this example a PET sample was kept at room temperature for a minute at first, then heated up to 110 °C for 10 hours, and finally cooled down to room temperature again. The film thickness increased quickly due to thermal expansion and had a plateau that we can interpret as the induction time of crystallization during this period. Then the film thickness dropped and decreased gradually due to crystallization and secondary crystallization, then finally drastically dropped by rapid cooling to room temperature (due to thermal contraction). On the other hand, the refractive index was changed as an inverse profile of thickness because a low density is correlated with a low refractive index. The density should be reduced by thermal expansion and increased by crystallization. Profiles of thickness and refractive index in figure 2.3 with temperature and time seem entirely reasonable. The absolute value of refractive index measured for the films also corresponds well to the actual PET refractive index [68].

There are three points we need to highlight. First of all, we can see profiles of thickness and refractive index very precisely with quite low noise. For example, 3% of 150 nm is about 4 nm or 5 nm and figure 2.3 shows that these profiles are very smooth lines without any noise. Ellipsometry enables this kind of highly sensitive measurement of thickness, and this is needed to see subtle thickness change caused by crystallization in these thin films.

Next, the validity and accuracy of this measurement is made possible by adaptability of ellipsometry and selection of appropriate samples. A risk of ellipsometry is that we cannot often distinguish thickness change and refractive index change. For example, an optical path length (by which I mean the actual wave number) increases when thickness or density of a thin film increases. Ellipsometry measurement circumvents this kind of problem by good model fitting with a wide range wavelength

(300 nm - 1000 nm) or various incident angles. Good model fitting needs adequate samples that, have a flat surface and are homogeneous. Therefore I managed to make good flat surface and homogeneous samples, discussed in more detail in Chapter 3. The combination of ellipsometry and appropriate sample design enables such a high accuracy and valid measurements to understand crystallization in thin PET films. In this section 2.2, the theory of ellipsometry, configurations and apparatus, and validity of measurements will be described.

Finally, I would like to mention the potential influences of birefringent optical properties and surface roughness in films with growing crystals. Ellipsometry measurements are influenced by birefringence because if a sample has birefringent property, the refraction and reflection of the incident beam are different according to the direction of sample. Therefore, in principle we need to take care with the sample direction if we measure a birefringent sample by ellipsometry. However, because my samples were made by spin coating, there is much less deviation of molecular orientations in in-plane direction than there would be for a single crystal, because we can expect a random orientation of crystallites within the plane of the film. The experimental data showed that, even though I rotated my samples, this did not lead to any measurable difference in the ellipsometry data. We may say that the influence of birefringence in ellipsometry measurement of my samples is not significant. Surface roughness would also influence ellipsometry measurements because the incident light is scattered in all directions by surface roughness; this would cause a decrease of the S/N ratio and increase non-specular reflection. In fact, the surface roughness, root mean square (RMS), was changed by crystallization from under 1 nm to about 4 nm at most (this is discussed in Chapter 5 in detail). However, there was little noise in my ellipsometry measurements even when sample was fully crystallized and I could acquire good reproducible data. We may say that the influence of surface roughness is not so crucial for this range of RMS.

2.2.2 Polarized light

Theories of ellipsometry are based on reflection and refraction of polarized light. From differences in the polarized light between incidence and reflection, information of thin films and its surface is gained by ellipsometry measurements.

Polarized light is categorized as plane polarized light and elliptically polarized light. Polarized light consists of p-waves, which are in the plane of incidence and

s-waves, which are perpendicular to that plane. Those electromagnetic waves are described as below [69].

$$E_p = |E_p| exp[i(\omega t - kz + \varepsilon_p)] \qquad (2.1)$$

$$E_s = |E_s| exp[i(\omega t - kz + \varepsilon_s)] \qquad (2.2)$$

Here, E_p and E_s are the amplitudes of the electric fields of the p-waves and the s-waves, $i = \sqrt{-1}$, ω is angular frequency, k is wave number, z is distance of axis direction of light propagation, and ε indicates phase shift.

Plane polarized light is normally used for the incidence path in ellipsometry. Because the change rates of amplitude and phase of p-waves and s-waves are different by reflection, the amplitude ratio and phase difference of p-waves and s-waves are different between incidence and reflection. Reflection usually results in elliptically polarized light.

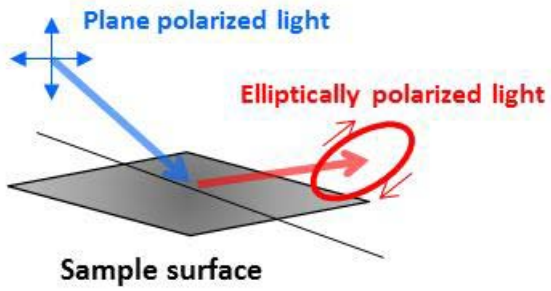

Figure 2.4: Reflection of polarized light on a sample surface.

This amplitude ratio and phase difference are described in terms of Ψ and Δ, which are related to the reflectances (which are predicted by the Fresnel equations, see section 2.2.3) thus [69]:

$$\frac{R^p}{R^s} = \tan\Psi\, e^{i\Delta} \qquad (2.3)$$

Here, R^p and R^s are reflectance of the p- and s-waves. The values of Ψ and Δ are measured directly in ellipsometry. The thickness and refractive index of thin films are then calculated from these values.

2.2.3 Reflection and transmission of polarized light at planar interface with Fresnel equations and Snell's law

Figure 2.5 shows that reflections and transmissions of light from multiple interfaces. There are three layers in our model, nitrogen atmosphere, PET thin film, and Silicon wafer substrate. Incident angle is θ_0, wavelength in nitrogen is λ, d is thickness, and n is refractive index. The subscript 0, 1, and 2 denote nitrogen, PET thin film, and Si wafer. For example, r_{01} denotes that a Fresnel reflection coefficient is for the interface between 0 and 1, and t_{01} denotes a transmission from 0 through 1.

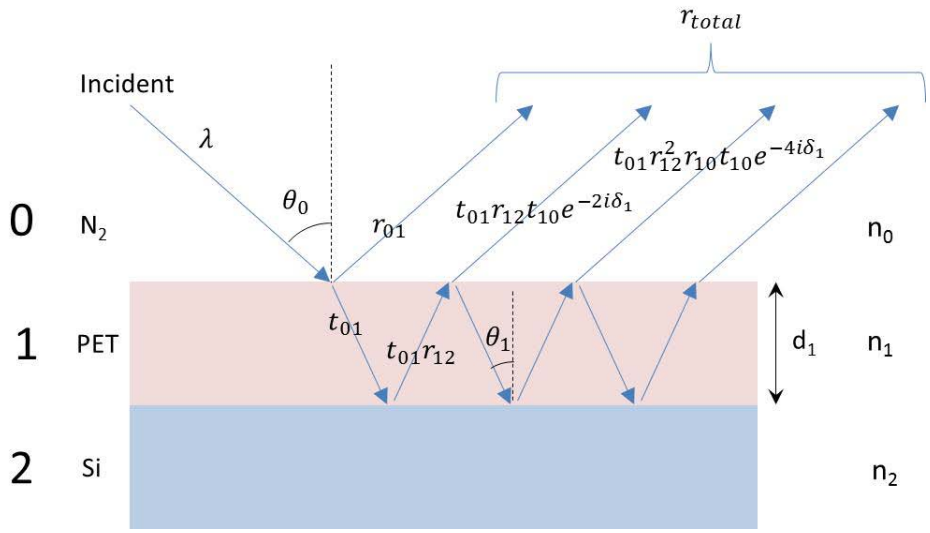

Figure 2.5: Reflections and transmissions with multiple interfaces by three layers, nitrogen atmosphere, PET thin film, and Si wafer.

Total reflection, r_{total} is described as below.

$$r_{total} = r_{01} + t_{01}r_{12}t_{10}e^{-2i\delta_1} + t_{01}r_{12}^2r_{10}t_{10}e^{-4i\delta_1} + \cdots + t_{01}r_{12}(r_{10}r_{12})^{m-1}t_{10}e^{-i2m\delta_1} \quad (2.4)$$

δ_1 denotes a complex number of phase shift by multiple reflections with wavelength λ, incident angle θ_1, refractive index n_1, and thickness of thin PET film d_1.

$$\delta_1 = 2\pi n_1 d_1 \cos\theta_1 / \lambda \qquad (2.5)$$

Considering multiple reflections in a PET thin film with a formula of infinite geometric series, we can rewrite the above equation 2.4 as+

$$r_{total} = r_{01} + \frac{t_{01} r_{12} t_{10} e^{-2i\delta_1}}{1 - r_{10} r_{12} e^{-2i\delta_1}} \qquad (2.6)$$

Here, we can use the following relationships below [69].

$$r_{10} = -r_{01},\ t_{01} t_{10} = 1 - r_{01}^2 \qquad (2.7)$$

Therefore, the equation for r_{total} is written as below.

$$\therefore r_{total} = \frac{r_{01} + r_{12} e^{-2i\delta_1}}{1 + r_{10} r_{12} e^{-2i\delta_1}} \qquad (2.8)$$

Then, the Fresnel reflection coefficients of p- and s-waves are described as below.

$$R^p = \frac{r_{01}^p + r_{12}^p e^{-2i\delta_1}}{1 + r_{01}^p r_{10}^p e^{-2i\delta_1}} \qquad (2.9)$$

$$R^s = \frac{r_{01}^s + r_{12}^s e^{-2i\delta_1}}{1 + r_{01}^s r_{10}^s e^{-2i\delta_1}} \qquad (2.10)$$

Here, if we use equation (2.3) $\frac{R^p}{R^s} = \tan\Psi\, e^{i\Delta}$,

$$\therefore \Psi = \tan^{-1}\frac{|R^p|}{|R^s|}, \quad \Delta = i \ln\left(\frac{R^p}{R^s}\frac{|R^s|}{|R^p|}\right) \qquad (2.11)$$

From Snell's law, which is defined by that the angles of incidence and refraction must be related by $n_0 \sin\theta_0 = n_1 \sin\theta_1$ in Figure 2.5 [69], we can describe reflections of p- and s-waves as below.

$$r_{01}^p = \frac{n_1 \cos\theta_0 - n_0 \cos\theta_1}{n_0 \cos\theta_1 + n_1 \cos\theta_0}, \quad r_{01}^s = \frac{n_0 \cos\theta_0 - n_1 \cos\theta_1}{n_0 \cos\theta_0 + n_1 \cos\theta_1}$$

$$r_{12}^p = \frac{n_2 \cos\theta_1 - n_1 \cos\theta_2}{n_1 \cos\theta_2 + n_2 \cos\theta_1}, \quad r_{12}^s = \frac{n_1 \cos\theta_1 - n_2 \cos\theta_2}{n_1 \cos\theta_1 + n_2 \cos\theta_2} \qquad (2.12)$$

We can see that Ψ and Δ can be written with refractive index, incidence angle, layer thickness, and wavelength. This indicates that the thickness of thin film can be described by Ψ, Δ, the refractive index, and the incidence angle, that is, R^p / R^s depends on the film thickness by equation 2.3. As pointed out by Heavens, when applying the above theory to practical film-substrate systems, the following conditions have to be met –(1) the lateral dimension of the film must be many times its thickness so that the multiply reflected and transmitted partial waves can be summed to infinity, (2) the source bandwidth, beam diameter, and degree of collimation, as well as film thickness must all be such that the multiply reflected and transmitted waves combine coherently, and (3) the film material must be smooth enough [70].

2.2.4 Configurations of ellipsometry

Ellipsometry measurements were performed using a rotating compensator ellipsometer, the J. A. Woollam M-2000V that uses a rotating compensator to illuminate a sample with light of a constantly varying polarisation state. Range of wavelength was from 370nm to 1000nm. Incidence and reflection angle was fixed at 70°. Measurements were implemented in a cell, which consists of a Linkam heating stage and a cover in order to illuminate the sample and collect reflection of the beam from the surface, whilst the keeping the sample under an inert nitrogen atmosphere.. Figures 2.6 and 2.7 show schematic diagrams of the J. A. Woollam M-2000V and the cell used.

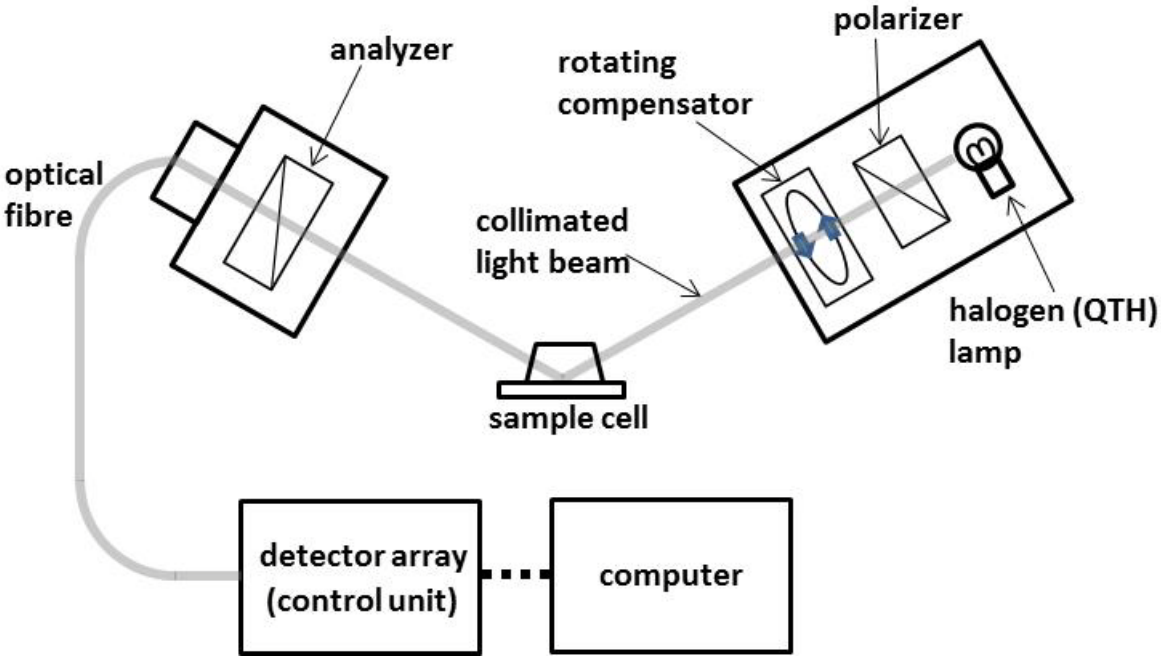

Figure 2.6: Schematic diagram of the J. A. Woollam M-2000V.

A 50W quartz tungsten halogen (QTH) lamp was used in this ellipsometry measurement [71].

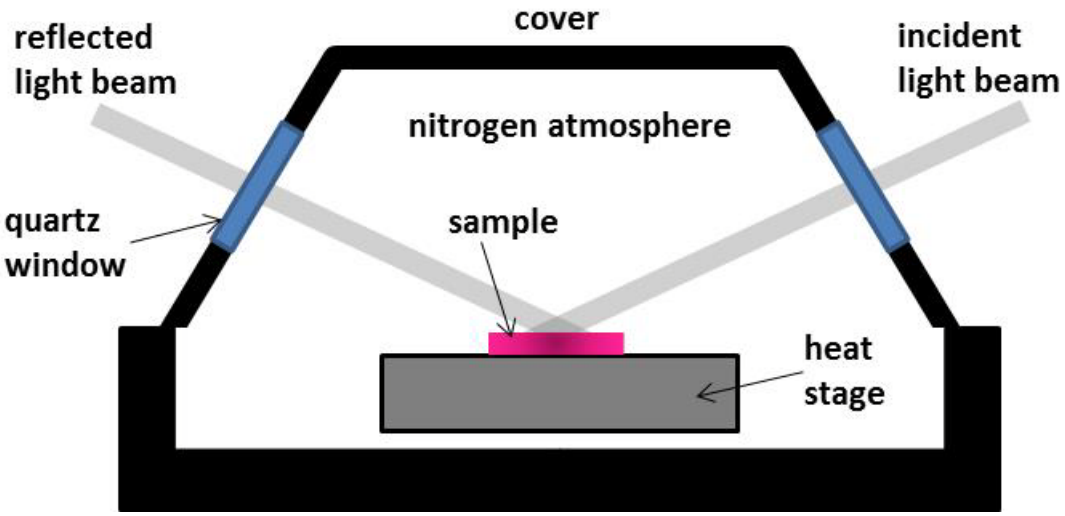

Figure 2.7: Schematic diagram of sample cell.

Figure 2.8 is an actual picture of this experimental system. By using this set up, sensitive ellipsometry measurement can be performed. Under nitrogen atmosphere and

blocking an environmental turbulence factor or temperature gradients by using the cover are especially important.

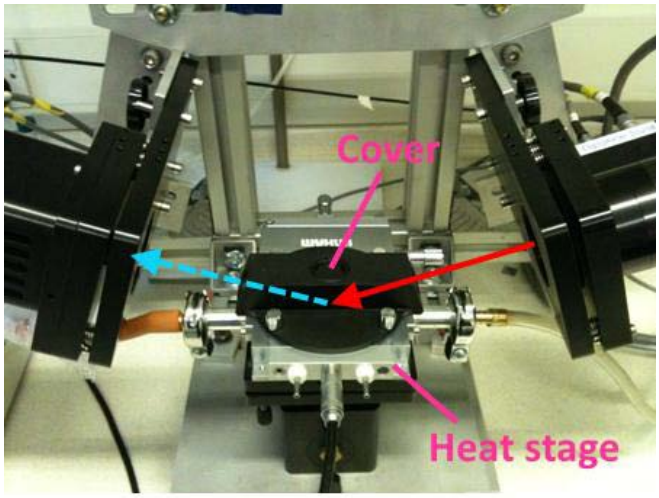

Figure 2.8: A picture of the ellipsometry configuration. A red solid arrow and blue broken arrow indicate the incident light and reflected light from sample surface, respectively.

2.2.5 Effective Approximation

Ψ and Δ are directly measured in ellipsometry. The film thickness and refractive index are calculated from these Ψ and Δ using model fitting. As I said above, a good sample is very important for ellipsometry measurement because a flat surface and homogeneous thin film can easily be represented using modelling. A good fit between a model and an actual component or structure brings accuracy and assures validity.

Figure 2.9 shows a scheme used for the calculation of film thickness d_1 and refractive index n_1 described in figure 2.5. First of all, a model deemed suitable is supposed with wavelength λ, incident angle between nitrogen and PET θ_0, between PET and Si wafer θ_1, refractive index of PET and Si wafer, n_1 and n_2, and PET film thickness d_1. From equations described above, calculated Ψ and Δ are expressed with these parameters.

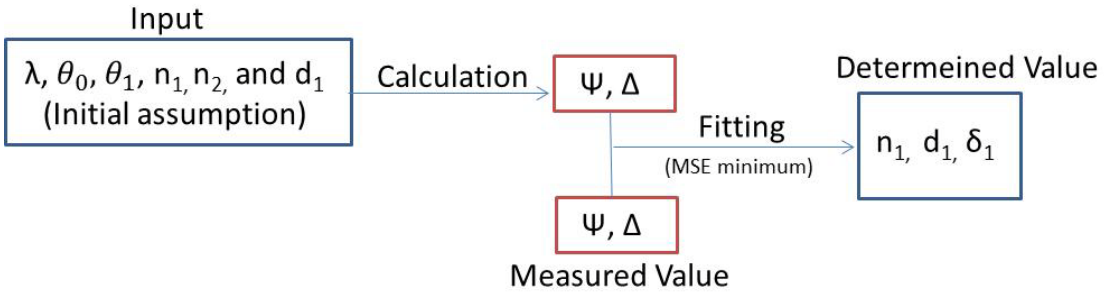

Figure 2.9: A scheme used for the calculation of film thickness d_1 and refractive index n_1 described in figure 2.5.

Next, the calculated Ψ and Δ are compared with actually measured Ψ and Δ using χ parameter and mean square error (MSE) described as (2.13) and (2.14) by a computer.

$$\chi^2 = (\Psi_{ex} - \Psi_{mod})^2 + (\Delta_{ex} - \Delta_{mod})^2 \qquad (2.13)$$

$$MSE = \frac{1}{2N - M} \sum_{i=1}^{N} \left[\left(\frac{\Psi_i^{\mathrm{mod}} - \Psi_i^{\exp}}{\sigma_{\Psi_i}^{\exp}} \right)^2 + \left(\frac{\Delta_i^{\mathrm{mod}} - \Delta_i^{\exp}}{\sigma_{\Delta_i}^{\exp}} \right)^2 \right] \qquad (2.14)$$

Here, Ψ_{ex} and Δ_{ex} are measured values, Ψ_{mod} and Δ_{mod} are calculated values. *N* and *M* is the number of measurement points and parameters, σ is standard deviation of Ψ_{ex} and Δ_{ex}. This calculation is repeated until χ^2 or MSE becomes small enough with changing input values n_1 and d_1 in order to find the smallest χ^2, that is, to find the model closest to actual component and structure. Generally, it is said that an acceptable MSE value should be lower than 20 in practical use [71]. We arbitrarily chose an MSE value that was less than 20 and used a single Cauchy layer to fit the data. The silicon substrate and oxide were fitted separately and maintained as non fitted parameters, i.e they were constrained. MSE values in this thesis were under 1 basically. When n_1 and d_1 are reached minimum, they are considered as practical refractive index and film thickness. The refractive index n is a function of wavelength. The equation for $n(\lambda)$ is often approximated by

$$n(\lambda) = N_1 + \frac{N_2}{\lambda^2} + \frac{N_3}{\lambda^4} \qquad (2.15)$$

Here, N_1, N_2, and N_3 are called "Cauchy coefficients." The refractive index is usually parametrized by N_1, N_2, and N_3 by this equation in spectroscopic ellipsometry measurements. The ellipsometry analysis must be performed with careful checking the validity of the results of optical parameters like figure 2.3 [72]. The validation of the optical parameters was done using the J. A. Woollam CompleteEase software where it is possible to look at if the fit has converged to a global minima or a local minima using the parameter uniqueness tool, by plotting out a range of N_1 values (Equation 2.15) for the Cauchy model (this is the dominant term in this equation, N_2 and N_3 describe the dispersion shape), other parameters such as thickness can be checked using this approach also. A much simpler check as to the validity of the fit was to examine the published literature values of the refractive index for PET and the ones measured using the fitting procedure of our ellipsometry data. This is discussed in the next section with Figure 2.15. The Cauchy model is not able to cope with optically absorbing materials (i.e. ones which have a k term). In this case however it is still possible to study optically absorbing films provided you choose a transparent wavelength region. The large wavelength range of the Woollam machine (370 nm -1000 nm as shown in Figure 2.10 and 2.11 in the next section) makes it possible to do this in most situations.

2.2.6 Validity of ellipsometry measurement for thin PET films on Si wafer

To analyse data from the ellipsometer, a custom ellipsometry data fitting program was created in the programming package MATLAB. This program followed equations and calculations for three layered system described above. Figure 2.10 shows a typical output of the MATLAB ellipsometry modelling program for a thin PET film on Si wafer. We can see that experimental data and fitting model were able to match to some extent of accuracy, and the parameters, for example, thickness or refractive index, could be determined from this fitting as mentioned above.

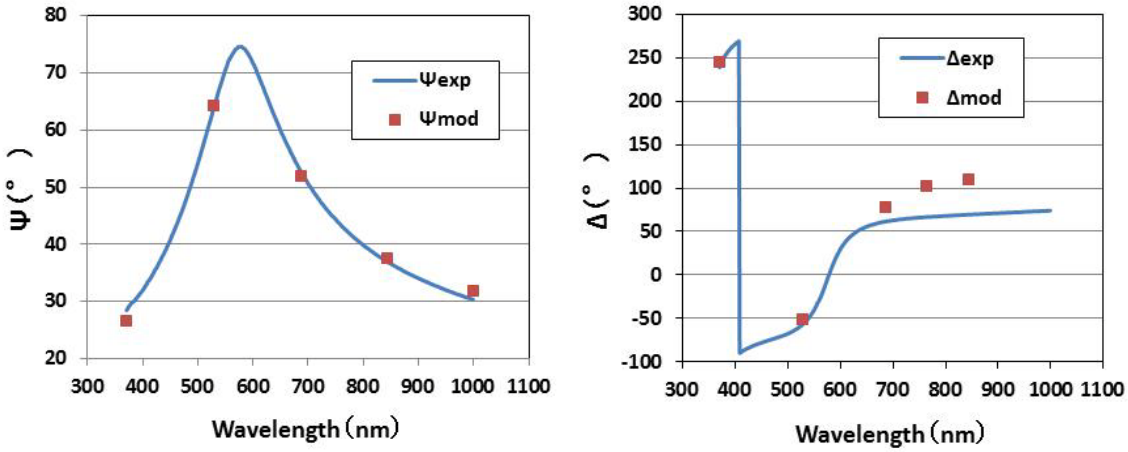

Figure 2.10: A typical output of the MATLAB ellipsometry modelling program for a thin PET film.

Although this original program was basically successful in fitting preliminary data and proved usefulness for data analysis of ellipsometry measurements, the efficiency of this calculation was very low because the algorithm was not optimized for calculation speed and data plot numbers. Besides, the calculated Δ values at large wavelength were a little displaced from the actual experimental values. This might be caused by a very thin (1 or 2 nm) silicon oxide layer on a Si wafer, not included in the three layered model described above.

The difference in prediction between a three layer model and a four layer model with a very thin oxide layer is small, because the phase difference, Δ, is affected by the amplitude ratio of a number of layers, without large changes of Ψ. The phase of light waves would be changed as the light is transmitted through the interfaces between the layers, although Ψ is not very much affected as long as the Si oxide layer is very thin and does not absorb light, because Ψ is a parameter related to the amplitude ratio of p- and s-waves as shown in equation (2.3) and (2.11). Here, it is also informative to include further discussion of the modelling of multi-layers using the matrix method, because the approach of summing the contributions from individual multiple reflections, as given in Figure 2.5 and equations from 2.4 to 2.8, is not always suitable for calculating the properties of multilayer films [73]. The basic concept of this matrix method consists of the generation of a characteristic matrix for each layer, film, which can be combined to a characteristic matrix of the whole structure by a matrix multiplication procedure [74]. For this approach each layer in the interface is represented by a cheractaristic matrix; thus for layer *m*

$$M_m = \begin{bmatrix} \exp(i\xi_{m-1}) & r_m \exp(i\xi_{m-1}) \\ r_m \exp(-i\xi_{m-1}) & \exp(-i\xi_{m-1}) \end{bmatrix} \qquad (2.16)$$

where ξ_m is the optical path length of layer m as defined below and r_m is the product of the Fresnel reflectance of the *m*th interface [75].

$$\xi_m = \frac{2\pi}{\lambda} n_m d_m \sin\theta_m \qquad (2.17)$$

where λ is wavelength, n_m, d_m, and θ_m are refractive index, thickness, and incidence angle of layer m. For total of *n* layers, pile of films, a resultant 2 by 2 matrix is obtained by multiplying these n charactaristic matrices [75]

$M = M_1 M_2 M_3 \ldots M_n \qquad (2.18)$

The reflection and transmission coefficients of the stratified structure can be determined by the matrix elements

$$M = \begin{bmatrix} m_{11} & m_{12} \\ m_{21} & m_{22} \end{bmatrix} \qquad (2.19)$$

The reflectivity of the whole multilayer is then obtained as

$$R_{total} = \frac{m_{21} m_{21}^*}{m_{11} m_{11}^*} \qquad (2.20)$$

This scheme lends itself well to computational calculation and, in principle, any number of layers can be incorporated, speed of processing being the limiting factor in simulating the reflectivity.

However, it is not so easy to obtain the matrix elements, and a calculation of four layered system is not fundamentally difficult, but is complicated and requires a longer calculation time in my primative program. The optimization of the program to the same level as commercial software was not the main subject of this study, therefore I used the CompleteEase software of the J. A. Woollam Co. Inc. This software calculates very efficiently with the same theory described above, including the Si oxide layer. Figure 2.11 shows a typical output of the CompleteEase ellipsometry modelling program for the thin PET film (150 nm thickness) dataset that is the same as the 3 layer model in figure 2.10. I would like to describe some physical explanations of why we see the particular shapes of curves for psi and delta as shown in Figure 2.11. We can see that both Ψ and Δ have wavelength dependence from equation (2.3), (2.5), (2.9), (2.10), and (2.11). If a wavelength of incidence is changed, the situations and conditions of interference, reflectance, and refraction are changed, and this causes a change of both Ψ and Δ. Oscillations and periodic behavior, in both Ψ and Δ are often observed in thin film measurements as follows [76]. When light enters a thin polymer film sample it reflects and transmits at each of the interfaces. The rays leaving the sample interfere

with each other and produce spectral oscillations in Ψ and Δ. The number of oscillations in both Ψ and Δ is related to the optical thickness of the film and increases with increasing film thickness and refractive index. However, because polymers absorb to some extent at a particular range of wavelength, the spectra of Ψ and Δ in practice are not as simple as shown in Figure 2.11. The shape of the data for a transparent material has a series of peaks in the curves for Ψ; the intensity of the peaks is correlated with the difference in refractive index between the film and the substrate. A larger difference in refractive index gives more intense peaks. The number of oscillations increases as the thickness increases. A jump of value of Δ at around 520 nm in Figure2.11 is an artifact simply caused by the discontinuity in the phase cycle of the device. Of course, intrinsically, the profile of Δ is smooth line.

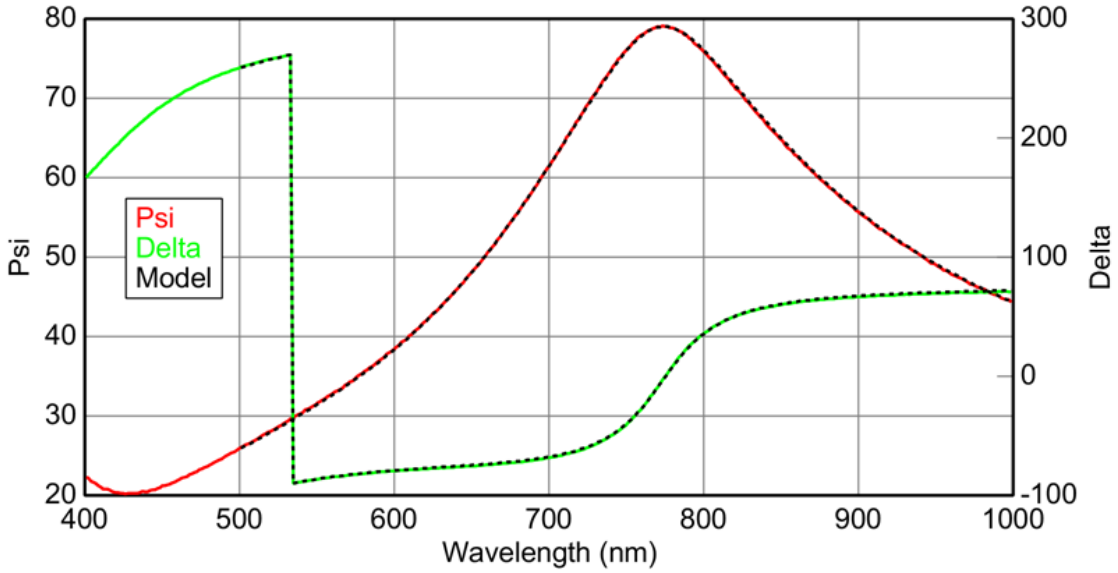

Figure 2.11: A typical output of the CompleteEase ellipsometry modelling program for a thin PET film. Solid red and green lines are experimental Ψ and Δ and dotted lines are calculated values from a model. The thickness of sample was 150 nm.

Ellipsometry can measure very slight change of thickness of thin PET film from changes of Ψ and Δ. Figure 2.12 shows that how raw data of Ψ and Δ change during annealing. Data points were shown as Figure 2.13, annealed at 120 °C for 200, 600, 1000, 2500, and 9000 seconds. Sample thickness was 150 nm. Changes of Ψ and Δ were shown between 700 and 900 nm wavelength because we can see the changes clearly. We can see Ψ and Δ were changed gradually, especially the peak of Ψ was shifted to small wavelength, as annealing proceeded and the change of the film

thickness as shown in Figure 2.13 was calculated from these changes of Ψ and Δ. We also can see that there are both the sensitive wavelength range and the not-sensitive wavelength range, for example, Ψ was not changed so much at 720 to 760 nm but very changed above 780 nm, on the other hand, Δ was changed at 720 to 760 nm. This indicates that data from broad range of wavelength could induce correct thickness value along with actual change of sample, vice versa, when using a single wavelength, the potential of ambiguity in film thickness increases because sensitive wavelength was different for Ψ and Δ and both of them were required for proper models in order to calculate actual thickness of samples.

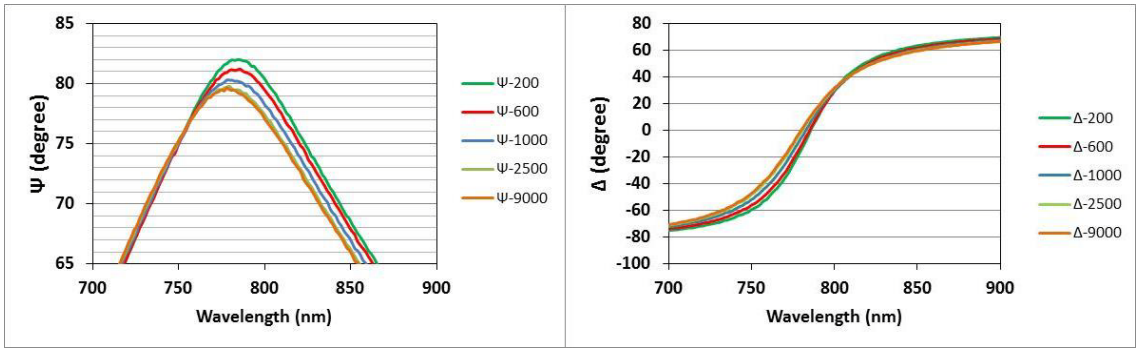

Figure 2.12: Change of raw data of Ψ and Δ during annealing at 120 °C for 200, 600, 1000, 2500, and 9000 seconds. Thickness of thin PET film sample was 150 nm.

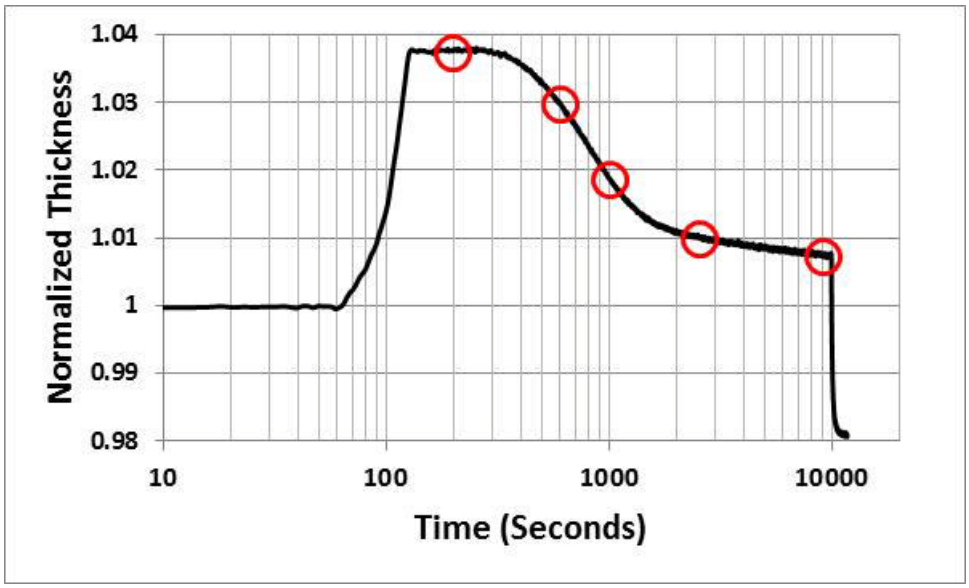

Figure 2.13: Thickness change of thin PET film sample calculated fromΨ and Δ shown in Figure 2.12. Circles indicate the data point of Figure 2.12, annealed for 200, 600, 1000, 2500, and 9000 seconds.

I assumed that if volume is changed by thermal expansion and crystallization, only the thickness is changed (area is not changed) because the thin PET film is strongly stuck to the Si substrate. Then an estimation of the volume fraction of crystal can be calculated. For example, if thickness decreased 1% from amorphous, a fraction of crystal is about 12 weight % as Figure 2.14. Here, density of PET (g/cm^3) is Crystal: 1.457 and Amorphous: 1.335 [77].

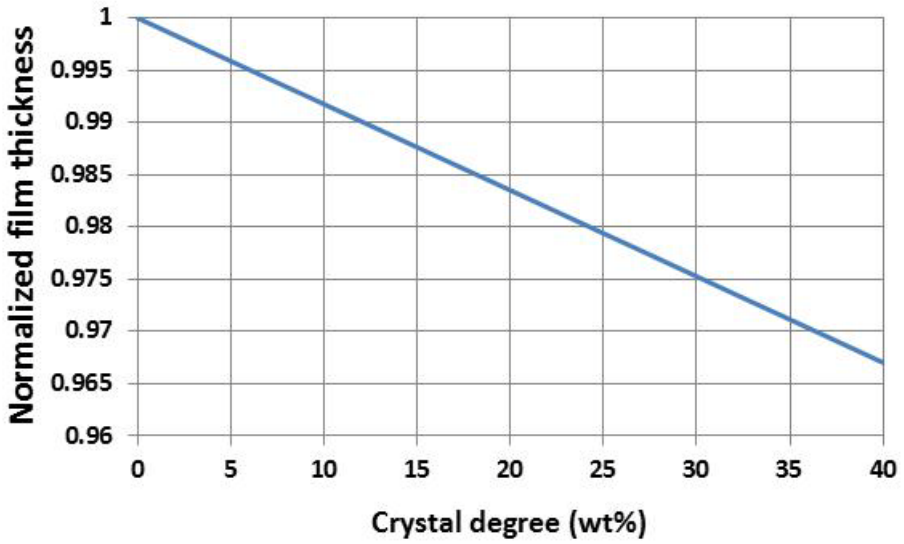

Figure 2.14: Calculated relationship between crystal degree (wt%) and normalized film thickness (film thickness / initial film thickness).

Figure 2.14 shows the calculated relationship between crystal degree (wt%) and normalized film thickness (film thickness / initial film thickness) using values of density described above at room temperature. From figure 2.3, the fraction of film thickness reduction caused by crystallization was about 1.8 or 1.9 % and this indicates that the crystal degree should be about 22 or 23 wt %. This corresponds well to the crystal degree of bulk PET crystalized by annealing [78, 79]. It seems in reasonable agreement.

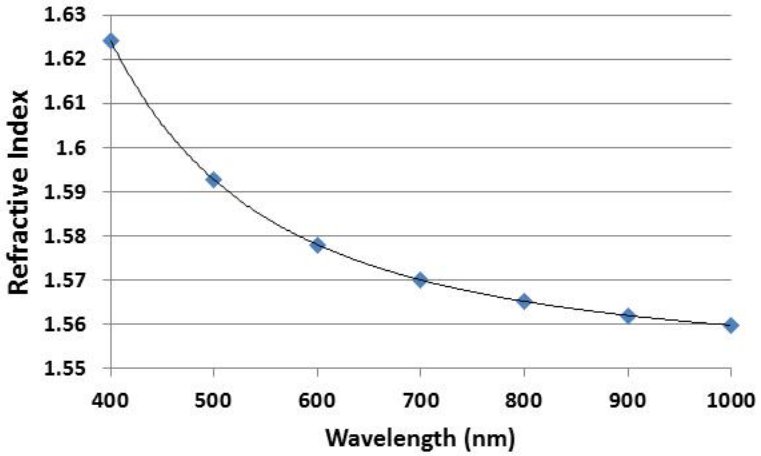

Figure 2.15: Wavelength dependency of the refractive index of PET measured by ellipsometer.

Figure 2.15 shows the wavelength dependency of refractive index measured by ellipsometry. The absolute values and graph profile of this figure corresponds to past studies for refractive index of PET [80, 81].

Refractive index also depends on density, that is, refractive index increases in high density materials, vice versa. Density is changed by temperature and crystallization, and crystallization proceeds by adequate temperature annealing, therefore refractive index is changed by temperature and time as right hand side graph of Figure 2.3, complex effects of simple thermal expansion and crystallization. These data and facts show that adequate model fitting was implemented of the ellipsometry measurements and reasonable values for the degree of crystallinity were acquired.

2.3 Atomic Force Microscope

2.3.1 Theories

Optical observations cannot resolve the crystallized structure due to them being below the diffraction limit. Observation of the PET crystallites requires methods that provide an analysis in the 10-100 nm size range. Atomic Force Microscope (AFM) is particularly suited for this purpose because of its good resolution of nanoscale features similar to the resolution of electron microscopy [82]. Although in AFM it is possible to measure the precise height information of a sample surface, which is useful for analysis

of crystallization, this is not possible using electron microscopy. Therefore AFM is widely used to see polymer crystalline materials and lamellae structures. In a typical AFM measurement, a small, area about 10μm scale is imaged, a pyramid shaped tip is mounted on a cantilever which acts as a spring, with a spring constant typically of order from 0.1 to a few tens Nm^{-1} [83].

There are three representative scanning types of tip in AFM, that is, contact mode, non-contact mode, and tapping mode. Tapping mode was adopted in this study because of its non-destructive nature and also high resolution. Using the tapping technique, during the scan an oscillating AFM tip probes the varying local viscoelastic properties. The curved edges of stacked flat lying lamellar crystallites are clearly apparent [82].

Figure 2.16 shows a schematic diagram of AFM. In many cases the tip and cantilever are micro-fabricated as a whole from silicon, silicon oxide, or silicon nitride. The cantilever is mounted on a piezo-electric drive that moves the tip in the vertical direction, while the cantilever onto a four-quadrant photodiode. The tip can be scanned in the horizontal plane using two further piezo-electric drives [83]. This quadrant photodiode detects displacement of the tip with bending a cantilever by displacement of the reflected laser beam, and translates this information to current signals of correct place of a tip. A feedback controller maintains the tip close to the surface and the centre position of the four-quadrant photodiode using highly precise piezo-electric drives during the scan. The integration of these scan lines becomes a two dimensional figure indicating detailed height information of the sample surface and morphology.

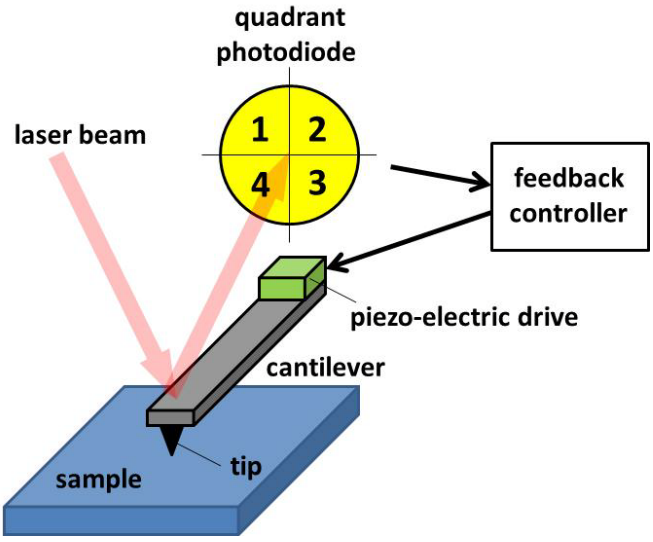

Figure 2.16: A schematic diagram of AFM.

In tapping mode, the cantilever is vibrated by piezo-electric drives close to the resonance frequency, and is very close to touching the sample surface. The tapping mode, because of just touching, does not damage the texture of the sample surface by dragging or scratching, but does yield a correct height position because of actually touching the sample surface. This is a very useful strong feature to investigate fine structures such surface crystals of thin polymer films. One more strong point of tapping mode is that a tapping force is quite small hence it is suitable to see fine surface structures. In general, relatively stiff cantilevers, which have a high spring constant (20 to 50 N/m) and a high quality factor, q, (100 to1000), are used in tapping mode to ensure that sufficient energy is stored in the cantilever to overcome any sticking. q is defined as below,

$$\mathrm{q} = \frac{m\omega_0}{b} \qquad (2.21)$$

with m being the mass of the cantilever, ω_0 is the resonance frequency, and b the damping coefficient [84]. If q is high, the signal to noise ratio is also high, but the response time of the system tends to be increased. Then, an amplitude setpoint of a cantilever may be established to be 10 nm less than the free oscillation amplitude, which may be on the order of 100 nm. Therefore, the energy in the lever oscillation is much higher than that lost in each cycle by striking the surface. The tapping force, i.e., the contact force exerted by the tip on the surface during striking in each cycle, is very small, and can be estimated from the change in the amplitude generated in each striking cycle. The amplitude change in one cycle, ΔA is approximately expressed by equation (2.22), where A_0 is the free amplitude of oscillation, and A_S is the amplitude setpoint.

$$\Delta A = \frac{(A_0 - A_S)}{q} \qquad (2.22)$$

The tapping force F is expressed as (2.23), where k is the spring constant.

$$F = k\Delta A \qquad (2.23)$$

For example, assuming an amplitude change of 10 nm, with q's of 100 to 1000, and a force constant of 20 to 50 nN, the force per strike, which equals to the amplitude multiplied by the force constant, is approximately 0.2 to 5 nN. This is considerably

smaller than that in the contact mode, thereby minimizing the deformation induced by the tip [84].

2.3.2 Apparatus and condition

AFM analyses were performed by digital instruments Nanoscope Ⅲ with Dimension 3100 using a tapping mode. Cantilever was the Bruker MPP-11100 made of Si, whose resonant frequency and spring constant were 300 kHz and 40N/m, and tip of radius was under 10 nm. The scanning frequency was from 0.5 to 1.5 Hz and the image size ranged from 1 to 30 μm. No special surface treatment or etching was needed to perform AFM, as the thin PET film surfaces were on a sample state. Measurements were carried out with an in-situ microscope image in order to focus the target position easily as in Figure 2.17. The cantilever was controlled by piezo-electric drives.

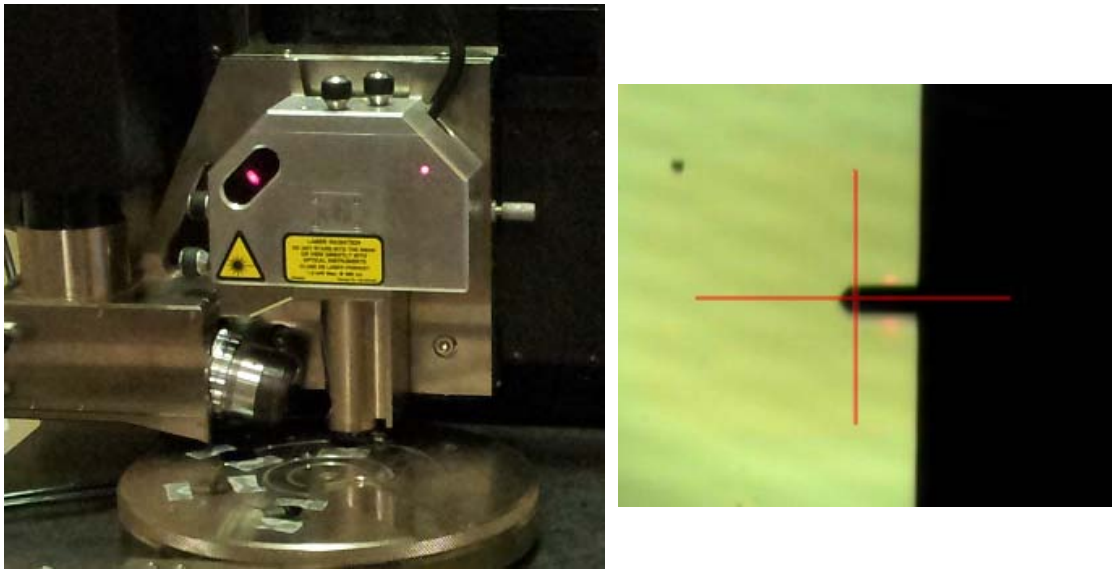

Figure 2.17: A head unit and sample stage of the Dimension 3100 AFM (Left) and a typical in-situ microscope image (Right). We can see where a cantilever is scanning is aligned and the laser positioned on the cantilever.

The AFM also has a damped air suspension system to remove any low frequency vibrations and oscillations from the floor, and a transparent plastic cover to reduce any acoustic pickup (noises and sounds from the room) (Figure 2.18). These kinds of countermeasure are very important for AFM because a vibrating tip scans the surface of samples with extreme sensitivity and image quality will be degraded by noise.

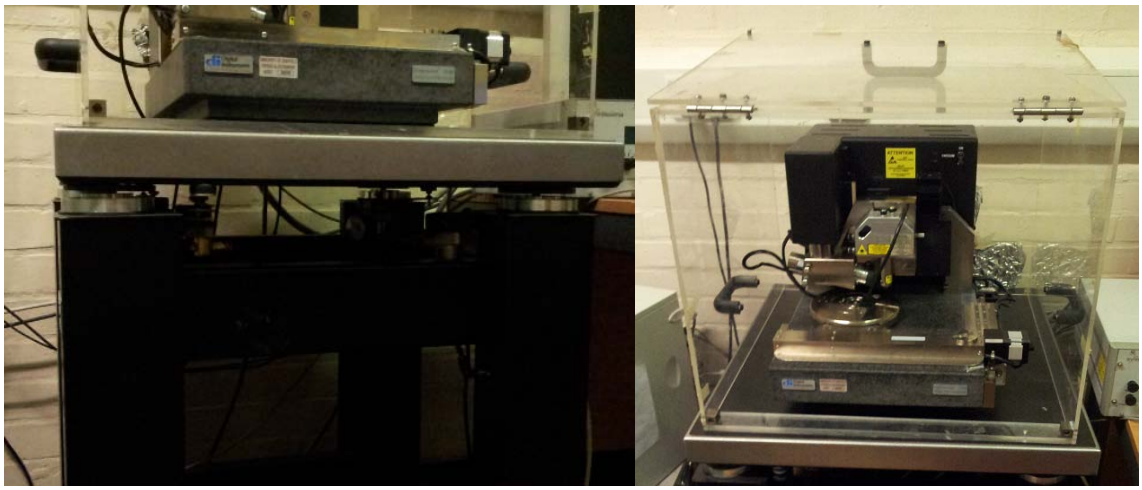

Figure 2.18: The air suspension table in the basement of the Hicks building with AFM to remove any vibrations and oscillations from the floor, and a transparent plastic cover to eliminate any sounds.

2.4 Grazing Incidence X-ray Scattering

2.4.1 The effectiveness of grazing Incidence X-ray Scattering for thin films

It is known that Grazing Incidence X-ray Scattering(GI-WAXS or -SAXS) is well suited for structural studies of thin films and structures because it capture the information of thin film samples very effectively shown in Figure 2.19. Ordinary XRD diffraction does not have enough information of thin film samples because its signal is mainly from the substrate (usually base metal). On the other hand, very small incidence angle like the critical angle, that is, grazing incidence, causes the total reflection and it gives strong and clear signals from thin films.

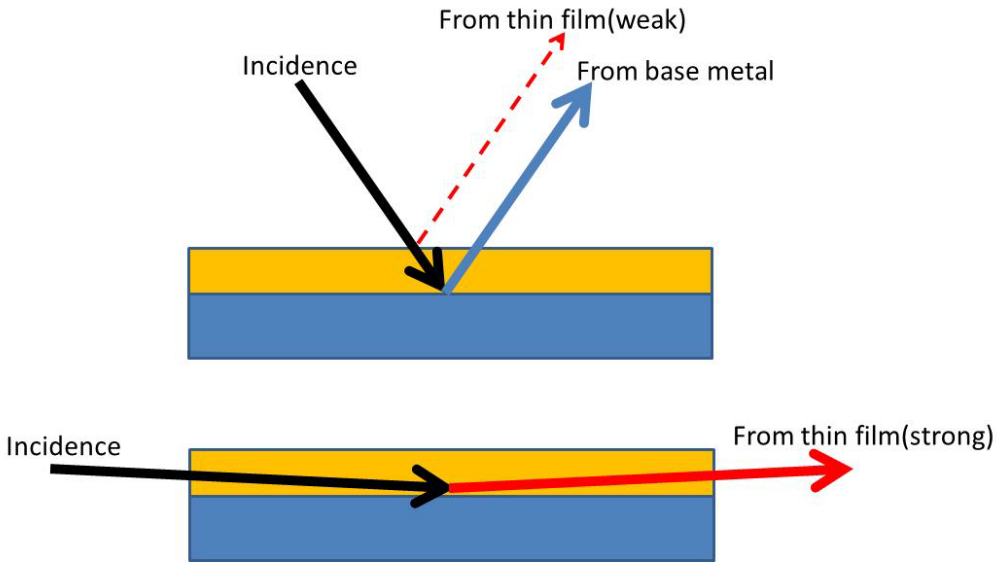

Figure 2.19: The schematic image showing that grazing incidence X-ray diffraction (GIXRD) is well suited for structural studies of thin films. Ordinary XRD diffraction does not have enough information of thin film samples because its signal is mainly from the substrate (usually base metal). On the other hand, very small incidence angle like a critical angle, that is, grazing incidence, causes the total reflection and it gives strong and clear signals from mainly a thin film.

Factor *et al.* pioneered the application of Grazing incidence X-ray diffraction (GIXRD) to polymer films, used also later by Kawana et al. [85, 86]. Factor's group investigated the near surface structure of aromatic polyimide films as a function of thermal treatment and film thickness. The structure parallel to the film surface was found to be more ordered at the air surface than bulk for the thick film. Macdonald *et al.* showed GIXRD provides a powerful method for determining the structure of the surface region of a polymer thin film [87]. By varying the angle of incidence of the X-ray beam around the critical angle for total reflection of the film, the penetration depth can be tuned to allow a direct comparison of molecular ordering in the surface and bulk of the film. GIXRD has provided a key tool for surface structural determination over the last decade and a half. The power of the technique lies in the fact that the X-ray penetration depth can be tuned by varying the incidence angle of the incoming beam, as shown in Figure 2.20 [87]. This shows the X-ray penetration depth as a function of incident angle for PET with a critical wave vector of 0.0143 $Å^{-1}$. By using an angle of incidence less than the critical angle α_c(typically of the order of 0.20°), the penetration of the X-ray beam can be limited to approximately 50 Å , allowing surface-sensitive measurement.

For larger values of α above the critical angle, the beam penetrates through the bulk of the film into the substrate, and the bulk scattering is measured.

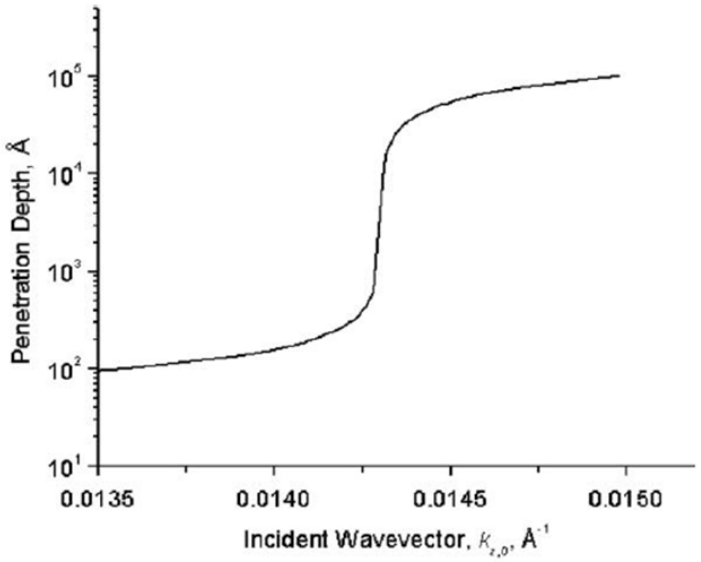

Figure 2.20 The X-ray penetration depth as a function of incident angle for PET with a critical wave vector of 0.0143 Å^{-1} [87].

Long-range surface and bulk ordering in PET films was characterized using GIXRD by Jukes *et al.* [51]. This technique was first applied to thin polymer films by Factor *et al.* [86] and has more recently been used to investigate molecular ordering in thin films of the conjugated polymers polyfluorene and poly-(3-hexylthiophene). The other principal advantage of the technique is that the structure both in the plane and out of the plane of the sample surface can be probed by employing one of two different scattering geometries. The principal geometry used in this work is the grazing incidence surface-plane scattering (GISPS) geometry, illustrated in Figure 2.21b [85]. In this geometry, the exit angle is kept equal to the (small) incident angle of the X-ray beam, and the detector is swept horizontally. The scattering vector Q is then primarily defined by the azimuthal displacement of the exit beam, giving information about correlations parallel to the sample surface and in-plane structure. A second geometry is grazing incidence asymmetric Bragg scattering (GIABS) in which the diffracted beam and the scattering vector Q are in the plane defined by the incident beam and the surface (Figure 2.21a). This gives information primarily about correlations normal to the sample surface.

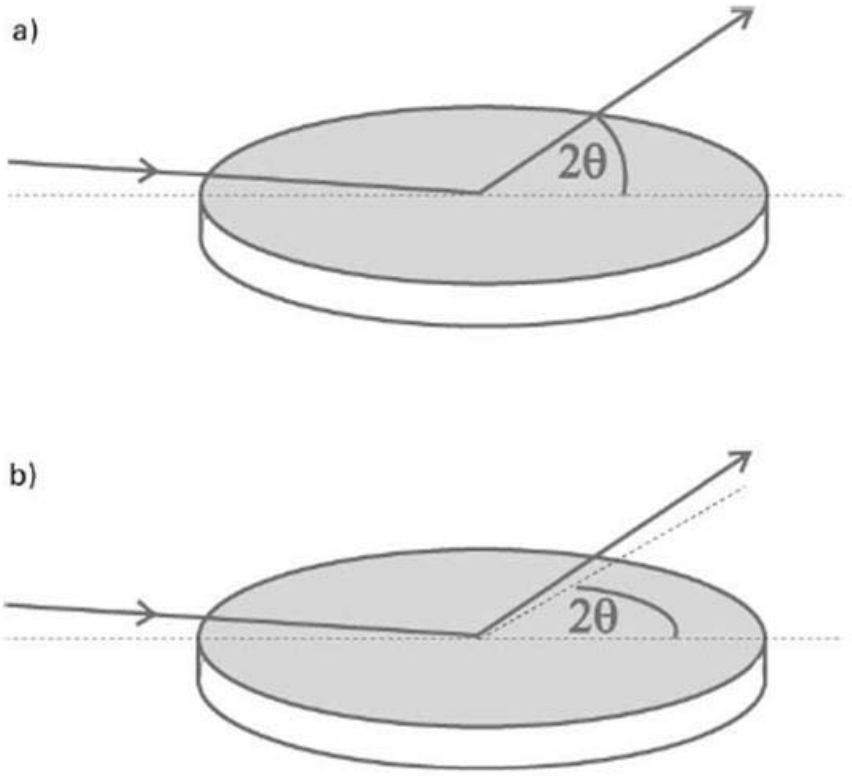

Figure 2.21: Schematic images of GIABS(a) and GISPS(b). [85] In GIABS geometry, the diffracted beam and the scattering vector Q are in the plane defined by the incident beam and the surface. This gives information primarily about correlations normal to the sample surface. In GISPS geometry, the exit angle is kept equal to the (small) incident angle of the X-ray beam, and the detector is swept horizontally.

2.4.2 Experimental facility, instruments, and apparatus

My measurements on PET were taken on the XMaS beamline at the European Sychrotron Radiation Facility (ESRF), Grenoble, France. The X-ray wavelength of 1.6Å was selected by successive reflections from two parallel Si(1 1 1) monochromator crystals in the nondispersive setting. The beam size of 1.0 × 0.5 mm was defined by four-jaw slits before the sample. Two sets of four-jaw slits on the detector arm were used to define the resolution and the surface area on the sample from which scattered radiation was collected by a Ge solidstate detector. An air-filled ion chamber located just before the sample was used as a monitor for the incident beam flux. The

experimental facility, instruments, and apparatus is shown in Figure 2.22 (XMaS: BM28 and its optics hutch).

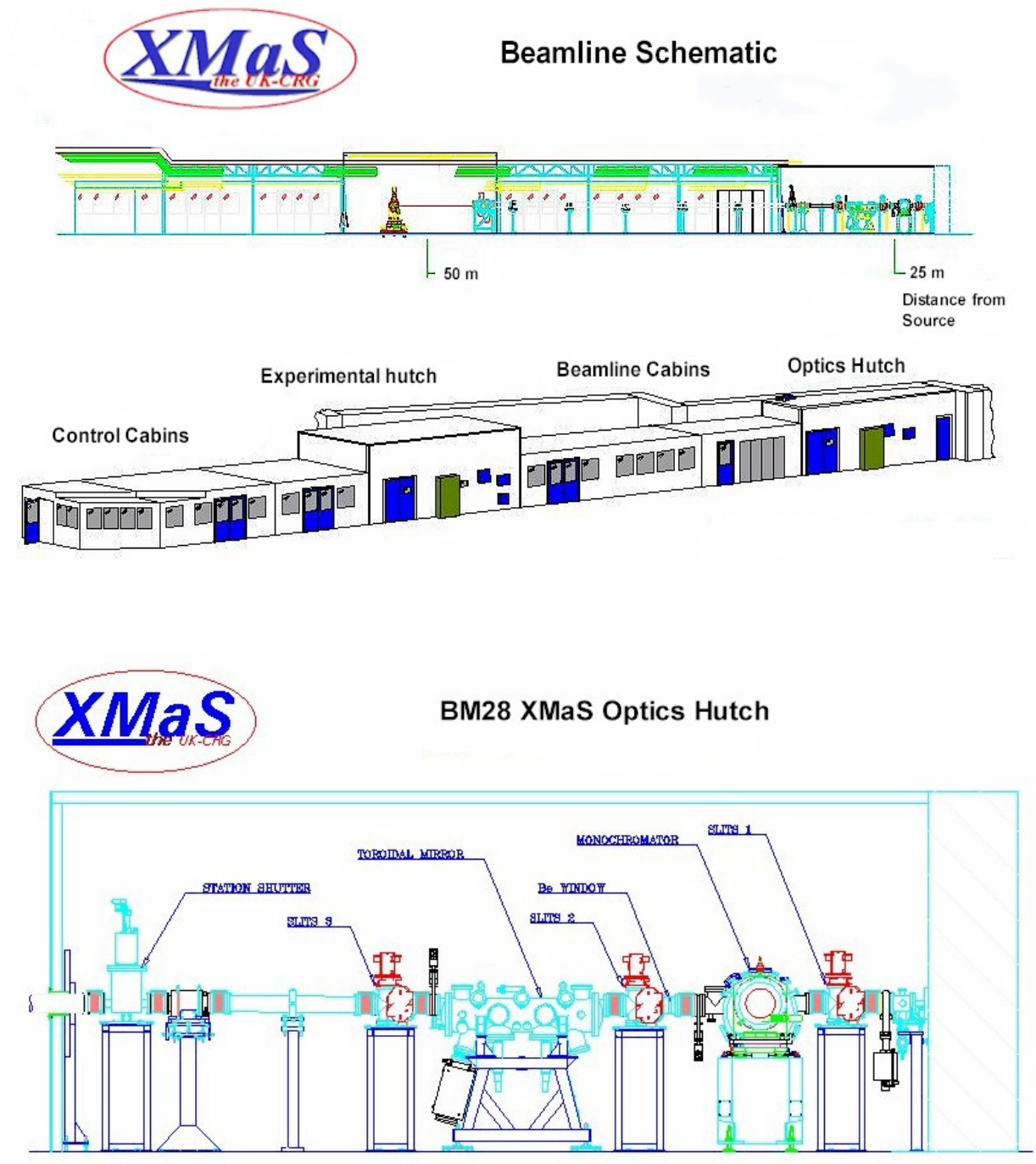

Figure 2.22: The schematic diagram of experimental facility, instruments, and apparatus. Beamline was XMaS: BM28 with optics hutch shown above.

In this study, both grazing incidence wide angle X-ray scattering (GI-WAXS) and grazing incidence small angle X-ray scattering (GI-SAXS) was employed. GI-WAXS is used for detecting crystallization in thin PET films and analysing its crystal structures. GI-SAXS is for observing long range ordering just before crystallization. The detailed results of measurements and discussions are in Chapter 5 and 6. Basic conditions of these measurements were as below.

GI-WAXS

- Facility and beam line: ESRF, BM28(XMaS)
- Beam energy and wavelength: 15keV, 0.827 Å
- Sample size: 10mm×10mm
- Detector: MCCD 2D detector
- Incident angle: 0.2°~3.5mrad

GI-SAXS

- Facility and beam line: ESRF, BM28(XMaS)
- Beam energy and wavelength: 7.085keV, 1.75 Å
- Sample size: 10mm×10mm
- Condition: We had slits on the detector and soller slits to give a low background
- Detector: a point detector, calibrated by our beam scientist.
- Incident angle: 0.2°~3.5mrad

Chapter 3

Improvement in the surface roughness of thin polymer films

In any study, making good samples is one of the most important factors for success and it is not too much to say it determines the quality of a study. In this chapter, I will describe in detail how to make good thin PET film samples by spin coating. The essential recipe for making good samples, control of film thickness, removal of solvent, and optimal suppression of crystallinity will be shown. These are very important for my study because thin film samples are required that are flat and uniform enough to be measured by ellipsometry and GI-Xray scattering and not to be crystalline for investigations of the early stage of crystallization. The presence of pre-existing crystals in the samples would strongly influence the kinetics of further crystallisation, particularly any nucleation steps, making it more difficult to interpret our investigations and measurements, especially in thin films. However, there are many difficulties of making good thin PET film samples. I would like to talk about this at first.

3.1 Difficulty of making thin PET film samples

The samples in my study are required to have surface flatness and not to have any pre-existing crystallinity because samples should be flat for GI-Xray scattering and ellipsometry measurements [88, 89, 90], and should be entirely amorphous in order to investigate the early stage of crystallization of a thin PET film. The surface roughness of liquid is usually under 1 nm [61, 62] and this is a benchmark for good flatness.

However, it is difficult to make flat thin PET amorphous film samples for a number of reasons. First of all, not many solvents can dissolve PET well [91, 92, 93]. Most of the possible solvents are dangerous and have fast evaporation rates: of course it is preferable not to use a dangerous solvent, and a quick evaporation rate, that is to say a

highly volatile solvent having a high vapour pressure, makes it very difficult to form a flat uniform thin film by spin-coating [94].

Secondly, PET is crystallized easily from the glassy state even at low temperature, thereby we need to cancel any crystals in the spin coated samples carefully [95]. As solvent behaves as a plasticizer which makes the molecular mobility higher, PET crystallization can be induced during crystallisation very easily [96, 97]. However, PET has high melting point (250 °C), therefore, if samples are heated at such a high temperature in order to melt out the crystals, degradation or surface coarsening could be induced and this would be critical for polymer thin films. We need to handle this procedure very carefully. PET is degraded if held at temperatures above around 285 °C [98].

Finally, PET degrades easily by hydrolysis with humidity in air at high temperature [99, 100, 101].

On the other hand, a much simpler polymer, for example Polystyrene (PS), is usually very easy to handle. PS is easily soluble in many kinds of solvents and there are not any problems of crystallization or degradation, hence it is easy to make good thin film samples, and there are many studies of thin PS films (for example, [10, 94, 102]). It is not too much to say that one of the difficulties and significant obstacles for studies of thin PET films is the difficult of preparation of good samples compared to PS or other common polymers.

In order to investigate the early stage of crystallization of thin PET films, samples are required to have flat surface and be amorphous. I would like to discuss how to make good thin PET film samples with Spin-coating from the next section.

3.2 Spin coating

3.2.1 Theory of spin coating

Spin coating is widely used for making thin polymer films [65]. By using spin coating, film thickness can be controlled easily by the rotational rate and solvent concentration [103], and very thin films can be made with low surface roughness comparatively by spin coating [104]. These are some of the many reasons why spin coating is so often used for academic field studies.

In order to discuss how to make good thin PET amorphous films by spin-coating, a basic theory of spin-coating should be described at first.

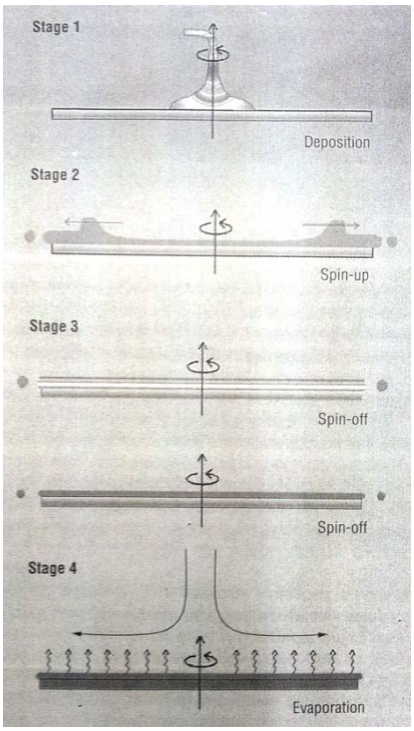

Figure 3.1: This figure shows the typical process of spin coating. Firstly, a solution of polymer is dropped on a substrate, then, droplets are spun-up and spun-off all areas of the substrate. Finally, a thin film is formed that thins with evaporating solvent [105].

Figure 3.1 shows the typical process of spin coating. At first, a solution of polymer is dropped on a substrate, then, droplets are spun-up and spun-off all area of the substrate. Finally, a thin film is formed and the solvent evaporates [105].

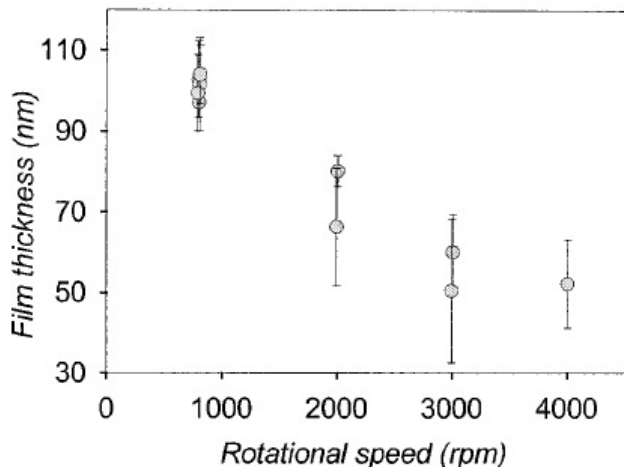

Figure 3.2: A typical relationship between rotational speed and film thickness [106].

Figure 3.2 shows a typical relationship between rotational speed of spin-coating and film thickness. As rotational speed rises up, the film thickness reduces as shown in this figure because spinning up and out process proceeds more efficiently at higher rotational speed [106].

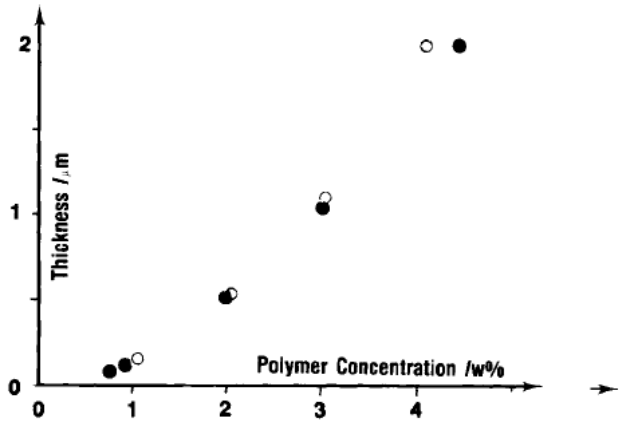

Figure 3.3: A typical relationship between polymer concentration and film thickness made by spin-coating [103].

Figure 3.3 shows a typical relationship between polymer concentration of a solution and film thickness made by spin-coating [103]. It is very easy to see that a more concentrated polymer solution would make thicker spin coated film than from a more dilute solution. The film thickness can be controlled by the spin rotation rate and the concentration of the polymer solution.

3.2.2 Experiments and results

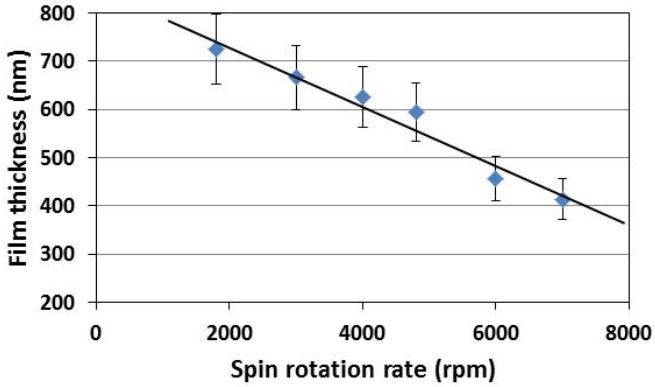

Figure 3.4: Spin rotation rate versus film thickness as measured by ellipsometry. PET solution was made with 1,1,1,3,3,3-Hexafluoro-2-propanol (HFIP) as 3wt% and dropped on Si wafer.

Figure 3.4 shows rotational speed versus film thickness as measured by ellipsometry. PET solution was made with 1,1,1,3,3,3-Hexafluoro-2-propanol (HFIP) as 3wt% concentration. Films were made on Si wafers. We can see that PET films became thinner as rotational speed increases, the same behaviour seen for typical spin coating theory mentioned above.

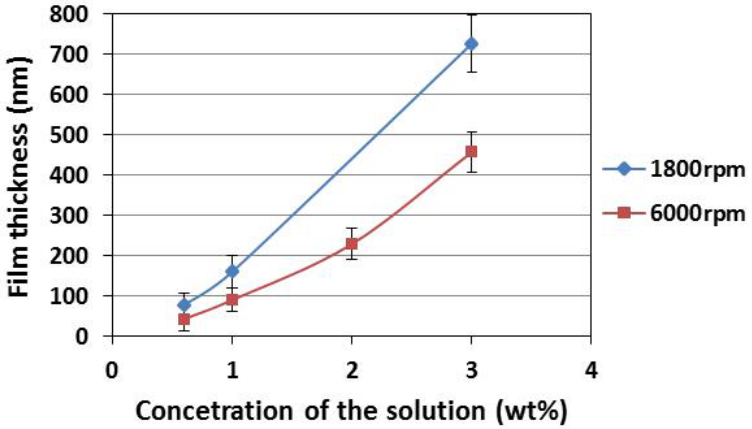

Figure 3.5: Film thickness vs concentration of PET solution (HFIP) at 1800 rpm and 6000 rpm of rotational rate.

The concentration of the solution also affects film thickness. Figure 3.5 shows the relationship between film thickness and concentration of PET solution at 1800 rpm and 6000 rpm of rotational rate of spin-coating. PET was dissolved with HFIP in these solutions. As shown in Figure 3.5, various thickness films were formed with different solution concentrations . For instance, under 400 nm thickness films could not be formed from 3wt% solution even at high spin speeds of 6000rpm, on the other hand, under 100 nm thickness films could be formed very easily with under 1wt% solutions.

However, these films had large surface roughness and did not have uniform thickness, therefore were not acceptable for GI-Xray scattering and ellipsometry. Surface roughness was measured by AFM as root mean squared (RMS) over a 30 μm square field. The representative surface roughness of these films was about 14 nm (made at 6000 rpm). A further problem was that there were clear striations on film surface as shown in Figure 3.6. These striations are interference colours coming from the unevenness of the film thickness.

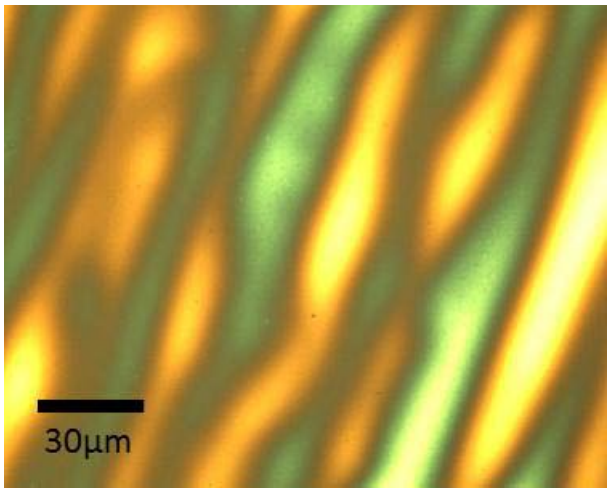

Figure 3.6: A typical optical microscope image of thin PET spin coated film made solely with HFIP solvent.

Although it is difficult to say that how large the critical roughness is for these measurements, large roughness and striations are sure to be undesirable [88, 89, 90]. In order to reduce surface roughness and striations of thin films by spin-coating, extending the film formation time during spin-coating is effective [94, 107]. Dunbar *et a*l suggest that this kind of defect is caused by evaporation-driven surface tension effects. For example, the early evaporation of light solvents can cause an enrichment of water and/or other less volatile species in the surface layer. In these circumstances, higher surface

tension can draw material in at regular intervals, with irregular evaporation leading to surface relief. Such blemishes can be reduced or minimized by selecting a different solvent with lower volatility or by adding surfactants to the coating solution [105].

During spin-coating process, the developing film is thinning with spinning up and off and evaporating solvent, then interference colour and fringes(striations) can be seen [108, 109]. We can estimate the film formation time roughly from this colour and fringe change and there are several ways to extend film formation time in spin-coating. The film formation time here is the time from the start of spinning to disappearance of the interference colour and fringes. Controlling rotational rate can be mentioned at the head of list of this problem. For example, if rotational speed is changed from 6000 rpm to 1800 rpm, the film formation time is changed to be roughly three times longer, from about 1 second to 3 seconds. However, this method was not effective to reduce surface roughness. Because higher rotational rate usually gives lower surface roughness [110], even if low rotational rate makes the film formation time extended, its effect for reduction of roughness would be counteracted. As a fact, this approach was not effective in my study.

The evaporation rate is controlled by atmosphere, kinds of solvent, and so on [111]. It is especially important, to control evaporation rate for spin-coating because it extends or shortens film formation time and affects the roughness and uniformity of the film surface. Strawhecker *et al* shows that surface roughnesses of thin films made by spin-coating becomes large with solvents which have high evaporation pressure, that is, fast evaporation rate solvents [94]. And vice versa, slow evaporation rates make films that are flat and uniform. Figure 3.7 shows a simulation of the degree of spin coating film uniformity vs dimensionless time at different values of the evaporation parameter M [107]. Large M indicates a large solvent evaporation rate. In this figure, large evaporation rates are linked to degradation in the film uniformity. Of course, linked to film uniformity, the surface roughness becomes larger with a highly volatile solvent [94].

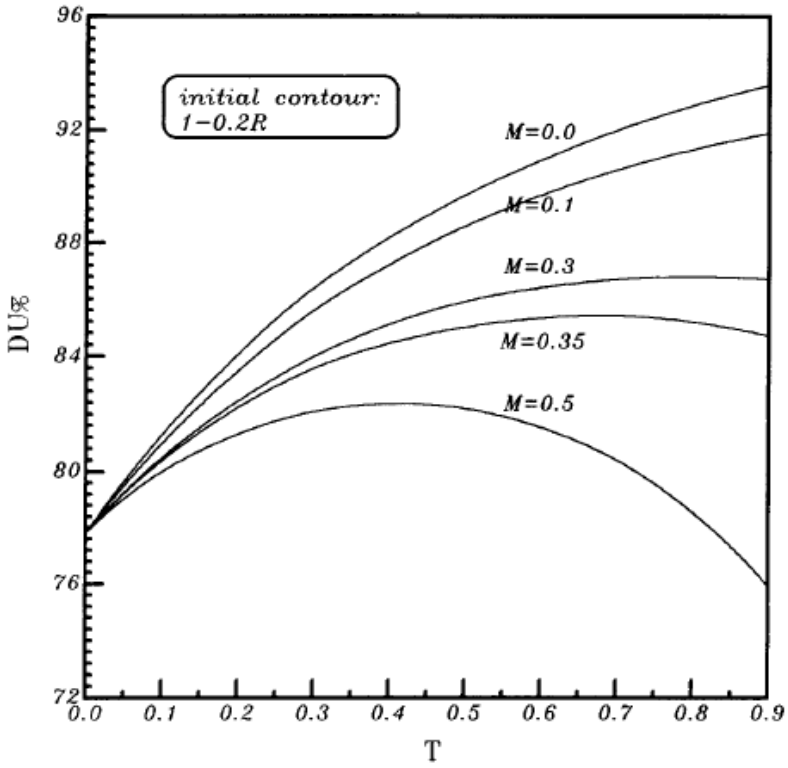

Figure 3.7: Degree of spin coating film uniformity vs dimensionless time at different values of the evaporation parameter M [107].

From the view point discussed above, I tried to change the atmosphere around the spin-coating stage with a cover shown in Figure 3.8. My idea was that if the atmosphere inside the cover is near the saturated vapour pressure of the solution solvent, then the evaporating rate of the solvent must slow down and the film formation time should be extended. A similar trial has been practiced by a member of our laboratory and it shows an extension of the film formation time [109].

Figure 3.8: The cover to control atmosphere around a spin-coating stage.

This chamber covers the entire spin-coating stage, the rubber cap (suba-seal) is on top of this cover, and a needle pierces it and introduces droplets of polymer solution for spin-coating, as shown in Figure 3.9. Only solvent, without solute PET, was introduced to the chamber at first, in order to saturate solvent atmosphere inside, this time was for example 10 or 20 minutes. Then I introduced droplets of polymer solution for spin-coating.

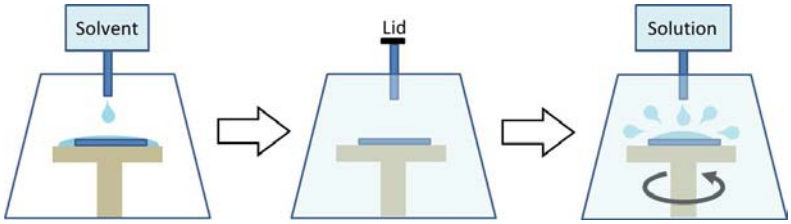

Figure 3.9: Schematic image of the spin-coating process with the cover.

The film formation time was extended by a factor of about 2 by this procedure, from 1 or 2 seconds to 3 or 4 seconds, but the surface roughness hardly changed. A representative RMS value of not-covered films was 14 nm, and that of covered films was similar at 12 ~ 13 nm, and the strong film striations still existed. It seems not to give enough improvement in the film quality.

Next, in order to extend film formation time much more, the solvent was changed to improve its properties, mainly the evaporation characteristics. The reason for the large surface roughness described above is that HFIP has a very high evaporation rate. Because a high evaporation rate is caused by having a low boiling point and high

evaporation pressure, I tried to reduce the overall evaporation rate using other solvents which have high boiling point and low evaporation pressure. However, as described above, because we do not have a lot of options of solvents to dissolve PET [91, 92, 93], the choice of solvent is limited. Accordingly, I choose a method as follows. A concentrated PET solution is made with HFIP first, then it is diluted by various kind of solvent. This method enables us to make different types and features of PET solutions very easily.

In this procedure, I mixed up the concentrated solution and a few different kinds of additional solvents, so those solvents are required to have not only a boiling point and evaporation pressure but also miscibility with PET and HFIP. And the ease of removability from thin films is also an important factor. A good balance of these properties is a key to this procedure.

I considered solubility parameter as an indicator of miscibility because solubility parameter is widely used in selection of solvents and the best known use of solubility parameter is for predicting solubility of polymers[112]. The solubility parameter is calculated from the sum of interaction energies of all molecules present in a unit volume of a solid or liquid. Interaction energies are caused from every element of a molecule, for example, the main segment and functional groups. The interaction energies consist of dispersion, polar, and hydrogen-bonded interactions. In the idea of the solubility parameter, if solubility parameters of different molecules are close to each other, they are miscible with each other easily. The definition equation is as below.

$$\delta = \sqrt{(\Delta H - RT)/V} \tag{3.1}$$

The idea of this equation is that the interaction which aggregates molecules as aliquid is only the intermolecule force. Therefore, the cohesive energy of liquid ΔE and the enthalpy of evaporation ΔH have a relasionship as below.

$$\Delta H = \Delta E + P\,\Delta V = \Delta E + RT \tag{3.2}$$

That is, the solubility parameter δ is the square root of evaporation energy to evaporate $1cm^3$ of liquid. Its dimension are $(cal/cm^3)^{0.5}$.

Boiling point can be used as a rough estimation for the extension of film formation time and removability of solvent from PET thin films, because a high boiling point solvent usually evaporates slowly with low evaporation pressure and needs to be heated at high temperature to be removed.

However, removability is controlled not only by boiling point but also by the solubility parameter because solubility parameter is related to the interaction of molecules, for example, hydrogen-bond and polar interactions [112]. In my study, it is a little difficult to predict what combination of solvent is preferable because low evaporation rate, solubility, and removability are tangled complicatedly. Consequently I needed to seek a balanced optimum point of boiling points and solubility parameters practically. Table 3.1 shows components of solvents used in this study and their properties and condition of films [112, 113, 114]. When additive solutions were selected, the criterion was miscibility with PET and HFIP and to have various boiling points. Considering that the solubility parameter of PET and HFIP are 10.5 and 8.6 $(cal/cm^3)^{0.5}$, I selected solutions which have solubility parameters between them mainly.

Table 3.1: Components of solvent and its properties, and condition of films

	Kind of Solvents and ratio (PET wt%)	Boiling point (°C)	Solubility Parameter （MPa）	Solution / Film conditions
Base	HFIP (3)	59	8.6	△：a little coarse
1	HFIP (2)	59	8.6	△：a little coarse
2	HFIP (1)	59	8.6	△：a little coarse
3	HFIP (0.6)	59	8.6	△：a little coarse
4	HFIP / toluene = 2 (1)	110（toluene）	8.9（toluene）	△～×：very rough
5	HFIP / IPA = 2 (1)	82.5（IPA）	12.0（IPA）	×：PET precipitate
6	HFIP / TrCE = 2 (1)	113（TrCE）	8.6（TrCE）	×：separates to 2 liquid phases
7	HFIP / TeCE = 2 (1)	121（TeCE）	10.6（TeCE）	×：separates to 2 liquid phases
8	HFIP / NB = 2 (1)	210（NB）	10.6（NB）	×：large cracks on the surface
9	HFIP：2CP ＝ 2：1 (2)	175（2CP）	10.1（2CP）	○：very flat, no striations
10	HFIP：2CP ＝ 2：1 (1)	175（2CP）	10.1（2CP）	○：very flat, no striations

IPA : iso-Propanol, TrCE : Trichloroethane, TeCE : Tetrachloroethane,
NB : Nitrobenzene, 2CP : 2-Chlorophenol

As a result, there were not very clear dependences between miscibility, flatness of thin films, and solubility parameters. For example, Tetrachloroethane and 2-Chlorophenol have similar solubility parameter,δ, 10.6 and 10.1 $(cal/cm^3)^{0.5}$. But their results were quite different. Although nearly perfect thin films were made by 2-Chlorophenol, on the other hand, Tetrachlorophenol was not able to act as a solvent. It might be caused by immisciblity of Tetrachlorophenol with HFIP and 2-Chlorophenol seems to have much more polar and hydrogen bonding than Tetrachlorophenol.

As I said above, solubility parameter has factors of dispersion, polar, and hydrogen-bonding, described as δ_d, δ_p, and δ_h. Even though total solubility parameters of two liquids are different, if these factors are similar, those two liquids might be miscible [112]. Solubility parameter δ and these factors are described as below.

$$\delta^2 = \delta_d^2 + \delta_p^2 + \delta_h^2 \tag{3.3}$$

Dispersion factors,δ_d, of tetrachloroethane and 2-chlorophenol are 9.2 and 9.1, polar factors,δ_p, are 2.5 and 3.3, and hydrogen-bonded factors,δ_h, are 4.6 and 6.8. It seems that hydrogen-bonded factors were a little different. This might be a reason why the results of them were so different. However, it seems sure that high boiling point solvents make film formation time extended, for example, 2-chlorophenol, boiling point is 175 °C, extended film formation time about10 times longer than HFIP, boiling point is 59 °C (HFIP: 1 or 2 seconds, 2-chlorophenol: about 15 seconds), furthermore, nitrobenzene has a much higher boiling point, 210 °C, and it extended film formation time much more. But, nitrobenzene could not make flat films and there were many large cracks on the surface. It is not simple to find a good balance point for making good thin PET films.

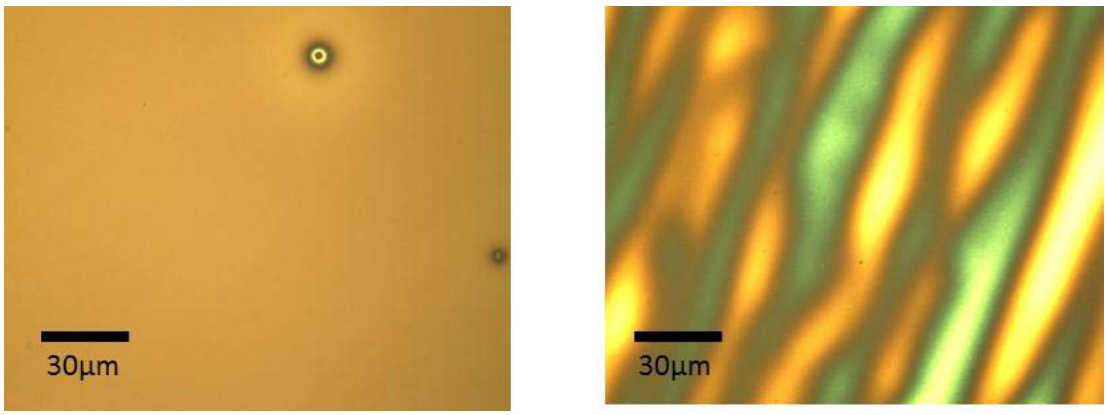

Figure 3.10: Microscope images of thin PET films. Right: Made from HFIP solution (Base solvent in Table 3.1, RMS:14 nm), Left: Made from HFIP +2-chlorophenol mixed solution (No.9 solvent in Table 3.1, RMS: 0.5nm)

Figure 3.10 shows microscope images of thin PET films. The right hand side image is made from HFIP solution, base solvent in Table 3.1, and left hand side is HFIP + 2-Chlorophenol solution, No.9 in Table 3.1. We can see their surface flatness are clearly different, there were no striations in the left hand side image. Their surface

roughness, RMS: Root Mean Squared, were measured by AFM in 30μm square area and they were 14 nm and 0.5 nm respectively. RMS value of 0.5 nm is nearly ideal flatness as liquid surface [61, 62]. This flatness should be enough for ellipsometry, GI-WAXS and GI-SAXS.

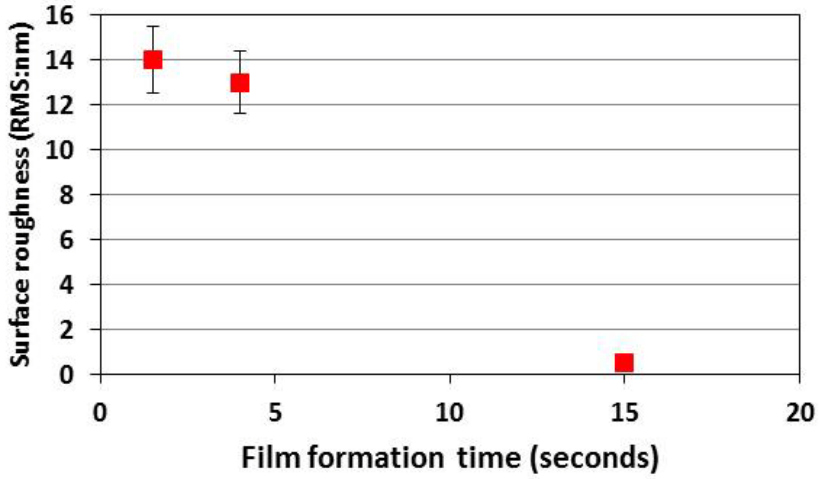

Figure 3.11: Relationship between film formation time and surface roughness.

Figure 3.11 shows the relationship between film formation time and surface roughness. We can see that long film formation time contributes to reducing the surface roughness of thin PET films. The point with film formation time 1 or 2 seconds and RMS 14 nm is for a film made from HFIP solution (Base solvent in Table 3.1). The second point with film formation time 4 seconds and RMS 13 nm is a film made from the same solution with an atmosphere control cover. The point with film formation time 15 seconds and RMS 0.5 nm is a film made from No.9 solution in Table 3.1 without the cover. The optimizing solvents were quite effective in this system, so there were no need to use the chamber cover again.

Through by this practice, I found that the contribution of spin rotation rate for film thickness was not changed with different solutions, and it seems that each of the process parameters of spin-coating can be controlled independently. This is not related to making good thin PET films directly, but I believe that this knowledge may be useful for researchers and students studying polymer materials. This is why I refer to and describe this interesting information here, and show Figure 3.12 and 3.13.

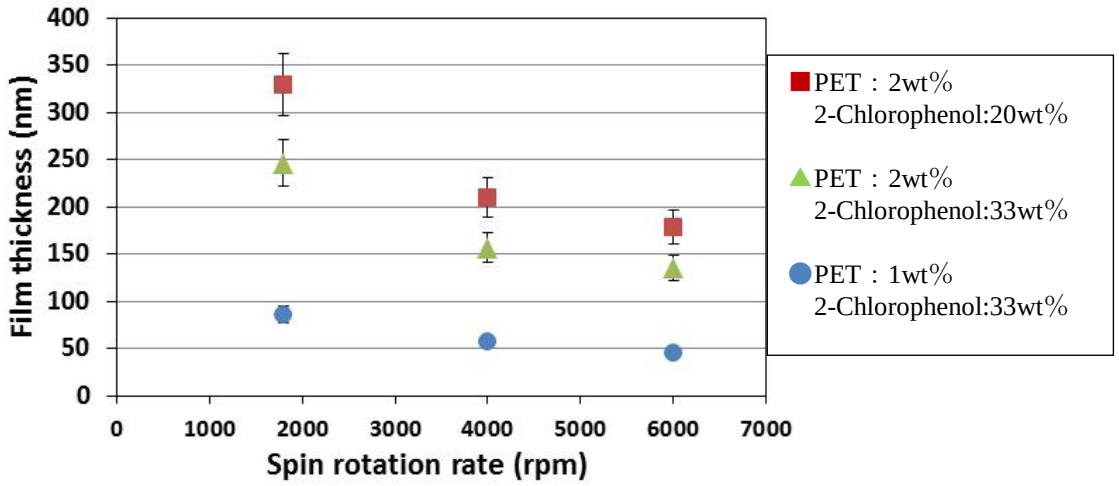

Figure 3.12: Relationship between spin rotation rate of spin-coating and film thickness for some PET solutions.

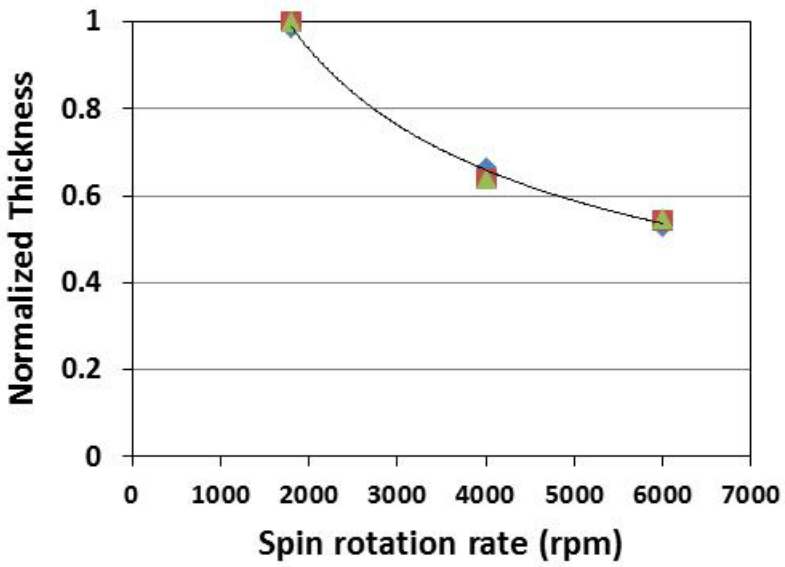

Figure 3.13: Relationship between spin rotation rate and the normalized film thickness. Contribution of spin rotation rate seems same for various PET solutions.

3.3 Removal of residual solvent

Thin films made by spin-coating usually include residual solvents. Because this could affect the dynamics of the experiment, it should be removed as much as possible. For example, residual solvents could behave as a plasticiser and the crystallization rate would be changed. Therefore, we need to remove residual solvents in order to investigate crystallization process precisely. Besides, if the thin film includes residual solvents, measurements of film thickness by ellipsometry would be in error because residual solvents swell the film thickness to a value greater than the actual pure polymer volume.

Figure 3.14 shows that a film thickness measured by ellipsometry of a sample which includes residual solvents with temperature. Solution was 3wt% PET with HFIP (Base solution in table 3.1), rotational rate was 6000rpm, a film was made on a Si wafer, and this sample was heat by a Linkam heat stage up to 120 °C with 90 °C/minutes under nitrogen atmosphere. We can see a large thickness reduction from about 60 °C. Because the boiling point of HFIP is 59 °C, we deduce that this reduction is caused by removal of residual solvents. This data shows that residual solvents might distort the true polymer film thickness measurements, and demonstrates the importance of solvent removal.

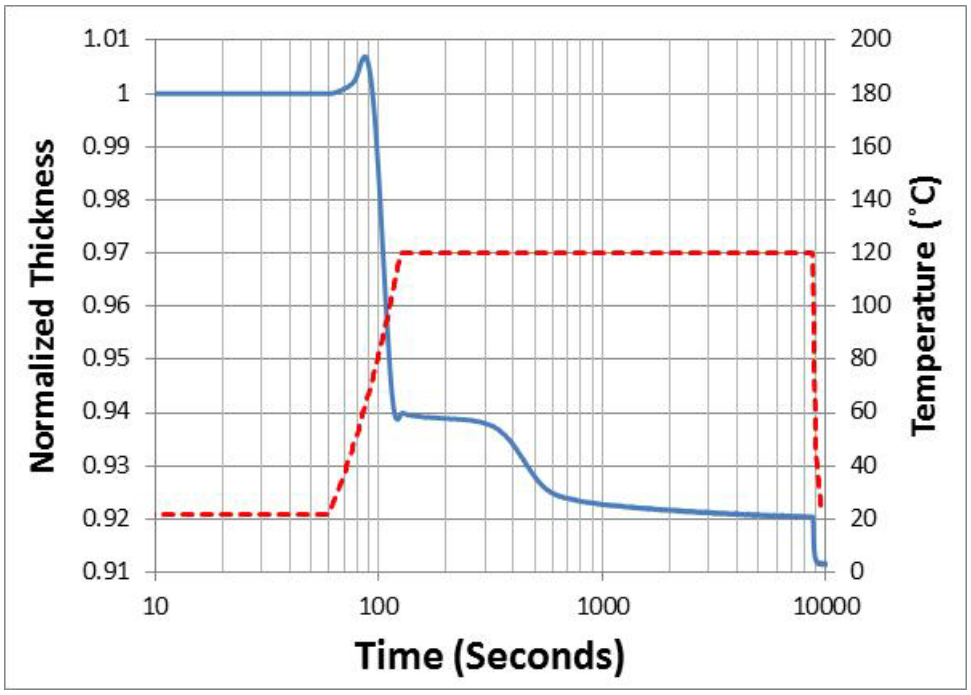

Figure 3.14: Relationship between temperature, and film thickness change for a sample which includes residual solvent measured by ellipsometry by time. Left hand side vertical axis indicates normalized film thickness and right hand side is temperature of the sample.

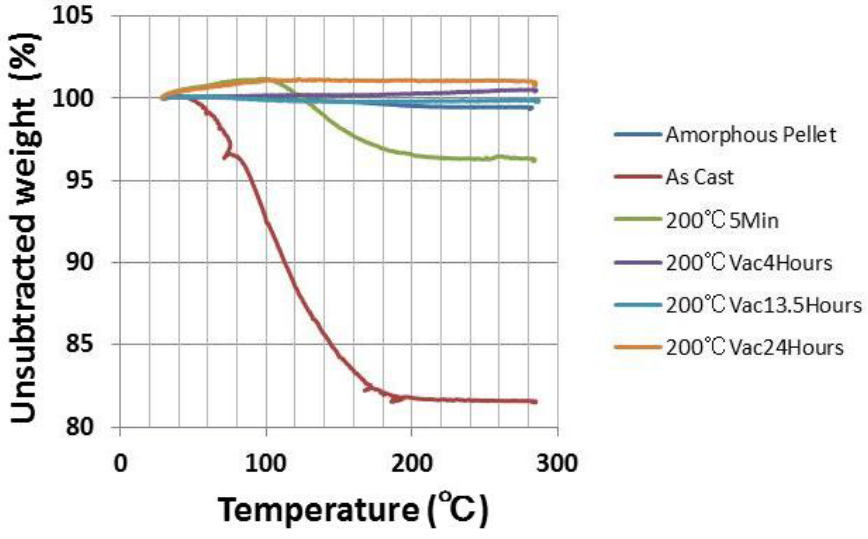

Figure 3.15: Thermal Gravity Analysis (TGA) of various PET samples.

Figure 3.15 shows Thermal Gravity Analysis (TGA) under nitrogen atmosphere of various PET samples. Amorphous pellet is a melt and quenched PET pellet (homo PET, *Mn*=27500 and polydispersity *Mw/Mn*=2.4, shown in Chapter 2), others were thin films made from solution of 3wt% PET with HFIP and 2-Chlorophenol (No.9 solution in table 3.1) and rotational rate was 1800rpm on a Si wafer. Except as cast, thin films were heated in a vacuum oven at 200 °C for 5 minutes, 4, 13.5, and 24 hours in order to remove residual solvent. Because the melt and quenched PET pellet does not have any solvent, its profile was very flat. This indicates there is no removal of solvents. On the other hand, the as cast film has a substantial residual solvent content. Hence its profile showed very large mass reduction because of the large amount of solvent removal. There was a certain reduction of weight in a profile heated at 200 °C for 5 minutes in the vacuum oven and this indicates that this sample does include some residual solvent. Profiles of 4 and 13.5 hours annealed films were very similar to amorphous pellet and this indicates they have no solvent. 24 hours annealed sample also has no reduction, but from a point of view that much long time anneal might cause degradation, it seems better to avoid 24 hours.

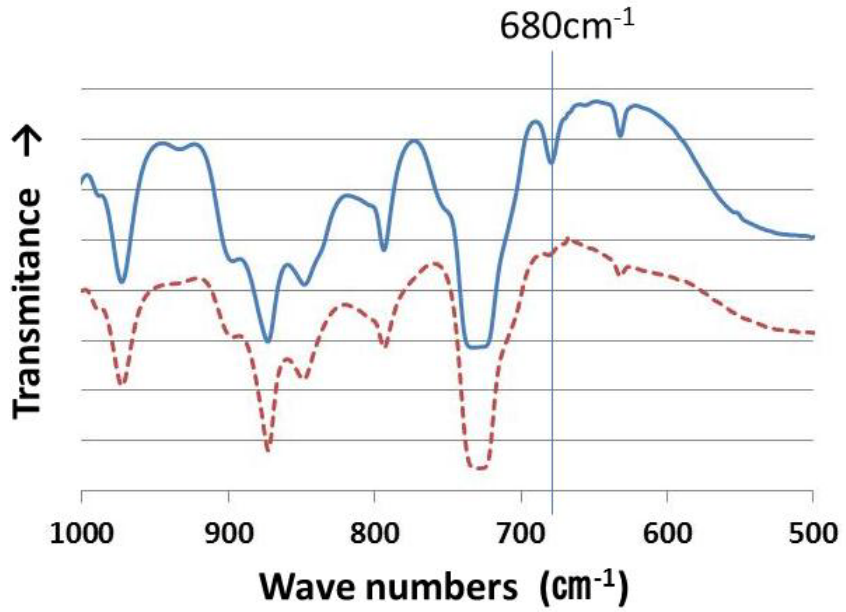

Figure 3.16: FTIR spectrum of samples which were dried in a vacuum oven at 200 °C for 5 minutes (Solid blue line) and 4 hours (Broken red line).

Figure 3.16 shows Fourier Transform Infrared Spectroscopy (FTIR) spectrum of samples heated at 200 °C for 5 minutes (Solid blue line) and 200 °C for 4 hours

(Broken red line) in a vacuum oven. From figure 3.15, a sample heated at 200 °C for 5 minutes should include some solvent and a sample heated at 200 °C for 4 hours should not. This FTIR spectrum data also supports it. 2-Chlorophenol and HFIP has a peak of IR absorbance at around 680 cm^{-1} (677 and 686 cm^{-1}). The solid blue line has a peak at 680 cm^{-1} but the broken red line does not or very weak. Because the boiling point of HFIP and 2-Chlorophenol are 59 °C and 175 °C, this peak seems to be from 2-Chlorophenol. Anyway, no peak in the red broken line should indicate that residual solvents was substantially removed . Other major peaks, for example, at 730 and 880 cm^{-1} are from PET independent from crystallinity. The FTIR spectrum of 2-Chlorophenol, HFIP, and PET are shown in Figure 3.17 [115, 116].

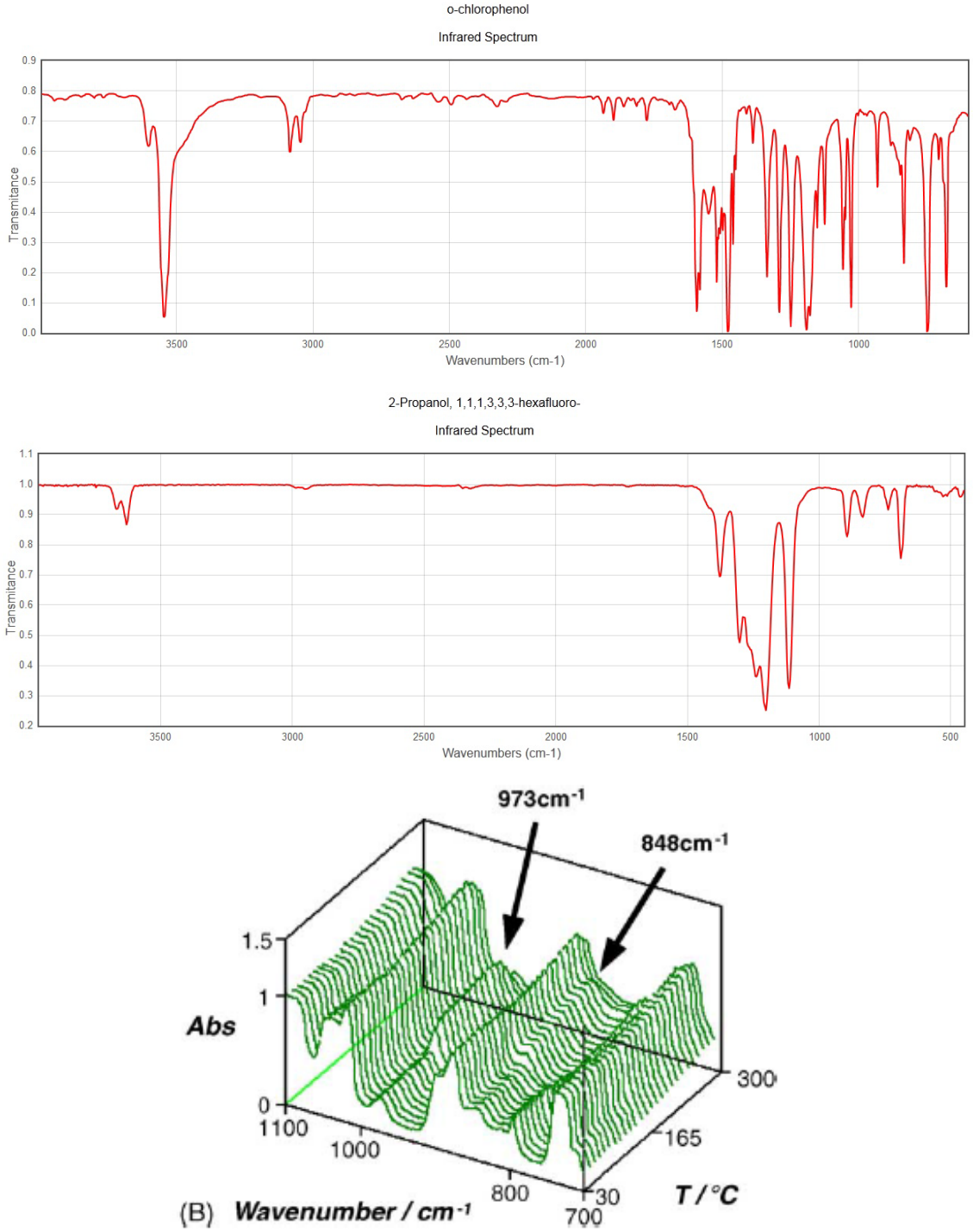

Figure 3.17: FTIR spectrum reference data of 2-Chlorophenol (upper), HFIP (middle), and PET (lower). 2-Chlorophenol and HFIP were from the "NIST Chemistry WebBook"[115] and PET was from a study by Yoshii *et al.* [116].

From these physical and chemical evidences, that is, TGA and FTIR, we can see that the condition of heating at 200 °C for 4 hours in vacuum oven is enough to remove residual solvents.

3.4 Influences of annealing atmosphere and time

In this study, crystals in any sample should be cancelled at the beginning of any measurements in order to investigate the early stage of crystallization. To cancel any crystals, samples should be heated above a melting point of PET, about 250 °C. However, 250 °C is a severely high temperature for thin polymer films. Because the surface is very sensitive, high temperature could cause some degradation easily, and most parts of thin films consist of surface. Figure 3.18 shows an example of degradation of thin PET films (left hand side image is normal PET spherulite and right hand side is degraded sample). After removal of residual solvents, in the case of a sample heated above melting point under air, almost certainly this kind of degradation emerged during annealing at around 120 °C for crystallization. On the other hand, in case a sample was heated under nitrogen, normal crystallization occurred. Of course, this strange structure and texture is undesirable for the study of crystallization and, above all else, this degraded structure had a very rough surface, rather fractured as if dewetting had occurred, hence ellipsometry was unreliable.

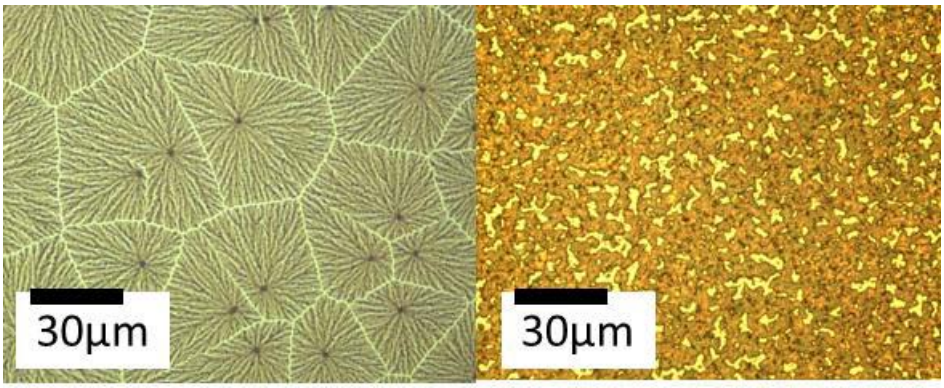

Figure 3.18: Normal spherulite of thin PET film (left hand side) and degraded texture of thin PET film (right hand side). Sample was annealed at 120 °C after heated at 250 °C in order to remove solvent under Nitrogen (left) and air (right).

PET is decomposed by hydrolysis and oxidation with humidity and oxygen in air at high temperature [99, 100, 101]. Figure 3.19 shows TGA data of melt-quenched PET pellets annealed under nitrogen (blue line) and air (red line). The lateral axis is time, left hand side vertical axis is normalized mass change, blue line is mass change under nitrogen, red line is under air, and right hand side vertical axis and green line indicate temperature. Under nitrogen, mass change was moderate and a reduction from 90 °C to 210 °C is due to removal of adsorbed water. Although the N_2 sample was heated up to 285 °C, there was not a marked mass reduction. On the other hand, under air, the mass changed very drastically. From just after the start of the measurement, the mass increased. This is perhaps due to the adsorption of water present in the ambient humid air. Then, mass was reduced rapidly and this should be desorption of adsorption water. The point is that, after reached 285 °C, the mass was rapidly reduced again. This would indicate decomposition with water and oxygen in air.

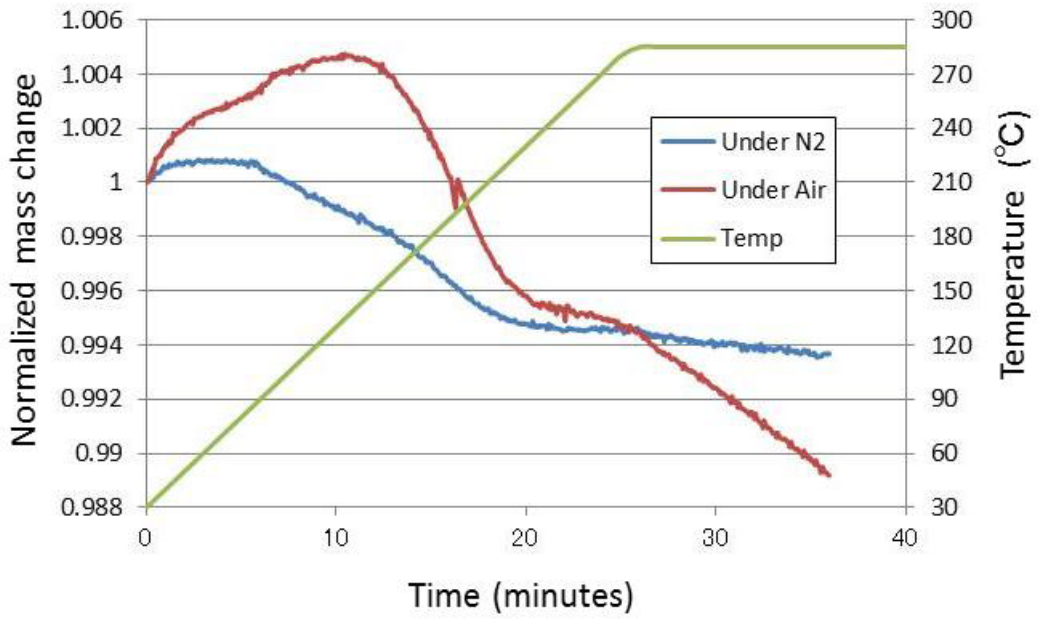

Figure 3.19: TGA data of melt-quenched PET pellets annealed under nitrogen (blue line) and air (red line).

Although I do not have any evidence about a relationship between the degraded structure and this decomposition shown by TGA, the fact that the degradation occurred from samples heated at 285 °C under air and the data that some kind of decomposition should be occurred at 285 °C under air seem to be related each other. The degraded texture seems like some kind of dewetting. And if molecules still remain as PET even

partially, crystallization should be occurred during annealing at 120 °C. If some decomposition does occur, the molecular weight of the polymer should decrease. However, I do not have any idea why dewetting was induced by decomposition and spherulites did not emerge—if PET is altered the amount of pure PET would be reduced and so crystallization would not be possible. To follow up this problem further would involve us in other factors than the main subject of this study and would take us beyond the scope of this thesis. Therefore, we may leave the details to other future studies. The important point here is that PET thin film samples should not be annealed under air and we should thermally anneal samples under nitrogen.

Figure 3.20 shows experimental apparatus for thermal annealing, to cancel any PET crystallites. A glove box was used for implementation of the inert nitrogen atmosphere for the thermal annealing at elevated temperatures. Inside the glove box, there are three Linkam heating stages for annealing and a bulk piece of metal for quenching the samples. Because I had to make many samples, the multiple heat stage systems made the process much more time efficient. After cancellation of crystals, the samples needed to be quenched in order to avoid crystallization. However, because water would degrade PET samples, I used bulk metal for quenching. Bulk metal was cooled stably by nitrogen flow.

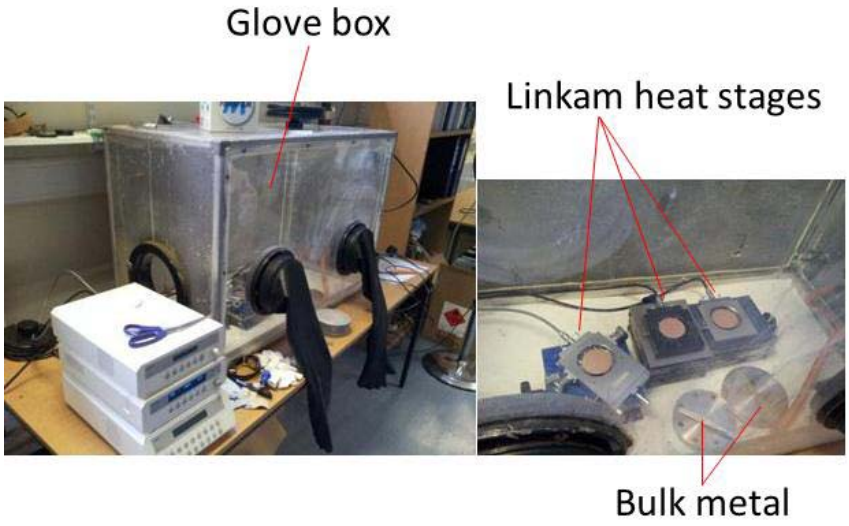

Figure 3.20: Experimental apparatus for thermal annealing to cancel any crystals. A glove box is used for implementation of nitrogen experiments (Right). Inside the glove box, there are three Linkam heat stages for annealing and a bulk metal for quenching (Left).

There was one more troublesome problem for polymer thin films, that is, the process of relaxation. Figure 3.21 shows the effect of annealing time of ellipsometry data for two film thicknesses, 50 nm and 250 nm. Thermal annealing was implemented at 285 °C for different period of time before cooling to room temperature. A short annealing time tended to shorten the induction time of crystallization (crystallization temperature was 120 °C), especially for thick films (250 nm). Here, induction time of crystallization is a part of plateau of ellipsometry measurement. I will explain this induction time in detail in Chapter 5. A short induction time indicates that PET crystals or some nucleating structures of sample might be not cancelled adequately. A long annealing time would cause plenty of relaxation of polymer molecules. Sufficient relaxation is preferable for a good entirely amorphous sample. But too long annealing at high temperature might cause undesired degradation, for example, even though its proportion is small, degradation might be caused even under nitrogen (Figure 3.19). I chose 20 minutes as annealing time because it seems a balance point to cancel any crystals with low degradation of film samples. As a fact, 20 minutes melting annealed samples showed clear shape of the induction time in ellipsometry profiles. Figure 3.22 shows raw ellipsometry data of Ψ and Δ for the wavelength between 500 nm and 1000 nm of crystallization at 120 °C for 400 seconds shown as a vertical red line in Figure 3.21. Ψ and Δ were changed by thermal annealing time (2, 5, 10, and 20 minutes) as same as Figure 3.21.

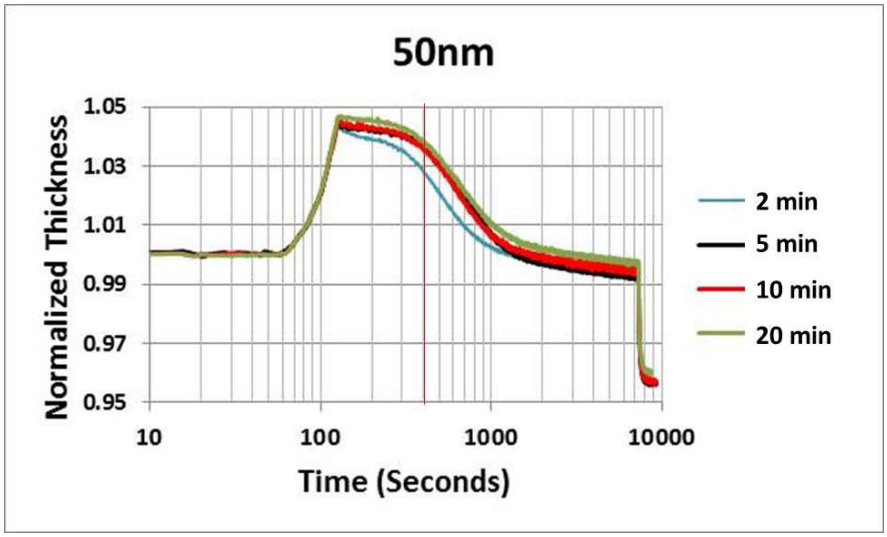

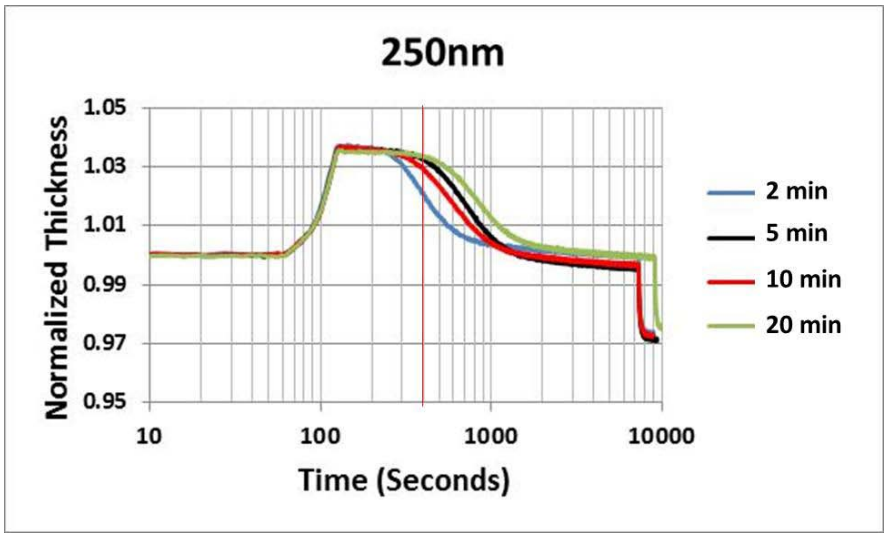

Figure 3.21: Affect of thermal annealing time (2, 5, 10, and 20 minutes) shown by ellipsometry data for two PET film thicknesses. The upper is 50 nm thickness and the lower is 250 nm thickness respectively. Crystallization temperature was 120 °C. The trend for all these data was that shorter period of melting annealing time reduces the induction time and this was more conspicuous in 250 nm than in 50 nm.

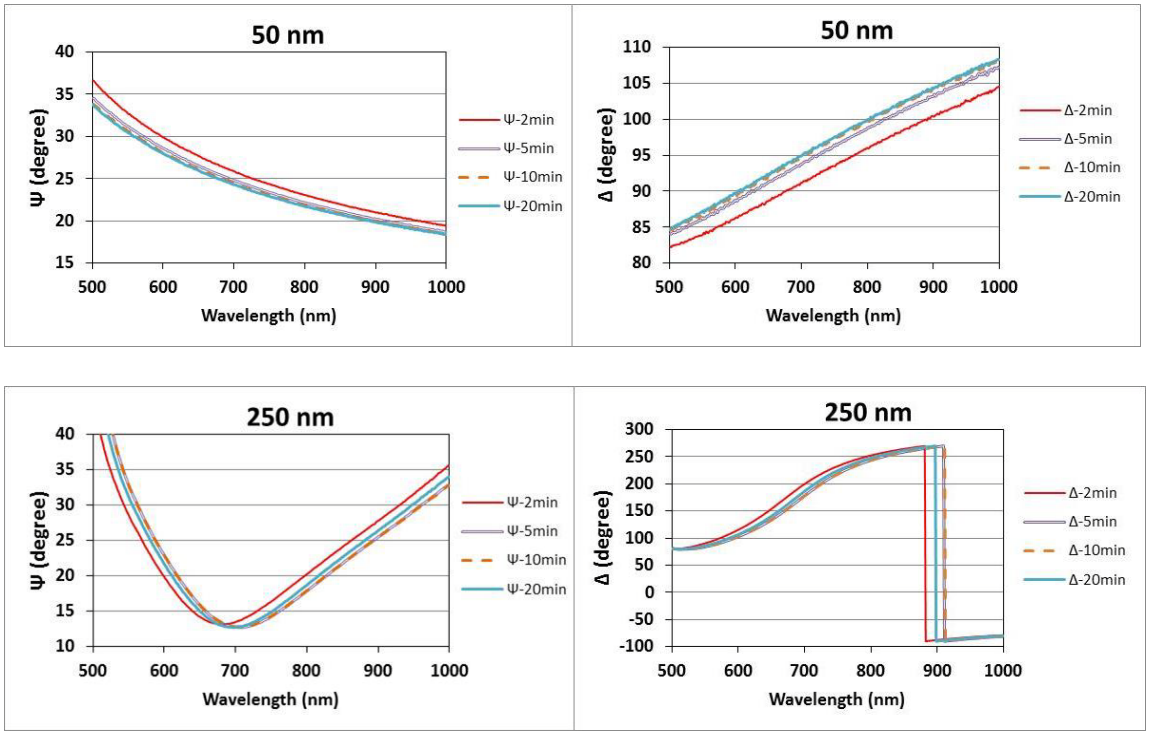

Figure 3.22: Raw ellipsometry data of Ψ and Δ for the wavelength between 500 nm and 1000 nm of crystallization at 120 °C for 400 seconds shown as a vertical red line in Figure 3.21. The upper is 50 nm thickness and the lower is 250 nm thickness respectively. Ψ an d Δ were changed by thermal annealing time (2, 5, 10, and 20 minutes) as same as Figure 3.21.

3.5 Summary

In this chapter, I have discussed how to make good thin PET film samples. This requires control over the spin-coating parameters and solution composition, as well as the confirmation of removal of solvents by physical and chemical analysis. Then there needs to be an adequate removal of any PET crystallites; finally, very flat (the surface roughness was under 1 nm, like a liquid surface) and good amorphous thin PET film samples were able to be made. Figure 3.23 is data and a fitting profile of neutron reflectivity for a thin PET film on a NiFe/Si substrate. I used this substrate because the experiment was on the instrument POLREF of ISIS (UK) and used magnetic reference layers to probe spin up and spin down states. This effectively gives us two contrasts and enables a more robust approach to modelling the data. Fitting model parameters were 80 nm thickness PET film and Ra ~ 0.3 nm, and calculated by the fitting software

“pro Fit”, produced and developed by QuantumSoft (Switzerland) and used widely, for example, [117]. This fitting agrees with the AFM analysis and shows that they are uniform over a large area. This also provides more evidence that my thin PET film samples were made adequately and are more than good enough for GI scattering measurements.

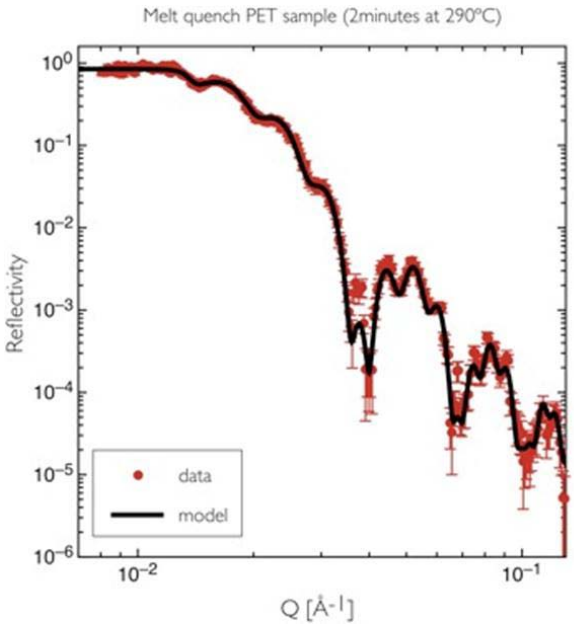

Figure 3.23: A data of neutron beam reflectivity of thin PET film on NiFe/Si substrate. Fitting model was 80 nm flat thin PET film.

I have summarized properties of spin-coating conditions quantitatively in this chapter, described the optimized PET solution, and found out that 2-chlorophenol contributes to flat surface. And I found out that 200 °C for 4 hours in vacuum oven is an adequate condition for removal of residual solvent, confirming this by TGA and FTIR. I showed clearly that the essential annealing for cancellation of any crystal of thin PET films needs to be implemented under nitrogen at 285 °C for 20 minutes, and constructed proper experimental apparatus to do this.

Chapter 4

Aging effects for thin films

4.1 Introduction

In this chapter, I would like to discuss the aging effect, which should be taken into account for studies of crystallization in thin polymer films. Through experiments in my study, the phenomena was observed that the induction time of crystallization was shortened or almost vanished if the annealing was implemented a long time after the sample was made, as shown in Figures 4.1 and 4.2. And the thickness reduction rate (i.e., crystallization rate) also seemed to become faster due to “aging” seen clearly in these figures.

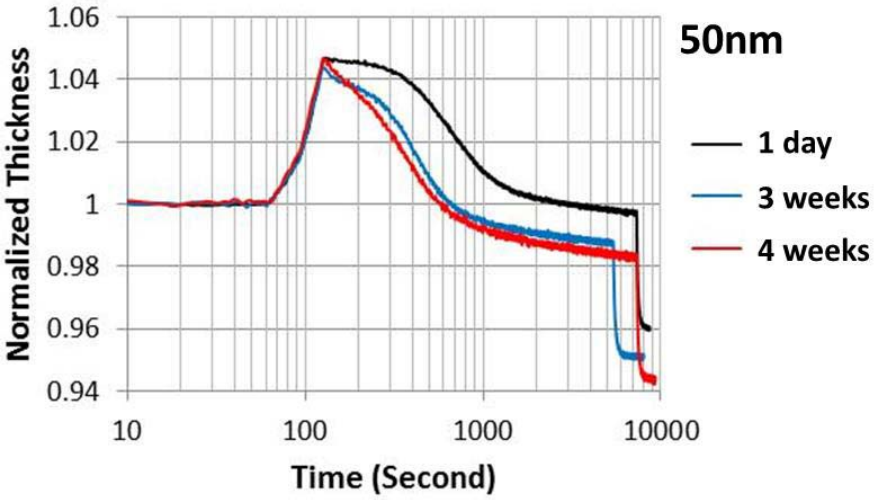

Figure 4.1: Ellipsometry data of several 50 nm film thickness samples annealed at 120 °C for 2 hours. Black, blue, and red solid lines were measured after 1 day, 3 weeks, and 4 weeks respectively after the samples were made.

Figure 4.1 shows Ellipsometry data of several 50 nm film thickness samples annealed at 120 °C for 2 hours. Black, blue, and red solid lines were measured after 1 day, 3 weeks, and 4 weeks respectively after the samples were prepared. The normalized thickness profile of the fresh sample, measured 1 day after preparation, had a clear crystallization induction time and this profile is a representative standard profile of ellipsometry measurements perfomed in this study. However, the induction time of the sample aged for 3 weeks became considerably shortened and less distinct, while, that of the sample measured 4 weeks later has almost vanished. We can see the aging, that is, the period after the sample is made and during which it is held at room termperature, strongly influences the kinetics or effectiveness of the crystallization, especially the early stage, for example during the induction time. Because one of the aims of this study is the investigation of the kinetics of the early stage of crystallization, particularly during the induction time, and how it is influenced by annealing temperature or film thickness, aging effects such as those shown in Figure 4.1 are a critical problem. Therefore, first of all, a rule was established in my experiments, that is, the annealing or ellipsometry measurements must be implemented within 1 or 2 days after the samples were made in order to reduce the influence of this aging effect as far as possible. All the data in this thesis follow this rule, unless otherwise clearly specified, for instance in this chapter.

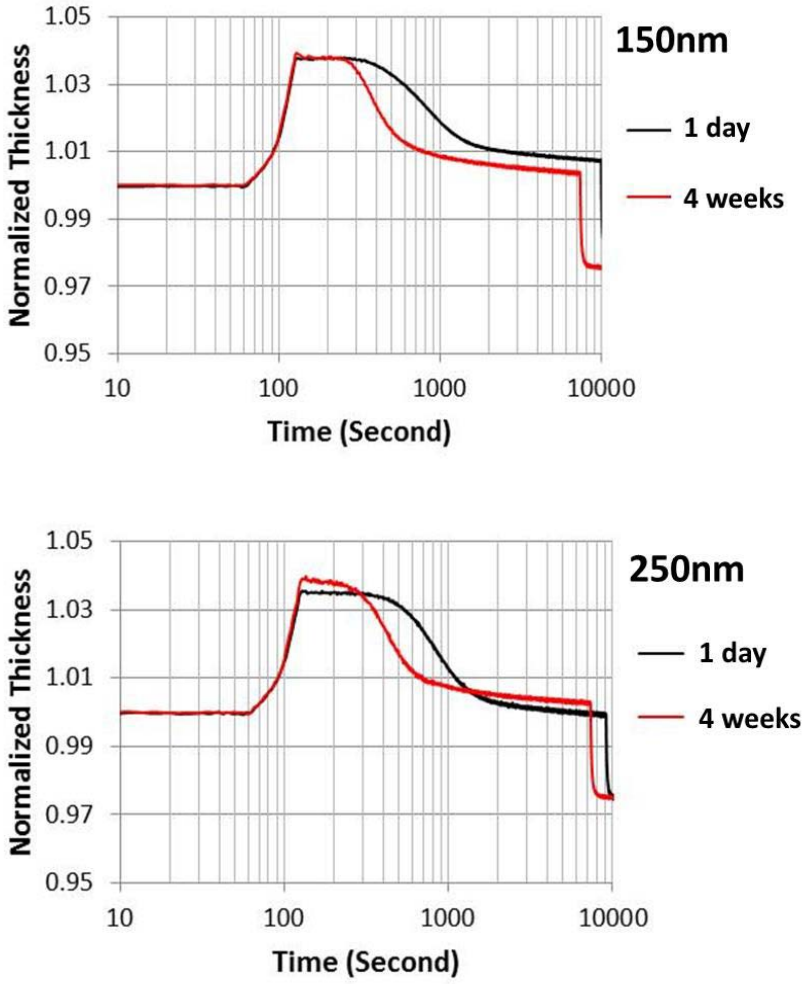

Figure 4.2: Ellipsometry data of 150 nm (upper) and 250 nm (lower) film thickness samples annealed at 120 °C for 2 hours. Black and red solid lines were measured 1 day and 4 weeks after the samples were prepared, respectively.

Figure 4.2 shows ellipsometry data of 150 nm (upper) and 250 nm (lower) film thickness samples annealed at 120 °C for 2 hours. The black and red solid lines were measured after they were prepared, 1 day and 4 weeks later, respectively. Compared with measurements of the 50 nm thickness samples, 150 nm or 250 nm samples seemed to be stable to some extent. Even if these samples had 4 weeks aging time, the induction time remained although it became shortened. However, it was obvious that aging shortened the induction times and the crystallization proceeded faster. This greater stability of the thicker films might be due to the dominance of the free surface and reduction in T_g for the 50 nm thick film as mentioned in Chapter 1.

Now I would like to discuss my data and the relevance between relaxation and crystallization of PET shown in the literature, and consider the reasons why this kind of aging effect takes place. This should be useful for understanding the induction time and pre-ordering in polymer crystallization, especially in very thin films.

4.2 Discussion for Aging effects and Relaxation of polymer crystallization

In bulk polymers, the literature reports that aging is the progression of densification and local conformational changes in initially amorphous PET, as detailed below. That is, aging may lead to lower barriers to nucleation and therefore a quicker crystallization rate. Radhakrishnan *et al* [118] report that the conformational changes accompanying the crystallization in oriented film samples are as following. The structural organization in the isothermal crystallization of oriented PET consists of three stages. The first stage involves the thermodynamic relaxation, when the samples are heated above T_g. The conformational transition in the chain from gauche to trans takes place, and the molecular orientation is relaxed into the nearly isotropic level in the first stage of the isothermal crystallization. The second stage is the self-organization process of the oriented amorphous structure, in which the degree of orientation markedly increases with time and the gauche conformation is transformed into the trans conformation. The SAXS studies showed that the isotropic density fluctuation develops in the early stage of reorganization, but the density fluctuation begins to orient to the stress direction in the latter half of the second stage. The third stage is the crystallization of oriented molecular chains into the crystal lattice [118].

There are some other papers reporting that the gauche conformation is the dominant conformation in amorphous PET and it changes to the trans conformation gradually as the crystallization progresses. Lu and Hay *et al* report that the gauche conformation is reduced and the trans conformation increases as the crystallization progresses [119]. Schmidt-Rohr *et al* also say that almost all the conformation in PET crystals is trans, on the other hand, the trans conformation is just 14 % in amorphous. Their NMR investigation revealed that the transition from gauche to trans occurred during crystallization [120]. Huang *et al* show detailed values of this kind of

conformation change accompanying crystallization and this is detailed in table 4.1 [121].

Table 4.1: Conformational changes of the methylene carbons in PET at various annealing conditions [121]

Annealing temperature (°C)	Annealing time (min)	*Trans* (%)	*Gauche* (%)	Crystallinity W_c (%)
Quenched PET	0	8.1	91.9	4.2
100	20	18.4	81.6	5.8
100	40	21.6	78.4	7.6
100	60	25.3	74.7	12.4
100	80	30.2	69.8	21.5
100	1440	51.9	48.1	
120	20	69.1	30.9	
120	40	69.5	31.5	
120	60	70.7	29.3	
120	80	71.4	28.6	
120	1440	78.8	21.2	
120	60	70.7	29.3	
140	60	71.9	28.1	
160	60	73.3	26.7	
180	60	79.5	20.5	
200	60	84.8	15.2	

The literature shows the gauche conformation is changed into the trans conformation by annealing with crystallization. Hence relaxation by annealing before crystallization should increase the trans conformation, which is similar to the order of molecules in the crystal, and pre-ordering or nucleation should also take place more easily. Consequently it is conceivable that the ageing phenomenon effect is responsible for the different crystallisation dynamics, this is most likely due to the change in the population of states from gauche to trans. The data is shown in Figures 4.1 and 4.2, here the induction time was reduced or vanished and the crystallisation progresses much faster in aged samples than samples measured very soon after being made, even though ageing was carried out at a room temperature.

Yoshii *et al* reported that molecular ordering is also observed in amorphous PET due to relaxation by annealing before crystallization as follows [116]. They observed the effect of structural relaxation of the glassy poly(ethylene terephthalate) (PET) caused by annealing below its glass transition temperature (T_g) on the cold-crystallization by the simultaneous DSC–FTIR and DSC–XRD methods and revealed that the nucleation and the conformational ordering processes proceeded faster by annealing. Then, in that conformational transition, it is also reported that the ordering

of aromatic units was faster than that of ethylene units during the cold-crystallization. Furthermore, the long range ordering such as ordering of position and orientation occurred earlier for the annealed PET than the quenched PET.

Alves *et al* showed that isothermal annealing induces chain relaxation and makes stable configuration of PET molecules, this was measured using detailed analysis of the shift in heat capacity. Figure 4.3 shows that the annealing produces a peak in C_p shifting towards higher temperatures and increasing in height with temperature, this happens because the mobility of the chain segments, which are necessary to promote the recovery of enthalpy, decrease during the ageing process. The magnitude of the peak was an indirect measure of the relaxation of enthalpy during the ageing process [122]. Because 62 °C is comparatively higher than room temperature, relaxation progressed much faster than aging at room temperature stored in laboratory. However, this also indicates aging effect related to relaxation and molecule configuration, conformation, or ordering, and it is possible that this process is a transition from gauche to trans.

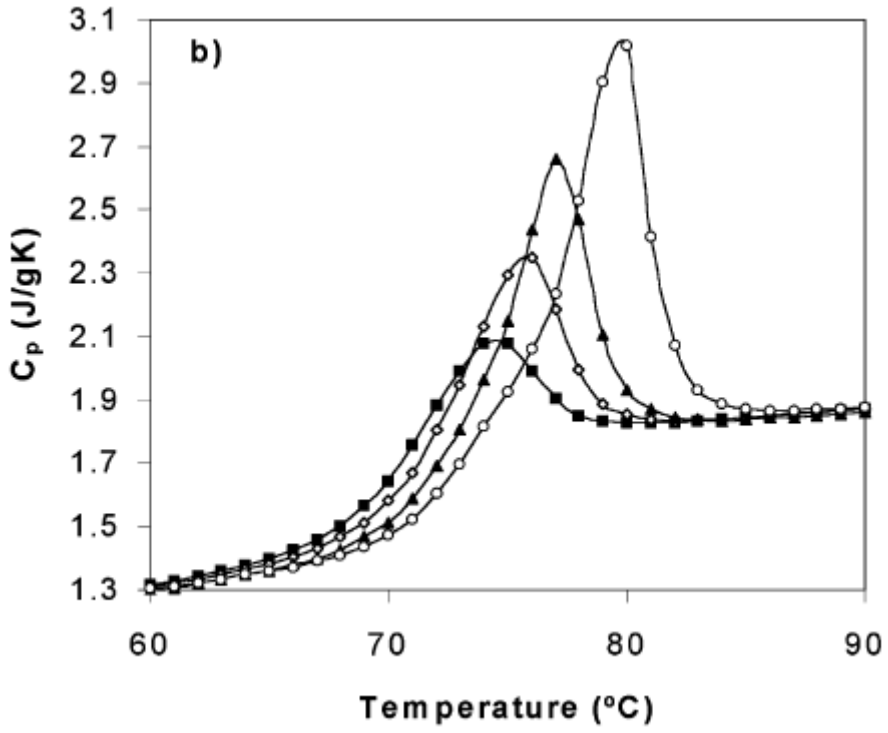

Figure 4.3: Temperature dependence of the heat capacity (C_p) measured using heating DSC scans on amorphous PET samples subjected to isothermal annealing. Thermograms measured after annealing at 62 °C for (■) 5, (◇) 10, (▲) 60, and (○) 120 minutes [122].

Rueda *et al*. say that the higher degree of internal order, i.e. containing a higher level of ”embryonic” ordered nanoregions, can take place if amorphous PET is stored for 40 days, and this aging makes the induction time of crystallization in higher degree of internal ordered sample short [123, 124]. However, Rueda *et al*. also reported that once crystallization starts, although the induction time of higher degree of internal ordered sample is shorter, the crystallization rate is slower than that of the random configuration sample (non-aged sample). Interestingly, the final degree of crystallinity for both of them is very similar. This phenomenon might be related to my data, I will discuss further in Chapter 7, that is, the induction time of the 50 nm thickness samples are shorter than that of 150 nm or 250 nm sample even though the induction time in bulk samples is shorter than thin films. It might be an important point to understand any special rules for the early stage of crystallization in thin film PET that might make some kind of confinement of molecule mobility.

Returning to my study, it seems possible that the phenomenon, described with the data reported by Rueda and shown in Figure 4.1 and 4.2, is considered as follows. Aging promotes the relaxation accompanying the conformational transition from gauche to trans described in literature above, and then the pre-ordering or nucleation stage happens much more easily, and the induction time becomes shorter or vanishes altogether. The conformation transition may be the higher degree of internal order explained by Rueda.

It is possible that this phenomenon might be much more significant in thin films, because the surface effect reduces T_g and molecules move more easily than in bulk. Kawana *et al*. discussed the relationship between relaxation and the surface mobility effect in thin polystyrene film samples in detail [10]. They find that T_g near the surface should be below than bulk and its influence makes many features of thin polymer film different from bulk, for example, relaxation, molecular mobility, and even adhesion. Therefore, in our studies of crystallization in PET thin polymer films, we need to take care to exclude the complication of relaxation by the prompt implementation of annealing schedules and subsequent measurements.

The conformational transition discussed above may occur during aging or annealing, and then following this step the crystallization progresses. However, this study is focused on detecting pre-ordering or intermediate states as shown in Chapter 5 and 6, and does not produce any direct data about the conformation. In future, consideration of the effects of different starting conformational states, as obtained by different ageing regimes, on the kinetics of crystallisation through pre-ordered or

intermediate states could be very illuminating. Therefore, I would like to suggest this as an important aspect of any future work.

Chapter 5

Analysis of the crystallization of thin PET films

5.1 Introduction

The aim of this study is to look at the very early stage of crystallization of thin PET films. In order to see this, it is important to know whether a sample has crystallized or is amorphous, what kind of structures and morphologies the crystals have, the precise kinetics of crystallization, and what the differences between thin films and bulk samples are. Therefore, GI-WAXS was used to check whether a sample is crystalline or amorphous, and whether crystals in thin films are different from the crystals in bulk or not. Ellipsometry is useful to measure the precise kinetics of crystallisation from slight film thickness changes. Then, AFM is adopted to observe surface morphologies of amorphous and crystallized thin PET films in order to look in more detail at the structure of the crystals. The key points of this chapter are discussions of these data as follows.

First of all, I confirmed whether a sample is crystalline or not, and that the crystals in thin PET film are identical to those seen in bulk material, using GI-WAXS. If I had been unable to confirm this then we could not discuss the early stage of crystallization and its kinetics at all. Therefore, this is the first important measurement of this study and the basis of all subsequent experiments. The results of GI-WAXS show that the crystallization of thin PET films started between 100 and 1000 seconds after being thermally annealed at 120 °C, and that the samples were clearly crystalline at around 7200 seconds. Clear crystallization was not observed before 1000 seconds from GI-WAXS. Accordingly, this period represents some kind of induction time of crystallization. From the comparison with the diffraction peak position of bulk samples

reported by the literature, we can conclude that the crystal structure of thin PET films is the same as bulk PET. Consequently, we can discuss the crystallization of thin PET films with our sample and experiments, and assume those crystals have the same crystal structure as ordinary PET crystals. From the 2D scattering images of GI-WAXS, (although we could not see the in-Plane direction) it seems that there is not a strong orientation of crystals.

Next, the kinetics of crystallization and how they are changed with annealing temperature and film thickness were measured by ellipsometry. With the data from GI-WAXS, we can regard that slight changes in film thickness measured by ellipsometry were caused by crystallization. In the same way, the plateau of ellipsometry graph just before crystallization should be interpreted as some kind of induction time, such as the pre-ordering reported by Olmsted *et al.* [28], or conventional nucleation. These assumptions are the conceptual basis of this study. As the annealing temperature rises from 90 °C to 160 °C, the higher temperature result in a faster crystallization rate and a shorter induction time. Because the mobility of PET molecules should be higher at higher temperature, molecules move easily to pack near one other for pre-ordering or nucleation. However, at much higher temperature, that is 200 °C, the crystallization rate seemed to reduce and the induction time increased again. This is caused by the fact that molecular packing became unstable as the temperature approaches the melting point. From the fact that 160 °C was an optimum temperature for crystallization has been reported by the literature, these ellipsometry data seem to give a reasonable result. The kinetics of crystallization was also changed by film thickness. Samples of initial film thickness of 50 nm, 150 nm, and 250 nm at room temperature were annealed at 120 °C for 2 hours, and analysed by ellipsometry. As a result, there was not so much difference between 150 nm and 250 nm, on the other hand, induction time and the thermal expansion rate of 50 nm were a little shorter and larger than others. This should be caused by surface effect because 50 nm thick films have a large surface area ratio, and such a thin film should be easily influenced by it. There are papers saying (for example, [8], [9], [10], [33], and [34]) that glass transition temperature (T_g) decreases and thermal expansion rate increases in thin polymer films under 100 nm thickness, and these are caused by surface effects. At the surface, molecular mobility is higher than in the internal part of the layer because constraints or interactions from other molecules are small, this increase in the degree of molecular mobility decreases T_g and increases the thermal expansion rate.

Finally, surface morphologies were observed by time with AFM. Initial and samples annealed for less than 100 seconds did not have any clear texture in the AFM

images. Then, nucleation of crystal for thin PET films and its growth were observed during annealing at 110 °C from 500 to 1000 seconds. From this, initial and less than 100 seconds annealed samples should be amorphous. For more than 3600 seconds (1 hour), crystal structure covered all surface of the sample and spherulite boundaries were also seen. After 9 hours, crystallization progressed, for example through the growth of lamellae, and the crystal structure became much clearer in the images. These morphology changes through time corresponded to the results of GI-WAXS and ellipsometry. High resolution AFM images, with 1 μm square visual field and tens of nm resolution, showed that there was an intermediate structure between amorphous and crystal in samples annealed from 500 to 1000 seconds. The time range of this structure corresponded to the induction time measured by ellipsometry, therefore, this structure could be interpreted as be some kind of intermediate state just before crystallization, like a pre-ordering. We can clearly see differences in the lengthscales of these three states, amorphous, intermediate, and crystal by fast Fourier transforming (FFT) the AFM height images. In AFM, because the cantilever actually taps surface of samples, precise quantitative analysis is possible, that is, the surface roughness. The root mean square (RMS) roughness value for the amorphous thin PET film, that is the initial as cast sample, was about 0.20 nm (dispersion was under ±10 %). This value is almost equal to liquid surface and shows that samples in this study had very good surface flatness. At the intermediate state, annealed at 110 °C for 500 seconds, the RMS roughness increased to about 0.47 nm, and for the crystallized samples, annealed for 1 and 9 hours, the RMS roughnesses were about 1.2 and 1.5 nm respectively. The differences between these 3 states were confirmed quantitatively, and it was reasonable that RMS roughness increases as crystallization progresses. AFM analysis also revealed differences in the surface morphologies caused by annealing temperature and film thickness. At higher annealing temperature and thicker films, the RMS surface roughness became larger. At higher annealing temperature, the crystal lamellae became larger or thicker, and this caused an increase of RMS roughness; however, for thicker films, the lamellar size was not changed but the waviness of the surface became large. This waviness seemed to be caused by to the spherulitic structure of PET, often reported as a “nodule structure” [125]. This structure is often seen in PET, and the scale of the nodule corresponds to the waviness. In thinner films, because there was not enough volume for the nodule, the waviness was smaller than for thicker films. From equation 1.6, we can see that it is acceptable that at higher annealing temperature, the lamellar size becomes large and this seems similar to bulk samples, however, the change of surface waviness is likely to be a property of thin films.

5.2 Crystal Structures measured by GI-WAXS

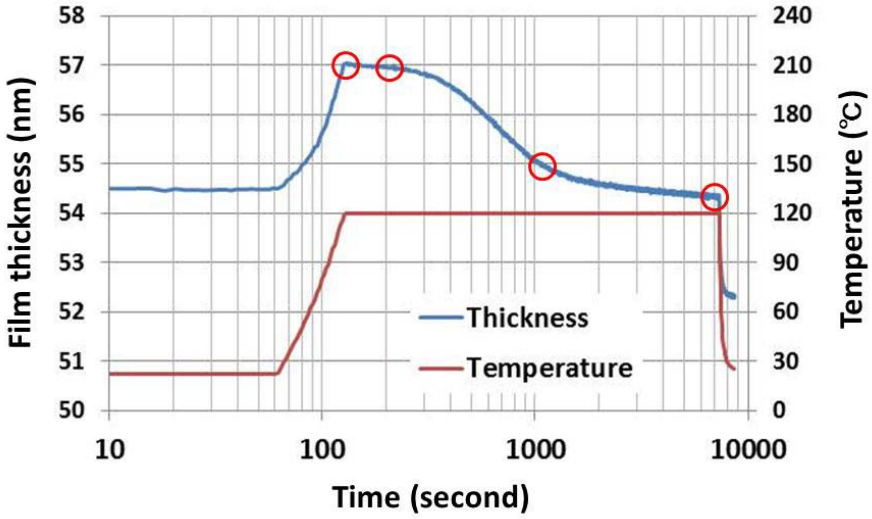

Figure 5.1: Ellipsometry data for a thin PET film showing the thickness change as a function of isothermal annealing temperature and time. The red open circles on the graph indicate the points measured by GI-WAXS.

The purpose of this section is to check whether a sample has crystallized or is amorphous, and whether PET crystals in thin films are different from crystals in bulk or not, using GI-WAXS. The principle of GI-WAXS and why GI-WAXS is suitable for investigation of structure of thin polymer films is contained in Chapter 2. GI-WAXS in this study was implemented at X-Mas, BL-22 of ESRF in Grenoble, France.

To check the state of samples, for example, whether amorphous or crystalline, and, if crystalline, what kind of crystal, is very important because if there is not this kind of information at the beginning of our studies, we cannot discuss the early stages evolution of crystallization and its kinetics at all. Therefore, this is the first important measurement of this study and the construction of the baseline for all other further experiments.

Figure 5.1 shows the sample annealing time as red circles measured by GI-WAXS with ellipsometry data. The samples are thin PET films made by spin-coating using the procedure to make samples described in Chapter 2 and 3. Then samples were annealed at 120 °C for 0, 100, 1000, and 7200 seconds (2 hours). The crystallization rate of PET is changed by annealing temperature as reported in the literature (for example, [126]). Just above T_g (For example 90 °C) is too low, so it

would take very long time to crystalize, on the other hand, 160 – 180 °C is too high, so crystallization would progress too quickly to see. Medium and moderate temperatures, for example 120 °C, are good to see the crystallization clearly.

The procedure for the 0 second samples was that a sample was heated just to 120 °C then quenched. We consider this is the sample representing the initial state. Using data from ellipsometry, we can clarify the priority order of measurements for our scarce GI-WAXS time. For a description of what ellipsometry data tells us, see Chapter 2. Here, I focused on the major points of sample thickness: that is, the initial state, just before the drastic drop in thickness, just after it, and during the final moderate decrease of thickness. The first purpose of this choice is to confirm my expectation that samples should be amorphous before the drop and be crystalline after it. Then, a comparison between the initial state and the state just before the drastic drop, and another comparison between the state just after the drop and the state during the moderate decrease was implemented in order to see some differences between amorphous samples and between crystallized samples (see red circles in Figure 5.1).

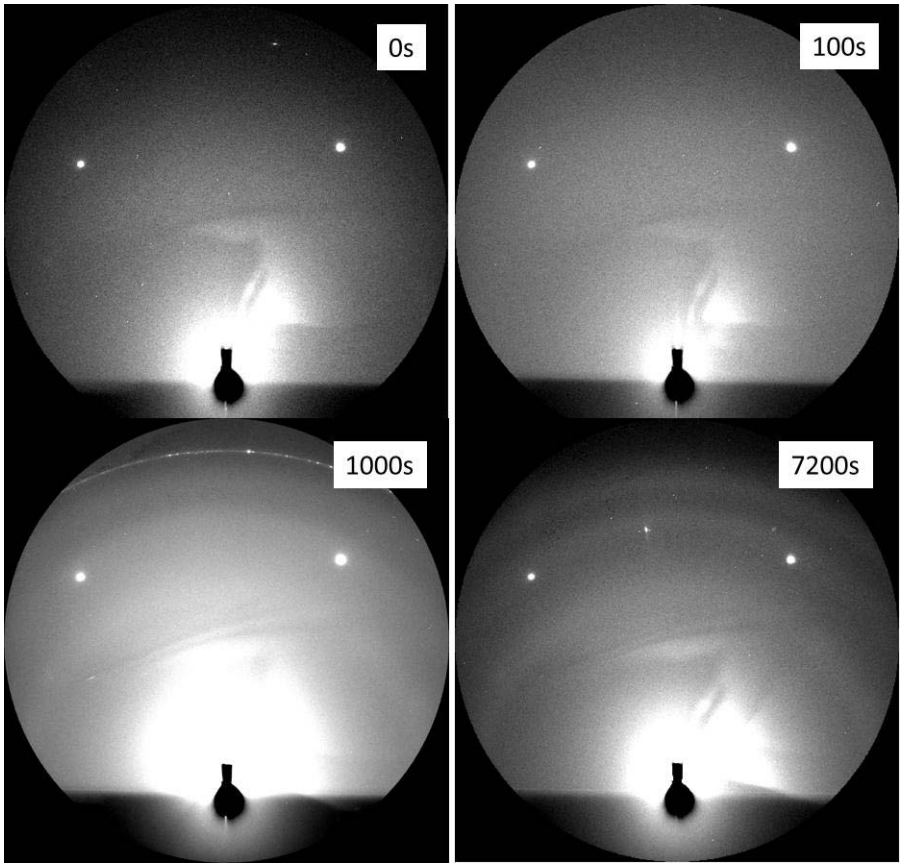

Figure 5.2: GI-WAXS 2D images of thin PET films (thickness : 50nm) annealed at 120 °C. The numbers in pictures are annealing time (second).

Of course, the peak positions given by GI-WAXS measurements were compared with those of bulk PET crystal to confirm whether or not crystals in thin PET films have the same structure as the bulk. Figure 5.2 shows GI-WAXS 2D images of thin PET films annealed at 120 °C. The numbers in the figure indicate annealing time. These thin PET film samples were annealed for 0, 100, 1000, and 7200 seconds. I need to say that, unfortunately, in this experiment, the apparatus condition was not good and there was a lot of background noise. There was not any structured scattering above a rather high background in the 2D images of the 0 and 100 seconds samples. On the other hand, we can see clear rings of scattering in 1000 and 7200 seconds annealed samples, and also see that those rings became clearer and stronger with annealing time. It is clear that these rings arise from crystallinity in these thin films. From these images, we may say that our samples are amorphous at the initial and 100 seconds annealing, and that crystallization proceeds to some extent at 1000 and 7200 seconds. This is the evidence that the drastic drop of film thickness measured in ellipsometry indicates crystallization. Because the density of amorphous polymer is smaller than crystalline, from 1.335 to 1.455 g/cm^3 [11], crystallization causes a reduction in volume. And it confirms that crystallization proceeds gradually – consistent with a process like secondary crystallization – during the moderate decrease of thickness that takes place after the initial drastic drop, because the scattered rings became clearer from 1000 seconds to 7200 seconds. A plateau in the thickness/time curve, in this case lasting about 100 seconds indicates the induction time of crystallization.

From these data and the subsequent discussion, the profile of film thickness change with time given by ellipsometry measurements should be considered in the following way. The first increase corresponds to thermal expansion during the first heating, the plateau is the induction time, a drastic drop represents the onset of crystallization, and the following moderate decrease indicates progress of crystallization or secondary crystallization. This scheme receives further support from images from the optical microscope shown in Figure 5.3.

The microscope image at the far left is the just heated sample and there was no surface texture. Dots in this image were some kind of particles, like defects, in the sample, which I just used for adjusting the focus on the surface. The image second from the left is during the plateau and there were a few nuclei of crystalline PET. The image third from the left shows growth of these nuclei and spherulites. The left end image is a crystallized PET thin film and the surface was fully covered by spherulites. This texture change corresponds well to results of GI-WAXS and agrees with our expectation.

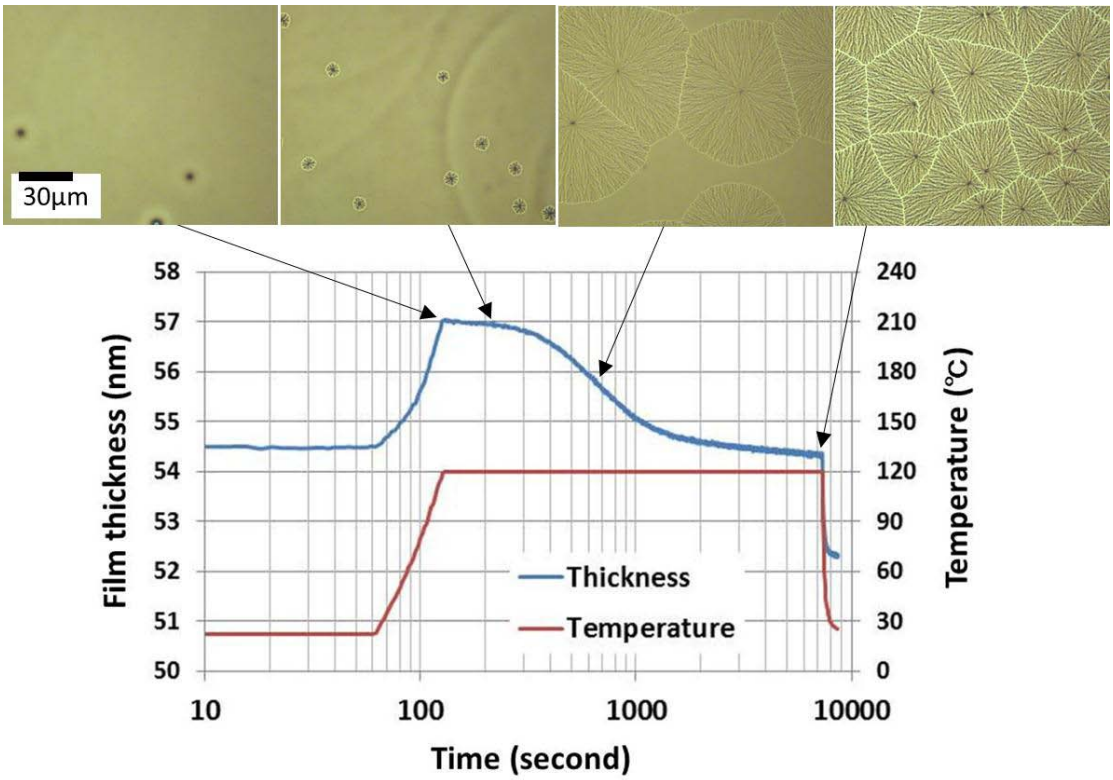

Figure 5.3: Optical microscope images with ellipsometry measurement.

Finally, I would like to add that we compared the initial state of sample, that is, not annealed, and the 0 seconds sample, just heated at 120 °C, and there were not any differences detectable in our GI-WAXS measurements. Although the scattering intensity from the actual in-plane direction was not measured because of the position of 2D detector, scattered rings were isotropic at least in the range shown in Figure 5.2. Therefore, crystals seemed not to be oriented strongly in any particular direction. However, the size of spherulite reached tens of μm, whereas thickness of thin films in this study is from 50 to 250 nm, that is, the aspect ratio of spherulite was quite high and spherulites might be distorted very much.

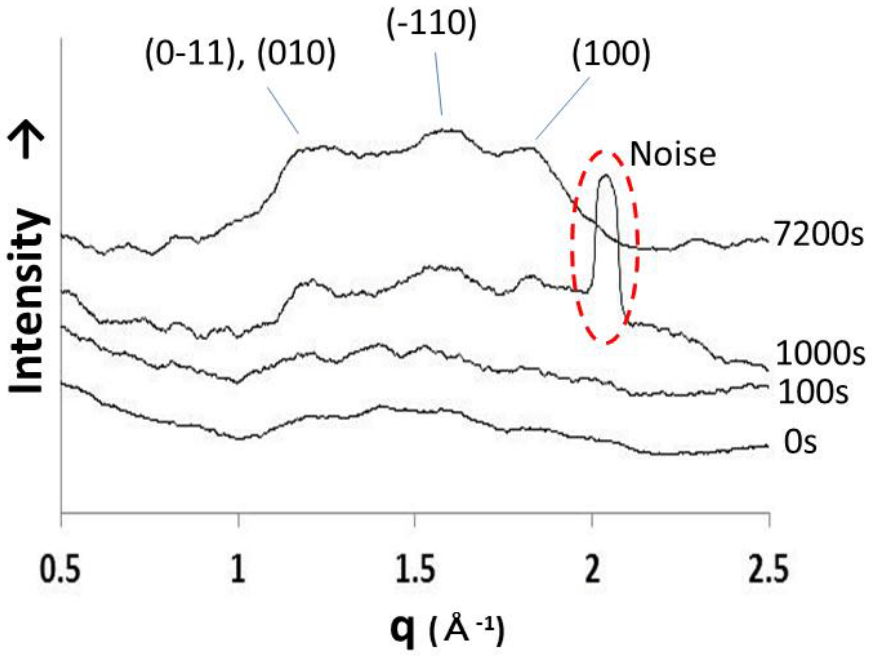

Figure 5.4: GI-WAXS profiles of thin PET films (out of plane) annealed at 120 °C for 0, 100, 1000, and 7200 seconds (2 hours).

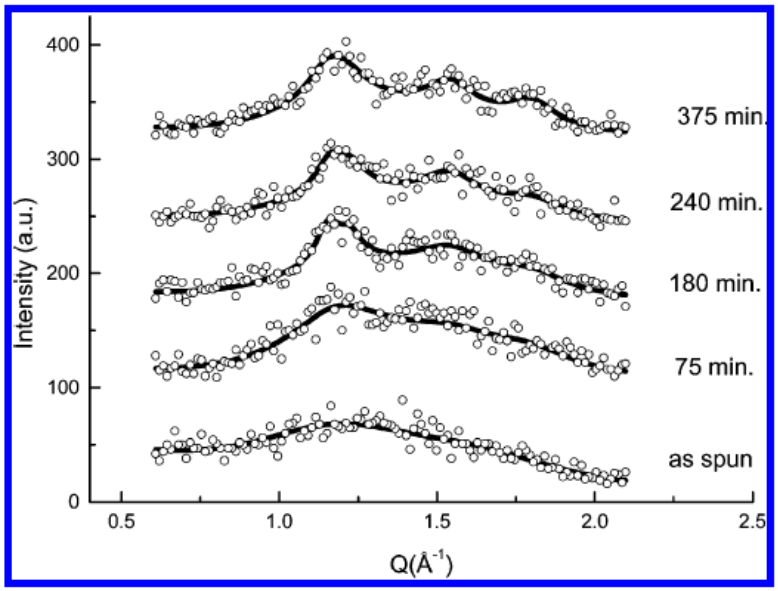

Figure 5.5: A GI-WAXS data of thin PET film from the literature as comparison [51]. Thickness of sample was 110 nm and annealed at 90 °C and sample was made by spin casting as same as this study. As spun was amorphous and we can see that as annealing proceeded, crystallization is progressed, and the peak positions of scattering from PET crystals are very similar to the peaks shown in Figure 5.4.

Figure 5.4 shows the out-of-plane direction line profiles of the GI-WAXS data. Although there was strong background noise present in our GI-WAXS measurement because of air scattering and the low volume of materials, this data suffices to check the peak position of scattering from the PET crystals. In conclusion, the peak positions of scattered rings were the same as PET crystals as reported by past studies [49, 51, 127]. The double peaks around q = 1.2 should be from (0-11) and (010), and peaks around q = 1.6 and 1.9 from (-110) and (110). This indicates that the crystal structure of thin PET film in this study is the same as seen for PET crystal in bulk and crystals reported by literature papers of thin PET films. Therefore, we can discuss data with an assumption that the crystal in this study is as same as ordinary PET crystal. Because these scattering curves come from thin semi crystallized polymer films, the intensity of peaks was not so strong and sharp. Therefore analysis of quantitative estimation of crystal degree is not easy. However, the scattering from samples annealed for 1000 and 7200 seconds indicates crystals of PET clearly, and these became clearer at longer annealed time. From the result that the intensity ratio of each peak was not so much different, we may say that there was not a strong orientation of crystals. Figure 5.5 shows a GI-WAXS data of thin PET film from the literature as comparison [51]. Thickness of sample was 110 nm and annealed at 90 °C and sample was made by spin casting as same as this study. As spun was amorphous and we can see that as annealing proceeded, crystallization is progressed, and the peak positions of scattering from PET crystals are very similar to the peaks shown in Figure 5.4.

5.3 Kinetics by temperature and film thickness

In this section, the kinetics of crystallization of thin PET films measured by ellipsometry is reported. As mentioned in previous section, the film thickness change measured by ellipsometry indicates crystallization. Besides, ellipsometry can detect very slight changes of thickness, therefore, the kinetics of crystallization is captured precisely and we can discuss these kinetics in detail with these data from ellipsometry.

The crystallization kinetics are influenced by the annealing temperature and film thickness, because those factors are likely to change molecule mobility. It is easy to imagine that molecular mobility should be large at high temperature, hence the crystallization rate should also be quick. However, it is not easy to say how quick it is

quantitatively. And, what would happen at much higher temperature? Near the melting point, crystals should become unstable, and the crystallization rate should slow. It is important to clarify these questions in order to understand the crystallization of thin films, and ellipsometry is the best tool for this.

In thinner films, the molecules might be too confined in narrow space to move freely, but they also might be influenced by the surface effect. The surface effect would make the chain mobility high, because there is no confinement from other molecules at the free surface. It is very interesting to confirm which factors are dominant in thin PET films.

Figure 5.6 shows the thickness change measured by ellipsometry for several film thicknesses, 50 nm, 150, and 250 nm. As discussed in Section 5.1 and above, the film thickness change due to crystallization can be measured precisely. The trend that the crystallization rate was smaller and the induction time was longer at lower temperature is common through all film thicknesses. This should indicate that crystallization progresses effectively at higher temperature. The reason of this is simple; molecular mobility is higher at higher temperature, and molecules move quickly and efficiently for alignment and packing of crystallization, while at lower temperature, the opposite is true. Here, it seems that there is an optimum temperature for crystallization rate from the 150 nm data. In this data, 160 °C is the most effective temperature for crystallization, that is, very short and ambiguous induction time and a quick crystallization rate. These kinds of optimum temperatures are reported in the literature and those for PET are also around 160 °C (for example, [126]). It is easy to imaginel that crystallization rate slows down above 160 °C because the alignment and packing of molecules for crystallization would become unstable, or maybe melt at this high temperature.

50nm

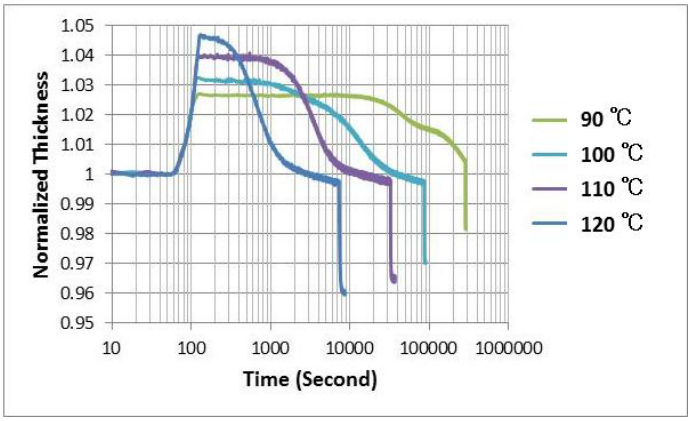

150nm

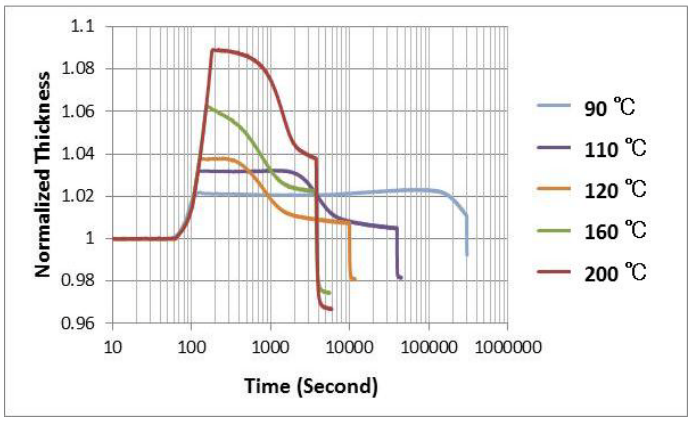

250nm

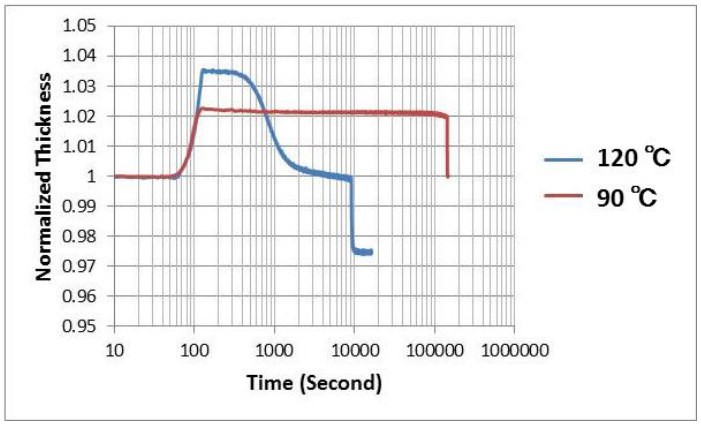

Figure 5.6: The thickness change measured by ellipsometry for several film thicknesses. Thicknesses were 50, 150, and 250 nm respectively.

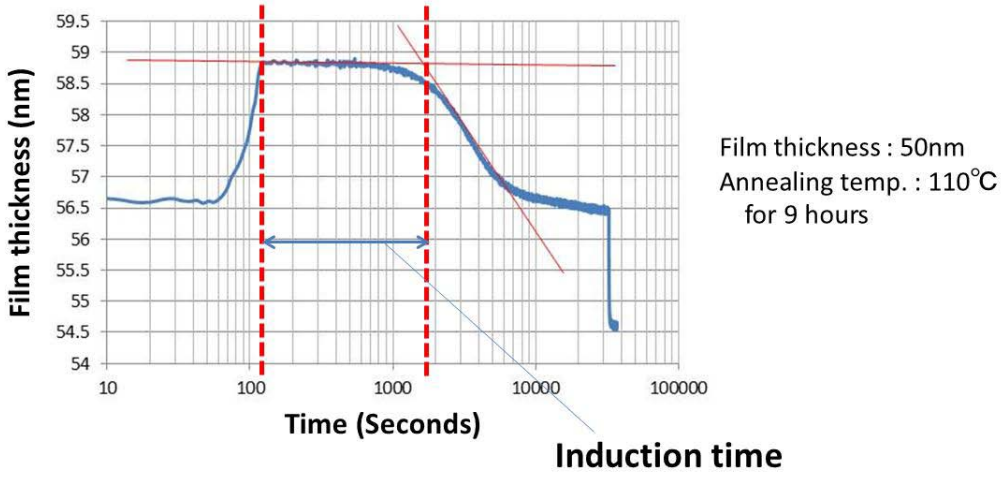

Figure 5.7: Procedure for determination of the induction time from the ellipsometry film thickness reduction data.

Figure 5.7 shows how to determine the induction time quantitatively. Two straight lines were drawn along the plateau and the slope of thickness decrease as in the figure (solid red lines). Then the induction time was determined from the start point of the plateau and the intersection point of the two lines, highlighted between the two broken red lines.

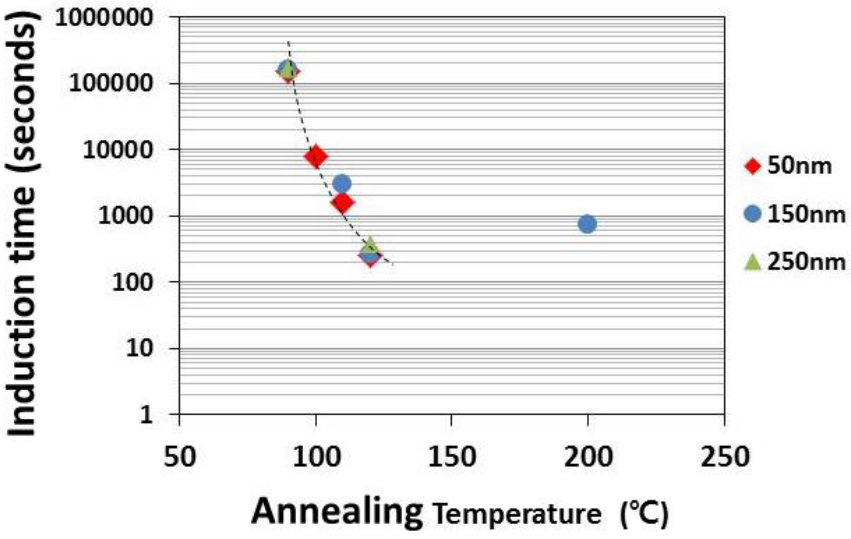

Figure 5.8: The relationship between temperature and induction time for several film thickness, 50, 150, and 250 nm, calculated from the data shown in Figure 5.6.

Figure 5.8 shows the relationship between temperature and induction time of several film thickness, 50, 150, and 250 nm, calculated from the data shown in Figure 5.6. The induction time of the sample annealed at 160 °C of 150 nm was not able to be acquired because there was not a plateau in the ellipsometry profile. From the data of 150 nm, it seems that there is the minimum induction time temperature around 150-160 °C. The induction time should consist of the time for nucleation of the crystal, pre-ordering for nucleation, moving molecule for pre-ordering. The effectiveness of nucleation and pre-ordering should be altered by changes in the molecular mobility and temperature influences it directly. It seems reasonable that the length of induction time is depend on temperature and there is atemperature which makes the induction time minimized. At low temperature, molecule mobility is low, therefore induction time should be long, on the other hand, at too high temperature, alignment or packing of molecules become difficult because excessive molecular mobility would break any interaction between molecules easily, therefore induction time should be long again. This is why there is a temperature at which the induction time is minimized. Detailed discussions for this topic and comparison of induction time between thin film and bulk will be in Chapter 6 and in 7.

And we can see also that there were two steps of induction time in the data of 50 nm thickness film annealed at 90 °C in Figure 5.6. This might arise from special features of the surface effect and I will discuss this in Chapter 7 in detail.

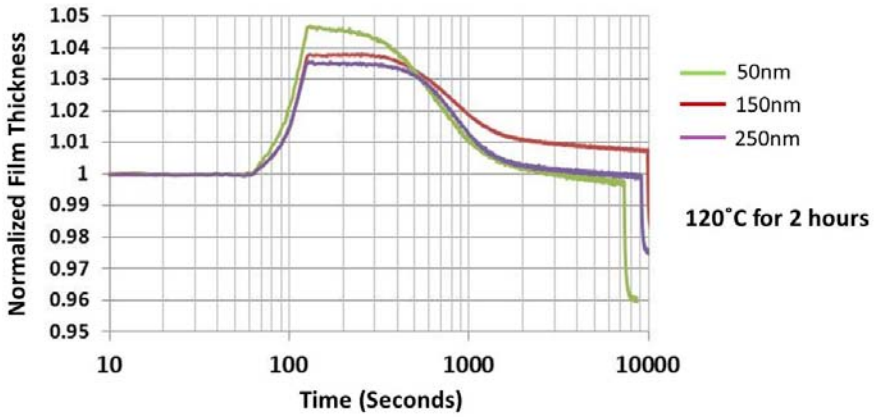

Figure 5.9: Comparison of the thickness change of several film thicknesses measured by ellipsometry.

Figure 5.9 shows a comparison of thickness changes of several film thickness annealed at 120 °C for 2 hours measured by ellipsometry with time. From this result, we

can see that the thermal expansion rate of 50 nm film was larger than thicker films, and the induction time of 50 nm film was a little shorter than thicker films. This trend follows past studies [60]. In literature, it is said that in ultra-thin films, for example under 100 nm, T_g decreases and thermal expansion rate increases because of their surface effect [60]. This might be related to the ellipsometry data in Figure 5.9. If molecular mobility is increased, induction time would also become short because pre-ordering and nucleation should occur more effectively with high molecular mobility. Besides, the surface area ratio at 50 nm must be larger than at 150 nm and 250 nm thicknesses. This large surface area ratio should be favourable for nucleation and can shorten the induction time [125]. The surface can be also some kind of direct source of nucleation, and possibly enhance the process. Further discussions of this will be in Chapter 7.

5.4 Surface Morphologies

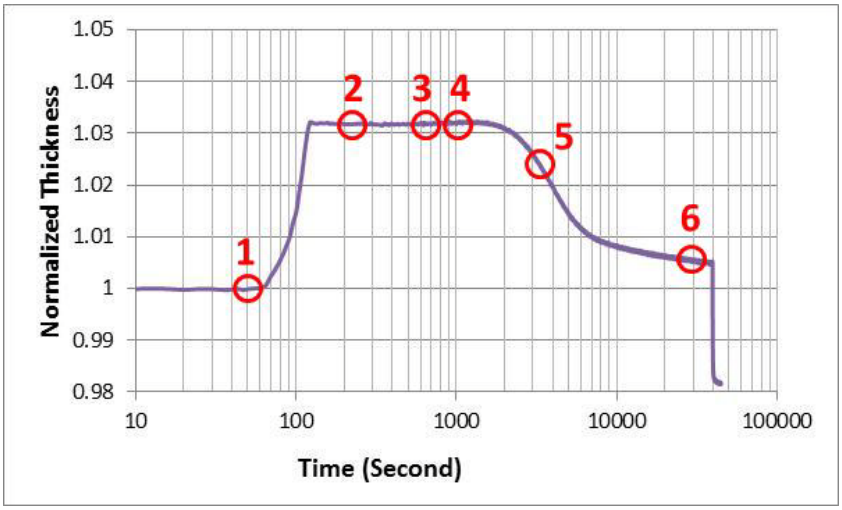

Figure 5.10: AFM images were measured at the time positions of the red circles. 1:Not annealed, 2:100 seconds, 3:500 seconds, 4:1000 seconds, 5:3600 seconds (1 hour), and 6:32400 seconds (9 hours) annealed each. This ellipsometry data is 150 nm annealed at 110 °C for 11 hours.

AFM is a very suitable way to study surface morphologies as mentioned in Chapter 2. AFM images of my samples were captured at red circles on the graph of ellipsometry in Figure 5.10. These were points of Not annealed, 100, 500, 1000, 3600, and 32400

seconds annealed at 110 °C. The film thickness was 150 nm. The AFM images are shown in Figure 5.11.

As mentioned above, the progression of crystallization slows down at low temperature. In these AFM measurements, the samples were annealed at low enough temperature, 110 °C, order to observe the time evolution of the morphology in detail at each point as in Figure 5.10. That is, the initial state, the early point of the plateau, the middle of the plateau, the later point of the plateau, midway through the drastic drop, and at the point of the moderate decrease. The reason why I choose 150 nm as the film thickness is that 150 nm is a standard film thickness between 50 nm and 250 nm. Of course, those thinner and thicker films were also observed, as I show influences for morphologies from film thickness later. AFM images here were height data and observed both 30 μm and 1 μm image scales to see both the macro and micro surface structure.

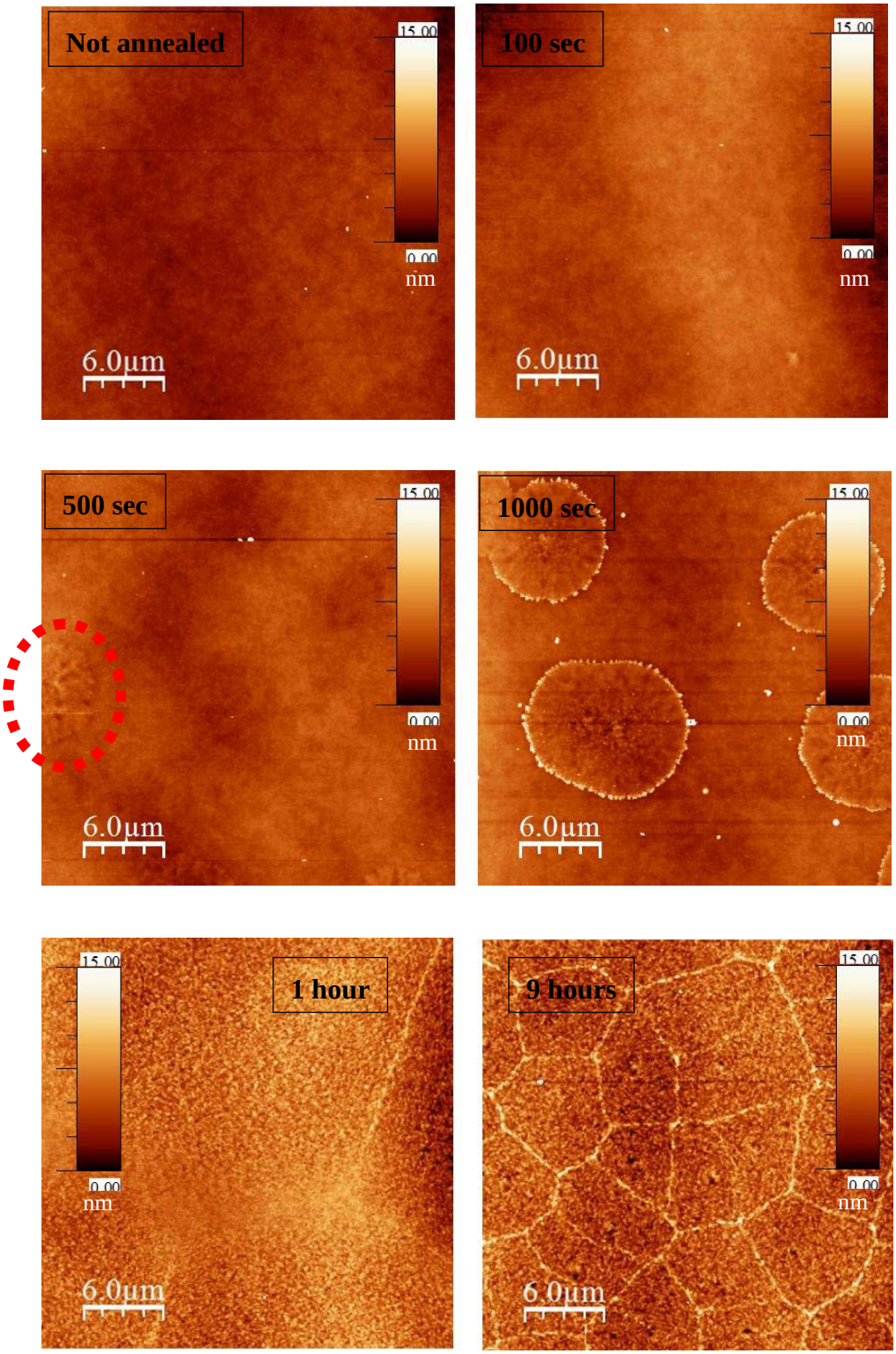

Figure 5.11: 30 µm scale AFM images of the surface structure of 150 nm PET films; not annealed, annealed at 110 °C for 100 seconds, 500 seconds, 1000 seconds, 1 hour, and 9 hours. Height scale is shown as the colour index in the figures, 15 nm scale.

First of all, 30 μm scale images were shown as Figure 5.11. The height scale is shown as a colour index in figures, with 15 nm scale. In both the not annealed and 100 seconds annealed images, the surfaces were very flat and there was no clear texture. These samples should be the same or very similar to the amorphous state. This corresponds to the results of GI-WAXS, that is, there were no scattered rings in the not annealed and annealed for 100 seconds samples. They should be amorphous because samples of GI-WAXS images annealed at 120 °C and the crystallization rate at 110 °C would be slower than 120 °C.

Next, particles like nuclei or fine crystals (in red broken circle) emerged in the 500 seconds annealed sample. Their sizes were about 5 - 7 μm, therefore, if they are nuclei or crystals, they are grown to some extent from actual nuclei. Detailed observation of such a particle and its boundary were shown and discussed later with a quantitative line profile analysis. The outside of this particle seemed amorphous like the not annealed sample and the 100 seconds annealed sample. The number of particle like nuclei of fine crystals increased in the 1000 seconds annealed sample and they seemed to have increased in size. All the surface of the sample annealed for 3600 seconds, 1 hour, was covered by the structure, which should be crystals with weak spherulite boundaries. This indicates that nuclei and crystal in the figure of 1000 seconds grew and spread all over the sample in 1 hour. The definitive and quantitative different between this crystalline structure and the initial amorphous structure is the surface roughness. The amorphous structure was very flat, like a liquid surface; that is, the RMS (Root Mean Squared) value of roughness (average roughness calculated from a certain area) was about 0.2 nm in a 1 μm squared image. On the other hand, RMS roughness data for crystalline structures were over 1 nm. This quantitative analysis will be discussed later in detail. Very clear spherulite boundaries were observed in the 9 hours annealed sample, and this clear crystalline image would indicate that crystalline growth had continued after all the surface was covered by spherulites, in a process of secondary crystallization. I say this because 9 hours is after the drastic drop of thickness in the ellipsometry measurement shown in Figure 5.6 and the gradual decrease of thickness after drastic drop seems to indicate secondary crystallization. As a result, this secondary crystallization increased the degree of crystallinity of the structure, making the AFM images of the crystals clearer. The quantitative differences are shown as RMS values later in Figure 5.15. Mean RMS values calculated from 1 μm square images of 1 hour and 9 hours annealed samples were 1.2 nm and 1.5 nm respectively.

The results and discussions above indicate that the crystallization process of thin PET films observed by AFM is very similar to the result of GI-WAXS and ellipsometry, that is, it starts from amorphous, the induction time of crystallization continues a couple of hundreds seconds at 110 or 120 °C and some nuclei appear during this time, then thorough crystallization occurs, and secondary crystallization or recrystallization progresses during keeping at those temperatures. AFM measurements revealed much more precise morphology transitions and changes as follows.

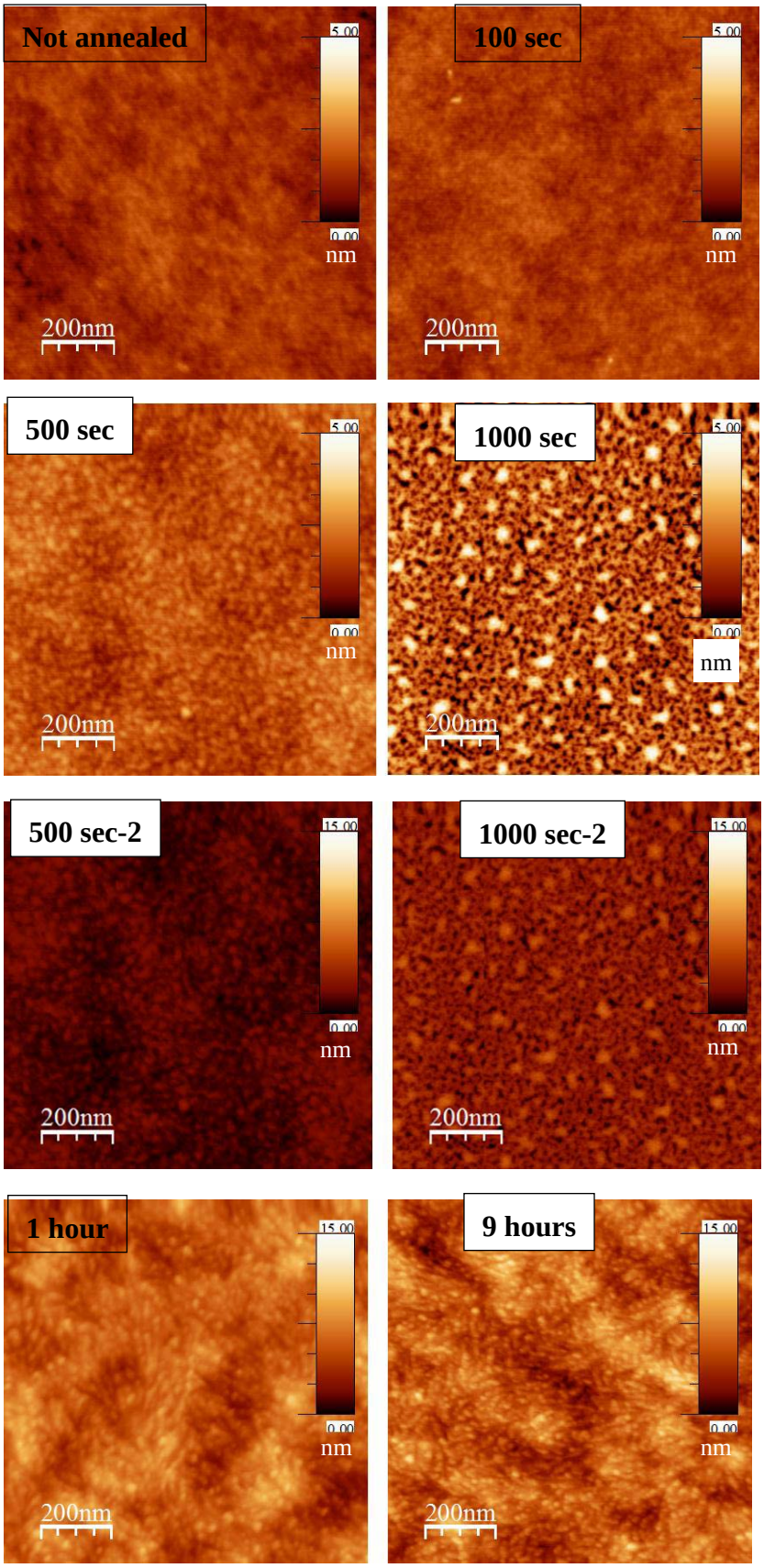
Not annealed
5.00
0.00
nm
200nm
100 sec
5.00
0.00
nm
200nm
500 sec
5.00
0.00
nm
200nm
1000 sec
5.00
0.00
nm
200nm
500 sec-2
15.00
0.00
nm
200nm
1000 sec-2
15.00
0.00
nm
200nm
1 hour
15.00
0.00
nm
200nm
9 hours
15.00
0.00
nm
200nm

Figure 5.12: Magnified 1 μm scale AFM images of the surface structure of 150 nm PET films; not annealed, annealed at 110 °C for 100 seconds, 500 seconds, 1000 seconds, 1 hour, and 9 hours. Height colour scale of 5 nm scale is in not annealed and 100 seconds images, 15nm scale is in 1 hour and 9 hours images. There are each 2 images of 500 seconds and 1000 seconds annealed. Both 5 nm and 15 nm height colour scale images are shown for those samples in order to compare easily to amorphous samples and crystallized samples because 500 seconds and 1000 seconds are very intermediate states.

Next, magnified images of Figure 5.11 are shown in Figure 5.12, that is, a much smaller scale reduced from 30 μm scale to 1 μm scale. The accompanying height scale is shown as colour index in figures. They are 5 nm scale in not annealed and 100 seconds, 15 nm height scale in 1 hour and 9 hours. Both 5 nm and 15 nm height colour scale images of 500 seconds and 1000 seconds are shown in order to easily compare to the amorphous samples and the crystallized samples because they are very intermediate states.

There was no clear texture in the not annealed and 100 seconds annealed samples, as was the case in the 30 μm scale images. However, the image of the not annealed sample seemed to have even less structure than the 100 seconds annealed sample. I suggest that this difference is caused by surface drift, although both samples are basically similar and amorphous. By “surface drift” I mean that molecules at the surface move very easily, like a liquid, and as a result, the image become vague. On the other hand, it is possible that molecules in the 100 seconds annealed sample are already slightly ordered if not pre-ordering, consequently, molecular movement is very weakly confined. This might account for surface drift being observed in the not annealed sample but not in the 100 seconds annealed sample.

The observed location of the 500 seconds annealed image was outside of a growing PET nucleus that was similar to amorphous in the larger 30 μm scale image. Although it looked amorphous in the 30 μm image, it was obviously different from the truly amorphous samples, such as the not annealed sample and the 100 seconds annealed sample. There is some kind of particle-like texture on the surface of the 500 seconds sample, and it was also very different looking from the later stage PET crystallized texture. This particle-like texture could indicate an intermediate state between amorphous and crystal in the annealing pathway for crystallization, that is to say, pre-ordering. In the image of the 1000 seconds annealed sample, this was also outside of nuclei in 30 μm scale image, the intermediate texture was still observed.

Compared with 500 seconds, there were much clearer particles. Although it is not yet clear what the difference between 500 seconds and 1000 seconds is, these clear particles do not resemble the crystalline structure. So they may also be some kind of intermediate state just before crystallization, like a densification of molecules just before chain packing. The height scale of these intermediate states was midway between that for the amorphous and crystalline states, hence both 5 nm and 15 nm colour scales were shown. Roughness, RMS values, of the amorphous (not annealed), intermediate (500 seconds annealed), and crystallized (9 hours annealed) samples were 0.18 nm, 0.37 nm, and 1.2 nm respectively. We can see that the intermediate states are rougher than the amorphous samples and flatter than the crystal. Discussions of roughness are mentioned with cross sectional profiles later.

Finally, observations of crystallized samples are shown in Figure 5.12 as 1 hour and 9 hours annealed. These samples were confirmed as crystallized films by GI-WAXS, ellipsometry, and 30 μm scale images of AFM. There were particles like chains of islands in these samples, and they can be identified with the lamellae of PET crystals. This assumption is reasonable from their size, about 10 nm ~ 20 nm, similar to the usually observed polymer crystal lamellae [for example, 125]. And these chains of particles seemed to be bunched up in 100 ~ 200 nm sized nodules. The nodule structure has observed in past studies of PET crystal in the literature [125]. This AFM observation seems to correspond to this special PET crystal morphology, because their sizes match each other; this is important data for studies of PET crystallisation. In the 9 hours annealed sample, these structures are much clearer. The crystallization process should be completed after this long time annealing, and they may be due to secondary crystallization. The roughness also increased more than 1 hour annealed sample (as shown later in Figure 5.15).

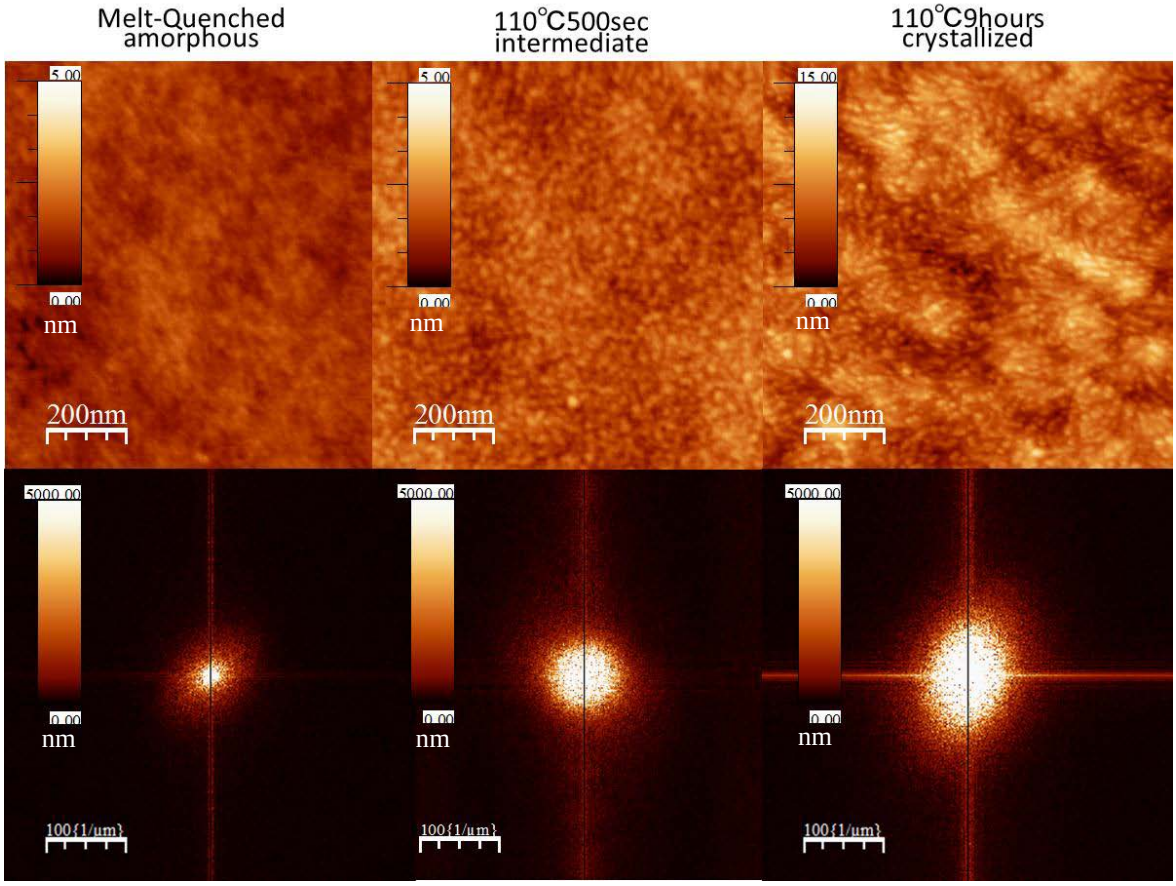

Figure 5.13: AFM height images of 150 nm samples not annealed and annealed at 110 °C for 500 seconds and 9 hours (1μm scale) and FFT images calculated from those AFM images of Not annealed (left: amorphous), 500 seconds annealed (centre: intermediate state), and 9 hours annealed(right: crystallized). Colour scale in FFT images are 5000 nm (Amplitude). The height images were also shown in Figure 5.12.

Next, a comparison of the AFM data, amorphous; not annealed, intermediate structure; 500 seconds annealed, and crystal; 9 hours annealed, is discussed with FFT (Fast Fourier Transform) images. Each AFM height image and FFT image are shown in Figure 5.13. FFT, this mathematical technique enables the quantitative comparison of the 2D images because it transforms height information, methodical texture, and orientation to intensity, ring radiation (nm^{-1}), and distortion or periodic pattern of ring like reciprocal space such as X-ray scattering images. The colour scale in FFT images is 5000 nm, this indicates the amplitude of the signal calculated from frequency of height in the AFM images. This FFT technique is very popular for AFM analysis, and we may leave the details of the FFT calculation process to more mathematical text books.

However, it is a little difficult to compare samples precisely with FFT images from AFM analysis because AFM images contain many noises and do not have enough resolution compared with X-ray scattering images. But we may say that there were three different states during crystallization of thin PET films, that is, amorphous, intermediate, and crystals from FFT images as same as AFM images.

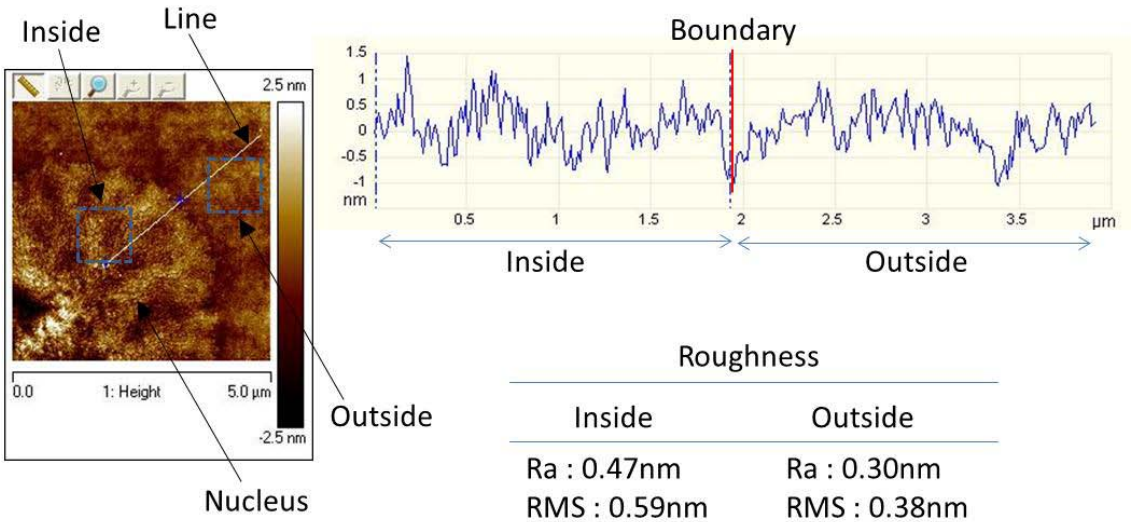

Figure 5.14: AFM images and a line profile of inside, outside, and boundary of a nucleus in a 150 nm thickness sample which is annealed at 110 °C for 500 seconds. The AFM image is 5 µm scale and its colour height scale is ±2.5 nm, as shown in the image. The position of the line profile is shown in the AFM image as a line. The line and its profile is drawn from left to right, that is, from the inside of the nucleus to outside. The roughness of inside and outside of a nucleus were calculated from separate 1µm square areas which sizes are shown in the AFM image. The values of roughness were mean value of 3 different areas in the sample rounded to two significant figures. Dispersion of the data was under 10 %.

Here, I would like to discuss line profiles of the sample surface in detail. Figure 5.14 shows an AFM image, a line profile, and roughness of 150 nm thickness sample annealed at 110 °C for 500 seconds and including a nucleus. The AFM image is 5µm scale and its colour height scale is ±2.5 nm as shown in the image. The position of the line profile is shown in the AFM image as a line. The line and its profile are drawn from left to right, that is, from the inside of the nucleus to the outside. The roughness of the inside and the outside of the nucleus were calculated from 1µm square area which size

is shown in the AFM image and the values were mean value of 3 different areas in the sample rounded to two significant figures. Dispersion of the data was under 10 %. Outside is a region considered as intermediate state, as mentioned above. In the line profile, we can see that there was a gap at the boundary of the nucleus. The boundary of spherulite shown in Figure 5.11 has a height ring but the boundary of nucleus has a gap. This difference might be caused by the difference between the front line of the growth in the amorphous material at the very early stage and the boundary of collision and competition of the growth with other spherulites. However, Figure 5.11 also shows the front lines with height contrast, of spherulites growing into amorphous material. I am not sure what has caused this difference; it may be the difference between the front lines of nuclei (at the very early stage of crystallization) and spherulites, or just and artefact of the measurements. The comparison of roughness between the inside and the outside shows that the inside was rougher than the outside. RMS values of the inside and the outside were 0.59 nm and 0.38 nm respectively. Because the outside is considered as intermediate state like pre-ordering and the packing of molecule of pre-ordering would be looser than the packing of crystal or crystal nucleus, it is reasonable that the shape or the texture of the inside is rougher than the outside.

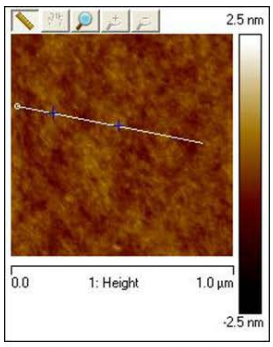

Melt Quenched

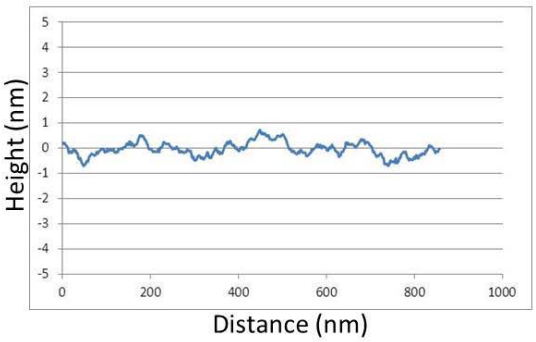

Ra : 0.18nm
RMS : 0.22nm

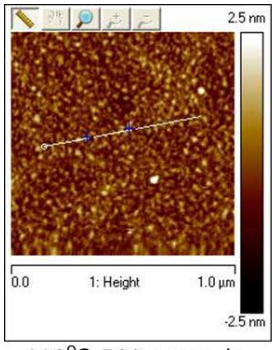

110°C 500 seconds

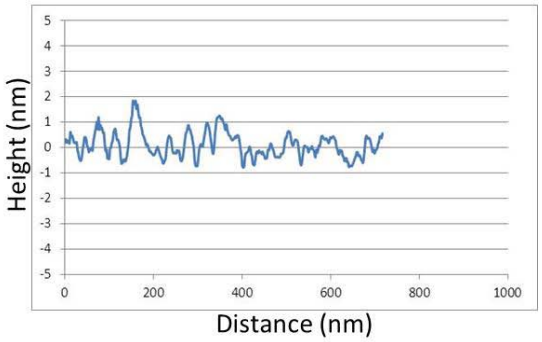

Ra : 0.37nm
RMS : 0.47nm

Peak to Peak
10 ~ 20nm

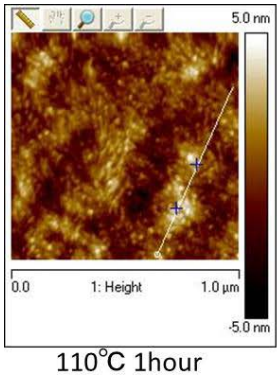

110°C 1hour

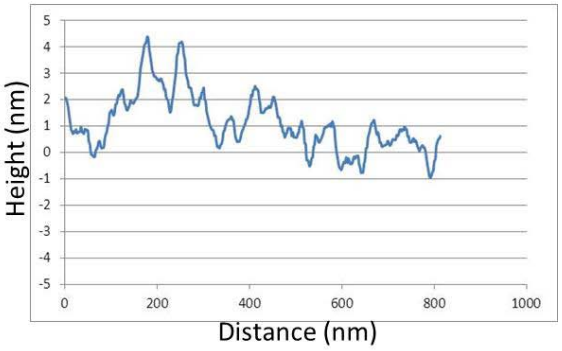

Ra : 0.97nm
RMS : 1.2nm

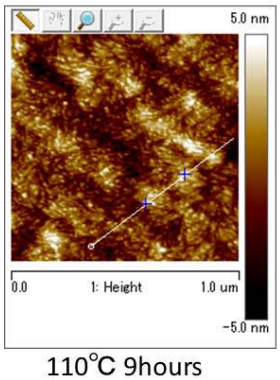

110°C 9hours

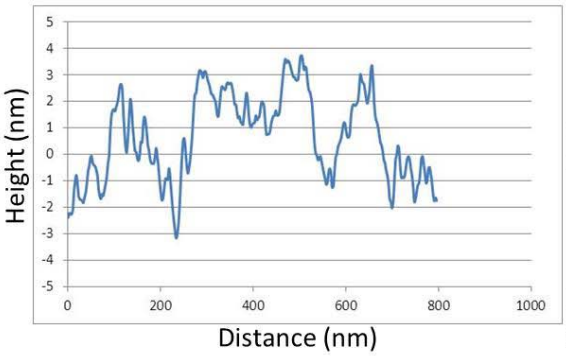

Ra : 1.2nm
RMS : 1.5nm

Peak to Peak
20 ~ 30nm

Figure 5.15: AFM images, line profiles, and roughness values of 150 nm thickness samples annealed at 110 °C for several time. The AFM image is 1 μm scale and its colour height scales are ±2.5 nm for melt-quenched and 500 seconds and ±5 nm for 1 hour and 9 hours as shown in the image. The position of the line profile is shown in the AFM image as a line. The line and its profile is drawn from left to right. Roughness values were calculated from each 1μm scale AFM image and were mean value of 2 or 3 measurements rounded to two significant figures. Dispersion of the data was under 10 %. The image of 1 hour and 9 hours were also shown in Figure 5.12 and 5.13.

Figure 5.15 shows AFM images, line profiles, and roughness values of 150 nm thickness samples annealed at 110 °C for different times. The AFM image is 1μm scale and its colour height scales are ±2.5 nm for melt-quenched and 500 seconds and ±5 nm for 1 hour and 9 hours as shown in the image. The position of the line profile is shown in the AFM image as a line. The line and its profile is drawn from left to right. Roughness values were calculated from each 1μm scale AFM image and were mean value of 2 or 3 measurements rounded to two significant figures. Dispersion of the data was under 10 %. The image of 1 hour and 9 hours were also shown in Figure 5.12 and 5.13.

We can see that the not annealed sample which was regarded as amorphous state had a very flat surface, subsequently the sample surface became more coarse and rougher at longer annealing time, from the AFM images and roughness values. This can be understood in terms of the progression of nucleation and crystallization making the surface rougher during annealing. We can also see the growth of crystal lamellae in the AFM images of 1 hour and 9 hours annealed. The AFM image of the 1 hour annealed sample was smooth and the roughness value was small but the image of 9 hours was sharp and fine, and the roughness increased. This should indicate the growth of crystal lamellae or secondary crystallization, that is, packing of molecules and structure became tighter and less disorder. The size of particles were estimated from the distance of peak to peak in the line profiles, and the particle size of the intermediate state seemed to range from about 10 nm to 20 nm, and the thickness of crystal lamellae annealed for 9 hours was estimated by same way of the particle size as the range from 20 nm to 30 nm. Not annealed and 500 seconds annealed samples have a flat baseline of the line profile, although there were fine surface features. On the other hand, 1 hour and 9 hours annealed samples have a rapidly altering structure with a period from 100 nm to 400 nm and a couple of nm height variance distinct from the surface roughness. This

indicates the nodule structure special to PET crystal, as introduced above, and their size and scale corresponds to the literature [125].

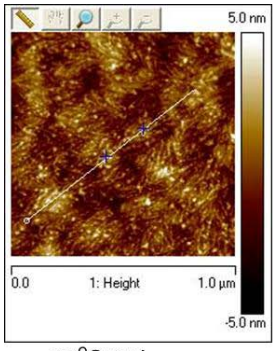

90℃ 84hours

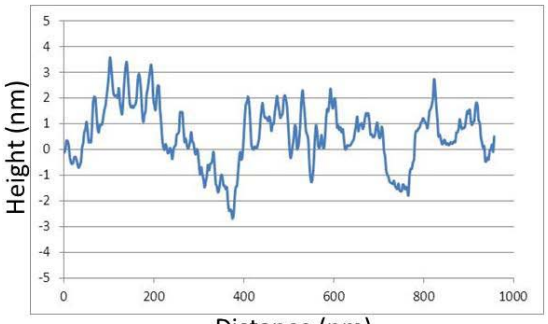

Ra : 0.96nm
RMS : 1.2nm

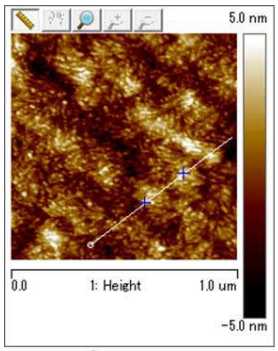

110℃ 9hours

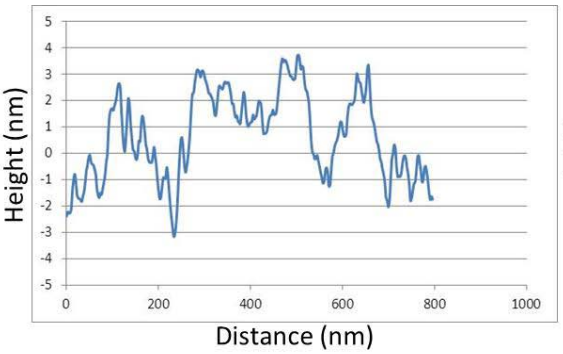

Ra : 1.2nm
RMS : 1.5nm

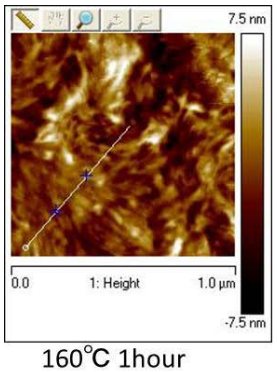

160℃ 1hour

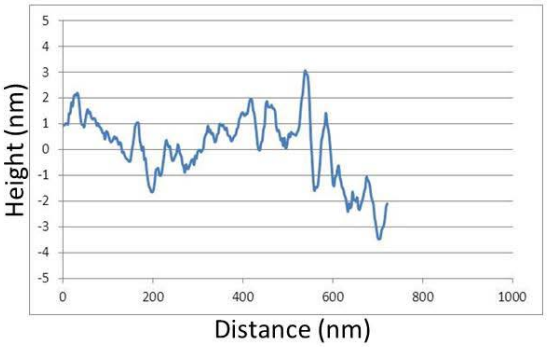

Ra : 1.8nm
RMS : 2.3nm

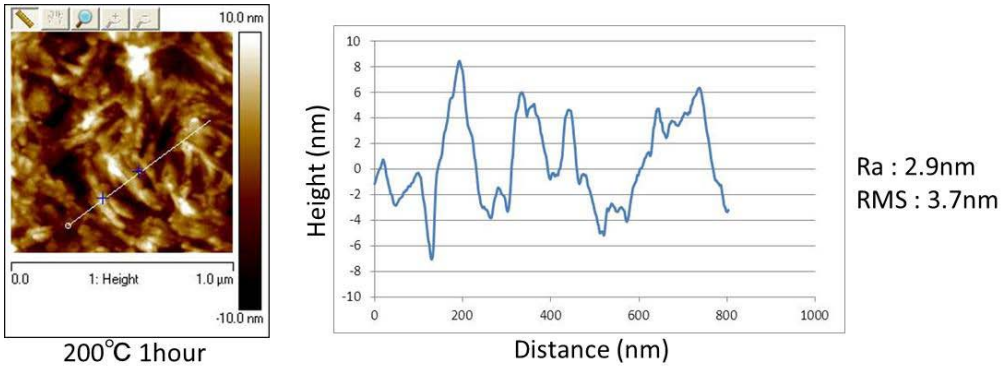

Figure 5.16: AFM images, line profiles, and roughness values of 150 nm thickness samples annealed at several temperatures. The AFM image is 1μm scale and its colour height scales are ±5 nm for 90 °C and 110 °C, and ±7.5 nm for 160 °C, and ±10 nm for 200 °C as shown in the image. The position of the line profile is shown in the AFM image as a line. The line and its profile is drawn from left to right. Roughness values were calculated from each 1μm scale AFM image and were mean value of 2 or 3 measurements rounded to two significant figures. Dispersion of the data was under 10 %. The image of 110 °C 9 hours was also shown in Figure 5.12, 5.13, and 5.15.

Next, the surface morphologies of fully crystalline samples, that is, samples at the point the moderate decrease in the film thickness after the drastic drop in the ellipsometry profile in Figure 5.6, were compared by annealing temperature. The sample annealed at 90 °C did not reached the same stage as the rest because annealing at 90 °C requires very long time for crystallization to proceed (see Figure 5.6). Figure 5.16 shows AFM images, line profiles, and roughness values for the 150 nm thickness samples annealed at several temperatures. All the AFM images are 1μm scale and colour height scales are changed as follows in order to see and compared with each other easily; ±5 nm for 90 °C and 110 °C, ±7.5 nm for 160 °C, and ±10 nm for 200 °C. The position of the line profile is shown in the AFM image as a line. The line and its profile are drawn from left to right. Roughness values were calculated from each 1μm scale AFM image and were mean value of 2 or 3 measurements rounded to two significant figures. Dispersion of the data was under 10 %. The images of 110 °C 9 hours were also shown in Figure 5.12, 5.13, and 5.15.

The morphology changed with temperature, the roughness and the line profiles were small and fine at low temperature, whilst at higher temperature large changes and larger features. The peaks in the line profiles are considered as crystal lamellae, therefore, the width of peaks are considered as lamellae thickness, that is, the lamellae thickness of samples annealed at higher temperature is thicker. This result agrees with

past studies, which showed that crystal lamella were thicker at higher temperature, for example, [128]. As shown by ellipsometry measurement in Figure 5.6, a longer annealing time is required for crystallization at lower temperature because the mobility of the molecules is smaller at lower temperature.

Very interestingly, the kind of morphology seemed to be altered between 110 °C and 160 °C. Crystal lamellae in 90 °C and 110 °C annealed samples were fine particles, like a chain of islands, and their size was about from 10 nm to 20 nm scale. On the other hand, lamellae changed to a clear line shape in 160 °C annealed sample and the line became thick in the 200 °C annealed sample. This might suggest an explanation for the difference between low temperature crystallization and high temperature crystallization seen in results in the literature [20], that is, in one case crystallization progressed by spinodal decomposition and in the other by bi-nodal nucleation. Of course, we cannot identify the mechanisms of the early stage of crystallization only from late stage (fully crystallized) morphologies with complete confidence, but the phase diagram (shown in Figure 6.10 discussed in Chapter 6 in detail) predicts that there should be different types of nucleation caused by the 2 kinds of phase separation, that is, spinodal and bi-nodal, and this might influence the size of lamellae later. The size of the crystal lamellae becomes large at high temperature with bi-nodal nucleation. The critical temperature where there is a switch between the two kinds of crystallization in bulk PET is about from 200 °C to 220 °C, as also reported in the literature (for example, [20, 129, 130]), however, this threshold temperature seemed to be shifted to lower temperature as from 120 °C to 160 °C in thin PET films. Then, this threshold temperature shift might be related to special features of thin polymer films, for example, the reduction in the apparent glass transition temperature and the slow crystallization rate. It is not strange because there is a difference in the T_g in thin films and its effect on the crystallization temperature, rate, and morphology. I will discuss the special kinetics and mechanisms of crystallization and induction time in thin PET films in Chapter 6 and 7 in detail.

I also checked this morphology shift by SEM as shown as below. 10000 times magnified SEM images of amorphous (Not annealed), annealed at 110 °C for 9 hours, 160 °C for 2 hours, and 200 °C for 1 hour are shown in Figure 5.17. The SEM was a field emission type by JEOL and the acceleration voltage was 5 kV. In order to image the samples stably using SEM a thin layer of Platinum was sputtered onto the sample surface under vacuum condition to render the surface conductive. There was no clear texture in the amorphous sample, but fine particles could be seen in the 110 °C 9 hours annealed sample. There were some lamellae like structures in 160 °C 2 hours annealed

sample, and they became large and clear in the 200 °C 1 hour sample. It is safe to bet that a sample annealed at 110 °C for 9 hours is crystallized from the data of ellipsometry and AFM images, however, we can see that the crystal morphology was quite different for the crystals in samples annealed at 160 °C or 200 °C not only by AFM but also by SEM. This kind of double check is very important to secure certainty and reliability of image data. Nevertheless, there might be a slight damage or influence to the vulnerable sample surface of thin polymer film from Pt sputtering under vacuum and electron beam during measurement, besides the Auger electron which would be generated to some extent under the surface. Therefore, AFM is much better technique in order to see just the surface of thin polymer films used in this study, and has good reliability for precise height information.

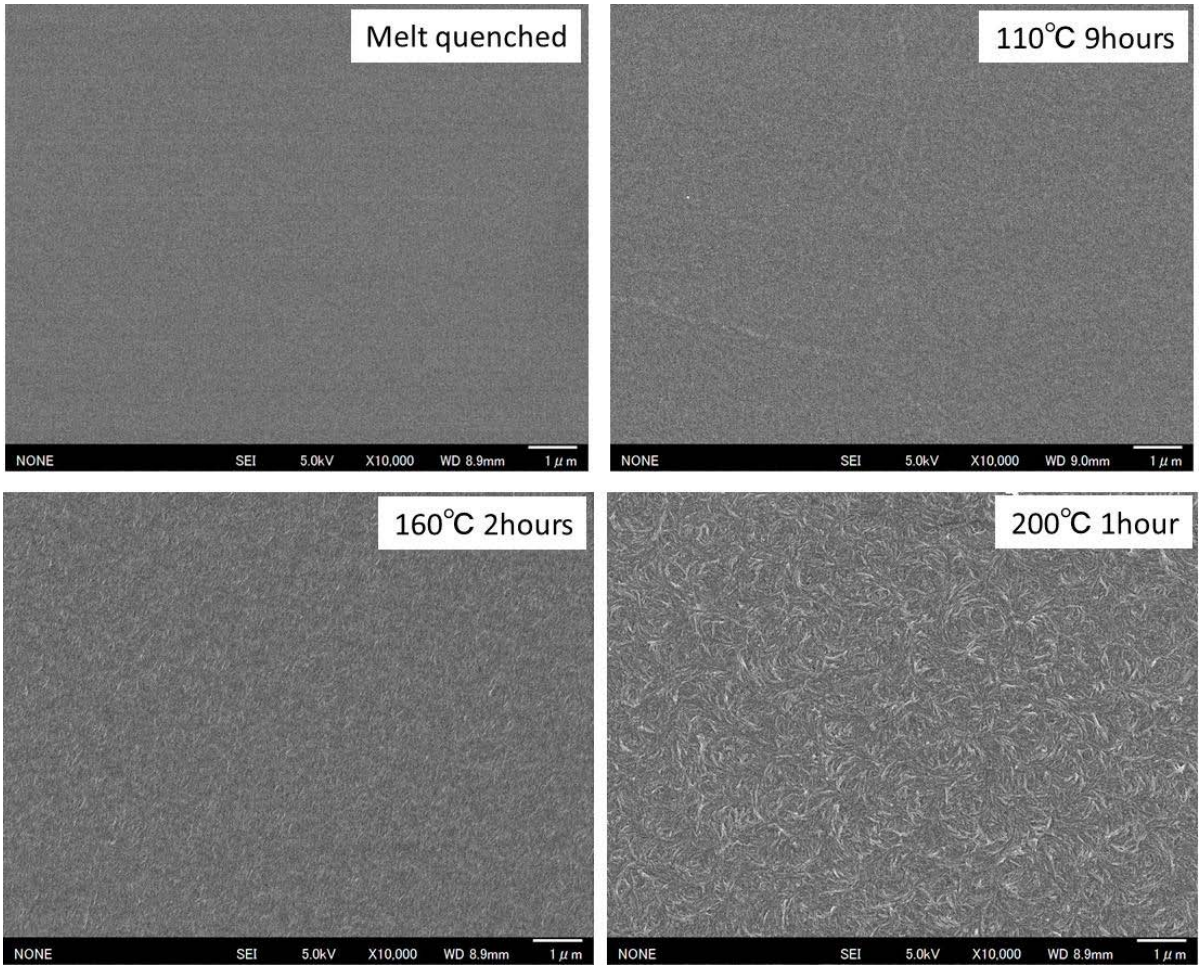

Figure 5.17: SEM images for crystalline 150 nm PET film samples annealed at different temperatures.

It should be interesting to show how the crystallization process is changed by different annealing temperatures. I would like to show it as following with detailed AFM analysis for the samples at different temperature prior to and for the fully crystalline surface coverage.

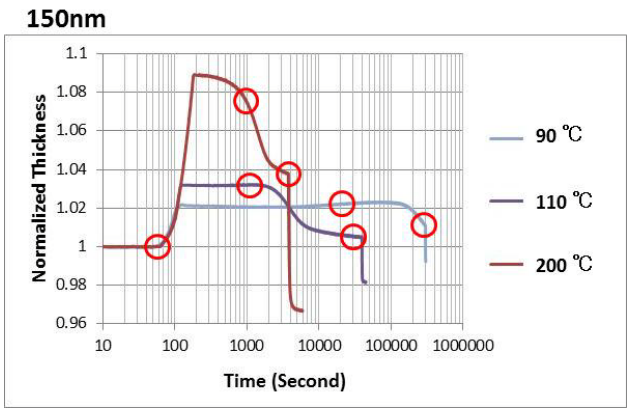
150nm
Normalized Thickness
1.1
1.08
1.06
1.04
1.02
1
0.98
0.96
10
100
1000
10000
100000
1000000
Time (Second)
90 ℃
110 ℃
200 ℃

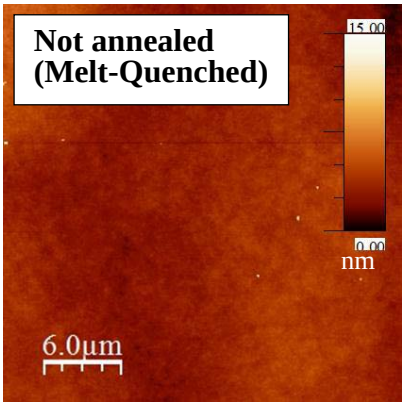
Not annealed
(Melt-Quenched)
15.00
0.00
nm
6.0μm

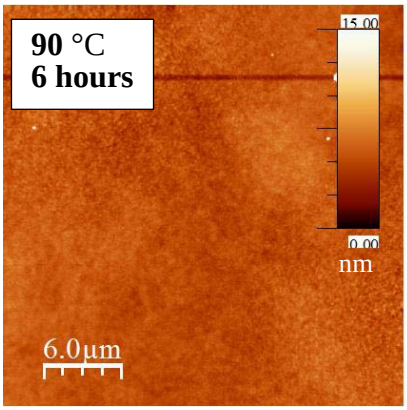
90 °C
6 hours
15.00
0.00
nm
6.0μm

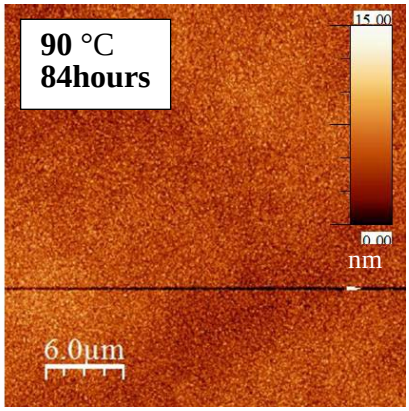
90 °C
84hours
15.00
0.00
nm
6.0μm

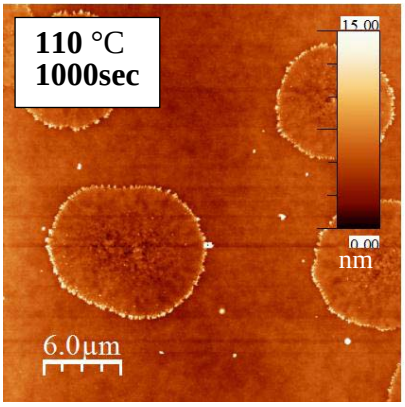
110 °C
1000sec
15.00
0.00
nm
6.0μm

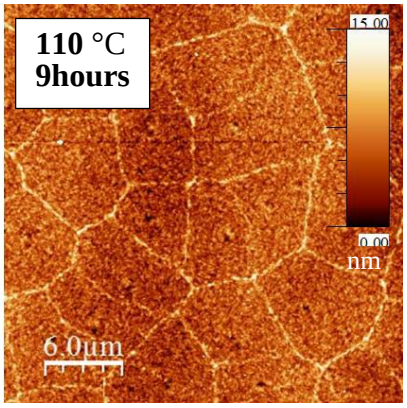
110 °C
9hours
15.00
0.00
nm
6.0μm

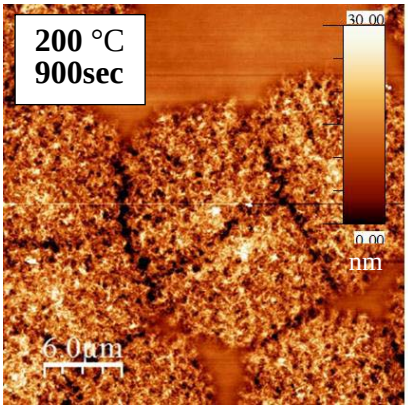
200 °C
900sec
30.00
0.00
nm
6.0μm

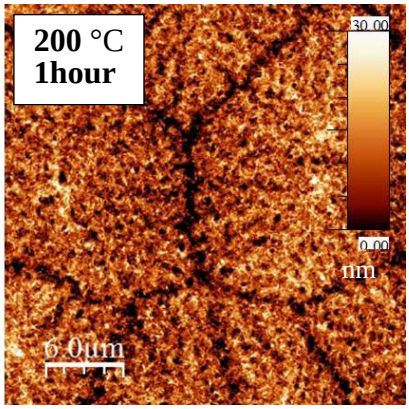
200 °C
1hour
30.00
0.00
nm
6.0μm

Figure 5.18: Ellipsometry graphs of 150 nm PET film samples annealed at 90 °C, 110 °C, and 200 °C and AFM images (30μm scale). Red circles on the ellipsometry graphs indicate the points on the AFM images, that is, samples annealed for 6 hours at 90 °C, for 1000 seconds at 110 °C, and for 900 seconds at 200 °C as intermediate or before the fully crystallized state. And 84 hours at 90 °C, 2 hours at 110 °C, and 1 hour at 200 °C are as fully crystallized samples. Thickness of all samples was 150 nm and height colour scales are shown in each image.

In order to discuss the kinetics of crystallization and the macro scale morphologies, Figure 5.18 shows that ellipsometry graphs of thin PET films annealed at 90 °C, 110 °C, and 200 °C and AFM images (30 μm scale). Red circles on the ellipsometry graphs indicate the points of AFM images, that is, samples annealed for 6 hours at 90 °C, for 1000 seconds at 110 °C, and for 900 seconds at 200 °C as intermediate or before fully crystallized state. And 84 hours at 90 °C, 2 hours at 110 °C, and 1 hour at 200 °C are as fully crystallized samples. Thickness of all samples was 150 nm and height colour scales are shown in each image.

In the intermediate state sample annealed at 90 °C, that is, the sample annealed for 6 hours during plateau of the ellipsometry graph, there was no clear texture. On the other hand, in the sample annealed at 110 °C for 1000 seconds, as mentioned above, there were sporadic crystal nuclei and outside of nuclei the intermediate state texture. In the sample annealed at 200 °C for 900 seconds, we can see there was clear lamellar texture, but the sample surface was not covered completely by this structure. The reason for this should be that 900 seconds was near the end of the plateau and it would be on the way to crystallization as same as 110 °C for 1000 seconds; that is, the crystal part was clearly separated from the not crystallized part. The magnified images of these lamellae are shown in Figure 5.19. The lamellae in 900 seconds annealed sample seemed to be crystallized to about the same extent as the fully crystallized lamellae. However, that image was a little vaguer than the image of 1 hour annealed sample. This difference might be caused by being before and after the occurrence of secondary crystallization.

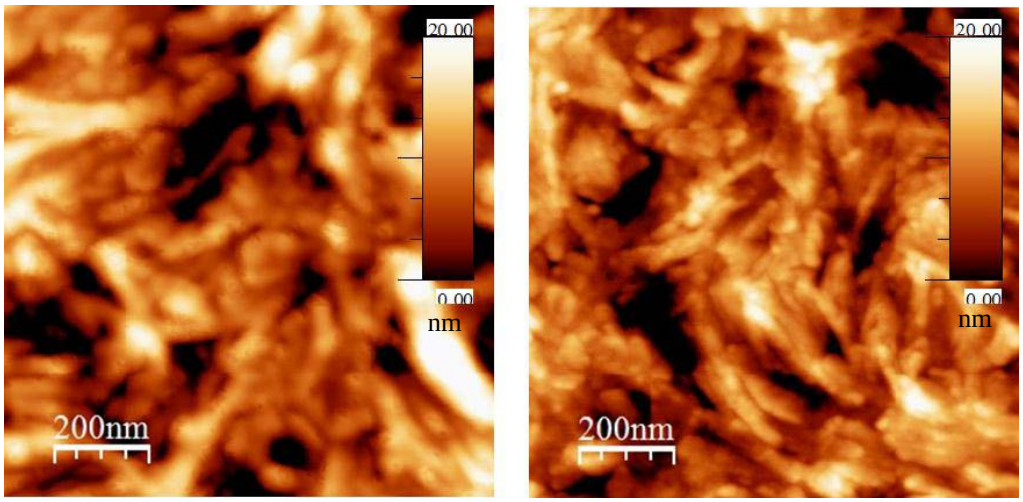

Figure 5.19: Magnified AFM images (1μm scale) of 150 nm film samples annealed at 200 °C for 900 seconds (left) and 1 hour (right).

The crystallization process and morphology of the sample annealed at 200 °C is different from that of the sample annealed at 110 °C, as shown in Figure 5.18 and 5.19. The sample annealed at 200 °C had large and clear lamellae, the spherulites in the 200 °C samples were well defined and had a large height scale, and the boundaries of the spherulites were valleys in the 200 °C samples. In contrast the boundaries for the 110 °C samples were hills. The reason for this is unclear but the lamellae thickness and size might influence the boundary of spherulites. High temperature annealing makes the lamellae thickness greater, as shown by equation 1.6 and Figure 5.16 and 5.17. However, the morphology of samples after a 1 hour crystallization process annealed at 90 °C and 110 °C were similar to each other in all respects except the time scale. This also might indicate that the crystallization at 110 °C is low temperature crystallization, the crystallization at 90 °C should be also low temperature.

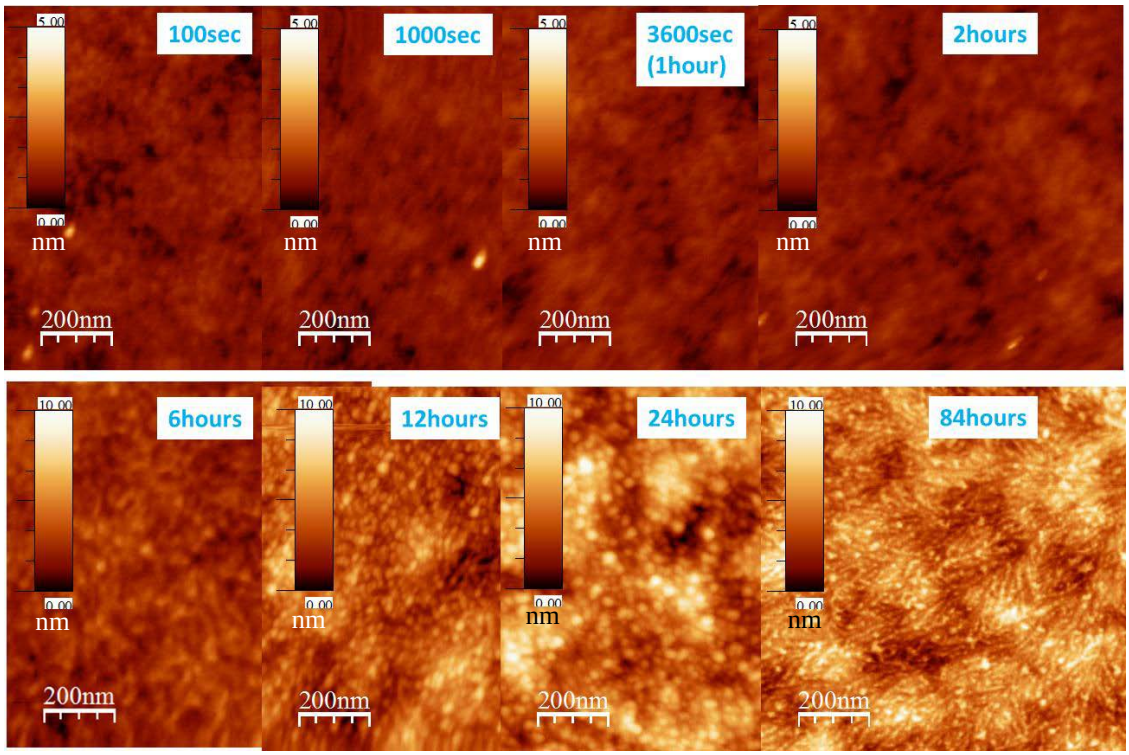

Figure 5.20: AFM images (1μm scale) of 150 nm PET film samples annealed for several times at 90 °C. The annealing times were 100 seconds, 1000 seconds, 3600 seconds, 2 hours, 6 hours, 12 hours, 24 hours, and 84 hours respectively.

Figure 5.20 shows magnified AFM images (1 μm scale) of samples annealed for several times at 90 °C. Measurement times were 100 seconds, 1000 seconds, 3600 seconds, 2 hours, 6 hours, 12 hours, 24 hours, and 84 hours respectively. Compared to those annealed at 110 °C, the time scale became much longer but the crystallization process and its morphology were basically similar. As the image of the 6 hours annealed seemed an intermediate state between amorphous and crystal, the intermediate state would begin after 2 hours and finish before 12 hours. At 110 °C, the amorphous structure changed to the intermediate state around 500 ~ 1000 seconds, therefore, the time scale of crystallization annealed at 90 °C was around 20 ~ 40 times longer than at 110 °C

We can see that there were some kind of particles in the 12 and 24 hour annealed samples. These annealing times are still on the plateau of the ellipsometry graph, which is meaning that the density of samples are not changed, and the particles seemed to be slightly different from both the lamellae in a crystallized sample, 84 hours (about 300 thousands seconds) annealed and amorphous. This might indicate that these intermediate states are very near to the true crystal structure (latter intermediate state)

that we can see them in only 90 °C annealed sample because the time scale is very long at 90 °C. Of course, there is a possibility that these particles might be structures inside nuclei, because nucleation should occur during the induction time of crystallization. Therefore it is difficult to judge what the particles are but we can say that they are not perfectly crystallized structure, that is, latter stage of intermediate state or early stage of crystals.

In the ellipsometry data of 90 °C, the thickness seemed to increase slightly over 10 thousands seconds (over 2.5 hours), so it deserved much more time to confirm in detail whether this increase was real or not. I say this because if there was a structure which is very near to the crystal, for example, the molecules are packed tightly and it makes pre-ordering much clearer, a density increase should occur even it is lesser than that for the crystal, and this would increase its refractive index. As a result, the increasing refractive index might be regarded as an increase of thickness, that is, an error of the ellipsometry measurement. Therefore, I think there should be a room to improve the fitting program for the samples annealed at 90 °C. And of course, there might be other kind of reasons, for example, sample drift or changing surface roughness. The measurement of 90 °C is over quite a long time and a sample may drift slightly. The surface roughness might be changed during the induction time of crystallization. Ellipsometry measurements are very sensitive and these phenomena could influence the measurements, so the apparent thickness increase might be caused by these.

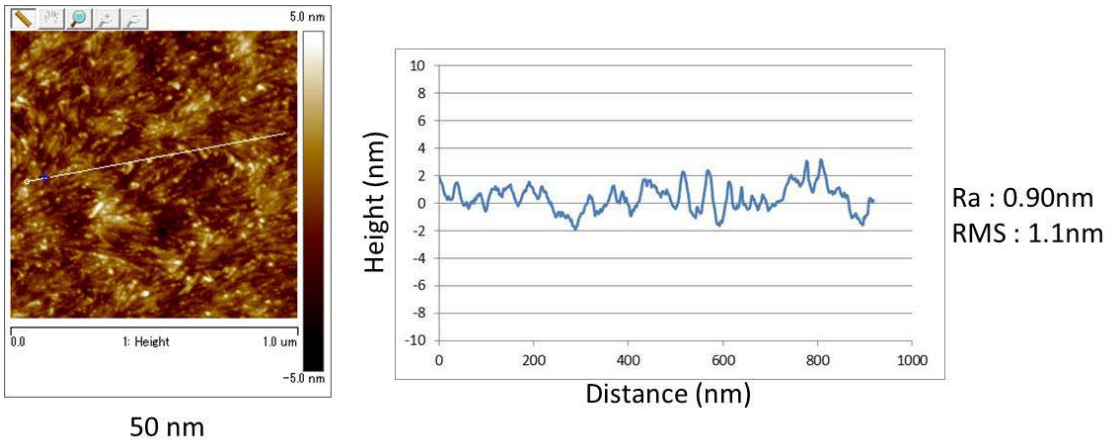

50 nm

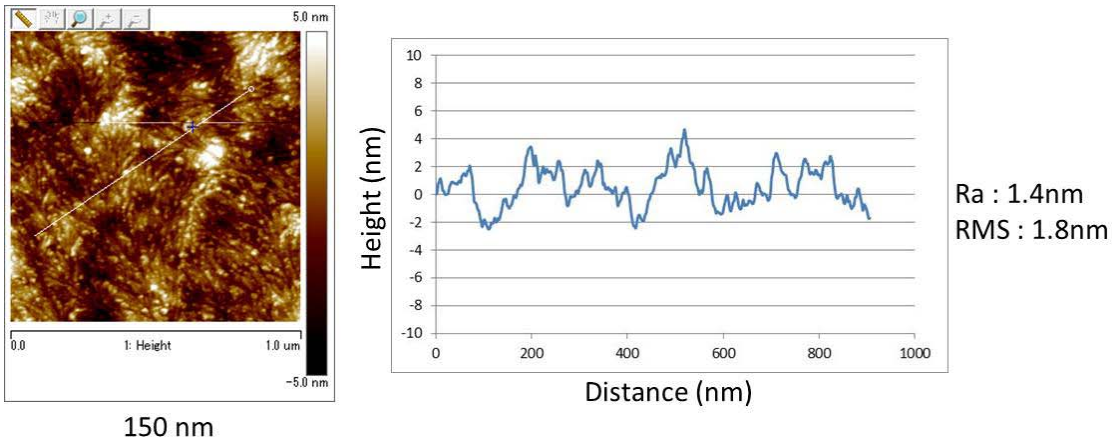

150 nm

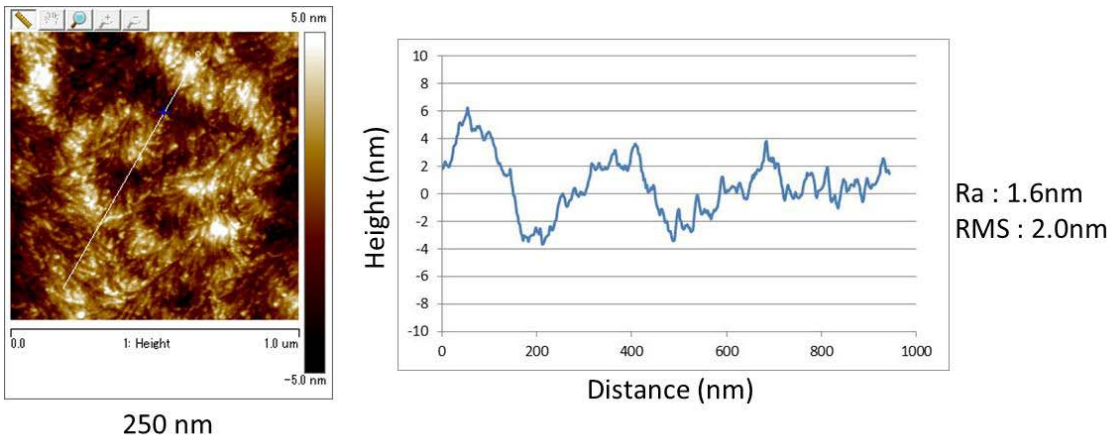

250 nm

Figure 5.21: AFM images, line profiles, and roughness values of different thickness samples annealed at 120 °C for 2 hours. Each thickness was 50 nm, 150 nm, and 250 nm respectively. The AFM images are 1μm scale and its colour height scales are ±5 nm as shown in the images. The position of the line profile is shown in the AFM images as a line. The line and its profile is drawn from left to right in 50 nm image, and the line is drawn from right to left in 150 nm and 250 nm images. Roughness values were

calculated from each 1μm scale AFM image. Roughness values were calculated from each 1μm scale AFM image and were mean value of 2 or 3 measurements rounded to two significant figures. Dispersion of the data was under 10 %.

Next, I would like to discuss the influence of film thickness on surface morphology. Figure 5.21 shows AFM height images and line profiles of samples annealed at 120 °C for 2 hours. Film thicknesses were 50 nm, 150 nm, and 250nm respectively. AFM images, line profiles, and roughness values of different thickness samples annealed at 120 °C for 2 hours. Each thickness was 50 nm, 150 nm, and 250 nm respectively. The AFM images are 1μm scale and its colour height scales are ±5 nm as shown in the images. The position of the line profile is shown in the AFM images as a line. The line and its profile is drawn from left to right in 50 nm image, and the line is drawn from right to left in 150 nm and 250 nm images. Roughness values were calculated from each 1μm scale AFM image.

The sizes of those lamellae shown in Figure 5.21 were all similar, and from those line profiles, the sizes seemed about 10 ~ 20 nm. However, we can also see that roughness values increased as film thickness increased. This should not be caused by size and number of crystal lamellae increased. A baseline of line profile was flat in the thin film, 50 nm, but it began to surge as film thickness increased. The reason for this should be that the nodule structure explained above emerged much more clearly in thicker films. That nodule structure made of PET crystal has a period from 100 nm to 400 nm, shown by line profiles in Figure 5.21 and this corresponds to the literature reported values for the nodule structure, as shown in Figure 5.22 [125]. The reason why the thicker film has clear nodule structure should be that the thicker film has both enough space for molecules to move and a lot of molecules, so swelling of nodule structure also become large in thicker films, and this caused the larger surface roughness values.

Finally, I would like to refer to sample – sample variation between ellipsometry and AFM measurements. The measurements were implemented on groups of samples which were made under the same conditions, numerical results were within a few % of variation, and images were very similar to each other. Therefore, if samples were made properly as described in Chapter 3, we can be confident that there are not major influences from sample – sample variation in this study.

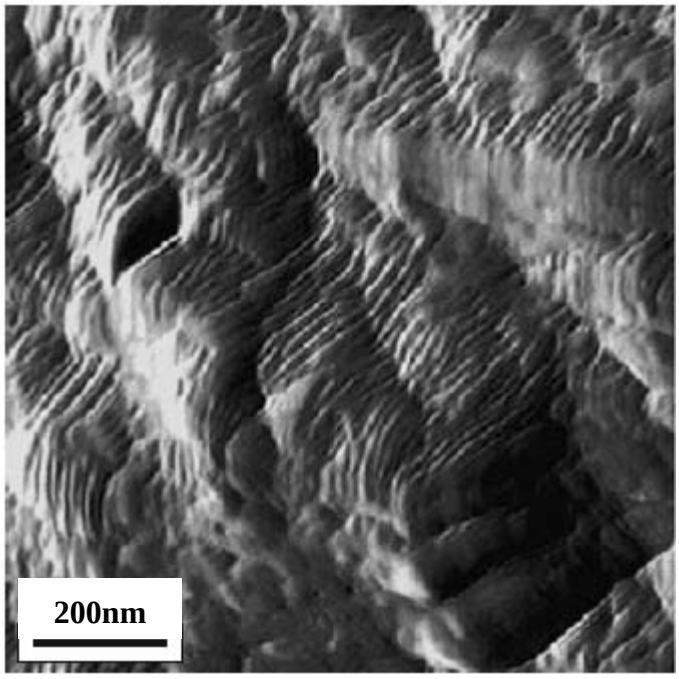

Figure 5.22: AFM image of surface of crystallized 100 μm thickness PET [125]. The surfing surface is nodule structure, which is distinct feature of PET crystals.

5.5 Summary

We have traced the kinetics of crystallization in thin PET films by ellipsometry and the crystalline structure was confirmed as that of bulk PET crystals by GI-WAXS.

The data from ellipsometry showed that lower temperature cause slower crystallization, however, there was an optimum temperature for crystallization, the same as seen in the bulk, but it seems somewhat lower than in the case of the bulk, with an optimum crystallization temperature for the 150 nm thickness film around 160 °C. At a thermal annealing temperature of 200 °C, the induction time and crystallization rate also slowed down again. At 50 nm thickness, the thermal expansion rate was larger and the induction time was a little shorter than for the 150 nm and 250 nm samples. This supports past studies, which say that T_g decreases and thermal expansion rate becomes larger for films under 100 nm in thickness, because of the high mobility of molecules, due to the surface effect. Besides, the nucleation rate is also large in thinner films because of the large surface area ratio.

Surface morphologies of samples were observed by AFM and the detailed kinetics of thin film PET crystallization was estimated. Before crystallization starts, there was an intermediate state, which was clearly different from both the amorphous and crystal states. The sizes of the structures in this state were around 10 to 30 nm. This might be the pre-ordering of the thin PET films. At higher temperatures, the surface roughness and crystal size became larger. This corresponds to the literature result that crystal lamellae become thicker at higher temperature. My AFM and ellipsometry analysis showed that a longer time is required for crystallization at lower temperature. However, AFM revealed that the process and the type of surface texture of 90 °C crystallization is similar to 110 °C crystallization but its time scale is quite different. For example, the induction time of the 90 °C annealed sample is longer by 20 ~ 40 times than 110 °C. The structure and morphology changes at various temperature before the film density starts to increase – but density changes are mostly (but maybe not always) accompanied by observable spherulites. At 90 °C annealing, there is a possibility that spherulites emerge during a plateau of ellipsometry measurements (i.e. with no change of density). The crystal lamellae size in 160 °C and 200 °C was quite large compared to 90 °C and 110 °C. There might be some kind of threshold temperature between low temperature crystallization and high temperature crystallization. This threshold temperature in thin films seems lower than the bulk. The reason of this should be related to special features of thin PET film, for example, low T_g and a large surface effect. The film thickness does not change the size of crystal lamellae but the nodule structure becomes clearer in thicker films than in thinner films. This could be due to the large volume in thicker films which allows molecules to move more easily than in thinner films, and this makes nodule more distinct. AFM is very important for my research because it shows higher resolution images than optical microscope and reveals much more quantitative information than SEM.

Chapter 6

Observation of the pre-ordering in thin PET films

6.1 Introduction

We discussed detailed morphologies of the crystals in thin PET films in Chapter 5 with the AFM data and there was a discussion about the intermediate state between amorphous and crystal. This intermediate state may be the pre-ordering predicted by the theory of Olmsted *et al.* and observed by Kaji *et al.* [28, 20], and to observe the pre-ordering in thin PET films is one of the important aims of this study. Small angle X-ray scattering(SAXS) and Small angle neutron scattering(SANS) are used to detect pre-ordering in the literature [20, 54] while grazing incidence small angle X-ray scattering(GI-SAXS) was used in this study in order to observe the pre-ordering because the samples were thin polymer films. In this Chapter, I will discuss the validity of results and the GI-SAXS data, and whether our GI-SAXS measurements detected the pre-ordering or not. Then, a quantitative analysis of the intermediate state was implemented by the mathematical calculation of the Power Spectrum Density (PSD) from the AFM data. Finally, I will come to a discussion the validity of my data and interpretations, and the relationship between my observations of pre-ordering in thin film samples and previous work in the literature on bulk samples.

In GI-SAXS measurements, there was a shoulder I supposed to be scattered from the pre-ordering, corresponding to a 15 nm length scale in a sample annealed at 110 °C, and this length scale was similar to a pre-ordering detected in a bulk sample reported by Imai *et al.* [26, 54]. In a sample annealed at 200 °C, there was also a similar shoulder, although it was weaker. Interestingly, that shoulder was shifted to low angle,

that is, long length scale; and this might correspond to the trend that crystal lamellae became larger at higher temperature annealing, such as at 200 °C. However, the much more interesting point is that there might be a pre-ordering state in even high temperature crystallization. In the experimental literature, pre-ordering was referred in only low temperature crystallization because it should be difficult to detect pre-ordering during quick crystallization at higher temperature.

The intermediate state supposed to be pre-ordering was analysed quantitatively by PSD calculated from the AFM data. As a result, there was a shoulder indicating the same length scale measured by GI-SAXS, and this should indicate the possibility that the intermediate state observed in AFM images corresponds to pre-ordering. Interestingly, a PSD profile of the sample annealed at 90 °C shows that the length scale of the intermediate state was larger than that of the sample annealed at 110 °C although the crystal lamellae of 90 °C annealed were finer than those of 110 °C annealed. However, this large length scale of intermediate state might be a very early stage of pre-ordering, that is, the packing of molecules could be loose and highly swollen. The crystallization process at 90 °C is very slow, so we might be able to capture its very early stages. As annealing time proceeds, 6 hours, 12~24 hours, and 84 hours, the ordered texture like pre-ordering or crystal lamellae became smaller, and the crystal structure of 84 hours annealed was finer than of those annealed at 110 °C. This crystallization process seems reasonable because the structure should become finer or more tight as the crystallization process proceeds and crystals made by low temperature crystallization should be smaller than high temperature crystallization. This data capturing the thin PET film crystallization process evolution at different temperature could be useful for studies of thin polymer film crystallization in future.

6.2 Observation and Investigation of pre-ordering by AFM and GI-SAXS

We discussed Figure 5.13 as AFM height images (1μm scale) and FFT images which imply there was an intermediate state between amorphous and crystalline. FFT images were calculated from the AFM images of Not annealed (left: amorphous), 500 seconds annealed (centre: intermediate state), and 9 hours annealed (right: crystallized). The

colour scale in the FFT images is 5000 nm (Amplitude). In past studies of PET crystallization, as shown in Figure 6.1 [54], the intermediate state was observed by SAXS (small angle X-ray scattering) or SANS (small angle neutron scattering), which are good to detect long range ordering structure. These methods can readily detect nanoscale ordered structures like pre-ordering in the size region from 10 nm to 20 nm, which is larger than crystal spacings, and cannot be analysed by WAXS (wide angle X-ray scattering). Figure 6.1 shows the time-resolved SAXS profiles at 80 °C in double logarithmic expression [54]. For convenience, each curve is shifted along the intensity axis. The scattering profiles of the samples annealed for 3, 23, 51, 75, and 115 minutes correspond to the induction period, and those for 147, 187, 243, and 313 minutes correspond to the crystallization stage. From these scattering profiles, it is noticed that after annealing for 3 min the scattering intensity in the Q range of 0.03 - 0.05 $Å^{-1}$ (20 nm – 12 nm) increases with annealing time during the induction period. After the induction period, another new scattering shoulder assigned to the crystal long period appears near Q = 0.06 $Å^{-1}$ (10 nm), and increases in intensity with time (crystallization progresses with time). This shift of shoulder indicates the pre-ordering state before crystallization. This should indicate the pre-ordering state of crystallization. The past studies mentioned above have reported the texture of the intermediate state resulting from spinodal decomposition to have a domain size of about 15 nm. Because the purpose of this study is to study the early stages of crystallization, we need an experimental method which can detect pre-ordering in thin film samples. Therefore, GI-SAXS was adopted to this study, in contrast to the bulk probes used in past studies. The principle and experimental condition of GI-SAXS and why GI-SAXS is suitable for the investigation of structure of thin polymer films is contained in detail in Chapter 2. GI-SAXS in this study was implemented at X-Mas, BL-22 of ESRF in Grenoble, France.

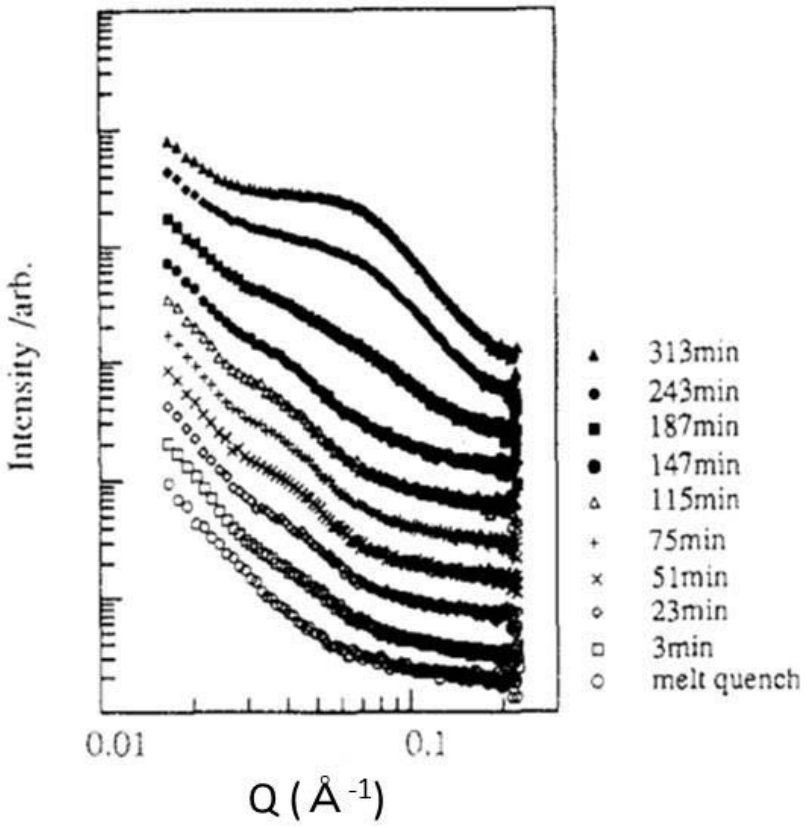

Figure 6.1: Time evolution of small angle X-ray scattering(SAXS) profiles when PET was annealed at 80 °C reported by Imai *et al* [54]. This is a representative past study of pre-ordering and crystallization of bulk PET.

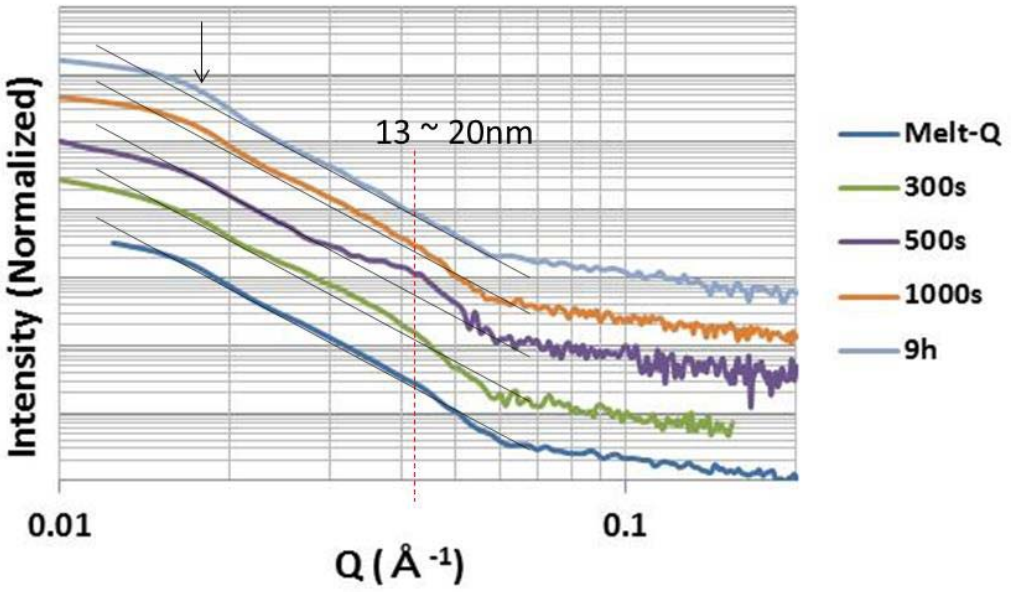

Figure 6.2: Time evolution of grazing incidence scattering - small angle X-ray scattering (GI-SAXS) profiles of 150 nm thickness PET films not annealed and annealed at 110 °C for 300 seconds, 500 seconds, 1000 seconds, and 9 hours with baseline. The size shown in the image indicates the length scale observed in SAXS bulk PET measurements and corresponds reasonably well to the hump in the scattering shoulder position. The measurements here were on a series of ex-situ annealed / quenched samples.

Figure 6.2 shows grazing incidence - small angle X-ray scattering (GI-SAXS) line profiles of 150 nm thickness samples not annealed, annealed at 110 °C for 300 seconds, 500 seconds, 1000 seconds, and 9 hours. There are also baselines in order to see each peak or some signals easily and the slope angle in the data is all the same. The length scale shown in the image indicates the length scale calculated from the scattering shoulder positions using the relation in Equation 6.1.

$Q = 2\pi / r$ （6.1）

where, Q is the scattering vector, $Q = 4\pi\sin\theta/\lambda$, and r indicates size (Å). Not annealed and annealed for 300 seconds are amorphous, annealed for 500 seconds and 1000 seconds during the intermediate state, and annealed for 9 hours has crystallized, respectively. There was very little structure in the amorphous sample, on the other hand, there was a broad shoulder at around $Q = 0.04(Å^{-1})$ in the 500 seconds annealed sample. This shoulder position indicates that there should be about 15 nm in size scale (with a

range from 13 nm to 20 nm) from Equation 6.1. Looking at the sloping baseline, it seems that there was some structure emerging in 300 seconds annealed sample, at about Q = 0.03～0.04($Å^{-1}$). Then, this shoulder became ambiguous and another shoulder stated to emerge at about Q = 0.018($Å^{-1}$) in the 1000 seconds annealed sample, finally, this later shoulder became clearer in the crystallized sample, that is a film annealed for 9 hours. Properly, from the literature, if some crystallization occurs, there should be scattering corresponding to lattice constants of the crystal, as in the WAXS data shown in Chapter 5.2, and there should be a peak or shoulder corresponding to the crystal-amorphous alternate structure in SAXS at about Q = 0.07～0.08($Å^{-1}$) as shown in Figure 6.1. However, in this GI-SAXS measurements, the range above Q = 0.06($Å^{-1}$) was just noise and such structure was not detectable because of the limitations of the instruments. The reason for the small signal was that the GI-SAXS detector was set to the in plane direction, as the reflectivity from the sample covers the out of plane direction. I would like to improve the quality of the experiment in future work with this experience. The shoulder observed in the crystallized sample at about Q = 0.018($Å^{-1}$) might indicate the size of lamellae, and this size scale corresponds to the AFM images shown in Chapter 5. It is very interesting that the length scale of pre-ordering measured by AFM was very similar to the GI-SAXS data. This would support the appropriateness of this GI-SAXS, although the crystal-amorphous alternate structure was not observed. I will mention and discuss the time scale of the process of pre-ordering and crystallization of bulk PET samples and how they are different from those of thin PET film samples in Chapter 7 in detail.

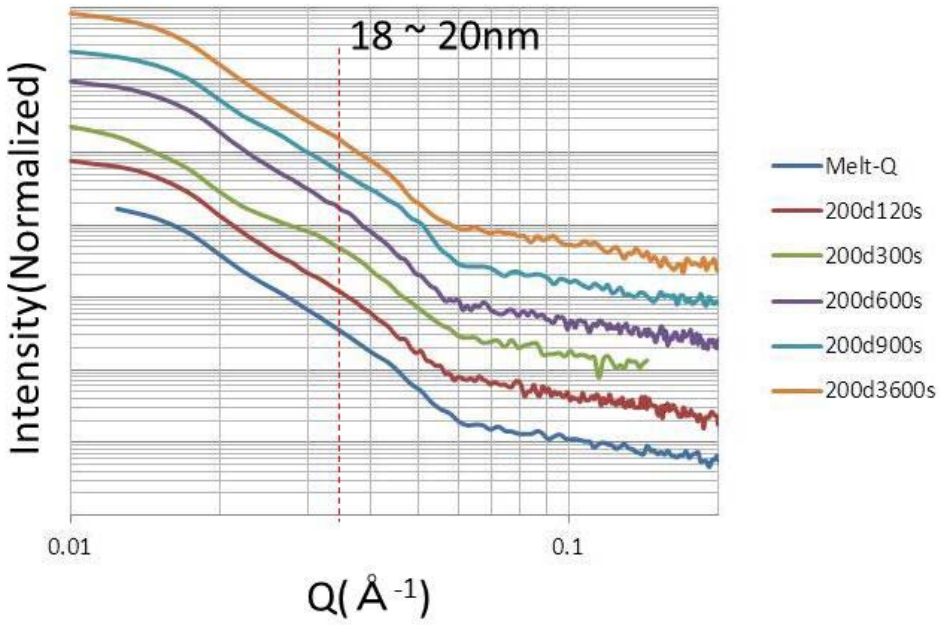

Figure 6.3: Time evolution of grazing incidence - small angle X-ray scattering (GI-SAXS) profiles of 150 nm thickness PET films not annealed, annealed at 200 °C for 120 seconds, 300 seconds, 600 seconds, 900 seconds, and 3600 seconds (1 hour). The length scale shown in the image indicates length scales calculated by scattering shoulder positions with Equation 6.1. The measurements here were on a series of ex-situ annealed / quenched samples.

Figure 6.3 shows the time evolution of grazing incidence - small angle X-ray scattering (GI-SAXS) profiles of the 150 nm thickness PET films not annealed, annealed at 200 °C for 120 seconds, 300 seconds, 600 seconds, 900 seconds, and 3600 seconds(1 hour). The lengthscale shown in the image indicates the lengthscale calculated from the hump in the scattering shoulder positions, again using equation 6.1. There was a weak and broad shoulder which might imply pre-ordering or some intermediate state at about Q = 0.033($Å^{-1}$) in the profile of the sample annealed at 200 °C for 300 seconds, the same as the annealed at 110 °C for 500 seconds. This shoulder position indicates 18 to 20 nm length scale and this was a little larger than 110 °C annealing. The crystal lamellae size of 200 °C was larger and clearer than those of 110 °C and this GI-SAXS shoulder difference interestingly this might relate to differences in the crystal size. Figure 6.4 shows ellipsometry data of samples annealed at 110 °C and 200 °C, the circles on the graphs indicate 500 seconds and 300 seconds respectively. We can see that these annealing conditions were on the plateau of the

ellipsometry graphs and the observation of shoulders at early times at 110 °C and 200 °C provides further (albeit slightly tentative) evidence of structure on the order of 10s nm before the film density has started to increase. Besides the plateau, the induction time of crystallization, at 200 °C was shorter than that of 110 °C, and it was also natural that pre-ordering of 200 °C annealing emerged quicker than 100 °C annealing. However, it is difficult to discuss crystals with Figure 6.3. Samples annealed at 200 °C had large and clear crystal lamellae, therefore there should be some strong sign of them. Actually, there seemed a peak or shoulder at about Q = 0.015($Å^{-1}$) in the crystallized sample, for example 1 hour, as same as Q = 0.018($Å^{-1}$) in the crystallized samples annealed at 110 °C. But the shoulder also emerged on the graph of the sample annealed for 120 seconds in Figure 6.3. It seems to need much more data and careful discussions for what a peak or shoulder at about Q = 0.015($Å^{-1}$) or 0.018($Å^{-1}$) indicates and how crystal lamellae of thin PET films are described in GI-SAXS. The 15 nm quoted in Figure 6.3 and 18 - 20 nm in Figure 6.4 are from a single sample, so these are tentative rather than robust length scales, not yet tested reproducibly.

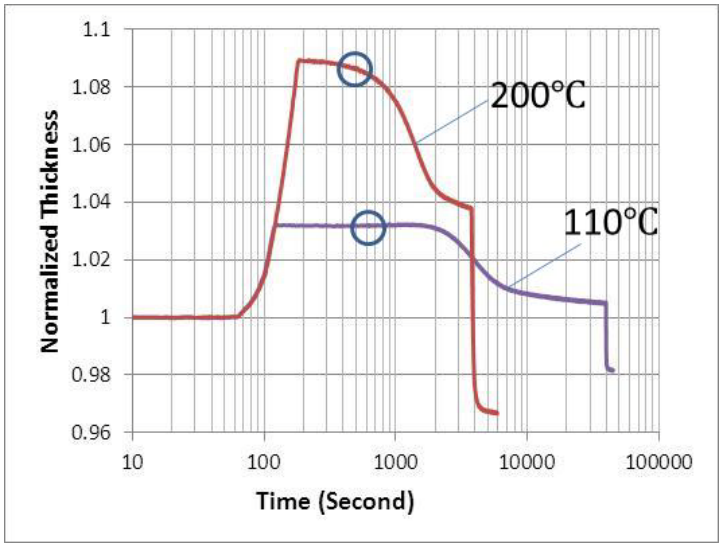

Figure 6.4: Thickness changing profiles of 150 nm thickness PET films annealed at 110 °C and 200 °C measured by ellipsometry. The intermediate state, pre-ordering, was observed by GI-SAXS during the induction time as blue circles in the figure.

Although there was no GI-SAXS data taken for the samples annealed at 90 °C because of experimental time limitations at the synchrotron facility, it is imaginable that there should be a peak or a shoulder of pre-ordering during the induction time, the same

as at 110 °C. I say this because the AFM images and analysis shown in Chapter 5 revealed that the crystallization process at 90 °C was similar to that of 110 °C although the time scales were definitely different. The Power Spectral Density analysis shown in the next section, Chapter 6.3, supports this conclusion to some extent.

6.3 Discussion for the validity of scale of pre-ordering

Next, I would like to discuss the length scale of the intermediate state, pre-ordering, with quantitative AFM image analysis. In this chapter, 6.3, I estimate the length scale of domains in the intermediate state with PSD (Power Spectral Density), calculated from the AFM images. This analysis method is a popular procedure for studies of materials, probing particle or domain length scale size and distribution. Figure 6.5 shows a typical application of this method to polymer materials, a PC/PMMA polymer alloy [131]. PSD can address the scaling behaviour of the surface roughness using AFM images. AFM directly provides the surface topography on a wide range of spatial lengths, on the other hand, PSD analysis allows us to determine the contribution to the surface topography from different spatial frequencies and yields the scaling exponents. The two-dimensional PSD of the Fourier transform of the topography h(x, y) is defined in Equation 6.2.

$$\mathrm{PSD}(f_x f_y) = \frac{1}{L^2}\left|\int_0^L \int_0^L e^{i2\pi f_x} e^{i2\pi f_y y}[h(x,y) - \bar{h}]\,dx\,dy\right|^2 \qquad (6.2)$$

where L is the image size, f_x and f_y are the frequencies along the x and y axes, and $\bar{h}$ is the mean height. The relevant spatial frequency range lies between the inverse image size (1/L) and the high-frequency limit f_{max}) N/2L (the Nyquist frequency), where N is the number of pixels per scan line.

By transforming Equation 6.2 into polar coordinates (r, θ) and by averaging over θ, the PSD can be expressed as a function of radial frequencies f to yield the radial PSD (Equation 6.3): Compared to 2D(two-dimensional)-PSD, the radial PSD, also called 2D isotropic PSD, is a more rigorous tool for the scaling analysis of anisotropic surfaces [132].

$$PSD(f) = \frac{1}{2\pi}\int_0^{2\pi} d\theta \; PSD(f,\theta) \qquad (6.3)$$

A self-affine surface exhibits a power-law decay ($PSD(f) \approx f^{-\gamma}$) over a finite range of f. The roughness scaling exponent α is related to γ by $\gamma = 2(1+\alpha)$. From the Wiener-Kinchine theorem (Equation 6.4), the integrated PSD yields the surface RMS roughness(σ) versus scale length r:

$$\sigma(r) = \left[\int_{1/r}^{f_{max}} PSD(f) f \, df\right]^{1/2} \qquad (6.4)$$

Here, the PSD analysis of the AFM images was carried out to quantify both the evolution of the average domain size and the surface roughness as a function of the annealing parameters and to provide information on the growth mechanism. Practically, 2D isotropic PSD spectra were taken on a representative set of AFM pictures of the annealed samples and then averaged. Figure 6.5 shows a typical example of PSD analysis and we can see that this is a very useful tool for quantitative analysis of domains in a polymer material from AFM images.

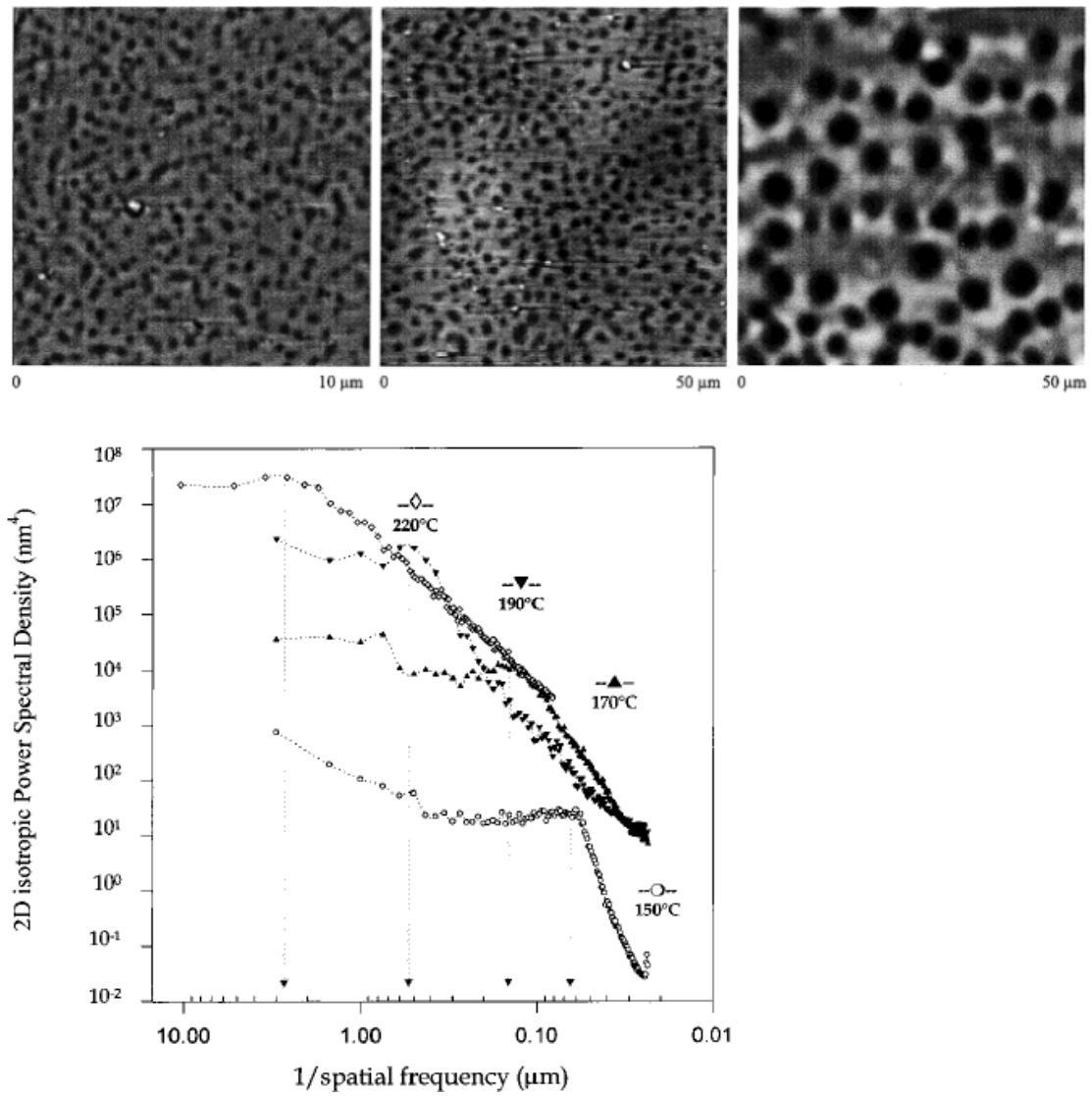

Figure 6.5: A study from the literature using PSD for analysis of the size and frequency of domains in a polymer material(PC/PMMA)[131]. Upper: AFM topographic images of PC/PMMA 50/50 blends annealed for 20 min at 190 °C (left), 210 °C (centre), and 220 °C (right). The vertical scale is 40, 300, and 300 nm, respectively. Lower: 2D-isotropic PSD curves of 3 ×µm3 ^{2} AFM images of PC/PMMA 50/50 blends annealed for 20 min at increasing temperatures (Open circles: 150 °C. Triangles: 170 °C. Inverted triangles: 190 °C. Diamonds: 220 °C.). The arrows indicate the estimate of the correlation length.

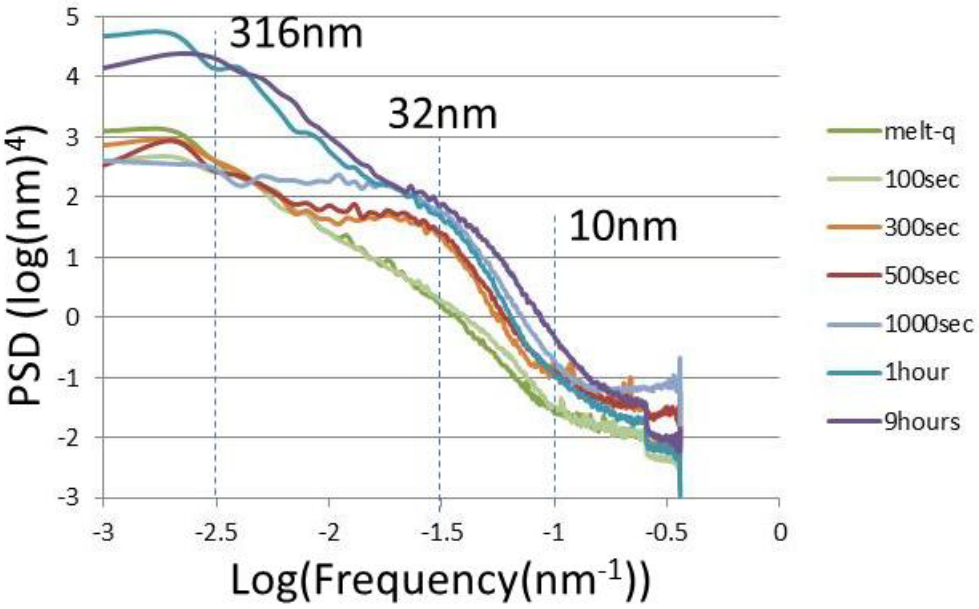

Figure 6.6: PSD analysis of 150 nm thickness PET films annealed at 110 °C. Samples were not annealed(Melt-quenched), annealed for 100 seconds, 300 seconds, 500 seconds, 1000 seconds, 1 hour(3600 seconds), and 9 hours. These PSD curves were calculated from the actual AFM images shown in Figure 5.12.

Figure 6.6 shows PSD analysis of 150 nm thickness PET films annealed at 110 °C. Samples were not annealed(Melt-quenched), annealed for 100 seconds, 300 seconds, 500 seconds, 1000 seconds, 1 hour(3600 seconds), and 9 hours. For the samples it is assumed that not annealed and annealed for 100 seconds samples were amorphous, and samples annealed for 300 seconds, 500 seconds, and 1000 seconds were in the intermediate state, and the samples annealed for 1 hour and 9 hours were crystallized. These PSD curves were calculated from the actual AFM images shown in Figure 5.12. The spatial frequency is plotted on the x-axis in Figure 6.6 and 6.7 and is 1/r, where r is the scale length. The typical radius of curvature of the AFM tips in this study is 8 nm.

The PSD gives the relative strength of each roughness component of a surface micro structures a function of spatial frequency [133]. The height and location of the "bump" in the PSD curve quantifies the surface micro-structure of thin film sample at a particular spatial frequency, for example, if the bump height is reduced, it indicates that the surface has a smoother structure, while if the bump is shifted further out in spatial frequency, it indicates the surface is growing with structures of smaller size [134]. According to the usual way of understanding these PSD profiles, if the surface

roughness, for example the RMS, becomes large, the slope of graph also becomes large [131, 132]. And if there is a shoulder or a peak at a frequency f (nm^{-1}), it indicates that there should be particles or domains whose size is around 1/f (nm) mainly. In Figure 6.6, profiles of amorphous samples were flat and this indicates that there were no clear particles or domains in these samples. In the profiles of the intermediate state, the shoulder rose up from around Log (f) = -1 and peaked out at around -1.6. This indicates that the number of particles or domains which size were above 10 nm increased, and major size of them should be about 15 to 30 nm. This corresponds well to GI-SAXS pre-ordering shoulder at around Q = 0.04($Å^{-1}$) indicating a length scale around 15 nm. Then, in the profiles of the crystallized samples, slope of the graphs became larger at all length scales. This should indicate that there are a lot of small and large particles, or domains and surface roughness became larger than others. PSD analysis is a numerical manipulation and representation of the AFM images, therefore, it is natural that this PSD profile correspond to features of AFM images. But it is very valuable that we can consider and discuss surface texture much more quantitatively and simply than from just images. For example, we can realize that there are three stages, amorphous, intermediate state, and crystalline, in PET thin film crystallization very clearly, as shown in Figure 6.6.

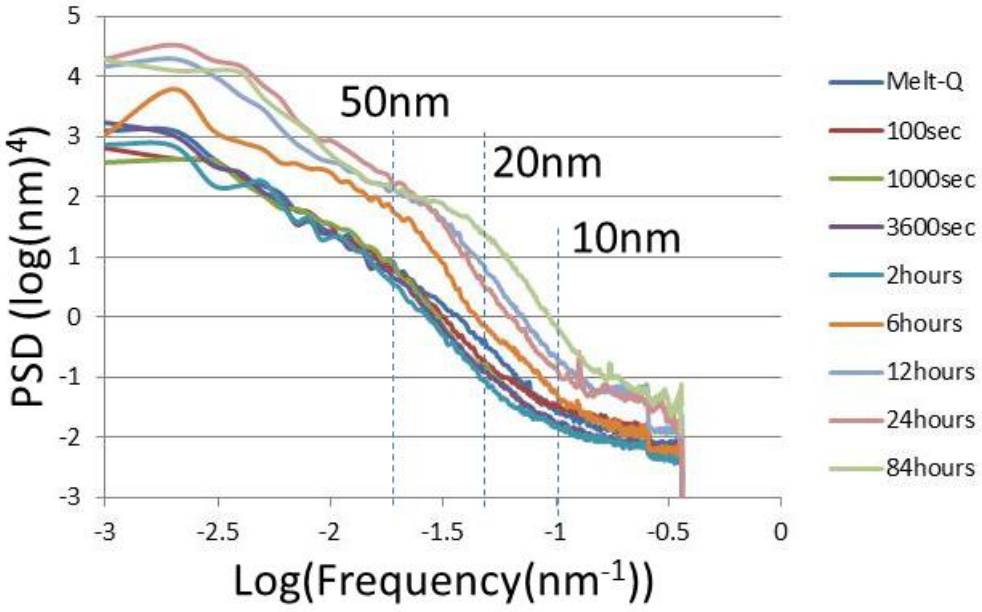

Figure 6.7: PSD analysis for 150 nm thickness PET films annealed at 90 °C. Samples were not annealed(Melt-quenched), annealed for 100 seconds, 1000 seconds, 1

hour(3600 seconds), 2, 6, 12, 24, and 84 hours. These PSD curves were calculated from the actual AFM images shown in Figure 5.20.

Figure 6.7 shows PSD profiles of samples of 150nm thickness annealed at 90 °C. Samples were not annealed(Melt-quenched), annealed for 100 seconds, 1000 seconds, 1 hour(3600 seconds), 2, 6, 12, 24, and 84 hours. In this figure, a pre-ordering shoulder corresponding to 500 seconds annealed at 110 °C emerged at 6 hours (solid orange line). This should be a quantitative recognition that low temperature annealing causes longer induction times and much slower pre-ordering dynamics, as shown in Chapter 5 by AFM images. However, there was a difference between 90 °C and 110 °C annealing. A shoulder of this intermediate state was around Log(f) = -1.7 or -1.8. This indicates that texture size of intermediate state of 90 °C was around 50 nm. It seems a little larger than that of 110 °C (15-30 nm). On the other hand, 90 °C annealed crystal size was smaller than 110 °C as shown in Chapter 5. PSD analysis also shows that a shoulder of crystallized sample, 84 hours annealed, is shifted to Log(f) = -1.4 or -1.3. This indicates crystal size is about 20 nm. A shoulder of 9 hours annealed at 110 °C is around -1.5 or -1.4, hence crystal size should be 25 - 30 nm. Basically, the crystallization process was similar for 90 °C and 110 °C but their time scales were quite different and length scales of the textures were a little different. However, I would like to refer to Figure 6.7, which shows the effect much less clearly than Figure 6.6, even though the images show similar behaviour. To check the reproducibility of this feature will be important future work.

Here, I would like to discuss what is a length scale calculated and observed by PSD and SAXS. PSD is calculated from AFM data and a length scale observed by AFM is related to roughness of surface texture, that is, distances between a peak and another peak of height information. What this surface texture is indicating was discussed in Chapter 5. Surfaces of amorphous samples were very flat and there is no texture, very much like a liquid surface, on the other hand, the surface of crystal samples had the texture of lamellae, and there were some kind of weak texture of pre-ordering on the surface of intermediate state samples. It is believed that pre-ordering was generated from the fluctuating density of molecules, like a spinodal decomposition, as reported by Imai and Olmsted *et al.* as mentioned in Chapter 6.1. This fluctuation of density is changed from homogeneous amorphous matrix, that is, the homogeneous matrix is separated to the dense parts and the dilute parts, then, this fluctuation makes surface unevenness or bumpiness. The AFM analysis in this study discussed in Chapter 5 s observed this texture as pre-ordering. On the other hand, SAXS observes diffraction or

scattering of X-rays, and this is caused by the density of electron distribution, that is, SAXS detects the structure or texture caused by regularity of molecules or density of samples in polymer materials. Imai et al used SAXS to detect pre-ordering because the length scale of the regular spacing or distance between dense parts and dilute parts were larger than the regularity of crystals and so WAXS could not detect it. Probably, both the length scale estimated by AFM, calculated by PSD, and the length scale detected by SAXS were the regular spacing or distance between dense parts and dilute parts. However, AFM investigates only just the sample surface, but SAXS or GI-SAXS bring information from the whole of the bulk or thin film. If there were some differences from those two analysis measurements, it might come from these technical differences in the way they sample the surface information.

The length scale of intermediate state texture given by GI-SAXS was around 15 nm at 110 °C but given by PSD was 15 to 30 nm, that is, values from the PSD analysis seem a little larger than GI-SAXS measurements. I think it was reasonable correspondence and there is a possibility of good reason for this.

Images from AFM sample only surface information, as described above, and the strong surface effects in thin films might influence the particle or domain size of any pre-ordering. Surfaces would promote molecule alignment and change the overall free energy condition of the molecules. If pre-ordering is caused by a spinodal-like decomposition from the amorphous state, its length scale should be determined by the depth of quench from spinodal temperature [135], and it would be changed by the free energy condition: for example, if the spinodal temperature was changed, the depth of quench should be also changed. One possible reason why we can discuss the depth of quench of spinodal decomposition in this problem is that it might be the same effect of low temperature annealing. The amorphous sample in this study were made by a quench from a temperature some way above the melting point to room temperature and so molecules are frozen immediately. If these samples are annealed at low temperature, but a little above T_g, pre-ordering or crystallization would occur and this situation should be similar to a large depth of quench in spinodal decomposition. Figure 6.8 shows a schematic image of the surface roughness changing from that of a very flat liquid like amorphous PET thin film (a) to the fully crystallized film (c) via the intermediate state (b). Coloured parts in (b) are dense parts separated from the lower density amorphous matrix. The values λ_1 and λ_2 indicate the distances of each dilute part of surface and the dense part of inside of thin film sample. λ_1 is directly indicating the distance of dilute part, however, if there are dilute parts isotropically and uniformly, λ_1 should be also indicating the distance of each dense parts of surface. Stripe structures in (c) indicate

crystal lamellae. “Unevenness” indicates the surface roughness observed by AFM as a whole range of length scales from the height images. We can see that the unevenness of the sample surface became large as crystallization progressed.

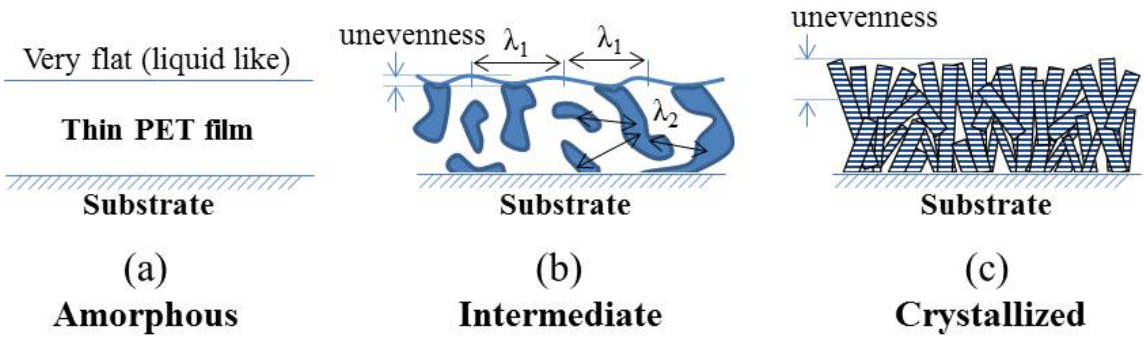

Figure 6.8: The schematic image of surface roughness changing from the very flat liquid like amorphous thin PET film (a) to the fully crystallized film (c) via the intermediate state(b). Coloured parts in (b) are dense parts separated from amorphous matrix. λ_1 and λ_2 indicate the distances of each dilute part of surface and dense part of inside of thin film sample. Stripe structures in (c) indicate crystal lamellae. “unevenness” indicates surface roughness observed by AFM as whole range scale of height images.

The thin PET film represented in Figure 6.8 (a) is an amorphous sample with a homogeneous and very flat layer surface, almost without roughness, like a liquid surface. In the case of the intermediate state there were dense parts and dilute parts. These structures were separated from each other like a spinodally decomposed state from the amorphous matrix, and the differences of these textures caused slight unevenness of surface. In the crystallized sample, the height scale range of crystal lamellae, that is, sharp edges between top and bottom, were large and very rough. This scheme was described by AFM analysis shown in Chapter 5. The texture length scale observed by AFM and GI-SAXS are λ_1 and λ_2 shown in (b). As described above, if the frequency of dense parts at the surface is different from that of inside of thin film sample, λ_1 seems to be measured as larger than λ_2.

The T_g at a surface is normally lower than in the bulk of the film because surfaces should behave as a free wall to molecule mobility, and this non-constraining side would induce a factor of disorder or ordering of molecules and change the free energy related to crystallization of its system. And temperature is the most important parameter on the phase diagram, so a phase diagram describing spinodal decomposition might be affected by surface effect and differences in the annealing temperature. I will discuss this kind of surface effect in Chapter 7 again.

6.4 Discussion for observed pre-ordering with the theories from past studies.

Next, I would like to consider and discuss my data concerning pre-ordering with theories and past studies about texture, length scale, and kinetics. I detailed my data in Chapter 5, 6.2, and Chapter 6.3, however here I put it in context with previous work in order to further understand the pre-ordering in detail. Of course, it may be better to have further data with many more annealing temperatures and annealing time in order to discuss the phase diagram or the detailed length scale of structure of thin films. I will leave this to future work, and here will discuss and focus on the theory and its relation to my results.

Olmsted *et al.* suggested that, in semicrystalline polymers, for example PET or PP, a dense/ dilute spinodal like phase separation should occur during the induction time as a pre-ordering prior to crystallization as shown in Figure 6.9, which is a schematic image of pre-ordering in semicrystalline polymers [28]. A single phase is assumed as an initial phase before crystallization, for example fluid or amorphous, and the dense parts are assumed to be formed from pre-ordering and alignment of molecules just before crystallization. The length of D is assumed the width of the dense part, analogous to a lamellar thickness, and length of Λ is assumed to be the distance between each dense domain. This dense part indicates just pre-ordering.

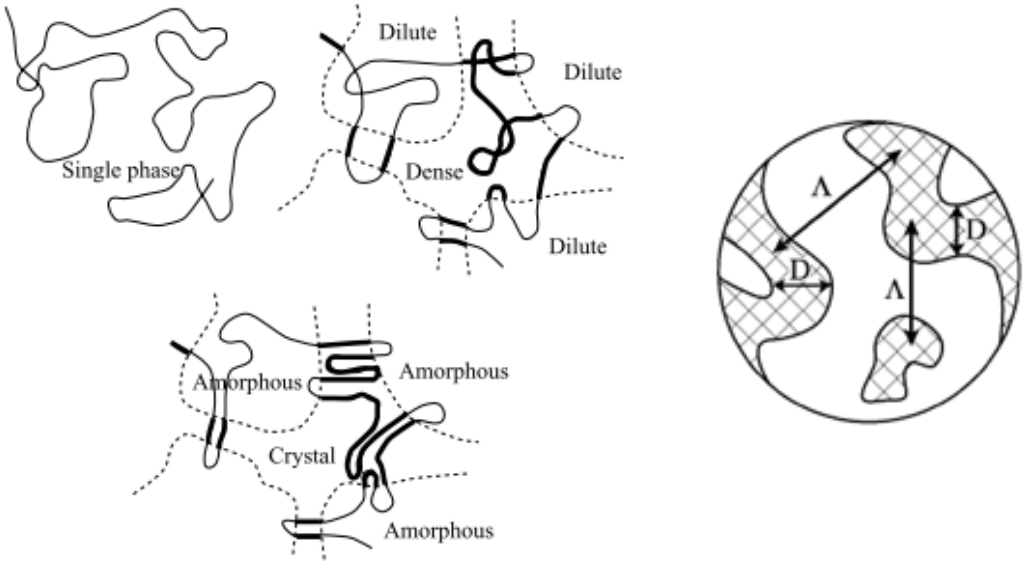

Figure 6.9: The schematic image of pre-ordering in semicrystalline polymers suggested by Olmsted *et al.*[28]. A single phase is assumed as an initial phase before crystallization, for example fluid or amorphous, and dense part is assumed as pre-ordering of molecules just before crystallization. Length of D is assumed the width of dense part like as lamellae thickness and length of Λ is assumed the distance of each dense part.

Olmsted *et al.* also discussed a phase diagram related to the schematic images shown in Figure 6.9 [28]. In low temperature crystallization, under T_s (the spinodal temperature) like in a model equilibrium phase diagram shown as Figure 6.10, dense/dilute phase separation induces nucleation or crystallization, and this takes place at a lower energy barrier than in the original melt phase.

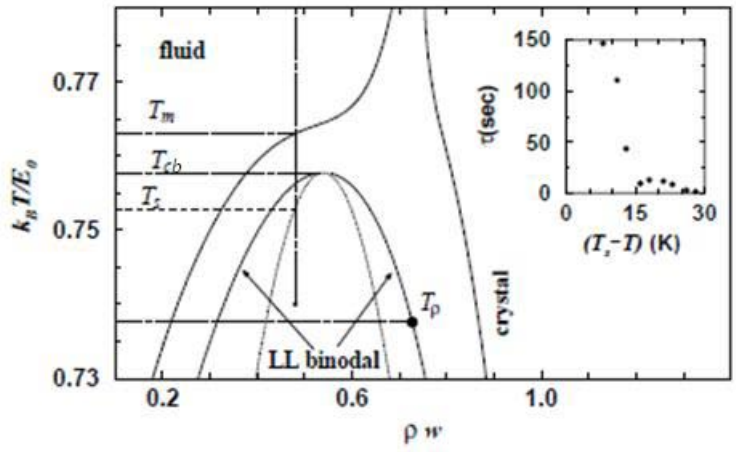

Figure 6.10: The model phase diagram suggested by Olmsted *et al.*[28]. T_m is the melting point, T_{cb} is critical temperature for binodal separation of fluid (or amorphous) and crystal, and T_s is spinodal temperature for spinodal decomposition of binodal separation.

Of course, I don't think that this phase diagram can be applied directly, however, to discuss my data from the view point of this phase diagram might be helpful to us in considering this kind of problem. T_{cb} (critical temperature), T_s, or T_s-15K (Olmsted *at el.* estimated that the relaxation time for pre-ordering τ should be the minimum at around T_s-15K) of PET in a phase diagram like as Figure 6.10 might be around 160 °C. I say this because 160 °C was a some kind of threshold temperature from our ellipsometry data and AFM analysis discussed in Chapter 5. The induction time became shorter at higher temperature up to 160 °C. At 160 °C, the induction time became ambiguous, and then at 200 °C, the induction time became longer again. The temperature of 160 °C seems to be the optimum temperature for crystallization and this seems to be some kind of a threshold between low and high temperature crystallization. This indicates that the mechanism controlling the induction time should change as a function of temperature. One possible explanation for this could be to do with the thermodynamics of the hypothetical buried spinodal transition. For example, if the sample was annealed below this threshold temperature, the intermediate state would arise through spinodal decomposition; that is, the threshold temperature would be identical to the spinodal temperature T_s in Figure 6.11. On the other hand, if the sample was annealed above the threshold temperature, for example 200 °C, either there would be no intermediate state, or if there were an intermediate state, it would have resulted

not from spinodal decomposition but from some other mechanism (as Kaji *et al*. have suggested [129]).

For low temperature crystallization, 90－110 °C showed in Figure 5.11, 5.12, and 5.20, the length scale of intermediate spinodal decomposition texture was similar to that of crystal lamella. These AFM images provide evidence indicating that there is an intermediate state, and that this might be pre-ordering. This also would be related to the paper of Olmsted *et al*, which argues that the length scale of the intermediate spinodal texture determines thickness of the first crystal lamella. The length scale of crystals of a thin PET film annealed for 1000 seconds at 110 °C in Figure 6.6 is similar to the length scale of pre-ordering annealed for 500 seconds. If the crystal in 1000 seconds is the first crystal lamella, an insistence of Olmsted *et al* seems to be right. This PSD analysis and especially AFM images shown in Chapter 5 might be evidence that the length scale of the intermediate state affects the crystallization morphology directly.

From the theory that the depth of quench determines the length scale of spinodal decomposition (for example, Ohnaga *et al.*[135]), the length scale of pre-ordering is greater at higher temperature. However, in my data, an inversion of this trend was observed as Figure 6.6 and 6.7, that is, the length scale of pre-ordering in the sample annealed at 90 °C, estimated by PSD, was larger than that of at 110 °C. A possible reason for this is that the temperature dependence of the length scale of pre-ordering might be not so strong in PET because of the strong interaction between benzene rings and rigidity of main chain. Therefore molecular mobility might be not be enough to move for separating clearly and a peak of pre-ordering became ambiguous, not a peak but just a shoulder, as Figure 6.7, then that shoulder looked as if shifted to small Q, indicating larger length scales.

At 200 °C annealing, there was a broad and subtle pre-ordering shoulder in my GI-SAXS data, shown in Figure 6.3. This weak shoulder seemed shifted to slightly smaller Q from the shoulder of 110 °C annealing (Figure 6.2) and indicates that the length scale became larger than for annealing at 110 °C. If there were really a peak or shoulder indicating pre-ordering at 200 °C annealing, although for the spinodal decomposition theory described above, the mechanism and factor of that intermediate state might be different from those of low temperature below the threshold like temperature, for example, 90-110 °C annealed samples as mentioned in the previous page. This is because the pre-ordering which Olmsted and Imai *et al*. proposed was for low temperature, and 200 °C should be above such a threshold temperature (it is very close to T_s (~213 ºC). Further data is needed to for various annealing temperatures in order to discuss the length scale of pre-ordering in detail, especially around the

threshold temperature, 160 °C. However, at this point it is enough to say that my data implies there might be another kind of intermediate state at higher temperature annealing, but I cannot say what kind of structure of it with my data so far. Therefore I would like to leave it for future work.

In the study of Olmsted *et al*, induction time is expressed as τ_i in the equation below, (6.5). Because the dependence of τ_s on temperature is small, we can see that induction time is longer at lower temperature. Here, τ_s is the time to reach an intermediate spinodal texture. This corresponds to my data and it is very understandable in the sense of temperature and its effect on the molecular mobility.

$$\tau_i \sim \tau_s + \text{const} \times e^{\Delta(T,\bar{\rho})/k_B T} \qquad (6.5)$$

Here, $\Delta(T, \bar{\rho})$ is the energy barrier of the conformation to the crystal phase from the melt. If the scheme of pre-ordering is as figure 6.9, the kinetics of phase separation would be dominated by molecule mobility, as in the equation above. My data clarified quantitatively that the length scale of pre-ordering in thin PET films was similar to that of bulk shown in literature, for example measured by Imai *et al.*[54], but the kinetics were quite different. The reason why the kinetics are different could be the thin film effect on molecular mobility. A detailed discussion of this is presented in Chapter 7.

However, I think that we need to consider the relationship of length scale of pre-ordering texture and crystal lamella thickness carefully. Olmsted *et al*. say that the final length scale of pre-ordering texture controls the thickness of the first crystal lamella. In my data, the length scales of intermediate texture were not so different (maybe a little different) for different temperatures, however, the lamella sizes of 90 ºC, 110 ºC, 160 ºC, and 200 ºC were very different from each other as shown in Figure 5.16. The lamellae size was estimated by the peak to peak distance in the cross sectional images. The mean values of the lamellae size were calculated from the length of the line divided by the number of peaks with 3 different lines and the mean values of 90 ºC, 110 ºC, 160 ºC, and 200 ºC were 21, 24, 33, and 42 nm respectively. Dispersion of the values were between 10 % and 15 %. Of course, these were not initial crystal lamella, rather near final thickness, and it is clear that annealing temperature determines the final lamella thickness from the many past studies which find lamellae to be thicker at higher temperature and thinner at lower temperature, as seen as in my study.

The length scale of intermediate state in samples annealed at 90 °C was larger than that of 110 °C but the crystal lamella size annealed at 90 °C was a little smaller than at 110 °C. This inversion of the length scale and size might be caused by differences in the mechanism of pre-ordering being different from that of crystallization.

Formation of spinodal decomposition should have no preferred direction and the length scale is determined by the depth of quench from the spinodal temperature. On the other hand, growth of crystal lamellae is along a straight line with adsorption of molecules as the lamellae thickness becomes larger at higher temperature, so we cannot compare these phenomena to each other easily. However, for thin polymer film materials my data show crystallization, where the growth of lamellae has a strong dependence on temperature, both lamellae size and growth kinetics. Also the kinetics of the intermediate state also has a strong dependence of temperature, whilst the length scale does not have such a clear dependence or trend with temperature. In order to discuss the phase diagram and the length scale of pre-ordering and crystal lamellae, we would need further detailed data and considerations as a future work. Besides, the phase diagram is basically described under condition of equilibrium, although experiments in this study are principally concerned with kinetics.

Chapter 7

General Discussion : Comparison of thin films and bulk

In this chapter, I would like to focus on discussing the differences in crystallization and pre-ordering between bulk and thin films of PET, with the detailed kinetics data measured using ellipsometry. The origin of the differences between the two geometries is that the surface area for a thin film is much larger than for the bulk, therefore effects from the surface and substrate strongly affect the kinetics of crystallization and pre-ordering. I will show a quantitative estimation of the surface effect and how thin films are different from the bulk.

7.1 Kinetics of induction time

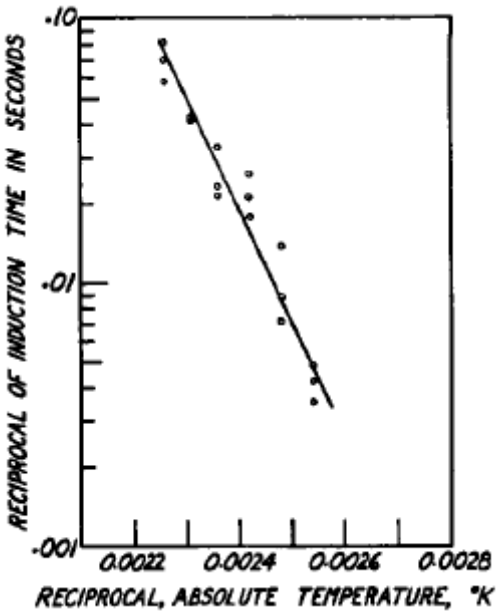

Figure7.1: Plot for evaluation of the activation energy for diffusion of chain segments in polyethylene terephthalate resulting in the value 20 kcal/mole [136].

First of all, I would like to explain how to compare various induction times. An old study from the 1950's by Cobbs *et al.* is a systematic study of PET crystallization [136]. Figure 7.1 indicates a graph of reciprocal absolute temperature vs logarithm of reciprocal of induction time. With this graph, we can compare values of the induction time and activation energy of diffusion for completing the induction time. The activation energy is calculated from Arrhenius plots. This paper says that "if the temperature is suddenly raised on such a quenched sample (amorphous, thickness is 24 μm) to some point between T and T_m, time is required for the embryos to alter and reach critical size at this new temperature. During such an induction or incubation period embryos alter in size by short-range diffusion of chain segments." This situation is very similar to my study. It also says that "a straight line with slope giving an activation energy for the diffusion of 20 kcal/mole of segments." We can make good use of this data for evaluation and comparison of the induction times measured by ellipsometry.

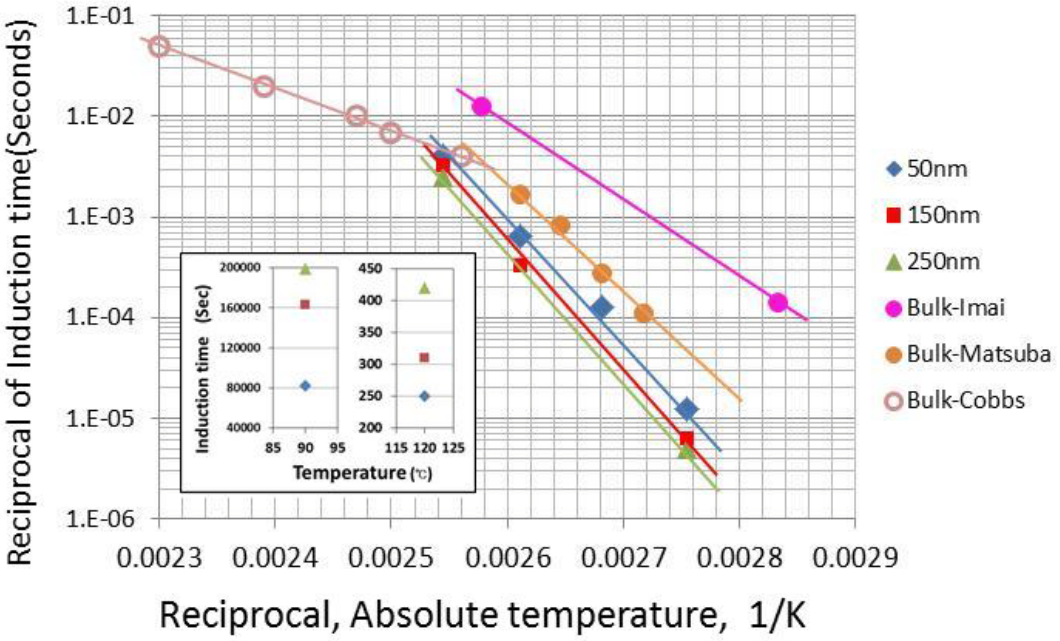

Figure 7.2; The relationship between temperature and induction time measured by ellipsometry in this study for various film thicknesses and bulk samples reported by the following references, “Bulk-Imai” [26, 27], “Bulk-Matsuba” [137], and “Bulk-Cobbs” [136]. 250 nm, 90 °C data point (extracted from Figure 5.6) is a lower bound. The 50 nm induction times displayed here at the lower 2 temperatures are found from the later step in the 2-step process observed at 90 and 100 °C. Inset window shows the linear axes of the induction time and temperature in order to see that the induction time of 50 nm was shorter than 150 and 250 nm clearly.

Figure 7.2 is the same type of graph as Figure 7.1 but is a composite of the thin film data from our ellipsometry measurements and bulk data from past studies, “Bulk-Imai”[26, 27], “Bulk-Matsuba”[137], and “Bulk-Cobbs”[136]. The induction times of the thin films (50 nm, 150 nm and 250 nm) were similar to each other. Induction times of bulk samples were different as measured in each paper from each reference papers, but were either similar to or longer than the values for the thin films in this study. The slopes of the bulk datasets were also the similar to or smaller than those of thin films. Because Cobbs’s study is focused at higher temperatures, from 120 °C to 240 °C, its slope is different from the lower temperature crystallization studies of Imai, Matsuba, and my study. However, there is an optimum temperature for crystallization

and the induction time disappears above that temperature, which is 170 °C in Cobbs's study. It is interesting that this is very similar to our ellipsometry data (in Chapter 5).

The gradients for the data of Cobbs, Imai, Matsuba, and this work on thin films in Figure 7.2 take values of about 20, 35, 51, and 58 kcal / mole respectively. The dispersion of my data was estimated to be about ± 3 kcal / mole. We can see that thin films have higher or at least the same activation energy to complete their induction time compared with the bulk. This activation energy indicates the energy for diffusion of polymer chain segments, that is, the movement of molecules for pre-ordering and nucleation. I believe that this implies that molecules in thin films are energetically harder to move and rearrange for crystallization including pre-ordering and nucleation. Here, I would like to call it the "confinement effect". This kind of confinement effect related to the kinetics and effectiveness of crystallization is shown in many reports [39, 46, 138, 139, 140, 141, and 142], for example, the crystallization rate in thin films is slower than the bulk because molecular movement is confined by the constrained space. This confine effect is discussed later.

The induction time is in total the combined time of pre-ordering and nucleation. As we discussed in Chapter 6 with GI-SAXS and AFM data, pre-ordering and nucleation occur during the induction time. These processes should progress efficiently if molecular diffusion takes place easily, that is, if the molecular mobility is high. Therefore, it is natural that the induction time for the bulk is short compared to thin film and proceeds efficiently with a small activation energy for diffusion. However, we need to pay attention to one more important feature in thin films, that is, the surface effect. In the vicinity of the surface, T_g decreases and molecular mobility increases [51, 60, 87], as a result, the crystallization rate and degree increase.

In our study, there was an aspect which could not be explained without this kind of surface effect.

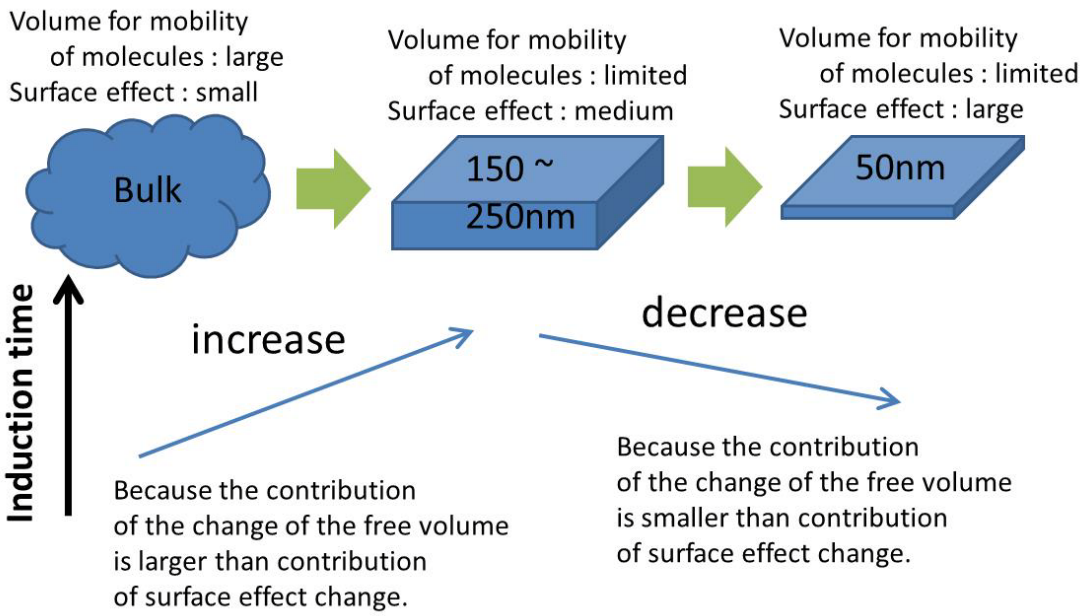

Figure 7.3: A schematic diagram detailing the physical mechanisms that alters the induction time from bulk to thin films.

My ellipsometry data showed that thin PET films have longer induction times than bulk PET reported in previous studies. However, the150 ~ 250 nm thickness films had longer induction time than the 50 nm thickness films. Interestingly, the change of induction time was not monotonic with sample thickness change. Therefore, I suggest a schematic sketch model to explain the differences in induction time from bulk to thin films as in Figure 7.3. In my estimation, the reason for the increase in induction time in going from the bulk to 150~250 nm thickness should be the confinement effect and the reason for the decreasing induction time from 150~250 nm thickness to 50 nm thickness is the surface effect. The confinement effect is reported by many studies of crystallization in thin polymer films and typically considered as the limitation of the direction of crystal lamellae growth or chain conformation in nucleation [for example, 138]. The thickness of lamellae is usually tens of nm and these can freely grow in any direction in bulk. But in thin films, for example under 1 μm, lamellae growth is limited to the in-plane direction (parallel to substrate), so molecules moving to join the edge of lamellae are hindered. In much thinner films, for example under tens of nm, changes in the chain conformation of molecules is limited by bulky parts of chain such benzene units. In thin films, basically, molecules should be limited to move because of narrow space and strong confinement due to the substrate, then diffusion of molecule is confined, and as a result, the rates of pre-ordering and nucleation should be slower than

bulk. However, in much thinner films, the surface effect cannot be ignored, and 50 nm is thin enough to observe this effect. Surface effects should contribute to an increase in molecule mobility, for example decreasing T_g, this is why induction time of 50 nm was shorter than 150~250 nm as shown in Figure 7.2.

At surfaces, besides decreasing T_g, the nucleation mechanism may be different from the bulk. That is, homogeneous nucleation mainly occurs at the surface and heterogeneous nucleation is dominant in the bulk, and the homogeneous nucleation rate is higher than the heterogeneous nucleation rate at low temperature. Heterogeneous nucleation occurs at interfaces, for example with impurities such as nucleation agents, and homogeneous nucleation does not need an interface and occurs spontaneously within the bulk. Whilst at high temperatures, the heterogeneous nucleation rate is higher than the homogeneous nucleation rate [138]. Because the nucleation rate of heterogeneous nucleation depends on purity of the sample and temperature, I can't say which nucleation mechanism is dominant in thin films but it seems that the induction time decreases at surfaces especially at lower temperatures.

And, as described in Chapter 4, Rueda *et al.* reported that amorphous PET samples aged for 40 days storage showed a higher degree of internal order, i.e., containing a higher level of "embryonic" ordered nanoregions during crystallization. In these samples which have a higher degree of internal order, the induction time was shortened, however, the crystallization rate became slower than for the not ordered samples at the later crystallization, although both had the same final degree of crystallinity [123]. This can be explained as follows. Although ordered molecules are advantageous for pre-ordering, ordered molecules must be rearranged for absorption of them by the growing crystal lamellae and this would take longer time than entirely disordered molecules, as ordered molecules should be confined to some extent by interactions from the surrounding molecules. This mechanism might be related to the result that the induction time of 50 nm thickness samples were longer than those of the 150 and 250 nm thickness samples as shown in Figure 7.2, although the induction time for the bulk was shorter than those for thin films. That is, the tiny volume in thin films confines the mobility of molecules and this makes the induction time longer than that of bulk samples, but, in much thinner films like 50 nm, there are not so many degrees of freedom for molecules and this situation is similar to "ordered molecules", then the induction time of such a thin film samples might be shorter again as reported by Rueda *et al*. And, the air-film surface should behave as "a free wall", therefore molecular movement might be not so slow and crystallization progresses faster. This is a very interesting feature of crystallization in thin films with the surface effect.

However, the surface effect may not to be as simple as described above. There might be further complications. I would like to discuss this in detail in the next section.

7.2 One more discussion for three layers in thin films

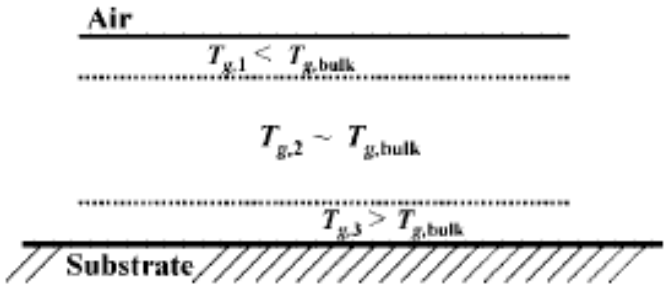

Figure 7.4: Schematic drawing of a three-layer T_g model a polymer suggested by Wang *et al* [143]. Glass transition temperatures of the surface layer, a bulk layer, and a layer near substrate are $T_{g,1}$, $T_{g,2}$, and $T_{g,3}$ respectively. The magnitude of these three T_g values follows the following pattern $T_{g,1} < T_{g,2} < T_{g,3}$.

The three layers theory shown in Figure 7.4 is suggested for considering crystallization and nucleation of thin polymer films by Wang *et al*.[143] The glass transition temperatures of a surface layer, a bulk layer, and a layer near substrate are $T_{g,1}$, $T_{g,2}$, and $T_{g,3}$ respectively. The relationship of these three T_g is that $T_{g,1} < T_{g,2} < T_{g,3}$. As mentioned above, the T_g of surface, $T_{g,1}$ in Figure 7.4, is lower than that of bulk, $T_{g,2}$ in Figure 7.4, and the thickness of that surface layer is estimated to be between 10 to 15 nm by Shinotsuka and Wang *et al.*[60, 143] and in this surface layer, the molecular mobility is higher. There is also a substrate layer, $T_{g,3}$ in Figure 7.4, distinguished from bulk. Its T_g is higher than the bulk because molecules near the substrate, the polymer interacts strongly and is pinned at this substrate interface, so molecular mobility is low. Finally, there should be an intermediate layer sandwiched between surface and substrate. Its T_g is considered similar to bulk. But actually, it should be a little different from bulk because there is confinement effect, as shown by many reports. The phenomenon which indicates that there should be a few layers in thin films was also observed in my ellipsometry data. There were two steps of induction time in 50 nm thickness annealed 90 °C as shown in Figure 7.5.

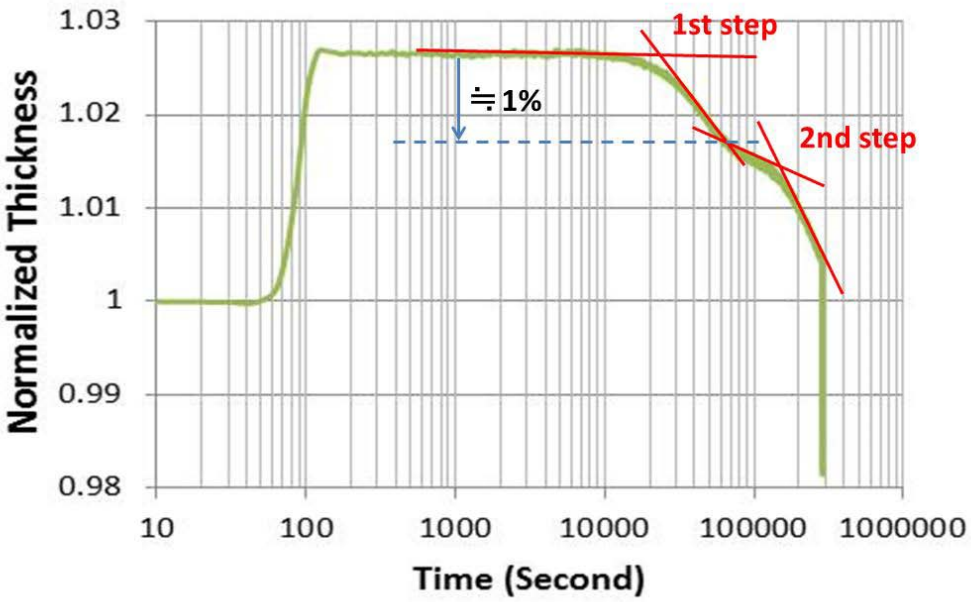

Figure 7.5: The ellipsometry data of 50 nm film thickness annealed at 90 °C. There were two steps during annealing with decrease the film thickness by the crystallization.

There are two steps during the induction time and this should indicate that there are at least two layers in having different dynamics in this film. The 1st step, the fast completion of the induction period, seems to indicate the induction time of the surface, because the T_g at the surface is lower and therefore the molecular mobility is increased. This first drop was about 1 % and this indicates that 11 % of total volume of this film was crystallized at its surface. Generally, the maximum crystal degree of PET at low temperature is about from 30 to 40% [78, 79]. Therefore, the one third of part which was able to be crystallized was crystallized at this first step. This surface layer is estimated to be about 10 to 15 nm thickness from past studies. It seems that there is good correspondence as one third of 50 nm is about 15 nm. However, this phenomenon was only observed clearly at low temperature, 90 °C, and only in the case of the 50 nm film. Figure 7.6 shows the result of annealed at 100 °C 50 nm thickness. Although there still were two steps, they became ambiguous compared with the sample annealed at 90 °C. Interestingly, the scale of the 1st drop seems nearly 1% consistent with the other result.

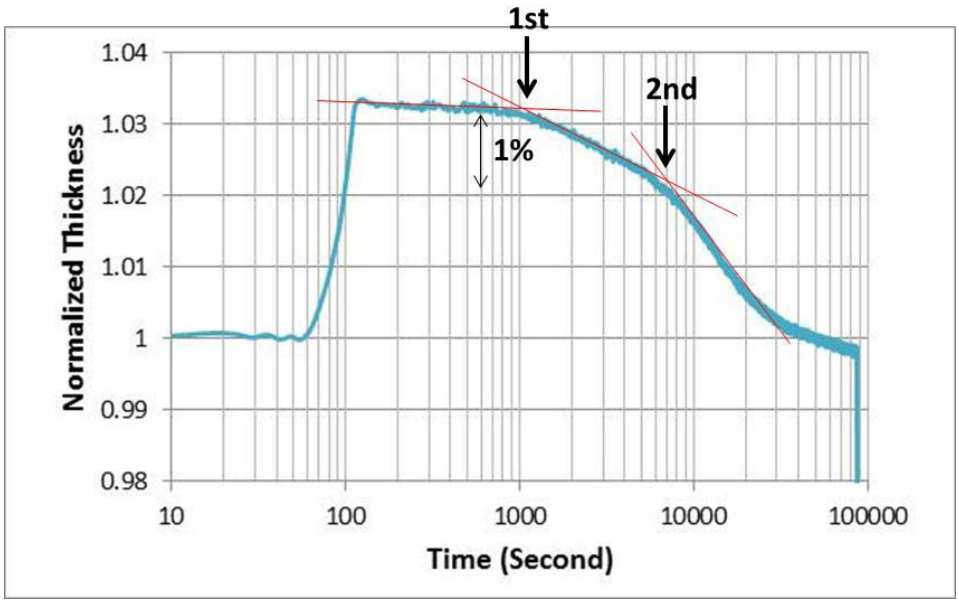

Figure 7.6: The ellipsometry data for the 50 nm film thickness sample annealed at 100 °C. There were still two steps but they become ambiguous compared with the sample annealed at 90 °C.

The reason there were two stages to the induction time which could be clearly seen in ONLY the 50 nm thickness is that 50 nm was thin enough to see an effect of the surface layer, because thinner films have larger area and volume of surface. For 150 nm or 250 nm, the ratio of surface layer should be under 5~10% of total thickness and crystallization would take place in only one third of it. The crystallization process must be dominated by an internal layer with 150~250 nm thickness. Because the surface molecular mobility should be higher than that of the intermediate and substrate layers, especially at low temperature, for example near T_g, pre-ordering would be completed quickly and homogeneous nucleation at the surface would be quicker than heterogeneous nucleation in the intermediate and substrate layers [144, 145, 146]. Therefore, the induction time at the surface should be shorter than the other layers.

Next, the reason why there were two steps of induction time clearly at 90 °C is that this particular temperature was low enough to see the crystallization kinetics in detail. At higher temperatures, pre-ordering and nucleation, and the total induction period are compressed in time and occur very quickly. There might be two steps for the sample annealed at 100 °C, but it was quite ambiguous. 100 °C seems critical, some kind of transition, temperature to see this phenomenon, I think.

There is one more interesting reason why I think 100 °C should be a critical temperature. There is a possibility that the maximum nucleation rate might be different

between surface and intermediate layer in three layered thin films. Figure 7.7 shows bell-shaped nucleation rate model suggested Wang *et al.* [143]. $T_{g,1}$, $T_{g,bulk}$, and $T_{g,3}$ are glass transition temperature of a surface layer, a bulk layer, and a layer near the substrate respectively. T_c and T_m are the temperature of the maximum nucleation rate and melting point respectively. It is generally accepted that the plot of the primary nucleation rate as a function of temperature is a bell-shaped curve with a maximum value at a temperature between T_g and T_m. This bell-shaped nucleation rate model indicates that the three-layered model can cause two steps in the induction time because a peak in nucleation rate for the surface might be offset from that of the bulk as in Figure 7.7 d. Because induction time consists of pre-ordering and nucleation, these two peaks for the maximum nucleation rate might make two steps in the induction time.

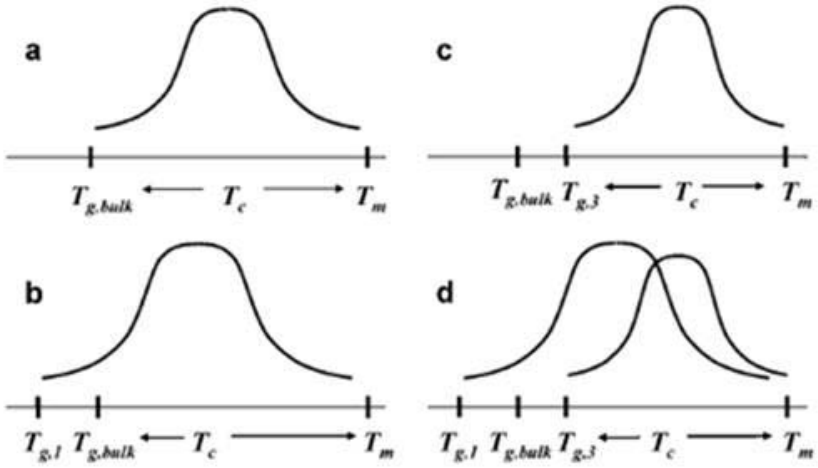

Figure 7.7: The Schematic image of "Bell-shaped curve of nucleation rate model" suggested by Wang *et al* [143]. $T_{g,1}$, $T_{g,bulk}$, and $T_{g,3}$ are glass transition temperature of a surface layer, a bulk layer, and a layer near substrate respectively. T_c and T_m are a temperature of the maximum nucleation rate and melting point.

Figure 7.8 indicates schematically why 100 °C is a critical temperature. The bulk T_m and T_g of the PET used in this study were measured by DSC as shown in Chapter 5, and those were 250 °C and 75 °C respectively. T_m at the surface should be the same or similar to that of the bulk because T_m is determined by the enthalpy of packing interaction of molecules and it should be same for both surface and bulk. However, there are some past studies reporting that T_m at the surface might be lower than that of bulk because there are some studies which report that crystal degree at very surface is low, for example, Durell *et al.*[58] or Frank *et al.*[141]. This might indicate that a

crystal at the surface is unstable or disordered compared with the bulk. Actually, there might be some influences on T_m at surface, but it seems small. On the other hand, T_g of the surface ($T_{g.s}$) is clearly different from bulk and this concrete value was suggested 48.1 °C by Shinotsuka *et al* [60]. Therefore, bell-shaped nucleation rates of surface and bulk should be shown as figure 7.8, blue line is a nucleation rate at surface and red line is bulk.

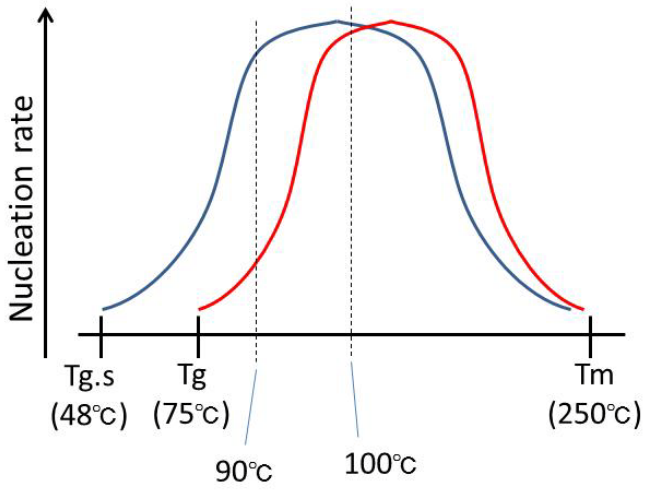

Figure 7.8: A schematic image estimating the effect of a bell-shaped nucleation rate model on the nucleation for thin PET films. Blue line is the nucleation rate at surface and red line is in the bulk.

The estimation of bell-shaped nucleation rates of a surface layer and a bulk layer are described in Figure 7.8. At 90 °C, the nucleation rate of surface is somewhat larger than that of bulk. A fast nucleation rate could make the induction time short. The point is that, even if we could not estimate the maximum nucleation rate, nucleation of the lower T_g layer starts and its peak comes earlier than others, as a result, induction times of low, intermediate, and high T_g layers would be different from each other. Therefore we can distinguish the short induction time from the surface and the later induction time from the bulk as 2 steps. At 100 °C, the nucleation rates of surface and bulk should become similar or maybe reversed. As a result, the two steps of induction time became indistinct. At much higher temperatures, 2 steps were not observed. The reason for this might be that rate of molecular motion is not slow enough to observe the induction time in detail at higher temperature, so we cannot see 2 steps well. The interesting point here is that induction time, being one of the processes of crystallization, was not observed as an average behaviour but as the contribution of each of the different layers respectively.

This is also implied by the study of Paul *et al*.[51] and Macdonald *et al.* [87] showing that the crystallization rate and crystal degree are different between surface and bulk when observed by GI-Xray scattering. Although we need some more evidence in order to show the reason why there are two steps in the induction time of 50 nm thickness film annealed at low temperature, the important point of this study is that the induction time of a surface layer is estimated quantitatively. It seems about one seventh of bulk or intermediate layer at both 90 and 100 °C.

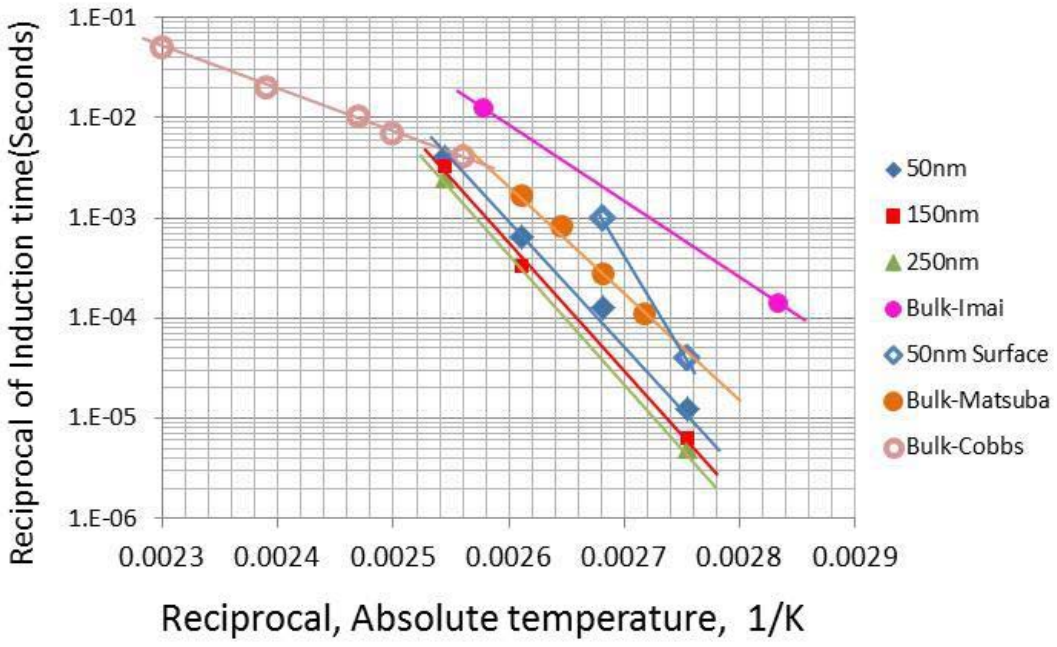

Figure 7.9: The relationship between temperature and induction time added surface induction time of 50 nm thickness. The induction time of surface is estimated from the 1st drop of Figure 7.5 and 7.6.

We can plot the induction time of the surface layer on the graph of the relationship between temperature and induction time using the 1st drop in thickness from figures 7.5 and 7.6 in Figure 7.9. The induction time of the surface was shorter than for thin films and this should indicate that the T_g of the surface layer is lower than both inner and substrate layers for the case of thin films. On the other hand, the gradient for these plots was quite large. I don't have any clear answers to explain this but it seems that this is not only from the molecular mobility by the diffusion of polymer molecule segments but it also strongly influences the conformation and interaction of molecules. In order to

discuss this problem further, we needs much more low temperature thermal annealing data. I would like to leave this interesting problem for future studies.

7.3 Summary for comparison of thin film and bulk

Properties between thin films and the bulk derived from this study and past studies are summarized in Table 7.1. This shows the essence of what I have discussed in this chapter. Characters shown in this table from (a) to (g) are indicative evidence for the reason for each cell as listed below the table.

Table7.1: Properties and features of thin films and bulk discussed in this study.

		Induction time			Crystal growth rate
		Total length	Pre-ordering	Nucleation type/rate	
Bulk		Short *From (a) and (b)*	Quicker than thin film *From (a) and (c)*	Heterogeneous (depends on purity) Quicker than homogeneous at high temperature *From (d) and (e)*	Medium *From (a), (d), (f), and (g)*
Thin Film	**As a whole**	Long *From (a) and (b)*	Slow *From (a) and (c)*	Homogeneous and Heterogeneous Depends on purity and temperature *From (d) and (e)*	Slow *From (a), (d), (f), and (g)*
	Surface layer	Shorter than other layers *From (a)*	Should be quicker than other layers because of low T_g *(assumption)*	Heterogeneous Quicker than homogeneous at low temperature *From (d) and (e)*	Quick *From (d), (f), and (g)*
	Intermediate layer	Should be longer than surface layer *(assumption)*	Should be slower than surface layer *(assumption)*	Should be mainly heterogeneous (depends on purity) Quicker than heterogeneous at high temperature *From (d) and (e)*	Should be slow *(assumption)*
	Substrate layer	Should be longer than intermediate layer *(assumption)*	Should be much slower than surface layer *(assumption)*	Heterogenous or homogenous? Should be slow *(assumption)*	Should be slow *(assumption)*

(a) My ellipsometry data and AFM images (Chapter 5)

(b) Comparison of my data and past studies (Figure 7.2)

(c) [27]Imai, et al, ***Polymer*** 1992, 33, 4457-4462

(d) [138]Wang, *et al*, ***macromolecules*** 2010, 43, 3359-3364

(e) [143]Wang, *et al*, ***macromolecules*** 2008, 41, 2548-2553

(f) [46]Massa, *et al*, ***Eur. Phys. J.*** 2003, E11, 191-198

(g) [141]Frank, *et al*, ***Science*** 1996, 273, 912-915

Basically, the induction time and the crystal growth rate of thin films were longer and slower than those in the bulk as measured by ellipsometry. The explanation for this should be from the "confinement effect" discussed in Chapter 7.1. But the surface effect would emerge in thinner films, such as the 50 nm film thickness, and this could cause

some interesting phenomenon because the surface effect is counter to the “confinement effect”. In this study, pre-ordering of thin PET film was observed, pre-ordering should occur during the induction time was shown, and the differences between thin films and bulk were discussed quantitatively. This knowledge and information will be of help for future studies in the field of polymer material science.

Chapter 8

Conclusion and Future work

8.1 Conclusion

Chapter 1 introduced the background and importance of this thesis. PET is one of the most important polymer materials for industrial fields because of its excellent material properties, many caused by its crystallinity. Therefore, it is very useful to investigate the kinetics and mechanism of PET crystallization in detail. The basic theories of polymers, their crystallization, and the special case underlying the physics in thin films and at the surface were suitably mentioned because crystallization in the bulk is different from the case of a thin film. There are already many studies of PET crystallization in the bulk but fewer for the case of thin films, especially the early stages, for example, any ordering before full crystallization, termed “pre-ordering”. Hence, this research tried to observe pre-ordering in thin PET films and investigate the kinetics, and the existing theories and literature for this study were described in Chapter 1.

Chapter 2 described the methodologies and theories of the experiments used in this study, that is, the protocol behind making thin PET samples, and the measurements used to study them; ellipsometry, atomic force microscope, and grazing incidence X-ray scattering. This chapter should be helpful for understanding how and why these methodologies were used in this study.

In Chapter 3, detailed the procedure to make good quality samples, that is, the improvement in the surface roughness of thin PET films, was described in detail. First of all, the difficulty of making thin PET film samples was shown with literature and my original data. There are very few solvents that suitably dissolve PET. PET is vulnerable and delicate to moisture and high temperature because they degrade PET, and PET is a crystalline polymer and so has high melting point. The procedures introduced in this chapter dealt successfully with these problems by choosing good combinations of

solvents and making samples under suitable conditions. Although this work might appear on the surface unsophisticated, this is one of the most important and useful sections in this thesis as high quality samples made the whole study possible.

In Chapter 4, the aging effect was found and discussed, this should be taken into account for studies of crystallization in thin polymer films. Aging, that is, the period after the sample is made strongly influences the kinetics or effectiveness of crystallization, especially during the early stages, like the induction time. The ellipsometry profile measured 1 day after preparation had a clear crystallization induction time, on the other hand, the induction time measured 3 or 4 weeks later became considerably shortened and indistinct or almost vanished. Therefore, a rule was established in my experiments, that is, the annealing or ellipsometry measurements must be implemented within 1 or 2 days after the samples were made in order to reduce the influence of this aging effect as far as possible. There was also an influence of sample thickness; the thicker film was more stable against this aging effect. This stability of the thicker films might be due to the dominance of the free surface and reduction in T_g for very thin films as mentioned in Chapter 1. I supposed this aging effect was caused by a relaxation related to molecule conformations, that is, the relaxation by annealing before crystallization should increase the trans conformation, which is similar to the order of molecules in the crystal, and pre-ordering or nucleation should also take place more easily. This phenomenon might be much more drastic in thin films because the strong surface effect reduces T_g and molecules move more easily than in the bulk.

In Chapter 5, the major part of this study, GI-WAXS, ellipsometry, and AFM were introduced. I confirmed whether a sample was crystalline or not, and that the crystals in thin PET film are identical to those seen in bulk material using GI-WAXS at first. Next, the kinetics of crystallization and how they are changed with annealing temperature and film thickness were measured by ellipsometry. The data from ellipsometry showed that lower temperature cause slower crystallization, however, there was an optimum temperature for crystallization, the same as seen in the bulk, but it seems somewhat lower than in the case of bulk because the optimum crystallization temperature of 150 nm thickness film was around 160 °C. At a thermal annealing temperature of 200 °C, the induction time and crystallization rate also slowed down again. Surface morphologies of samples were observed by AFM. Before crystallization starts, there was an intermediate state, which was clearly different from both the amorphous and crystal states in the morphology. The size of this structure was around from 10 to 30 nm. This might be the pre-ordering of thin PET film.

The validity of results of measurements related to the pre-ordering and whether it detects the pre-ordering or not were discussed with the literature in Chapter 6. It was not only GI-SAXS data but also quantitative analysis of the intermediate state implemented by the mathematical calculation of the Power Spectrum Density (PSD) from the AFM data. In the GI-SAXS measurements, there was a peak supposed to be scattered from the pre-ordering as 15 nm length scale in a sample annealed at 110 °C, and this length scale was similar to the literature in which pre-ordering detected in the bulk sample. In a sample annealed at 200 °C, there was also a similar peak although it became weak. Interestingly, that peak was shifted to lower q, that is, larger length scales, and this might correspond to the trend that crystal lamellae became larger at higher temperature annealing, such as at 200 °C. However, the much more interesting point is that there might be a pre-ordering state even for high temperature crystallization. In experimental literature, pre-ordering was referred to only for low temperature crystallization because it is difficult to detect pre-ordering during quick crystallization at higher temperature. In the discussion of the PSD, there was a peak indicating the same length scale measured by GI-SAXS, and this should indicate the possibility that the intermediate state observed in AFM images corresponds to pre-ordering. Interestingly, a PSD profile of the sample annealed at 90 °C shows that the length scale of the intermediate state was larger than that of the sample annealed at 110 °C although the crystal lamellae of 90 °C annealed samples were finer than those of 110 °C annealed samples. However, this large length scale of intermediate state might be the very early stage of pre-ordering, that is, the packing of molecules could be loose and highly swollen. The crystallization process at 90 °C is very slow, so we might be able to capture the very early stages of it. As annealing time proceeds, 6 hours, 12~24 hours, and 84 hours, the ordered texture, whether pre-ordering or crystal lamellae, became smaller, and the crystal structure of 84 hours annealed was finer than of those annealed at 110 °C. This crystallization process seems reasonable because the structure should become finer or tighter as the crystallization process proceeds and crystals made by low temperature crystallization should be smaller than for high temperature crystallization. This data capturing the thin PET film crystallization process evolution at different temperature could be useful for studies of thin polymer film crystallization in future.

Differences in crystallization and pre-ordering between bulk and thin films of PET with detailed data of kinetics measured by ellipsometry were shown in Chapter 7. Basically, the induction time and the crystal growth rate of thin films were longer and slower than those in the bulk as measured by ellipsometry. The explanation for this should be from the “confinement effect”. But the surface effect would emerge in thinner

films such as the 50 nm film thickness and this could cause some interesting phenomenon because the surface effect is counter to the “confinement effect”. In this study, pre-ordering of thin PET films was observed, that pre-ordering should occur during the induction time was shown, and the differences between thin films and bulk were discussed quantitatively. This knowledge and information will be of help for future studies in the field of polymer materials science.

8.2 Future work

The current procedure of making samples performed in Chapter 3 opened up a new path to make good thin PET film samples for studies of this kind of polymer films which are required to be flat and difficult to make. To establish this procedure has been one of the most important works of this study, and the mechanism of the pre-ordering or the very early stage of crystallization in thin PET film were predicted using samples made by this procedure. Finally, I would like to suggest some directions for future work.

8.2.1 What do we know for certain or not in this study?

The pre-ordering in thin PET films introduced in this thesis was discussed in Chapter 6 in terms of the profiles from GI-SAXS and the PSD analysis carried out on AFM data. This intermediate state between amorphous and crystal was certainly observed quantitatively for kinetics and length scale. The mechanism of the pre-ordering and the very early stage of crystallization in thin PET film were predicted as shown in Chapter 7. However, GI-SAXS profiles were limited at 150 nm thickness for 110 °C and 200 °C annealing and AFM images shown in Chapter 5 were not enough clear to see the characteristic of the pre-ordering. Hence there is room for further investigation of the pre-ordering, and the detailed structure of it was not confirmed yet in this study.

In order to solve these problems, a much greater variety of data should be effective. For example, a wide range of film thicknesses and annealing temperatures would establish the theory firmly, and much higher resolution AFM or other kind of high resolution morphology analysis would reveal whether molecules were actually ordered or not. In-situ morphology analysis would be also effective for this. Recently, there are very short measurement time AFMs, for instance, The Dimension Icon® from

Bruker Corporation and these enable in-situ observations of surface morphology. The combination of this kind of in-situ AFM and low temperature annealing would reveal how the pre-ordering progresses much more clearly.

The influence of molecular weight was not implemented in this study, but I think it should be interesting. I say this because the molecular weight would strongly influence the kinetics of nucleation and crystallization, that is, smaller / longer chains would have different reputation times and change the chain mobility and overall dynamics. Thermodynamically, the molecular weight might influence the phase diagram of liquid – liquid phase separation in the model of Olmsted *et al* [28]. If there is some kind of correlation between molecular weight and the kinetics of pre-ordering, it could be used to understand what happens during the intermediate state.

From an industrial viewpoint, the investigation of the differences between homo PET and PET copolymer would be very worthwhile, because many kinds of PET copolymers are used practically for industrial applications. Besides, if there were some trends or correlations by certain kinds of monomers, this would be a very useful clue to consider key points of the pre-ordering. Then, we can choose many kinds of monomers for the PET copolymers to accelerate or retard the crystallization behaviour, this would broaden the range of experiments and bring a wealth of important data.

8.2.2 What is undergoing during the induction time?

If we had much more evidence about pre-ordering, we could discuss very interesting and intrinsic topics, that is, “Why does spinodal-decomposition-like pre-ordering progress spontaneously?” This is very debatable and still not revealed precisely in detail yet, but the procedures to make good samples and the data acquired by this study would be the basis of further investigation for these essential questions. And in order to solve this question, attention should also be paid to molecular conformation because it affects molecule packing and crystallization kinetics mentioned in Chapter 4. For this investigation, in-situ micro-range Fourier Transform Infrared Spectroscopy (FTIR) analysis might be useful, because FTIR could detect differences of the molecular conformations and the packing of molecules. However, it may very difficult to acquire strong enough and good S/N ratio signals from very thin polymer films using FTIR measurements. But it should be worthwhile to try. A precise and detailed investigation of how a molecule moves and makes conformations during the induction time would

give insight into the intrinsic mechanisms of the thin polymer film crystallization process.

List of Figures

Bibliography

[1] Ibaragi, M. *et al.* Development of Laminated Stainless Steel Foil, “LAMINELIGHT”, for High-strength, Soft-pack Battery Packaging. *Electrochemistry* **78,** 357–359 (2010).

[2] Defosse T., M. PET demans stay solid despite slight fall-off. *Mod. Plast. Intl.* **29,** 52 (1999).

[3] Jorgensen, G. J. *et al.* Moisture transport, adhesion, and corrosion protection of PV module packaging materials. *Sol. Energy Mater. Sol. Cells* **90,** 2739–2775 (2006).

[4] Roekens, H. & Beyer, A. Big Opportunity for the Plastics Industry. *Kunststoffe Int.* 92–95 (2007).

[5] Kahnn, B. E. *et al.* The Impact of Plate Imaging Techniques on Flexographic Printed Conductive Traces. **14,** 1–8 (2012).

[6] Mahon, J. K., Brown, J. J., Zhou, T. X., Burrows, P. E. & Forrest, S. R. Requirements of flexible substrates for organic light emitting devices in flat panel display applications C3 - Proceedings, Annual Technical Conference - Society of Vacuum Coaters. *Proc. 1999 42nd Annu. Tech. Conf. Proc.* 456–459 (1999).

[7] Choi, K. H. *et al.* Characteristics of flexible indium tin oxide electrode grown by continuous roll-to-roll sputtering process for flexible organic solar cells. *Sol. Energy Mater. Sol. Cells* **93,** 1248–1255 (2009).

[8] Keddie, J. L., Jones, R. A. L. & Cory, R. A. Size-Dependent Depression of the Glass Transition Temperature in Polymer Films. *Europhys. Lett.* **27,** 59–64 (2007).

[9] Keddie, J. L., Jones, R. A. L. & Cory, R. A. Interface and surface effects on the glass-transition temperature in thin polymer films. *Faraday Discuss.* **98,** 219–230 (1994).

[10] Kawana, S. & Jones, R. A. L. Character of the glass transition in thin supported polymer films. *Phys. Rev. E - Stat. Nonlinear, Soft Matter Phys.* **63,** 1–6 (2001).

[11] Brandrup, J. & E. H. Immergut. *Polymer Handbook 3rd Edition*. I/12 (Wiley, 1989).

[12] Jones, R. A. L. *Polymers at Surface and Interfaces1st Edition*. p18, p50 (Cambridge University Press, 1999).

[13] Jones, R. A. L. *Soft Condensed Matter 1st Edition*. pp129-135 (Oxford University Press, 2002).

[14] Strobl, G. *The Physics of Polymer 3rd Edition*. p237 (Springer, 2007).

[15] Jones, R. A. L. *Soft Condensed Matter 1st Edition*. p17 (Oxford University Press, 2002).

[16] Strobl, G. *The Physics of Polymer 3rd Edition*. pp165-181 (Springer, 2007)

[17] Strobl, G. *The Physics of Polymer 3rd Edition*. pp181-205 (Springer, 2007)

[18] Allegra, G. & Meille, S. Pre-crystalline, high-entropy aggregates: A role in polymer crystallization? *Interphases Mesophases Polym. Cryst. III* 87–135 (2005). doi:10.1007/12

[19] Strobl, G. Colloquium: Laws controlling crystallization and melting in bulk polymers. *Rev. Mod. Phys.* **81,** 1287–1300 (2009).

[20] Kaji, K. *et al.* Spinodal crystallization of polymers: Crystallization from the unstable melt. *Adv. Polym. Sci.* **191,** 187–240 (2005).

[21] Yeh, G. S. Y. & Geil, P. H. Crystallization of polyethylene terephthalate from the glassy amorphous state. *J. Macromol. Sci. Part B* **1,** 235–249 (1967).

[22] Yeh, G. S. Y. A structural model for the amorphous state of polymers: Folded-chain fringed micellar grain model. *J. Macromol. Sci. Part B* **6,** 465–478 (1972).

[23] Uhlmann, D. R. Electron microscopy and SAXS studies of amorphous polymers. *Faraday Discuss. Chem. Soc.* **68,** 87–95 (1979).

[24] Geil, P. H. Additional remark. *Faraday Discuss. Chem. Soc.* **68,** 141–144 (1979).

[25] Flory, P. J. Statistical Thermodynamics of Semi-Flexible Chain Molecules. *Proc. R. Soc. London A Math. Phys. Eng. Sci.* **234,** 60–73 (1956).

[26] Imai, M., Mori, K., Mizukami, T., Kaji, K. & Kanaya, T. Structural formation of poly (ethylene terephthalate) during the induction period of crystallization: 1. Ordered structure appearing before crystal nucleation. *Polymer (Guildf).* **33,** 4451–4456 (1992).

[27] Imai, M., Mori, K., Mizukami, T., Kaji, K. & Kanaya, T. Structural formation of poly(ethylene terephthalate) during the induction period of crystallization: 2. Kinetic analysis based on the theories of phase separation. *Polymer (Guildf).* **33,** 4457–4462 (1992).

[28] Olmsted, P., Poon, W., McLeish, T., Terrill, N. & Ryan, A. Spinodal-assisted crystallization in polymer melts. *Phys. Rev. Lett.* **81,** 373–376 (1998).

[29] Mykhaylyk, O. O. *et al.* Control of structural morphology in shear-induced crystallization of polymers. *Macromolecules* **43,** 2389–2405 (2010).

[30] Terrill, N. J. *et al.* Density fluctuations: The nucleation event in isotactic polypropylene crystallization. *Polymer (Guildf).* **39,** 2381–2385 (1998).

[31] Strobl, G. *The Physics of Polymer 3rd Edition*. pp205-216 (Springer, 2007)

[32] Jones, R. A. L. *Polymers at Surface and Interfaces 1st Edition*. p8 (Cambridge University Press, 1999)

[33] Ellison, C. J. & Torkelson, J. M. The distribution of glass-transition temperatures in nanoscopically confined glass formers. *Nat. Mater.* **2,** 695–700 (2003).

[34] Hall, D. B., Hooker, J. C. & Torkelson, J. M. Ultrathin Polymer Films near the Glass Transition: Effect on the Distribution of α-Relaxation Times As Measured by Second Harmonic Generation. *Macromolecules* **30,** 667–669 (1997).

[35] Ferreiro, V., Douglas, J. F., Warren, J. & Karim, A. Growth pulsations in symmetric dendritic crystallization in thin polymer blend films. *Phys. Rev. E - Stat. Nonlinear, Soft Matter Phys.* **65,** 1–16 (2002).

[36] Padden, F. J. & Keith, H. D. Crystallization in thin films of isotactic polypropylene. *J. Appl. Phys.* **37,** 4013–4020 (1966).

[37] Billon, N., Escleine, J. M. & Haudin, J. M. Isothermal crystallization kinetics in a limited volume. A geometrical approach based on Evans' theory. *Colloid Polym. Sci.* **267,** 668–680 (1989).

[38] Billon, N. & Haudin, J. M. Overall crystallization kinetics of thin polymer films. General theoretical approach. I. Volume nucleation. *Colloid Polym. Sci.* **267,** 1064–1076 (1989).

[39] Schultz, J. M. Effect of specimen thickness on the crystallization rate. *Macromol. Rapid Commun.* **29,** 3022–3024 (1996).

[40] Dalnoki-Veress, K., Forrest, J., Massa, M., Pratt, A. & Williams, A. Crystal growth rate in ultrathin films of poly (ethylene oxide). *J. Polym. Sci. Part B Polym. Phys.* **39,** 2615–2621 (2001).

[41] Zhang, Q. M. *et al.* Critical thickness of crystallization and discontinuous change in ferroelectric behavior with thickness in ferroelectric polymer thin films. *J. Appl. Phys.* **89,** 2613 (2001).

[42] Despotopoulou, M. M., Frank, C. W., Miller, R. D. & Rabolt, J. F. Kinetics of Chain Organization in Ultrathin Poly (di- n -hexylsilane) Films. *Macromolecules* **29,** 5797–5804 (1996).

[43] Taguchi, K. *et al.* Growth shape of isotactic polystyrene crystals in thin films. *Polymer (Guildf).* **42,** 7443–7447 (2001).

[44] Massa, M. V, Dalnoki-Veress, K. & Forrest, J. a. Crystallization kinetics and crystal morphology in thin poly(ethylene oxide) films. *Eur. Phys. J. E. Soft Matter* **11,** 191–198 (2003).

[45] Sawamura, S., Miyaji, H., Izumi, K., J. Sutton, S. & Miyamoto, Y. Growth Rate of Isotactic Polystyrene Crystals in Thin Films. *J. Phys. Soc. Japan* **67,** 3338–3341 (1998).

[46] Ma, Y., Hu, W. & Reiter, G. Lamellar crystal orientations biased by crystallization kinetics in polymer thin films. *Macromolecules* **39,** 5159–5164 (2006).

[47] Schönherr, H. & Frank, C. W. Ultrathin films of poly(ethylene oxides) on oxidized silicon. 1: Spectroscopic characterization of film structure and crystallization kinetics. *Macromolecules* **36,** 1188–1198 (2003).

[48] Hutchinson, J. M. Physical aging of polymers. *Prog. Polym. Sci.* **20,** 703–760 (1995).

[49] Murthy, N. S., Correale, S. T. & Minor, H. Structure of the amorphous phase in crystallizable polymers: poly(ethylene terephthalate). *Macromolecules* **24,** 1185–1189 (1991).

[50] Sakai, Y., Imai, M., Kaji, K. & Tsuji, M. Growth Shape Observed in Two-Dimensional Poly(ethylene terephthalate) Spherulites. *Macromolecules* **29,** 8830–8834 (1996).

[51] Jukes, P. C. *et al.* Kinetics of surface crystallization in thin films of poly(ethylene terephthalate). *Macromolecules* **38,** 2315–2320 (2005).

[52] Hobbs, J. K., Humphris, a. D. L. & Miles, M. J. In-situ atomic force microscopy of polyethylene crystallization. 1. Crystallization from an oriented backbone. *Macromolecules* **34,** 5508–5519 (2001).

[53] Imai, M., Kaji, K., Kanaya, T. & Sakai, Y. Ordering process in the induction period. *Phys. Rev. B* **52,** 12696 (1995).

[54] Imai, M., Kaji, K. & Kanaya, T. Structural Formation of Poly(ethylene terephthalate) during the Induction Period of Crystallization. 3. Evolution of Density Fluctuations to Lamellar Crystal. *Macromolecules* **27,** 7103–7108 (1994).

[55] J. Ryan, A., Patrick A. Fairclough, J., J. Terrill, N., D. Olmsted, P. & C. K. Poon, W. A scattering study of nucleation phenomena in polymer crystallisation. *Faraday Discuss.* **112,** 13–29 (1999).

[56] Blundell, D. J. *et al.* Characterization of strain-induced crystallization of poly(ethylene terephthalate) at fast draw rates using synchrotron radiation. *Polymer (Guildf).* **37,** 3303–3311 (1996).

[57] Keum, J. K. *et al.* Crystallization and transient mesophase structure in cold-drawn PET fibers. *Macromolecules* **36,** 9873–9878 (2003).

[58] Durell, M. *et al.* The Role of Surface-Induced Ordering in the Crystallisation of PET Films. *EPL (Europhysics Lett.* **58,** 844–850 (2002).

[59] Bertoldo, M., Labardi, M., Rotella, C. & Capaccioli, S. Enhanced crystallization kinetics in poly(ethylene terephthalate) thin films evidenced by infrared spectroscopy. *Polymer (Guildf).* **51,** 3660–3668 (2010).

[60] Shinotsuka, K., Bliznyuk, V. N. & Assender, H. E. Near-surface crystallization of PET. *Polymer (Guildf).* **53,** 5554–5559 (2012).

[61] Seydel, T., Tolan, M., Ocko, B. M., Seeck, O. H., Weber, R., DiMasi, E., & Press, W. Freezing of capillary waves at the glass transition. *Phys. Rev. B* **65,** 1–7 (2002).

[62] Doerr, A. K., Tolan, M., Pange, W., Scklomka, J. –P., Seydel, T., & Press, W. Observation of Capillary Waves on Liquid Thin Films from Mesoscopic to Atomic Length Scales. *Phys. Rev. Lett.* **83,** 3470–3473 (1999).

[63] Sokkar, T. Z. N., El-Farahary, K. A. & El-Bakary, M. A. Determination of optical properties, dispersion, and structural parameters of poly(ethylene terephthalate) fibers using automatic variable wavelength interferometry technique. *J. Appl. Polym. Sci.* **89,** 1737–1742 (2003).

[64] Jukes, P. C., Heriot, S. Y., Sharp, J. S. & Jones, R. A. L. Time-Resolved Light Scattering Studies of Phase Separation in Thin Film Semiconducting Polymer Blends during Spin-Coating. *Macromolecules* **38,** 2030–2032 (2005).

[65] Heriot, S. Y. & Jones, R. A. L. An interfacial instability in a transient wetting layer leads to lateral phase separation in thin spin-cast polymer-blend films. *Nat. Mater.* **4,** 782–786 (2005).

[66] Dunbar, A. D. F. *et al.* A solution concentration dependent transition from self-stratification to lateral phase separation in spin-cast PS:d-PMMA thin films. *Eur. Phys. J. E* **31,** 369–375 (2010).

[67] Wang, T. *et al.* The development of nanoscale morphology in polymer:fullerene photovoltaic blends during solvent casting. *Soft Matter* **6,** 4128–4134 (2010).

[68] Dunn, D. S. & Ouderkirk, A. J. Chemical and physical properties of laser-modified polymers. *Macromolecules* **23,** 770–774 (1990).

[69] Azzam, R. M. A. and Bashara, N. M. *Ellipsometry and Polarized light Paperback Edition*. Chapter 4 (North-Holland Physics Publishing a division of Elsevier Science Publishers B. V., 1987).

[70] Heavens, O. S. in *Physics of Thin Films*, vol.2, Hass, G. and Thun, R. E. Eds. (Academic Press, New York, 1967).

[71] *M-2000V Spectroscopic Ellipsometer Hardware Manual*. (J. A. Woollam Co. Inc., 2008).

[72] *Guide to using WVASE32. 2008*. (J. A. Woollam Co. Inc., 2008).

[73] Passaglia, E., Stromberg, R. R., Kruger, J. *Ellipsometry in the measurement of surfaces and thin films : symposium proceedings Washington 1963* pp161-164 (National Bureau of Standards (U.S), 1964).

[74] Roseler, A. Infrared Spectroscopic *Ellipsometry* pp35-37 (Akademie-Verlag Berlin, 1990).

[75] Jones, A. L. R. & Richards, R. W. *Polymers at Surface and Interfaces* pp61-63 (Cambridge University Press, 1999).

[76] Ogieglo, W., Wormeester, H., Eichhorn, K-J., Wessling, M., Benes, N. E. *Progress in Polymer Science* **42,** 42–78 (2015).

[77] Brandrup, J. & E. H. Immergut. *Polymer Handbook 3rd Edition* in VI–59 (Wiley, 1989).

[78] Fontaine, F., Ledent, J., Groeninckx, G. & Reynaers, H. Morphology and melting behaviour of semi-crystalline poly(ethylene terephthalate): 3. Quantification of crystal perfection and crystallinity. *Polymer (Guildf).* **23,** 185–191 (1982).

[79] Flores, A., Pieruccini, M., Nöchel, U., Stribeck, N. & Baltá Calleja, F. J. Recrystallization studies on isotropic cold-crystallized PET: Influence of heating rate. *Polymer (Guildf).* **49,** 965–973 (2008).

[80] Iiyama, K., Ishida, T., Ono, Y., Maruyama, T. & Yamagishi, T. Fabrication and characterization of amorphous polyethylene terephthalate optical waveguides. *IEEE Photonics Technol. Lett.* **23,** 275–277 (2011).

[81] Martínez-Antón, J. C. & Bernabeu, E. Spectrogoniometry and the WANTED method for thickness and refractive index determination. *Thin Solid Films* **313–314,** 85–89 (1998).

[82] Strobl, G. R. *The Physics of Polymers 3rd Edition*. P168 (Springer, 2007).

[83] Jones, R. A. L. *Polymers at Surface and Interfaces*. p121 (Cambridge University Press, 1999).

[84] Kowalewski, T. & Legleiter, J. Imaging stability and average tip-sample force in tapping mode atomic force microscopy. *J. Appl. Phys.* **99,** 1–5 (2006).

[85] Kawana, S. *et al.* X-ray diffraction study of the structure of thin polyfluorene films. *Polymer (Guildf).* **43,** 1907–1913 (2002).

[86] Factor, B. J., Russell, T. P. & Toney, M. F. Grazing incidence x-ray scattering studies of thin films of an aromatic polyimide. *Macromolecules* **26,** 2847–2859 (1993).

[87] Macdonald, J. E. *et al.* Applications of grazing incidence diffraction to polymer surfaces. *Radiat. Phys. Chem.* **71,** 811–815 (2004).

[88] Marques, M. J., Pina, J. C. P. & Dias, A. M. Influence of Surface Roughness on the Quality of Data Obtained by Pseudo-Grazing Incidence X-Ray Diffraction. *Mater. Sci. Forum* **514-516,** 1618–1622 (2006).

[89] Streinz, C. C., Wagner, J. w., & Kruger, J. Analysis of Passive Film Growth by Dynamic Imaging Microellipsometry. *J. Electrochem. Soc.* **139,** 711 (1992).

[90] Ohlídal, I., Luke, F. & Navrátil, K. Rugositéthe Problem of Surface Roughness in Ellipsometry and Reflectometry. *Le J. Phys. Colloq.* **38,** C5–77–C5–88 (1977).

[91] Moore, W. R. & Sanderson, D. Viscosities of dilute solutions of polyethylene terephthalate. *Polymer* **9,** 153–158 (1968).

[92] Sushkov, V. I., Gusev, S. S., Perepelkin, A. N., Minyailo, S. A. & Bablyuk, Y. B. Study of the active influence of some solutions on the surface of polyethylene terephthalate films. *Polymer Science U.S.S.R.* **26,** 2560–2569 (1984).

[93] Ohoya, S., Hasegawa, T., Tsubakiyama, K., & Matsuo, T. Ultracentrifugal Characterization of Poly(ethylene terephthalate) in Dilute Solutions. *Polymer Journal* **33,** 113-120 (2001)

[94] Strawhecker, K. E., Kumar, S. K., Douglas, J. F. & Karim, A. The Critical Role of Solvent Evaporation on the Roughness of Spin-Cast Polymer Films. *Macromolecules* **34,** 4669–4672 (2001).

[95] Kiflie, Z., Piccarolo, S., Brucato, V. & Baltá-Calleja, F. J. Role of thermal history on quiescent cold crystallization of PET. *Polymer* **43,** 4487–4493 (2002).

[96] Desaif, A. B. & Wilkes, G. L. SOLVENT-INDUCED CRYSTALLIZATION OF POLYETHYLENE TEREPHTHALATE. **319,** 291–319 (1974).

[97] Kulshreshtha, A. K., Khan, A. H. & Madan, G. L. X-ray diffraction study of solvent-induced crystallization in polyester filaments. *Polymer* **19,** 819–823 (1978).

[98] Samperi, F., Puglisi, C., Alicata, R. & Montaudo, G. Thermal degradation of poly(ethylene terephthalate) at the processing temperature. *Polym. Degrad. Stab.* **83,** 3–10 (2004).

[99] Allen, N. S., Edge, M., Mohammadian, M. & Jones, K. Physicochemical Aspects of the Environmental Degradation of Poly(Ethylene-Terephthalate). *Polym. Degrad. Stab.* **43,** 229–237 (1994).

[100] Sammon, C., Yarwood, J. & Everall, N. FT-IR study of the effect of hydrolytic degradation on the structure of thin PET films. *Polym. Degrad. Stab.* **67,** 149–158 (2000).

[101] Al-AbdulRazzak, S. & Jabarin, S. A. Processing characteristics of poly(ethylene terephthalate): hydrolytic and thermal degradation. *Polym. Int.* **51,** 164–173 (2002).

[102] Jones, R. A. L., Norton, L. J., Shull, K. R., Kramer, E. J., Felcher, G. P., Karim, A., & Fetters, L. J. Interfacial segment density profiles of end-anchored polymers in a melt. *Macromolecules* **25,** 2359–2368 (1992).

[103] Weill, A. & Dechenaux, E. The spin-coating process mechanism related to polymer solution properties. *Polym. Eng. Sci.* **28,** 945–948 (1988).

[104] Haas, D. E., Birnie, D. P., Zecchino, M. J. & Figueroa, J. T. The effect of radial position and spin speed on striation spacing in spin on glass coatings. *J. Mater. Sci. Lett.* **20,** 1763–1766 (2001).

[105] Birnie, D. P. Solving spin-coating problems. *Solid state Technol.* S31–S33 (1999).

[106] Mellbring, O., Øiseth, S. K., Krozer, a, Lausmaa, J. & Hjertberg, T. Spin Coating and Characterization of Thin High-Density Polyethylene Films. *Macromolecules* 7496–7503 (2001).

[107] Wang, C.-T. & Yen, S.-C. Theoretical analysis of film uniformity in spinning processes. *Chem. Eng. Sci.* **50,** 989–999 (1995).

[108] Gu, J., Bullwinkel, M. D. & Campbell, G. A. Solvent concentration measurement for spin coating. *J. Appl. Polym. Sci.* **57,** 717–725 (1995).

[109] Mokarian-Tabari, P., Geoghegan, M., Howse, J. R., Heriot, S. Y., Thompson, R. L., & Jones, R. A. L. Quantitative evaluation of evaporation rate during spin-coating of polymer blend films: Control of film structure through defined-atmosphere solvent-casting. *Eur. Phys. J. E* **33,** 283–289 (2010).

[110] Kozuka, H. & Hirano, M. Radiative striations and surface roughness of alkoxide-derived spin coating films. *J. Sol-Gel Sci. Technol.* **19,** 501–504 (2000).

[111] Skrobis, K. J., Denton, D. D. & Skrobis, A. V. Effect of early solvent evaporation on the mechanism of the spin-coating of polymeric solutions. *Polym. Eng. Sci.* **30,** 193–196 (1990).

[112] Gardon, J. L. & Teas, J. P. *Volume 2: Characterization of Coatings: Physical Techniques Part 2 Chapter 8: Solubility Parameters*. *Treatise on Coatings* (Marcel Dekker, INC., 1976).

[113] Jaw, C. G., Chen, I. M., Yen, J. H. & Wang, Y. S. Partial solubility parameters of chlorobenzene and chlorophenol compounds at equilibrium distribution in two immiscible phases. *Chemosphere* **39,** 2607–2620 (1999).

[114] Brandrup, J. & E. H. Immergut. *Polymer Handbook 3rd Edition*. VII-556 (Wiley, 1989).

[115] National Institute of Standards of Technology (USA). NIST Chemistry WebBook. at < http://webbook.nist.gov/chemistry/name-ser.html>

[116] Yoshii, T., Yoshida, H. & Kawai, T. Effect of structural relaxation of glassy PET on crystallization process observed by the simultaneous DSC-XRD and DSC-FTIR. *Thermochim. Acta* **431,** 177–181 (2005).

[117] Kingsley, J. W., Marchisio, P. P., Yi H., Iraqi, A., Kinane, C. J., Langridge, S. , Thompson, R. L., Cadby, A. J., Pearson, A. J., Lidzey, D. G., Jones, R. A. L., Parnell, A. J. Molecular weight dependent vertical composition profiles of PCDTBT:PC71BM blends for organic photovoltaics. *Nature Scientific Reports* art No. 5286 (2014).

[118] Radhakrishnan, J. & Kaito, A. Structure formation during the isothermal crystallization of oriented amorphous poly (ethylene terephthalate) films. *Polymer* **42,** 3859–3866 (2001).

[119] Lu, X. F. & Hay, J. N. Crystallization orientation and relaxation in uniaxially drawn poly(ethylene terephthalate). *Polymer* **42,** 8055–8067 (2001).

[120] Schmidt-Rohr, K. Elucidation of the Chain Conformation in a Glassy Polyester, PET, by Two-Dimensional NMR. *Science* **280,** 714–717 (1998).

[121] Huang, J., Hu, W. & Zumbulyadis, N. Conformational changes and molecular motion of poly(ethylene terephthalate) annealed above glass transition temperature. *Polymer* **41,** 1741–1748 (2000).

[122] Alves, N. M., Mano, J. F., Balaguer, E. & Duen, J. M. M. Glass transition and structural relaxation in semi-crystalline poly(ethylene terephthalate): A DSC study. *Polymer* **43,** 4111–4122 (2002).

[123] Rueda, D. R., Gutiérrez, M. C. G., Calleja, F. J. B. & Piccarolo, S. Order in the amorphous state of poly(ethylene terephthalate) as revealed by microhardness: Creep behavior and physical aging. *Int. J. Polym. Mater. Polym. Biomater.* **51,** 897–908 (2002).

[124] Baltá Calleja, F. J., García Gutiérrez, M. C., Rueda, D. R. & Piccarolo, S. Structure development in poly(ethylene terephthalate) quenched from the melt at high cooling rates: X-ray scattering and microhardness study. *Polymer* **41,** 4143–4148 (2000).

[125] Zia, Q., Ingolič, E. & Androsch, R. Surface and bulk morphology of cold-crystallized poly(ethylene terephthalate). *Colloid Polym. Sci.* **288,** 819–825 (2010).

[126] Jackson, J. B. & Longman, G. W. The crystallization of poly(ethylene terephthalate) and related copolymers. *Polymer (Guildf).* **10,** 873–884 (1969).

[127] Yang, H., Bhimaraj, P., Yang, L., Siegel, R. & Schadler, L. S. Crystal growth in alumina/poly(ethylene terephthalate) nanocomposite films. *J. Polym. Sci. Part B Polym. Phys.* **45,** 747–757 (2007).

[128] Santa Cruz, C., Stribeck, N., Zachmann, H. G. & Balta Calleja, F. J. Novel aspects in the structure of poly(ethylene terephthalate) as revealed by means of small angle x-ray scattering. *Macromolecules* **24,** 5980–5990 (1991).

[129] Kaji, K. *Structure Formation in PET during the Induction Period of Crystallization*. *Handbook of Thermoplastic Polyesters* (2005). doi:10.1002/3527601961.ch4a

[130] Nishida, K., Kaji, K., Kanaya, T., Matsuba, G. & Konishi, T. Spinodal patterns indicating unstable regime of polymer crystallization. *J. Polym. Sci. Part B Polym. Phys.* **42,** 1817–1822 (2004).

[131] Viville, P., Biscarini, F. & Bre, J. L. Scaling Aspects of the Kinetics of Thermally Induced Phase Separation in Bisphenol A Polycarbonate / Poly (methyl methacrylate) Blends. *J. Phys. Chem.* **105,** 7499–7507 (2001).

[132] Dumas, P. *et al.* Quantitative Microroughness Analysis down to the Nanometer Scale. *Europhys. Lett.* **22,** 717–722 (2007).

[133] Duparre, A. Light scattering of thin dielectric films, Thin films for optical coatings, ed. Hummel, R. & Guenther, K., pp. 273-303 (CRC Press, Boca Raton, 1995).

[134] Duparre, A., Kaiser, N., & Heaton, M. G. Using Atomic Force Microscopy (AFM) for Enginnering Low-Scatter Thin Film Optics, (Application note of Bruker corp.).

[135] Ohnaga, T., Chen, W. & Inoue, T. Structure development by reaction-induced phase separation in polymer mixtures: computer simulation of the spinodal decomposition under the non-isoquench depth. *Polymer (Guildf).* **35,** 3774–3781 (1994).

[136] Cobbs, W. H. & Burton, R. L. Crystallization of polyethylene terephthalate. *J. Polym. Sci.* **10,** 275–290 (1953).

[137] Matsuba, G., Kaji, K., Kanaya, T. & Nishida, K. Detailed analysis of the induction period of polymer crystallization by depolarized light scattering. *Phys. Rev. E* **65,** 61801 (2002).

[138] Wang, H., Keum, J. K., Hiltner, A. & Baer, E. Crystallization kinetics of poly(ethylene oxide) in confined nanolayers. *Macromolecules* **43,** 3359–3364 (2010).

[139] Escleine, J. M., Monasse, B., Wey, E. & Haudin, J. M. Influence of specimen thickness on isothermal crystallization kinetics. A theoretical analysis. *Colloid Polym. Sci.* **262,** 366–373 (1984).

[140] Napolitano, S. & Wübbenhorst, M. Effect of a reduced mobility layer on the interplay between molecular relaxations and diffusion-limited crystallization rate in ultrathin polymer films. *J. Phys. Chem. B* **111,** 5775–5780 (2007).

[141] Frank, C. W. *et al.* Structure in Thin and Ultrathin Spin-Cast Polymer Films. *Science* **273,** 912–915 (1996).

[142] Flores, a. *et al.* Finite size effects in multilayered polymer systems: Development of PET lamellae under physical confinement. *Polymer (Guildf).* **51,** 4530–4539 (2010).

[143] Wang, Y., Chan, C.-M., Ng, K.-M. & Li, L. What Controls the Lamellar Orientation at the Surface of Polymer Films during Crystallization? *Macromolecules* **41,** 2548–2553 (2008).

[144] Forrest, J. A., Dalnoki-Veress, K. & Dutcher, J. R. Interface and chain confinement effects on the glass transition temperature of thin polymer films. *Phys. Rev. E* **56,** 5705–5716 (1997).

[145] Forrest, J. A. & Mattsson, J. Reductions of the glass transition temperature in thin polymer films: Probing the length scale of cooperative dynamics. *Phys. Rev. E* **61,** R53–R56 (2000).

[146] Forrest, J. A., Dalnoki-Veress, K., Stevens, J. R. & Dutcher, J. R. Effect of Free Surfaces on the Glass Transition Temperature of Thin Polymer Films. *Phys. Rev. Lett.* **77,** 2002–2005 (1996).